

Computational fluid dynamics simulation of fluidized bed polymerization reactors

by

Rong Fan

A dissertation submitted to the graduate faculty
in partial fulfillment of the requirements for the degree of
DOCTOR OF PHILOSOPHY

Major: Chemical Engineering

Program of Study Committee:
Rodney O. Fox, Major Professor
David K. Hoffman
James C. Hill
Dennis R. Vigil
Francine Battaglia

Iowa State University

Ames, Iowa

2006

Copyright © Rong Fan, 2006. All rights reserved.

UMI Number: 3229070

INFORMATION TO USERS

The quality of this reproduction is dependent upon the quality of the copy submitted. Broken or indistinct print, colored or poor quality illustrations and photographs, print bleed-through, substandard margins, and improper alignment can adversely affect reproduction.

In the unlikely event that the author did not send a complete manuscript and there are missing pages, these will be noted. Also, if unauthorized copyright material had to be removed, a note will indicate the deletion.

UMI[®]

UMI Microform 3229070

Copyright 2006 by ProQuest Information and Learning Company.

All rights reserved. This microform edition is protected against unauthorized copying under Title 17, United States Code.

ProQuest Information and Learning Company
300 North Zeeb Road
P.O. Box 1346
Ann Arbor, MI 48106-1346

Graduate College
Iowa State University

This is to certify that the doctoral dissertation of
Rong Fan
has met the dissertation requirements of Iowa State University

Signature was redacted for privacy.

Major Professor

Signature was redacted for privacy.

For the Major Program

TABLE OF CONTENTS

LIST OF TABLES	vi
LIST OF FIGURES	viii
CHAPTER 1. INTRODUCTION	1
1.1 Motivation and Objectives	1
1.2 Outline	4
CHAPTER 2. REVIEW OF FLUIDIZED BED POLYMERIZATION RE- ACTORS	6
2.1 Fluidized Bed Polymerization Reactors	6
2.2 Simplified Kinetic Mechanism of Olefin Copolymerization	8
CHAPTER 3. BASIC THEORY AND NUMERICAL METHODS	12
3.1 Multi-Fluid Continuum Model	12
3.1.1 Governing Equations	13
3.1.2 Constitutive Relations	15
3.1.3 Kinetic Theory of Granular Flow	24
3.2 DQMOM for Population Balance Equation	27
3.2.1 Monovariate Population Balance	28
3.2.2 Bivariate Population Balance	32
3.2.3 Aggregation and Breakage Equation	36
3.2.4 DQMOM-Multi-Fluid Model	39
3.3 Numerical Methods	42
3.3.1 Discretization	42

3.3.2	Solution Algorithm	43
3.3.3	Time-Splitting Method	44
3.3.4	Grid Resolution Study	45
CHAPTER 4. APPLICATION OF DQMOM TO POLYDISPERSE GAS-		
SOLID FLUIDIZED BEDS		
4.1	Introduction	50
4.2	The DQMOM-Multi-Fluid Model	54
4.2.1	Multi-Fluid Model for Gas-Solid Flow	54
4.2.2	Direct Quadrature Method of Moments	57
4.3	Implementation of Aggregation and Breakage	62
4.4	Results and Discussion	65
4.4.1	Constant Kernels	67
4.4.2	Kinetic-Theory Kernels	75
4.4.3	Effect of the Aggregation Success Factor	78
4.4.4	Effect of the Fragment Distribution Function	80
4.5	Conclusions	81
CHAPTER 5. SEGREGATION IN POLYDISPERSE FLUIDIZED BEDS:		
VALIDATION OF A MULTI-FLUID MODEL		
5.1	Introduction	84
5.2	Multi-Fluid Model Description	86
5.3	Results and Discussion	90
5.3.1	Binary PSD	90
5.3.2	Continuous PSD	96
5.4	Conclusions	103
CHAPTER 6. COMPUTATIONAL FLUID DYNAMICS MODELING OF		
UNIPOL GAS-PHASE REACTORS		
6.1	Introduction	113
6.2	Polymerization Kinetics and Multi-fluid Model	116

6.2.1	Polymerization Kinetics for Metallocene Catalyst	116
6.2.2	Multi-Fluid Model	117
6.3	Results and Discussion	120
6.3.1	Validation of Fluid Dynamics for a PE Pilot-Scale Fluidized Bed	121
6.3.2	Chemical Reaction Engineering Model and Kinetic Parameters Study	134
6.3.3	Effect of Catalyst PSD on the Overheating and Final Polymer PSD	140
6.3.4	Effect of Intrinsic Kinetics on the Overheating and Final Polymer PSD	149
6.3.5	Investigation of Particle Segregation and Hot Spots in a Fluidized Bed Using CFD	152
6.4	Conclusion	153
CHAPTER 7. Conclusion and Future Work		157
ACKNOWLEDGEMENTS		170
APPENDIX Matlab codes used in Chapter 6		171

LIST OF TABLES

Table 2.1	Comparison of three major industrial processes for the productions of PP and PE.	7
Table 3.1	Particle properties and parameters used in the simulation.	46
Table 3.2	Results comparison for three different resolutions.	47
Table 4.1	Constitutive relations for gas and solids stress tensors and the solids collision parameters.	56
Table 4.2	Gas-solid and solid-solid interaction forces	57
Table 4.3	The computational domain and solids physical properties in the simulation.	66
Table 4.4	Initial values of particle diameters ($d_{p\alpha}$) and solid-phase volume fractions ($\varepsilon_{s\alpha}$) for $N = 2, 3$ and 4 for the same initial PSD.	66
Table 5.1	Constitutive relations for gas and solids stress tensors.	88
Table 5.2	Different cases simulated with Eulerian-Eulerian model	91
Table 5.3	Properties of solid phases used in the Eulerian-Eulerian simulation. . .	91
Table 5.4	Simulation system properties.	97
Table 5.5	Particle diameters and weights for System 1 with $N = 2 - 4$	98
Table 5.6	Particle diameters and weights for System 4 using $N = 2 - 4$	102
Table 6.1	Typical operating conditions for gas-phase polymerization reactors. . .	124
Table 6.2	Multiprocessor performance for 3D simulations using 2, 4, 8, 16 and 32 processors.	131

Table 6.3	Different cases conducted in Univation Technology for a lab reactor. . .	136
Table 6.4	Kinetic rate data ($\ln k = \ln k_0 - \Delta E/RT$) for Cases 1-5 obtained from two sites model fitting at middle temperature [normalized by the rate data of case 5 (site 2)].	137
Table 6.5	Relative temperature rise and age associated with each node	153

LIST OF FIGURES

Figure 1.1	Length scales and phenomena involved in polyolefin processes.	3
Figure 1.2	CFD algorithm for simulation of FB polymerization reactors.	5
Figure 2.1	The simplified picture of a polymer particle with catalyst fragments.	9
Figure 2.2	Schematic representation of a polymerization fluidized bed reactor unit	10
Figure 3.1	Three main forms of viscous dissipation in a granular flow	20
Figure 3.2	General principle of dissipation in the granular kinetic theory	26
Figure 3.3	A staggered grid for a computation cell	42
Figure 3.4	The fluidized bed geometry for the simulation	47
Figure 3.5	Instantaneous contour plots of gas volume fraction at 5s with different resolutions. Left: coarse grid. Middle: medium grid. Right: fine grid.	48
Figure 3.6	Instantaneous vector plots of gas velocity at 5s with different resolutions. Left: coarse grid. Middle: medium grid. Right: fine grid.	48
Figure 3.7	Instantaneous contour plots of granular temperature at 5s with different resolutions. Left: coarse grid. Middle: medium grid. Right: fine grid.	49
Figure 4.1	Volume-average mean particle size (d_{32}) for $N = 2$ (filled symbols), $N = 3$ (empty symbols) and $N = 4$ (lines).	68
Figure 4.2	PSD at the middle of the FB at 0, 5, 10 and 15 s for Case 2.	69
Figure 4.3	PSD at the middle of the FB at 0, 5, 10 and 15 s for Case 3.	69
Figure 4.4	Volume-average normalized moments for Case 2 using $N = 2$ (filled symbols), $N = 3$ (empty symbols) and $N = 4$ (lines).	70

Figure 4.5	Volume-average, normalized moments for Case 3 using $N = 2$ (filled symbols), $N = 3$ (empty symbols) and $N = 4$ (lines).	71
Figure 4.6	Time evolution of the spatial distribution of the mean particle size (d_{32}) for Case 2 using $N = 2$	72
Figure 4.7	Time evolution of the spatial distribution of the mean particle size (d_{32}) for Case 2 using $N = 3$	73
Figure 4.8	Time evolution of the spatial distribution of the mean particle size (d_{32}) for Case 2 using $N = 4$	74
Figure 4.9	Volume-average mean particle size for Case 4.	77
Figure 4.10	Volume-average mean particle size for Case 5.	77
Figure 4.11	Contour plots of the gas volume fraction at 6 s. a: Case 1. b: Case 4. c: Case 5.	78
Figure 4.12	Pressure drop fluctuations in gas-solid fluidized bed for three different values of the aggregation success factor. a: $\Psi_a = 0.001$. b: $\Psi_a = 0.0005$. c: $\Psi_a = 0.0001$. Note that the pressure fluctuations cease when the bed defluidizes.	79
Figure 4.13	Effect of the value of the aggregation success factor (Ψ_a) on the volume-average mean particle size.	80
Figure 4.14	Effect of symmetric fragmentation versus erosion on the volume-average mean particle size.	81
Figure 4.15	Comparison between symmetric fragmentation (solid lines) and erosion (dashed lines). a: abscissas. b: solid volume fractions. c: weights.	82
Figure 5.1	Evolution of relative segregation with time for base case.	92
Figure 5.2	Snapshots of the void fraction of large particles from simulation for case 1.	93
Figure 5.3	Snapshots of the void fraction of large particles from simulation for case 2.	93

Figure 5.4	Evolution of relative segregation rate with time. Left: case 1. Right: case 2.	95
Figure 5.5	The volume-fraction-weighted, bed-averaged granular temperature as a function of time from simulation. Left: case 1. Right: case 2.	95
Figure 5.6	The normalized mean diameter of the local size distribution along the bed height for System 1.	104
Figure 5.7	The normalized standard deviation of the local size distribution along the bed height for System 1.	105
Figure 5.8	The normalized mean diameter of the local size distribution across the bed for System 1.	106
Figure 5.9	The normalized standard deviation of the local size distribution across the bed for System 1.	107
Figure 5.10	The normalized mean diameter of the local size distribution along the bed height for System 2.	108
Figure 5.11	The normalized mean diameter of the local size distribution along the bed height for System 4.	109
Figure 5.12	The normalized standard deviation of the local size distribution along the bed height for System 4.	110
Figure 5.13	The normalized mean diameter of the local size distribution across the bed for System 4.	111
Figure 5.14	The normalized standard deviation of the local size distribution across the bed for System 4.	112
Figure 6.1	Gas-phase fluidized bed olefin polymerization process (UNIPOL process)	122
Figure 6.2	Sketch of PE pilot-scale fluidized bed reactor	123
Figure 6.3	Instantaneous gas void fraction at 2 s, 4 s, 6 s, 8 s and 10 s from 2D simulation.	125
Figure 6.4	Instantaneous gas void fraction at 2 s, 4 s, 6 s, 8 s and 10 s from 3D simulation.	126

Figure 6.5	Comparison of pressure drop along the two taps for 2D and 3D simulations.	127
Figure 6.6	Comparison of time-averaged gas velocity for 2D (blue) and 3D (red) simulations.	128
Figure 6.7	The normalized pressure drop signal for experiment, 2D and 3D simulations.	129
Figure 6.8	The power spectra of the pressure fluctuation from experiments, 2D and 3D simulations	129
Figure 6.9	Power spectra results at low frequency from experiments, 2D and 3D simulations.	130
Figure 6.10	Speed up for 3D simulations of pilot-scale fluidized bed using 2, 4, 8, 16 and 32 processors on hpc3.	132
Figure 6.11	Efficiency for 3D simulations of pilot-scale fluidized bed using 2, 4, 8, 16 and 32 processors on hpc3.	133
Figure 6.12	Two sites model fitted with experimental data for Case 1. Red: high temperature; Green: middle temperature; Blue: Low temperature) (the reaction rate and time are scaled by a constant).	137
Figure 6.13	Two sites model fitted with experimental data for Case 2. Red: high temperature; Green: middle temperature; Blue: Low temperature) (the reaction rate and time are scaled by a constant).	138
Figure 6.14	Two sites model fitted with experimental data for Case 3. Red: high temperature; Green: middle temperature; Blue: Low temperature) (the reaction rate and time are scaled by a constant).	138
Figure 6.15	Two sites model fitted with experimental data for Case 4. Red: high temperature; Green: middle temperature; Blue: Low temperature) (the reaction rate and time are scaled by a constant).	139

Figure 6.16	Two sites model fitted with experimental data for Case 5. Red: high temperature; Green: middle temperature; Blue: Low temperature) (the reaction rate and time are scaled by a constant).	139
Figure 6.17	Flow chart of combining QMOM with CRE model to investigate the effect of catalyst PSD on the overheating and final polymer PSD (drive-moments.m, odefunc.m, quad.m).	142
Figure 6.18	Catalyst particle size distribution.	143
Figure 6.19	Evolution of particle diameters with age using two nodes for case 5. . .	144
Figure 6.20	Evolution of particle temperature rise with age using two nodes for case 5.	144
Figure 6.21	Evolution of particle diameters with age using three nodes for case 5. .	145
Figure 6.22	Evolution of particle temperature rise with age using three nodes for case 5.	146
Figure 6.23	Comparison of PSD of catalyst and polymer with predicted PSD from QMOM using two nodes or three nodes for case5.	148
Figure 6.24	Percentage of polymer particle above a certain temperature for case 5.	148
Figure 6.25	Evolution of particle temperature rise with particle size using three nodes for case 1.	149
Figure 6.26	Evolution of particle temperature rise with particle size using three nodes for case 2.	150
Figure 6.27	Evolution of particle temperature rise with particle size using three nodes for case 3.	150
Figure 6.28	Evolution of particle temperature rise with particle size using three nodes for case 4.	151
Figure 6.29	Evolution of particle temperature rise with particle size using three nodes for case 5.	151
Figure 6.30	Comparison of PSD of catalyst and polymer with predicted PSD from QMOM using three nodes for case 1 to case 5.	152

Figure 6.31	Average particle size along the bed height.	154
Figure 6.32	The number of particles for each node at 15 s, a: first node b: second node c: third node.	155
Figure 6.33	Average particle temperature rise profile at 15 s.	156

CHAPTER 1. INTRODUCTION

1.1 Motivation and Objectives

Fluidized beds (FB) reactors are widely used in the polymerization industry due to their superior heat- and mass-transfer characteristics. Nevertheless, problems associated with local overheating of polymer particles and excessive agglomeration leading to FB reactors defluidization still persist and limit the range of operating temperatures that can be safely achieved in plant-scale reactors. Many people have been worked on the modeling of FB polymerization reactors, and quite a few models are available in the open literature, such as the well-mixed model developed by McAuley, Talbot, and Harris (1994), the constant bubble size model (Choi and Ray, 1985) and the heterogeneous three phase model (Fernandes and Lona, 2002). Most these research works focus on the kinetic aspects, but from industrial viewpoint, the behavior of FB reactors should be modeled by considering the particle and fluid dynamics in the reactor. Computational fluid dynamics (CFD) is a powerful tool for understanding the effect of fluid dynamics on chemical reactor performance. For single-phase flows, CFD models for turbulent reacting flows are now well understood and routinely applied to investigate complex flows with detailed chemistry. For multiphase flows, the state-of-the-art in CFD models is changing rapidly and it is now possible to predict reasonably well the flow characteristics of gas-solid FB reactors with mono-dispersed, non-cohesive solids.

Different length scales and phenomena are involved in the polyolefin process. Fig. 1.1 shows that the reactor diameter is on the order of meters, the particles are tens to hundreds of microns, the sub-fragments are on the order of hundreds of nanometers and the active site is even smaller, only 1-100 Å. At the early stage of polymerization, single particles fragment into a large number of small sub-particles. The monomers and other species are transported

through the particle boundary layer and by a network of macropores inside the particle, and diffuse through the polymer phase to the active sites where the polymerization reactions occur. Simultaneously, the heat produced by the reaction is removed out of the particle in the opposite direction. Particles can also agglomerate and swarm into a big particle when the particles are overheated or charged. The particles can also break into small fragments if the temperature in the bed is too cold. Thus a broad distribution of particle sizes exist in the FB reactors, and segregation and mixing coexist in the bed due to the mobility of the particles. Therefore, the detailed mathematical modeling of polymerization FB reactors is very complex and poses many challenges for us:

- Poly-dispersed polymer particles play an important role in the behavior of the reactor. Large particles produced by the polymerization reaction or agglomeration can migrate to the bottom of the bed for removal. Unreacted particles or small particles produced from breakage are elutriated with the incoming gas. Local particle size distribution (PSD) is related with many phenomena, such as, segregation, agglomeration, breakage and elutriation.
- Heat and mass transfer to the particle surface controls the local particle temperature and hence the rate of agglomeration and breakage.
- Catalyzed, free-radical polymerization chemistry occurs on the surface of the catalyst and is strongly influenced by mass and heat transfer to the active catalyst sites.
- All of these phenomena are highly coupled and can have a strong influence on the fluid dynamics (e.g., defluidization due to particle agglomeration).

To address these challenges, several researchers have investigated on this subject from different aspects. Mckenna, Spitz, and Cokljat (1999) study the heat transfer from catalyst or polymer particles of different sizes during polymerization in a gas-phase reactor using CFD calculation. Their work shows that the particle shape does not have an overwhelming influence on convective heat-transfer coefficients. Conduction can make a significant contribution to heat removal for particles less than $100 \mu m$, and particle-particle and particle-wall interaction

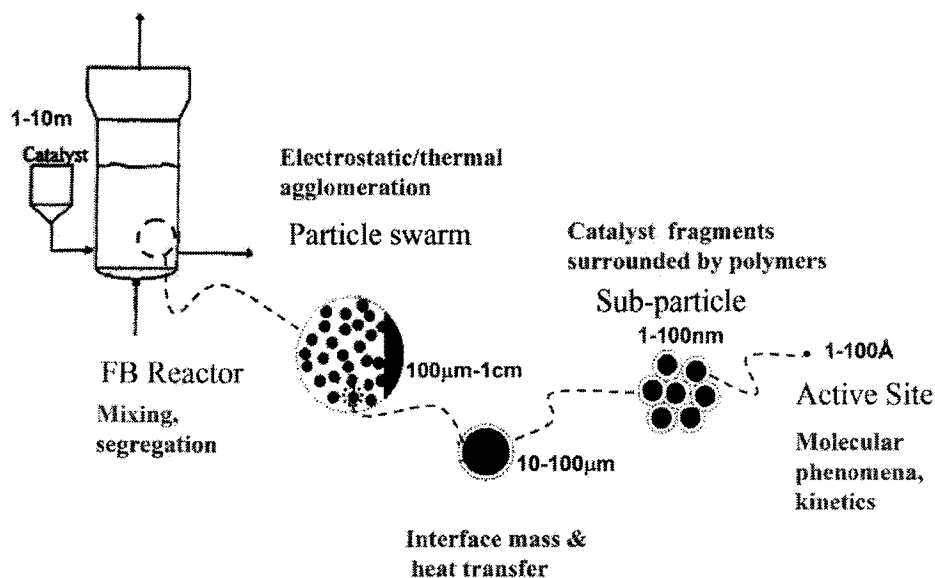


Figure 1.1 Length scales and phenomena involved in polyolefin processes.

is important in some cases. Maggioris et al. (1998) use CFD to predict the PSD in suspension polymer reactors, and a two-compartment population balance model was developed for predicting the nonhomogeneities of droplet size in the reactor. A satisfactory agreement was obtained between the simulation results and experiment data. Recently, the discrete element method (DEM) was used to simulate gas-phase olefin polymerization reactors (Kaneko, Shiojima, and Horio, 1999). A constant particle size is used during the simulation, the temperature profile in the FB bed is given, and hot spot formation is observed on the distributor near the wall of the fluidizing column. It was also found that the degree of mixing can be used as an effective index to identify and prevent hot spot formation. Later, the agglomerate phenomena in a FB with fine cohesive particles was studied by Kuwagi and Horio (2002) using 2D DEM simulation. High particle pressure and agglomerate growth in the bubble wake region and breakage of agglomerates in the upper region of bubbles were confirmed. The agglomerate size obtained by numerical simulation agreed fairly well with the one from the theoretical model.

However, in order to completely describe all the phenomena we mentioned in the context of CFD, the simultaneous numerical solution of the equations for continuity, momentum, energy and chemical species is required. In addition, for polydisperse solids a population balance

equation (PBE) is also needed to describe the PSD in the beds. To our knowledge, such work has not been undertaken, so our objective is to develop a comprehensive model for polydisperse fluidized bed polymerization reactors and describe all the phenomena in the bed.

The CFD algorithm for simulation of FB polymerization reactors is shown in Fig. 1.2. It is based on a multi-fluid model, such as MFIX, and combined with two user defined functions (UDF). As we know, most of today's CFD calculations for gas-solid flows are carried out assuming that the solid phase is monodispersed. However, in order to properly model the evolution of a polydisperse solid phase, the PBE must be coupled with other equations. So the recently formulated direct quadrature method of moments (DQMOM) is implemented in a multi-fluid CFD code to simulate the dynamic change of particle size in a FB reactor. The change of particle temperature and mass fraction due to the aggregation and breakage is also investigated using bivariate population balance equations. For the chemical source terms, if a simplified two-site copolymerization kinetic scheme is used, in situ adaptive tabulation (ISAT) or a chemical look-up table can be used to solve efficiently the solid species equations. The model for heat and mass transfer from/to polymer particle need to be developed for the multi-fluid CFD model.

1.2 Outline

This thesis is organized into seven chapters. In Chapter 2, an overview of fluidized bed polymerization reactors is given, and a simplified two-site kinetic mechanism are discussed. Some basic theories used in our work are given in detail in Chapter 3. First, the governing equations and other constitutive equations for the multi-fluid model are summarized, and the kinetic theory for describing the solid stress tensor is discussed. The detailed derivation of DQMOM for the population balance equation is given as the second section. In this section, monovariate population balance, bivariate population balance, aggregation and breakage equation and DQMOM-Multi-Fluid model are described. In the last section of Chapter 3, numerical methods involved in the multi-fluid model and time-splitting method are presented. Chapter 4 is based on a paper about application of DQMOM to polydisperse gas-solid fluidized beds.

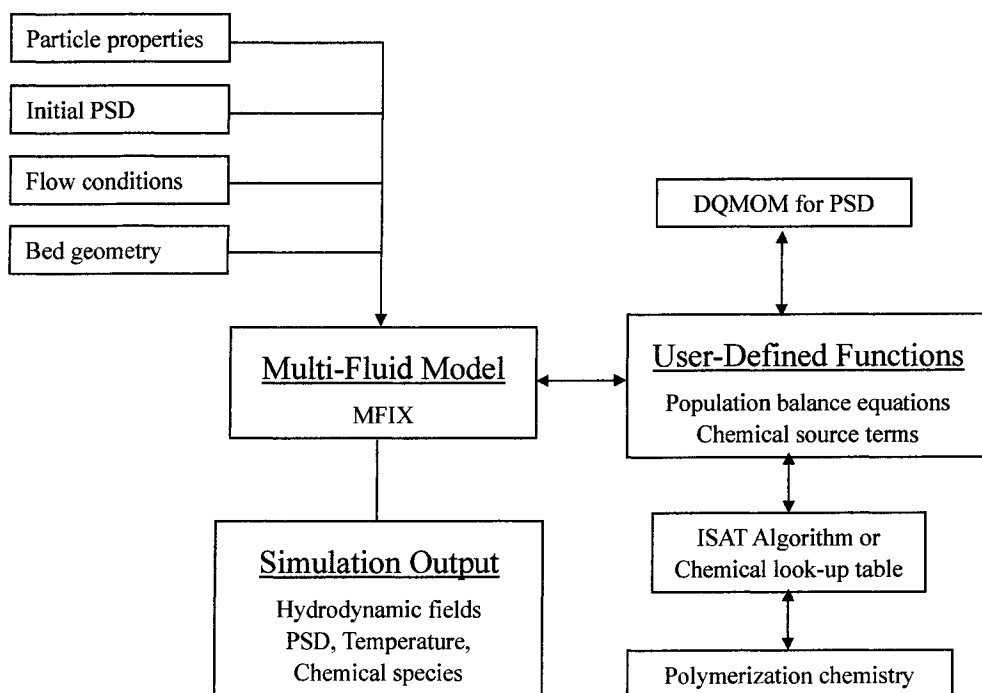


Figure 1.2 CFD algorithm for simulation of FB polymerization reactors.

Results for a constant aggregation and breakage kernel and a kernel developed from kinetic theory are shown. The effect of the aggregation success factor and the fragment distribution function are investigated. Chapter 5 shows the work on validation of mixing and segregation phenomena in gas-solid fluidized beds with a binary mixture or a continuous size distribution. The simulation results are compared with available experiment data and discrete-particle simulation. Chapter 6 presents the project with Univation Technologies on CFD simulation of a Polyethylene pilot-scale FB reactor. The fluid dynamics, mass/heat transfer and particle size distribution are investigated through CFD simulation and validated with available experimental data. The conclusions of this study and future work are discussed in Chapter 7.

CHAPTER 2. REVIEW OF FLUIDIZED BED POLYMERIZATION REACTORS

2.1 Fluidized Bed Polymerization Reactors

Polyolefins, especially polypropylene (PP) and polyethylene (PE), have become the most popular resins due to the merit of low price, flexibility of molding and ease of disposal or recycling (Kaneko, Shiojima, and Horio, 1999). The global PP market is one of the fastest growing industries and the production exceeds 30 million tons in 2000 throughout the world. A lot of PE products including low density polyethylene (LDPE), linear low density polyethylene (LLDPE), ethylene-propylene rubber (EPR) and high density polyethylene (HDPE) are widely used in our daily life and industrial processes. Nowadays, most polyolefin polymerization processes are executed in a liquid- or gas-phase reactor or a combination of both. Three major industrial processes for the production of PP and PE are compared in the Table 2.1. The reactor type, reaction temperature, operation pressure and other reaction parameters are listed for the three processes: the gas-phase Novolen PP process, the gas-phase Unipol PE process and liquid-pool Spheripol PP process. Compared to the conventional liquid slurry reactor, FB polymerization reactors have more advantages due to such reasons as: capability of continuous operation and transport of solids in and out of the bed; high heat and mass transfer rate from gas to particle leading to fast reaction and uniform temperature in the bed; no need for drying and separation of polymers from solvents; operation at lower pressure and moderate temperature and better heat removal.

In a catalytic gas-phase olefine polymerization fluidized bed reactor, small catalyst particles (usually 20-80 μm) are continuously fed into the reactor at a point above the gas distributor, and react with the incoming monomer gas to produce a broad size distribution of polymer

Table 2.1 Comparison of three major industrial processes for the productions of PP and PE.

Process stage		Novolen		Unipol		Spheripol	
		1st reactor	2nd reactor	1st reactor	2nd reactor	1st reactor	2nd reactor
Polymer	–	PP	EPR	LLDPE	LLDPE	PP	PP
Reaction medium	–	Gas	Gas	Gas	Gas	Liquid pool	Liquid pool
Reactor type	–	Vertical stirred bed	Vertical stirred bed	Fluidized bed	Fluidized bed	Loop	loop
Monomers	–	Propylene	Propylene Ethylene	Ethylene 1-Butene	Ethylene 1-Butene	Propylene	Propylene
Temperature	K	343	333	361	361	343	343
Polymer melting point	K	433	–	373-473	373-473	433	433
Pressure	bar	25	20	22	20	40	35
Average residence time	h	2.1	1.5	2.0	1.2	1.0	0.7
Polymer yield	g/g-cat	10,500	4,500	20,000	7,200	20,000	9,100
Rate of polymerization	g/(g-cat · h)	5,000	3,000	10,000	6,000	20,000	13,000
Heat of polymerization	Kcal/mol	25.8	25.8	25.8	25.8	25.8	25.8
Activation energy	Kcal/mol	10	10	10	10	10	10
Catalyst type	–	Z-N	Z-N	Z-N	Z-N	Z-N	Z-N
Average catalyst size	μm	67	67	67	67	67	67
σ_{cat}	–	0.25	0.25	0.25	0.25	0.25	0.25

particles. At the early stage of polymerization, the catalyst particles fragment into a large number of small particles (see Fig 2.1), which are quickly encapsulated by the newly-formed polymer and grow continuously, reaching a typical size of 200-3000 μm . Due to the differences in the polymer particle sizes, segregation occurs and fully-grown polymer particles migrate to the bottom where they are removed from the reactor as soon as reasonable conversions have been achieved. The smaller pre-polymerized particles and fresh catalyst particles tend to migrate to the upper portions of the reactor and continue to react with monomers. The recycled and make-up monomer feed streams are continuously fed to the reactor. An external heat exchange is used to remove the polymerization heat from the recycled gas stream. The schematic representation of a polymerization fluidized bed reactor unit is shown in Fig. 2.2. Usually, industrial FB polymerization reactors operate at temperatures of 348-383 K and pressures of 20-40 bar (Xie, McAuley, Hsu, and Bacon, 1994). The single-pass monomer conversion in the FB polymerization reactors is low, only 2% to 5 %, whereas the overall monomer conversion can be as high as 98 % (McAuley, Talbot, and Harris, 1994).

Because polymerization is exothermic, the temperature of particles in the fluidized bed tends to increase and sometimes it will rise above the melting point of the polymer, then agglomeration occurs and small particles stick together and form lumps in the beds which may then cause defluidization. On the opposite situation, if the bed is too cold, the particles can become brittle and may fracture forming small fragments that elutriate with the gas. Thus the PSD in the bed is related to a couple of phenomena: particle growth, particle agglomeration, breakage and elutriation.

2.2 Simplified Kinetic Mechanism of Olefin Copolymerization

Hutchinson, Chen, and Ray (1992) proposed a comprehensive multisite kinetic model for the copolymerization of olefins over heterogeneous Ziegler-Natta (Z-N) catalysts. In here, a simplified two-site copolymerization scheme (Hatzantonis et al., 2000) is presented to describe the molecular and compositional developments in a FB polymerization reactor. This scheme includes a series of elementary reactions, namely, site activation, chain propagation, site deacti-

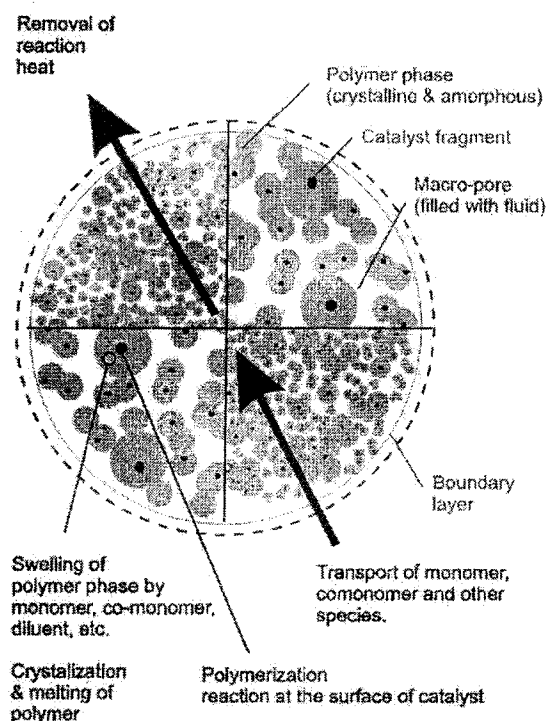


Figure 2.1 The simplified picture of a polymer particle with catalyst fragments.

vation, and chain transfer. In general, each site type is associated with different rate constants for the elementary reactions. Pseudo kinetic rate constants are used in the development of model. In what follows, the subscript k refers to the different site types, and $k = 1, 2$.

Activation of Active Sites

Potential active sites of type k undergo a formation reaction with the heterogeneous Z-N catalysts. This reaction can be described as:



where S_p^k is a potential catalyst active site of type k , and P_0^k is an catalyst active site of type k with no attached monomer, or a vacant active site of type k . $[A]$ is a cocatalyst site, usually it is Aluminum Alkyl.

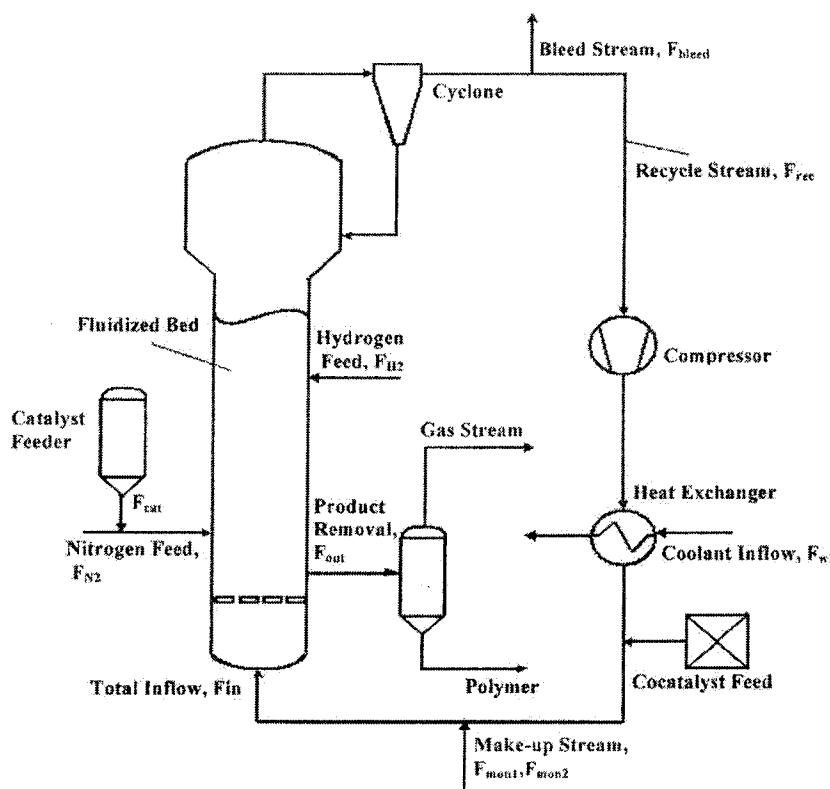


Figure 2.2 Schematic representation of a polymerization fluidized bed reactor unit

Initiation of Active Site and Propagation

The newly formed sites P_0^k can react with monomers ($[M]$ can be either ethylene or 1-butene or both, in our work only ethylene is considered.) and form a living polymer chain



P_1^k is a living polymer chain of length one, then the living polymer chains can grow by the following propagation reactions,



P_n^k is a living polymer chain of length n with terminal monomer attached to the active center of type k .

Deactivation Reactions

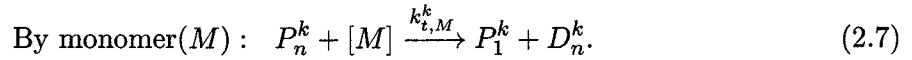
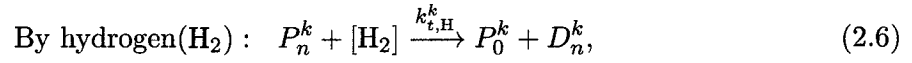
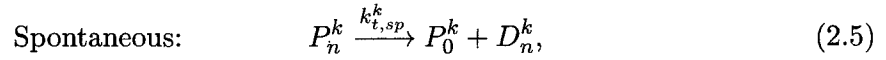
Active sites may decay spontaneously to form dead sites and dead polymer chains



where D_n^k is a dead polymer segment of length n which can not undergo any further reaction and C_d^k is deactivated k catalyst active site.

Chain Transfer Reactions

Most dead polymer chains are produced by chain transfer reactions. These reactions occur with monomer, hydrogen and as well, it can happen spontaneously. Hydrogen is usually added to industrial FB polymerization reactor to make linear polyethylene and then control the molecular weight of the produced polymers.



Note that transfer reactions with monomer produce living polymer chains of length one P_1^k , which has the same reactive characteristics as the sites produced by site initiation, and it also can propagate to form new polymer chains.

In order to formulate a practical kinetic model, the method of moments is often used to reduce equations into a low-order system, which can easily be solved (Hatzantonis et al., 2000). All the kinetic rate constants in the equations can be expressed as, $k = k_0 \exp(-E_a/RT)$, where k_0 , E_a , R and T are the pre-exponential factor, activation energy, ideal gas constant and solid absolute temperature.

CHAPTER 3. BASIC THEORY AND NUMERICAL METHODS

3.1 Multi-Fluid Continuum Model

In the last few decades considerable progress has been made in the area of hydrodynamic modelling of gas-solid flow. Generally speaking two different classes of models can be distinguished, namely discrete particle (Lagrangian) models and continuum (Eulerian) models.

The Newtonian equations of motion are solved for each individual solid particle by using discrete particle models, thus the trajectory of every particle can be tracked. The interactions between the particles can be described by either the soft-sphere model (Tsuji et al., 1993) or by the hard-sphere model (Hoomans et al., 1996). For the soft-sphere model, contact forces between the particles are calculated from the overlap between the particles, however, for the hard-sphere model, the particles are assumed to interact through instantaneous, binary collisions. The drawbacks of the Lagrangian approach are the larger memory requirements and the long calculation time, and empirical relations are required to calculate the fluid-particle interaction unless the continuous phase is described using direct numerical simulations (DNS).

Alternately, Eulerian models treat both the gas phase and the solid phases as continuous and fully interpenetrating phases. The equations employed are a generalization of the Navier-Stokes equations for interacting continua. Owing to the continuum representation of the particulate phase, closure relations for the solid stress tensor and the fluid-particle drag are required to describe the rheology of the solid phase. In most recent years, kinetic theory of granular flow extended from classical gas kinetic theory has been incorporated (Kuipers et al., 1992; Gidaspow, 1994; Balzer et al., 1995). Due to the less computation time, the Eulerian method is still the only feasible approach for performing simulations of an industrial scale gas-solid flow system and has been widely used for the gas-solid simulations.

Since there are many types of multiphase flows and different flow regimes exist, general applicable Eulerian models and methods are not available. To date, there is even still no agreement on the governing equations. In addition, the constitutive relations for the solids phase stress tensor and the interphase momentum transfer are still partially empirical (van Wachem et al., 2001). Two different sets of governing equations for the continuum models originated from the works of Anderson and Jackson (1967) and Ishii (1975) exist. From the work of van Wachem et al. (2001), it is shown that Ishii's (1975) treatment is appropriate for a dispersed phase consisting of fluid droplets, and that Anderson and Jackson's (1967) treatment is appropriate for a dispersed phase consisting of solid particles. Modifications need to be made for the Ishii's (1975) equations to describe gas-solid flows (such as Enwald et al. (1996)'s work). The results from both formulations for the governing equations are similar in terms of the macroscopic flow behavior, but differ on a local scale such as individual bubbles or localized solids distribution.

As follows, firstly the modified governing equations from Ishii's (1975) work are given, and then several constitutive relations, such as gas-phase equation of state, fluid-solids and solids-solids momentum, mass and heat transfer, and fluid and solids phase stress tensor are listed. The kinetic theory of granular flow is discussed as last part.

3.1.1 Governing Equations

The multi-fluid continuum model assumes that different phases behave as interpenetrating continua and the instantaneous variables are averaged over a region that is large compared with the particle spacing but much smaller than the flow domain. Multiple solid phases are accounted for describing phenomena such as segregation and elutriation. Each particle phase is characterized by a unique diameter, density and other properties. A new field variable, phasic volume fractions, are introduced to track the fraction of the averaging volume occupied by various phases. By definition, the volume fractions of all of the phases must sum to one:

$$\varepsilon_g + \sum_{\alpha=1}^N \varepsilon_{s\alpha} = 1, \quad (3.1)$$

where N is the total number of solid phase, ε_g and $\varepsilon_{s\alpha}$ are the volume fractions of the gas and α^{th} solid phases, respectively. The gas phasic volume fraction is also known as the void fraction.

The continuity equations for the gas and solid phases are

$$\frac{\partial \varepsilon_g \rho_g}{\partial t} + \nabla \cdot (\varepsilon_g \rho_g \mathbf{u}_g) = - \sum_{\alpha=1}^N M_{g\alpha} \quad (3.2)$$

and

$$\frac{\partial \varepsilon_{s\alpha} \rho_{s\alpha}}{\partial t} + \nabla \cdot (\varepsilon_{s\alpha} \rho_{s\alpha} \mathbf{u}_{s\alpha}) = M_{g\alpha}, \quad (3.3)$$

where ρ_g and $\rho_{s\alpha}$ are the gas- and solid-phase densities, \mathbf{u}_g and $\mathbf{u}_{s\alpha}$ are the gas- and solid-phase velocities, and $M_{g\alpha}$ is the mass-transfer rate from the gas to the α^{th} solid phase due to the chemical reactions or physical processes, such as evaporation.

The momentum equations for the gas and solid phases are

$$\frac{\partial}{\partial t} \varepsilon_g \rho_g \mathbf{u}_g + \nabla \cdot (\varepsilon_g \rho_g \mathbf{u}_g \mathbf{u}_g) = \nabla \cdot \boldsymbol{\sigma}_g + \sum_{\alpha=1}^N \mathbf{f}_{g\alpha} + \varepsilon_g \rho_g \mathbf{g} \quad (3.4)$$

and

$$\frac{\partial}{\partial t} (\varepsilon_{s\alpha} \rho_{s\alpha} \mathbf{u}_{s\alpha}) + \nabla \cdot (\varepsilon_{s\alpha} \rho_{s\alpha} \mathbf{u}_{s\alpha} \mathbf{u}_{s\alpha}) = \nabla \cdot \boldsymbol{\sigma}_{s\alpha} - \mathbf{f}_{g\alpha} + \sum_{\beta=1, \beta \neq \alpha}^N \mathbf{f}_{\beta\alpha} + \varepsilon_{s\alpha} \rho_{s\alpha} \mathbf{g}, \quad (3.5)$$

where $\boldsymbol{\sigma}_g$ and $\boldsymbol{\sigma}_{s\alpha}$ are the gas- and solid-phase stress tensors, $\mathbf{f}_{g\alpha}$ is the interaction force between the gas and the α^{th} solid phase, $\mathbf{f}_{\beta\alpha}$ is the interaction force or momentum transfer between the β^{th} and α^{th} solid phases, and \mathbf{g} is the gravity vector.

The energy balance for the gas phase is written in term of the gas temperature T_g as:

$$\varepsilon_g \rho_g C_{pg} \left(\frac{\partial T_g}{\partial t} + \mathbf{u}_g \cdot \nabla T_g \right) = - \nabla \cdot \mathbf{q}_g - \sum_{\alpha=1}^N H_{g\alpha} - \Delta H_{rg} + H_{wall}(T_{wall} - T_g), \quad (3.6)$$

where \mathbf{q}_g is the gas-phase conductive heat flux, $H_{g\alpha}$ describes the interphase heat transfer between gas and α^{th} solids, and ΔH_{rg} is the heat of reaction in the gas phase. The last term accounts for heat loss to the wall, and it will only apply to gas in the boundary layer near the wall.

The energy balance equations for the solid phases are written in term of the α^{th} solid phase temperature $T_{s\alpha}$ as:

$$\varepsilon_{s\alpha} \rho_{s\alpha} C_{ps\alpha} \left(\frac{\partial T_{s\alpha}}{\partial t} + \mathbf{u}_{s\alpha} \cdot \nabla T_{s\alpha} \right) = - \nabla \cdot \mathbf{q}_{s\alpha} + H_{g\alpha} - \Delta H_{rs\alpha}, \quad (3.7)$$

where $\mathbf{q}_{s\alpha}$ is the solid-phase conductive heat flux, and $\Delta H_{rs\alpha}$ is the heat of reaction in the solid-phase. In the formulation of energy balance equations (3.6) and (3.7), heat transfer between different solid phases and radiative heat transfer are ignored.

The gas and solids phases may contain an arbitrary number of chemical species, N_g and $N_{s\alpha}$. The species equations for the gas phase and solid phases are:

$$\begin{aligned} \frac{\partial \varepsilon_g \rho_g X_{gn}}{\partial t} + \nabla \cdot (\varepsilon_g \rho_g X_{gn} \mathbf{u}_g) &= R_{gn} - \sum_{\alpha=1}^N M_{g\alpha n}, \\ \frac{\partial \varepsilon_{s\alpha} \rho_{s\alpha} X_{s\alpha n}}{\partial t} + \nabla \cdot (\varepsilon_{s\alpha} \rho_{s\alpha} X_{s\alpha n} \mathbf{u}_{s\alpha}) &= R_{s\alpha n} + M_{g\alpha n}, \end{aligned} \quad (3.8)$$

where X_{gn} and $X_{s\alpha n}$ are the mass fractions of gas- and solid-phase species. R_{gn} and $R_{s\alpha n}$ are the rate of formation of gas and solid-phase species n . $M_{g\alpha n}$ is the mass-transfer rate from the gas to α^{th} solid phase for species n .

3.1.2 Constitutive Relations

To proceed further toward solving practical problems of interest, it is necessary to supply specific constitutive relations to complete the governing equations. This challenging task is accomplished by using a variety of approaches, ranging from empirical information to kinetic theory. Many researchers have worked on it and different closure relations based on the different assumptions are given in the literature and commercial codes. The closure relations used in this research are listed below.

Gas Phase Equation of State

The gas density ρ_g is related to the temperature T_g and the pressure P_g by the idea gas law:

$$\rho_g = \frac{P_g M_w}{RT_g}, \quad (3.9)$$

where M_w is the average molecular weight of gas and R is the gas constant. For an incompressible phase the density is assumed to be constant.

Gas-Solids Momentum Transfer

From the studies on the dynamics of a single particle in a fluid, many mechanisms contribute to the momentum transfer term $\mathbf{f}_{g\alpha}$ (Fan and Zhu, 1998). In the present work, only the buoyancy, caused by the fluid pressure gradient, drag force, caused by the velocity difference between the gas-solid phase and momentum transfer due to mass transfer between the phases are accounted for. Thus the gas-solids momentum transfer can be written as:

$$\mathbf{f}_{g\alpha} = \varepsilon_{s\alpha} \nabla P_g - F_{g\alpha}(\mathbf{u}_g - \mathbf{u}_{s\alpha}) - M_{g\alpha}[\xi_{g\alpha} \mathbf{u}_{s\alpha} + (1 - \xi_{g\alpha}) \mathbf{u}_g], \quad (3.10)$$

where the first term on the right-hand side describes buoyancy, the second term is drag force, and the last term is momentum transfer due to gas-solid mass transfer $M_{g\alpha}$, and

$$\xi_{g\alpha} = \begin{cases} 1 & \text{for } M_{g\alpha} < 0, \\ 0 & \text{for } M_{g\alpha} \geq 0. \end{cases} \quad (3.11)$$

Typically, the gas-solid drag coefficient $F_{g\alpha}$ is obtained experimentally from pressure drop measurements in fixed, fluidized, or settling beds. The drag models which are more widely used are Syamlal-O'Brien model, Wen-Yu model and Gidaspow model. The detail information on the comparison of these three drag models on the flow patten can be found in Taghipour's work (2005).

In Syamlal-O'Brien model (Syamlal, Rogers, and O'Brien, 1993), the gas-solid drag coefficient derived by Schaeffer (1987) is used:

$$F_{g\alpha} = \frac{3}{4} C_D \frac{\varepsilon_{s\alpha} \varepsilon_g \rho_g}{V_{r\alpha}^2 d_{p\alpha}} |\mathbf{u}_g - \mathbf{u}_{s\alpha}|, \quad (3.12)$$

where $d_{p\alpha}$ is the particle diameter and $V_{r\alpha}$ is the terminal velocity correlation for the α^{th} solid phase. A closed formula for $V_{r\alpha}$ can be derived from a correlation developed by Garside and Al-Dibouni (1977):

$$V_{r\alpha} = \frac{1}{2} \left[A - 0.06 Re_\alpha + \sqrt{(0.06 Re_\alpha)^2 + 0.12 Re_\alpha (2B - A) + A^2} \right], \quad (3.13)$$

where

$$A = \varepsilon_g^{4.14}, \quad (3.14)$$

$$B = \begin{cases} 0.8\varepsilon_g^{1.28} & \text{if } \varepsilon_g \leq 0.85, \\ \varepsilon_g^{2.65} & \text{if } \varepsilon_g > 0.85. \end{cases} \quad (3.15)$$

The Reynolds number of the α^{th} solid phase is given by:

$$Re_{p\alpha} = \frac{d_{p\alpha} |\mathbf{u}_g - \mathbf{u}_{s\alpha}| \rho_g}{\mu_g}. \quad (3.16)$$

The single-sphere drag function has the simple formula proposed by Dalla Valle (1948):

$$C_D = \left(0.63 + 4.8 \sqrt{\frac{V_{r\alpha}}{Re_\alpha}} \right)^2. \quad (3.17)$$

In the Wen-Yu drag model, the gas-solid drag coefficient is (Wen and Yu, 1966):

$$F_{g\alpha} = \frac{3}{4} C_D \frac{\varepsilon_{s\alpha} \rho_g \varepsilon_g |\mathbf{u}_g - \mathbf{u}_{s\alpha}|}{d_{p\alpha}} \varepsilon_g^{-2.65}, \quad (3.18)$$

and C_D has a different function from Syamlal-O'Brien's model,

$$C_D = \begin{cases} \frac{24}{\varepsilon_g Re_{p\alpha}} (1 + 0.15(\varepsilon_g Re_{p\alpha})^{0.687}) & \text{if } \varepsilon_g Re_{p\alpha} \leq 1000 \\ 0.44 & \text{if } \varepsilon_g Re_{p\alpha} > 1000 \end{cases} \quad (3.19)$$

Gidaspow (1994) follows Wen and Yu model for gas volume fraction larger than 0.8, but apply Ergun equation for gas volume fraction lower than 0.8. The gas-solid drag coefficient for Gidaspow model is:

$$F_{g\alpha} = \begin{cases} 150 \frac{\varepsilon_{s\alpha} (1 - \varepsilon_g) \mu_g}{\varepsilon_g d_{p\alpha}^2} + 1.75 \frac{\varepsilon_{s\alpha} \rho_g |\mathbf{u}_g - \mathbf{u}_{s\alpha}|}{d_{p\alpha}} & \text{if } \varepsilon_g \leq 0.8 \\ \frac{3}{4} C_D \frac{\varepsilon_{s\alpha} \rho_g \varepsilon_g |\mathbf{u}_g - \mathbf{u}_{s\alpha}|}{d_{p\alpha}} \varepsilon_g^{-2.65} & \text{if } \varepsilon_g > 0.8 \end{cases} \quad (3.20)$$

Solids-Solids Momentum Transfer

Compared to gas-solids momentum transfer, much less is known about solids-solids momentum transfer. Only drag force between solids phases and momentum transfer due to mass transfer are presented. In the present work, the solids-solids momentum transfer $\mathbf{f}_{\beta\alpha}$ can be written as:

$$\mathbf{f}_{\beta\alpha} = -F_{\beta\alpha} (\mathbf{u}_{s\beta} - \mathbf{u}_{s\alpha}) - M_{\beta\alpha} [\xi_{\beta\alpha} \mathbf{u}_{s\alpha} + (1 - \xi_{\beta\alpha}) \mathbf{u}_{s\beta}], \quad (3.21)$$

where $M_{\beta\alpha}$ is the mass transfer from solids phase- β to solid phase- α , and

$$\xi_{\beta\alpha} = \begin{cases} 1 & \text{for } M_{\beta\alpha} < 0, \\ 0 & \text{for } M_{\beta\alpha} \geq 0. \end{cases} \quad (3.22)$$

Usually momentum transfer due to mass transfer is small compared to drag force, so it can be ignored in most simulations.

The drag coefficient $F_{\beta\alpha}$ is necessary to correctly predict segregation among particles of different sizes, and it has an expression of the form

$$F_{\beta\alpha} = \frac{3(1+e)\left(\frac{\pi}{2} + \frac{C_{f\beta\alpha}\pi^2}{8}\right)\epsilon_{s\alpha}\rho_{s\alpha}\epsilon_{s\beta}\rho_{s\beta}(d_{p\beta} + d_{p\alpha})^2 g_{0\beta\alpha} |\mathbf{u}_{s\beta} - \mathbf{u}_{s\alpha}|}{2\pi(\rho_{s\beta}d_{p\beta}^3 + \rho_{s\alpha}d_{p\alpha}^3)} + C_1 P^*. \quad (3.23)$$

The first term is obtained from kinetic theory for granular flow, where e and $C_{f\beta\alpha}$ are the coefficient of restitution and coefficient of friction between particles, respectively. Coefficient of restitution e accounts for the inelasticity of collisions between particles, and e would be equal to one for perfectly elastic collisions. However, usually the granular collisions are slightly inelastic, so it is between zero and one. The radial distribution function $g_{0\beta\alpha}$ describes the probability of finding two particles in close proximity. This function is equal to one for very low concentrations of solid particles but it increases due to the increase volume occupied by the solids particles. This function has many possible definitions and the model derived by Lebowitz (1964) for a mixture of hard spheres is used:

$$g_{0\beta\alpha} = \frac{1}{\epsilon_g} + \frac{3d_{p\beta}d_{p\alpha}}{\epsilon_g^2(d_{p\beta} + d_{p\alpha})} \sum_{\lambda=1}^N \frac{\epsilon_{s\lambda}}{d_{p\lambda}}. \quad (3.24)$$

The second term $C_1 P^*$ represents the ‘‘hindrance force’’ due to enduring contact in a closed packed system. P^* is the total solid stress tensor in plastic regime, it will be explained in the later section of solid phase stress tensor. C_1 is a constant. It depends on the segregation rate between two solid phases, and usually, it can be obtained from experiment data. ϵ_g^* is the close-packed-bed void fraction or minimum void fraction.

Gas Phase Stress tensor

The stress tensor for the gas phase is related to the pressure and viscous stress tensor $\boldsymbol{\tau}_g$ by

$$\boldsymbol{\sigma}_g = -P_g \mathbf{I} + \boldsymbol{\tau}_g. \quad (3.25)$$

The viscous stress tensor is assumed to have a Newtonian form and can be expressed as:

$$\boldsymbol{\tau}_g = 2\varepsilon_g \mu_g \mathbf{D}_g - \frac{2}{3} \varepsilon_g \mu_g \text{Tr}(\mathbf{D}_g) \mathbf{I}, \quad (3.26)$$

where μ_g is molecular viscosity for gas phase, \mathbf{I} is the identity tensor and \mathbf{D}_g is the strain rate tensor for the gas phase, and

$$\mathbf{D}_g = \frac{1}{2} [\nabla \mathbf{u}_g + (\nabla \mathbf{u}_g)^T]. \quad (3.27)$$

Solids Phase Stress tensor

Two different methods have been used to calculate the solids phase stress tensor. In the earlier studies of the solid stress tensor, the total solid stress tensor is expressed as the sum of kinetic, collision and frictional tensors. In the dilute part of granular flow, solid particles randomly fluctuate and translate, this form of viscous dissipation and stress is named kinetic effect. When the concentration of solid particles increases, in addition to dissipation, solid particles can collide shortly with other particles and thus enhance dissipation and stress, and this kind of effect is called collision effect. At very high concentrations (usually more than 50 % in volume), particles start to endure long, sliding and rubbing contacts, which gives rise to a totally different stress from kinetic and collision stress, and it is called frictional effect. These three main forms of stress tensors in a granular flow are shown in Fig. 3.1 (Dartevelle, 2003). Using this method, kinetic and collision stress is calculated from kinetic theory of granular flow, and the frictional tensor is specified as a function of void fraction that becomes very large as the void fraction approaches the packed-bed void fraction ε_g^* . The actually magnitude of the term itself is not very important, as long as it prevents the void fraction from becoming unphysically small.

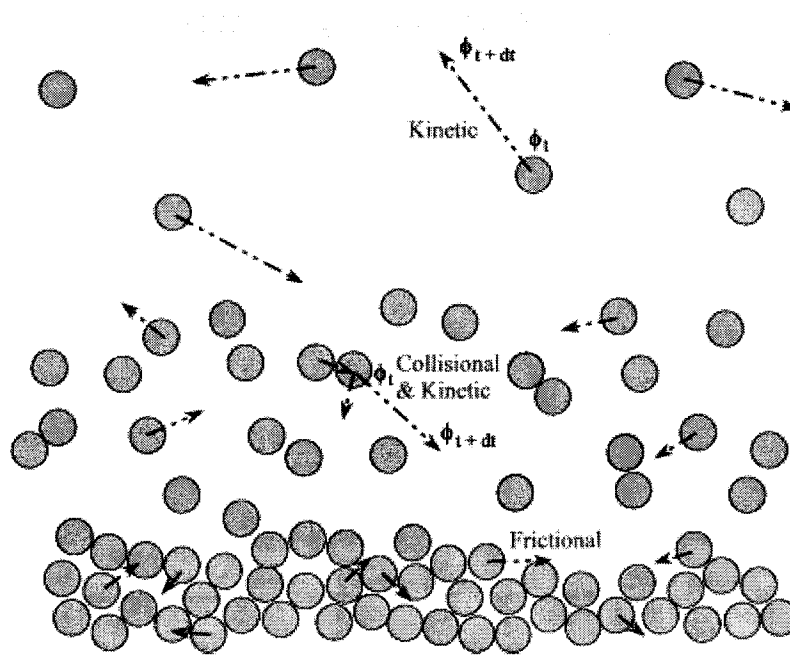


Figure 3.1 Three main forms of viscous dissipation in a granular flow

In order to avoid the need to specify an arbitrary frictional stress tensor for the solid phase, Syamlal and O'Brien (1988) suggest to treat the granular media as incompressible fluid at a certain critical void fraction (or maximum packed-bed void fraction) ε_g^* . In such a formulation, a solid pressure is calculated so as to keep the void fraction from becoming less than the packed-bed void fraction. This pressure becomes zero when the void fraction becomes greater than the packed-bed void fraction. Using this method, granular flow is classified into two different regions: a viscous or rapidly shearing regime, in which stresses arise because of collisional or translational transfer of momentum (similar to kinetic and collisional regime), and a plastic or slowly shearing granular flow, in which stresses arise due to Coulomb friction between solids particle in enduring contact (similar to the frictional regime). Two entirely different approaches are used to describe the solid stress tensor in these two flow regimes, and they are “switched” at a critical packing-bed void fraction ε_g^* ,

$$\sigma_{s\alpha} = \begin{cases} -P_{s\alpha}^p \mathbf{I} + \tau_{s\alpha}^p & \text{if } \varepsilon_g \leq \varepsilon_g^*, \\ -P_{s\alpha}^v \mathbf{I} + \tau_{s\alpha}^v & \text{if } \varepsilon_g > \varepsilon_g^*. \end{cases} \quad (3.28)$$

$P_{s\alpha}$ is the solid pressure and $\boldsymbol{\tau}_{s\alpha}$ is the viscous stress in the α^{th} solids phase. The superscript p stands for plastic regime and v for viscous regime. The granular stress tensor in the viscous regime is based on the kinetic theory for granular flow. The granular pressure and stress in the viscous regime are given by,

$$P_{s\alpha}^v = K_{1\alpha} \varepsilon_{s\alpha}^2 \Theta_\alpha, \quad (3.29)$$

and

$$\boldsymbol{\tau}_{s\alpha}^v = 2\mu_{s\alpha}^v \mathbf{D}_{s\alpha} + \lambda_{s\alpha}^v \text{Tr}(\mathbf{D}_{s\alpha}) \mathbf{I}, \quad (3.30)$$

where Θ_α is the granular temperature for the α^{th} solid phase and the detailed information of about computing this term will be discussed in Sec. 3.1.3. $\mathbf{D}_{s\alpha}$ is the strain rate tensor and is given by:

$$\mathbf{D}_{s\alpha} = \frac{1}{2} [\nabla \mathbf{u}_{s\alpha} + \nabla \mathbf{u}_{s\alpha}^T]. \quad (3.31)$$

The shear viscosity $\mu_{s\alpha}^v$ and second coefficient of viscosity for the α^{th} solid phase $\lambda_{s\alpha}^v$ are expressed as:

$$\lambda_{s\alpha}^v = K_{2\alpha} \varepsilon_{s\alpha} \sqrt{\Theta_\alpha}, \quad (3.32)$$

$$\mu_{s\alpha}^v = K_{3\alpha} \varepsilon_{s\alpha} \sqrt{\Theta_\alpha}. \quad (3.33)$$

$K_{1\alpha}, K_{2\alpha}, K_{3\alpha}$ are constants and they are derived from kinetic theory for granular flow. The formulas are:

$$K_{1\alpha} = 2(1 + e) \rho_{s\alpha} g_{0\alpha\alpha}, \quad (3.34)$$

$$K_{2\alpha} = 4d_{p\alpha} \rho_{s\alpha} (1 + e) \frac{\varepsilon_{s\alpha} g_{0\alpha\alpha}}{3\sqrt{\pi}} - \frac{2}{3} K_{3\alpha}, \quad (3.35)$$

$$K_{3\alpha} = \frac{d_{p\alpha} \rho_{s\alpha}}{2} \left[\frac{\pi^{1/2}}{3(3 - e)} [1 + 0.4(1 + e)(3e - 1)\varepsilon_{s\alpha} g_{0\alpha\alpha}] + \frac{8\varepsilon_{s\alpha} g_{0\alpha\alpha} (1 + e)}{5\sqrt{\pi}} \right]. \quad (3.36)$$

In the plastic regime, the stresses are usually described by theories from the study of soil mechanics. An arbitrary function that allows a certain amount of compressibility in the solid phase represents the solid pressure term in the plastic regime:

$$P_{s\alpha}^p = \varepsilon_{s\alpha} P^*, \quad (3.37)$$

where P^* is represented by an empirical power law:

$$P^* = 10^{25}(\varepsilon_g^* - \varepsilon_g)^{10}. \quad (3.38)$$

The solid stress tensor is calculated from a simpler model proposed by (Schaeffer, 1987):

$$\boldsymbol{\tau}_{s\alpha}^p = 2\mu_{s\alpha}^p \mathbf{D}_{s\alpha}, \quad (3.39)$$

where

$$\mu_{s\alpha}^p = \frac{P^* \sin \phi}{2\sqrt{I_{2D}}}, \quad (3.40)$$

and ϕ is the angle of internal friction, usually it is between 15° or 45° . I_{2D} is the second invariant of the deviator of the strain rate tensor, and it can be expressed as:

$$I_{2D} = \frac{1}{6} [(D_{s\alpha 11} - D_{s\alpha 22})^2 + (D_{s\alpha 22} - D_{s\alpha 33})^2 + (D_{s\alpha 33} - D_{s\alpha 11})^2] \\ + D_{s\alpha 12}^2 + D_{s\alpha 23}^2 + D_{s\alpha 31}^2. \quad (3.41)$$

Gas-Solids Heat Transfer

The heat transfer between the gas and solids is assumed to be a function of the temperature difference:

$$H_{g\alpha} = \gamma_{g\alpha}(T_g - T_{s\alpha}), \quad (3.42)$$

where $\gamma_{g\alpha}$ is the overall heat-transfer coefficient. The latter can be related to a solid-side coefficient (γ_α) and a gas-side coefficient (γ_g) by

$$\frac{1}{\gamma_{g\alpha}} = \frac{1}{\gamma_g} + \frac{1}{\gamma_\alpha}. \quad (3.43)$$

The gas-side heat-transfer coefficient is corrected from the coefficient γ_g^0 by adding the influence of the interphase mass transfer,

$$\gamma_g = \frac{C_{pg} M_{g\alpha}}{e^{(C_{pg} M_{g\alpha} / \gamma_g^0)} - 1} \quad (3.44)$$

and the coefficient γ_g^0 is related to the particle Nusselt number (Syamlal et al., 1993):

$$\text{Nu}_\alpha = (7 - 10\varepsilon_g + 5\varepsilon_g^2)(1 + 0.7\text{Re}_\alpha^{0.2} Pr^{1/3}) + (1.33 - 2.4\varepsilon_g + 1.2\varepsilon_g^2)\text{Re}_\alpha^{0.7} Pr^{1/3}, \quad (3.45)$$

by

$$\gamma_g^0 = \frac{6k_g \text{Nu}_\alpha}{d_{p\alpha}^2}. \quad (3.46)$$

The Prandtl number is defined as:

$$Pr = \frac{C_{pg}\mu_g}{k_g}, \quad (3.47)$$

and Reynolds number Re_α is defined in Eq. 3.16. The solid-side heat-transfer coefficient γ_α can be estimated as (Yao et al., 2003):

$$\gamma_\alpha = \frac{2\pi^2 k_{p\alpha} \varepsilon_{s\alpha}}{9d_{p\alpha}^2}, \quad (3.48)$$

where k_g and $k_{p\alpha}$ are the thermal conductivities of the gas and solid phase, respectively.

Gas-Solids Mass Transfer

The mass-transfer rate between gas and solids for species n can be expressed as

$$M_{g\alpha n} = \kappa_{g\alpha n}(X_{gn} - X_{s\alpha n}), \quad (3.49)$$

where $\kappa_{g\alpha n}$ is the overall mass-transfer coefficient for species n , which can be related to a solid-side coefficient ($\kappa_{\alpha n}$) and a gas-side coefficient (κ_g). Usually the gas-side mass transfer coefficient can be ignored, only a model for the solid-side coefficient need to be derived. After performing a lumped mass-transfer analysis (Yao et al., 2003), this model can be expressed as

$$\kappa_{g\alpha n} = \kappa_\alpha = \frac{\pi^2 D_n \varepsilon_{s\alpha} \rho_{s\alpha}}{3d_{p\alpha}^2}, \quad (3.50)$$

where D_n is the diffusivity of species n in the solid phase.

Other Relations

The conductive heat flux for the gas phase is described by Fourier's Law:

$$\mathbf{q}_g = -\varepsilon_g k_g \nabla T_g. \quad (3.51)$$

For solids phases, the solid-side conductive heat flux is necessary to calculate bed-to-wall heat coefficients and the conductive heat flux is assumed to have a similar form to that in gas phase:

$$\mathbf{q}_{s\alpha} = -\varepsilon_{p\alpha} k_{s\alpha} \nabla T_{s\alpha}. \quad (3.52)$$

For heat of reaction, the partitioning of the heat of reaction between the phases is arbitrary since the averaging is required to derive the hydrodynamic equations does not contain any information regarding the gas-solids interface. The actual chemical reactions occur in an interface between solids and gas phase. However the partitioning of the heat of reaction must be based on physical argument. For example, in most polymerization reactions, the heat of reaction is assigned to the solid phase.

3.1.3 Kinetic Theory of Granular Flow

Kinetic theory of granular flow is based on a deep analogy with the classical kinetic theory of dense gas. Taking the analogy, a granular temperature Θ_α is defined for each solid phase, and it is described as the specific kinetic energy of the random fluctuating component of the particle velocity:

$$\begin{aligned} E_{\Theta_\alpha} &= \frac{3}{2}\Theta_\alpha = \frac{1}{2}\langle \mathbf{C}_\alpha^2 \rangle \\ \Theta_\alpha &= \frac{1}{3}\langle \mathbf{C}_\alpha^2 \rangle \end{aligned} \quad (3.53)$$

where E_{Θ_α} is the granular fluctuating energy and \mathbf{C}_α is the random fluctuating component of the instantaneous velocity \mathbf{c}_α of the α^{th} solid phase defined by

$$\mathbf{c}_\alpha = \mathbf{u}_{s\alpha} + \mathbf{C}_\alpha. \quad (3.54)$$

The symbol $\langle \rangle$ means an ensemble averaging. Notice here, for a solids mixture, we just simply extend the two phase kinetic theory to multiple granular phases. More general and accurate kinetic theories for multi-solids phases need to be derived in the future, and recently a couple of researchers' work are reported (Goldschmidt, 2001).

In the granular flow or gas-solid flow, the mechanical energy of granular flow is first transformed into random particle motion and then dissipated into internal energy. It is quite different from the conventional dissipation mechanism. This general principle of dissipation in the granular kinetic theory is presented in Fig. 3.2. Thus a conservation of energy equation for this fluctuating kinetic energy is given by

$$\frac{3}{2} \left[\frac{\partial(\varepsilon_{s\alpha}\rho_{s\alpha}\Theta_\alpha)}{\partial t} + \nabla \cdot (\varepsilon_{s\alpha}\rho_{s\alpha}\Theta_\alpha)\mathbf{u}_{s\alpha} \right] = \boldsymbol{\sigma}_{s\alpha} : \nabla \mathbf{u}_{s\alpha} - \nabla \cdot \mathbf{q}_{\Theta_\alpha} - \gamma_{\Theta_\alpha} + \phi_{g\alpha}. \quad (3.55)$$

The first term on the right hand side represents the work done by the surface forces, e.g; the viscous dissipation and the production of fluctuations by shear. The second term represents the conduction of the granular temperature, where $\mathbf{q}_{\Theta_\alpha}$ is the diffusive flux of granular temperature and can be defined by a Fourier type law

$$\mathbf{q}_{\Theta_\alpha} = -k_{\Theta_\alpha} \nabla \Theta_\alpha, \quad (3.56)$$

where the diffusion coefficient for granular energy, k_{Θ_α} is described by

$$k_{\Theta_\alpha} = \frac{15d_{p\alpha}\rho_{s\alpha}\varepsilon_{s\alpha}\sqrt{\pi\Theta_\alpha}}{4(41-33\eta)} \left[1 + \frac{12}{5}\eta^2(4\eta-3)\varepsilon_{s\alpha}g_{0\alpha\alpha} + \frac{16}{15\pi}(41-33\eta)\eta\varepsilon_{s\alpha}g_{0\alpha\alpha} \right], \quad (3.57)$$

and

$$\eta = \frac{1}{2}(1+e). \quad (3.58)$$

The third term $-\gamma_{\Theta_\alpha}$ is the loss of granular energy due to the inelastic collisions between particles. It can be described as

$$\gamma_{\Theta_\alpha} = K_{4\alpha}\varepsilon_{s\alpha}^2\Theta_\alpha^{\frac{3}{2}}, \quad (3.59)$$

where

$$K_{4\alpha} = \frac{12(1-e^2)\rho_{s\alpha}g_{0\alpha\alpha}}{d_{p\alpha}\sqrt{\pi}}. \quad (3.60)$$

The last term $\phi_{g\alpha}$ represents the dissipation rate due to the interaction between solids and gas phase. It can be expressed as a function of gas-solid drag coefficient:

$$\phi_{\Theta_\alpha} = -3F_{g\alpha}\Theta_\alpha. \quad (3.61)$$

Inserting all the constitutive relations into the granular temperature equations, for N solids phases, N coupled partial differential equations (PDEs) need to be solved and it is a very onerous work. However, this work can be simplified by solving a single PDE that represents the granular energy equation for a mixture granular temperature Θ . The ‘‘mixture granular energy equation’’ is formed by summing over all particles and after some manipulation it can be expressed as:

$$\frac{3}{2} \left[\frac{\partial}{\partial t} \rho_s \Theta + \nabla \cdot \rho_s \Theta \mathbf{u}_s \right] = \sum_{\alpha=1}^N [\boldsymbol{\sigma}_{s\alpha} : \nabla \mathbf{u}_{s\alpha} - \nabla \cdot \mathbf{q}_{\Theta_\alpha} - \gamma_{\Theta_\alpha} + \phi_{g\alpha}]. \quad (3.62)$$

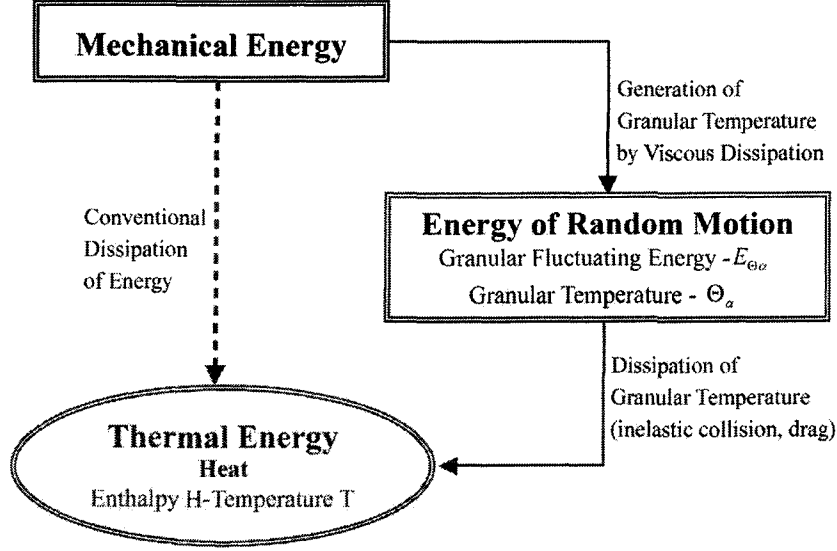


Figure 3.2 General principle of dissipation in the granular kinetic theory

The mixture granular temperature or averaged granular temperature is defined as:

$$\Theta = \frac{\sum_{\alpha=1}^N (\varepsilon_{s\alpha} \rho_{s\alpha} \Theta_{\alpha})}{\sum_{\alpha=1}^N (\varepsilon_{s\alpha} \rho_{s\alpha})}. \quad (3.63)$$

Equipartition of granular energy $m_{p\alpha} \Theta_{\alpha} = m_{p\beta} \Theta_{\beta}$ is assumed in the derivation, where $m_{p\alpha}$ is the mass of the particles that constitute solids phase α . Then the granular temperature for α^{th} solid phase can be obtained by

$$\Theta_{\alpha} = \frac{\rho_{s\alpha} \Theta}{\rho_{s\alpha} d_{p\alpha}^3 \sum_{\beta=1}^N (\varepsilon_{s\beta} \rho_{s\beta})}. \quad (3.64)$$

The implementation of the detailed mixture granular energy equation described by Eq. 3.62 is still under development. Currently, an algebraic expression for granular temperature Θ_{α} is calculated by assuming that the granular energy is dissipated locally and neglecting the convection and diffusion contributions, only keeping the first term (generation term) and the third term (dissipation term) on the right hand side (ignoring the dissipation rate due to the interaction between solids phase and gas phase and diffusive flux of granular temperature).

The resulting algebraic granular energy equation becomes:

$$\Theta_{\alpha} = \left(\frac{-K_{1\alpha} \varepsilon_{s\alpha} \text{Tr}(\mathbf{D}_{s\alpha}) + \sqrt{K_{1\alpha}^2 \text{Tr}^2(\mathbf{D}_{s\alpha}) \varepsilon_{s\alpha}^2 + 4K_{4\alpha} \varepsilon_{s\alpha} [K_{2\alpha} \text{Tr}^2(\mathbf{D}_{s\alpha}) + 2K_{3\alpha} \text{Tr}(\mathbf{D}_{s\alpha}^2)]}}{2\varepsilon_{s\alpha} K_{4\alpha}} \right)^2. \quad (3.65)$$

3.2 DQMOM for Population Balance Equation

In order to describe the PSD in a multiphase flow, a PBE needs to be solved along with continuity equation, momentum equation and energy equation. Many different methods exist for solving the PBE and a lucid description of the mathematical and numerical issues involved are discussed by Ramakrishna (2000). The most direct method is the discretized population balance (DPB) approach or classes method (CM), in which the internal coordinate (e.g, particle length or volume) is discretized into a finite series of bins. The main disadvantage of this method is requiring a large number of classes (e.g., 20-30) to get reasonable results, so that the DPB method is not a feasible approach for CFD calculations. An alternative approach is Monte-Carlo simulations. This approach is based on the solution of the PBE in terms of its stochastic equivalent. A population of particles undergoes the “real” physical processes, and events occur according to the appropriate probabilities. The work of Smith and Matsoukas (1998) and Lee and Matsoukas (2000) give more details on this approach. Although this approach is theoretically applicable for CFD application, especially for Lagrangian-Eulerian simulations, in order to reduce the statistical error a very large number of particles must be used. Due to limitations on the computational resources, the full incorporation of Monte-Carlo methods with CFD codes is at the moment intractable (Maded, Falk, and Plasari, 2001, 2003).

An attractive alternative is represented by the method of moments (MOM) where the PSD is tracked through its moments by integrating out the internal coordinate. The main advantage of MOM is that the number of scalars required is very small (i.e., usually 4-6), which makes the implementation in CFD codes feasible. However, due to the difficulties related with expressing transport equations in terms of the moments themselves, the method has not been widely used. This is the so-called closure problem, pointed out first by Hulburt and Katz (1964), and recently reviewed by Diemer and Olson (2002). As an alternative, McGraw (1997) developed the so-called quadrature method of moments (QMOM), which is based on the approximation of the unclosed terms by using an ad-hoc quadrature formula. The quadrature approximation (i.e., its abscissas and weights) can be determined from the lower-order moments by resorting to the product-difference (PD) algorithm. QMOM has been extensively validated for several

problems with different internal coordinates (Barret and Webb, 1998; Marchisio, Vigil, and Fox, 2003b; Marchisio, Pikturna, Fox, Vigil, and Barresi, 2003a). One of the main limitations of QMOM is that since the solid phase is represented through the moments of the distribution, the phase-average velocity of the different solid phases must be used to solve the transport equations for the moments. Thus, in order to use this method in the context of the multiphase flows, it is necessary to extend QMOM to handle cases where each particle size is convected by its own velocity.

In order to address these issues, the DQMOM has been formulated and validated by Marchisio and Fox (2005). DQMOM is based on the direct solution of the transport equations for weights and abscissas of the quadrature approximation. The calculation of the quadrature approximation through this direct formulation presents the advantage of being directly applicable to multi-variate PBE (i.e., PBE with more than one internal coordinate). Moreover, as it will become clear below, each node of the quadrature approximation can be treated as a distinct solid phase. DQMOM thus offers a powerful approach for describing polydisperse solids undergoing segregation, growth, aggregation and breakage processes in the context of CFD simulations.

As follows, the detailed derivation of DQMOM for a monovariate population balance is explained and then the method is applied to bivariate variables: particle size L and particle temperature T_s . The bivariate population balance equations can be also extended to other variables, such as solid mass fraction X_s . Then the moment transformation of aggregation and breakage equation for monovariate and bivariate are presented in the third part. At last, the combination of DQMOM method with multi-fluid model is discussed.

3.2.1 Monovariate Population Balance

The population balance for the PSD with number density function $n(L; \mathbf{x}, t)$ can be written in terms of one internal variable, particle size length L , as follows:

$$\frac{\partial n(L; \mathbf{x}, t)}{\partial t} + \nabla \cdot [\langle \mathbf{u}_s | L \rangle n(L; \mathbf{x}, t)] = S(L; \mathbf{x}, t), \quad (3.66)$$

where $S(L; \mathbf{x}, t)$ represents the net rate of introduction of new particles into the system (e.g., due to the chemical reaction, aggregation and breakage) and $\langle \mathbf{u}_s | L \rangle$ is the mean velocity conditioned on the particle length L , by definition, $\langle \mathbf{u}_s | L = L_\alpha \rangle = \mathbf{u}_{s\alpha}$. \mathbf{x} is the spatial coordinate and t is the time.

Using DQMOM, $n(L; \mathbf{x}, t)$ can be approximated in terms of a summation of N Dirac delta functions (presumed finite-mode PSD):

$$n(L; \mathbf{x}, t) = \sum_{\alpha=1}^N \omega_\alpha(\mathbf{x}, t) \delta[L - L_\alpha(\mathbf{x}, t)], \quad (3.67)$$

where ω_α is the *weight* of the delta function centered at the *characteristic length* L_α . If Eq. 3.67 is substituted into Eq. 3.66, it is possible to derive transport equations for the N weights ω_α and the N characteristic lengths L_α .

The population balance in terms of the presumed finite-mode PSD becomes:

$$\sum_{\alpha=1}^N \delta(L - L_\alpha) \left[\frac{\partial \omega_\alpha}{\partial t} + \nabla \cdot (\omega_\alpha \mathbf{u}_{s\alpha}) \right] - \sum_{\alpha=1}^N \delta'(L - L_\alpha) \left[\omega_\alpha \left(\frac{\partial L_\alpha}{\partial t} + \mathbf{u}_{s\alpha} \cdot \nabla L_\alpha \right) \right] = S(L, T) \quad (3.68)$$

where $\delta'(L - L_\alpha)$ is the first derivative of the Dirac delta function $\delta(L - L_\alpha)$ and after some manipulation, Eq. 3.68 becomes:

$$\sum_{\alpha=1}^N \delta(L - L_\alpha) a_\alpha - \sum_{\alpha=1}^N \delta'(L - L_\alpha) [b_\alpha - L_\alpha a_\alpha] = S(L, T), \quad (3.69)$$

where

$$\frac{\partial \omega_\alpha}{\partial t} + \nabla \cdot (\omega_\alpha \mathbf{u}_{s\alpha}) = a_\alpha, \quad (3.70)$$

$$\frac{\partial(\omega_\alpha L_\alpha)}{\partial t} + \nabla \cdot (\omega_\alpha L_\alpha \mathbf{u}_{s\alpha}) = b_\alpha. \quad (3.71)$$

Moment transforms can be applied to determine the functional forms of a_α and b_α and then solving the PBE. The k^{th} moment of the PSD is defined as

$$m_k(\mathbf{x}, t) = \int_0^\infty n(L; \mathbf{x}, t) L^k dL \approx \sum_{\alpha=1}^N \omega_\alpha L_\alpha^k. \quad (3.72)$$

Given that:

$$\begin{aligned} \int_0^\infty \delta(L - L_\alpha) L^k dL &= L_\alpha^k, \\ \int_0^\infty \delta'(L - L_\alpha) L^k dL &= -k L_\alpha^{k-1}, \\ \int_0^\infty \delta''(L - L_\alpha) L^k dL &= k(k-1) L_\alpha^{k-2}, \end{aligned} \quad (3.73)$$

then the moment transform of Eq. 3.69 yields:

$$\sum_{\alpha=1}^N a_{\alpha} L_{\alpha}^k (1 - k) + k b_{\alpha} L_{\alpha}^{k-1} = \bar{S}_k, \quad (3.74)$$

where

$$\bar{S}_k = \int_0^{\infty} S(L) L^k dL. \quad (3.75)$$

As it is possible to see from Eq. 3.74, the source terms of the transport equations of the N weights ω_{α} and characteristic lengths L_{α} are defined through a linear system involving the first $2N$ moments of the population balance equation (e.g., $k = 0, \dots, 2N - 1$). This linear system can be written in matrix form as:

$$\mathbf{A}\mathbf{x} = \mathbf{d}, \quad (3.76)$$

where the $2N \times 2N$ coefficient matrix $\mathbf{A} = \begin{bmatrix} \mathbf{A}_1 & \mathbf{A}_2 \end{bmatrix}$ is defined by

$$\mathbf{A}_1 = \begin{bmatrix} 1 & \dots & 1 \\ 0 & \dots & 0 \\ -L_1^2 & \dots & -L_N^2 \\ \vdots & \ddots & \vdots \\ 2(1 - N)L_1^{2N-1} & \dots & 2(1 - N)L_N^{2N-1} \end{bmatrix} \quad (3.77)$$

and

$$\mathbf{A}_2 = \begin{bmatrix} 0 & \dots & 0 \\ 1 & \dots & 1 \\ 2L_1 & \dots & 2L_N \\ \vdots & \ddots & \vdots \\ (2N - 1)L_1^{2N-2} & \dots & (2N - 1)L_N^{2N-2} \end{bmatrix}. \quad (3.78)$$

$$\mathbf{x} = \begin{bmatrix} a_1 & \dots & a_N & b_1 & \dots & b_N \end{bmatrix}^T = \begin{bmatrix} \mathbf{a} \\ \mathbf{b} \end{bmatrix}, \quad (3.79)$$

$$\mathbf{d} = \begin{bmatrix} \bar{S}_0 & \dots & \bar{S}_{2N-1} \end{bmatrix}^T. \quad (3.80)$$

If $N = 1$ the PSD is represented by only one delta function and \mathbf{A} is the identity matrix. The source terms are:

$$\begin{bmatrix} a_1 \\ b_1 \end{bmatrix} = \begin{bmatrix} \bar{S}_0 \\ \bar{S}_1 \end{bmatrix}. \quad (3.81)$$

If $N = 2$ the PSD is described by two delta functions, and

$$\mathbf{A} = \begin{bmatrix} 1 & 1 & 0 & 0 \\ 0 & 0 & 1 & 1 \\ -L_1^2 & -L_2^2 & 2L_1 & 2L_2 \\ -2L_1^3 & -2L_2^3 & 3L_1^2 & 3L_2^2 \end{bmatrix}. \quad (3.82)$$

By inverting \mathbf{A} , we can get the source term:

$$\begin{bmatrix} a_1 \\ a_2 \\ b_1 \\ b_2 \end{bmatrix} = \begin{bmatrix} (3L_1 - L_2)L_2^2 & -6L_1L_2 & 3(L_1 + L_2) & -2 \\ (L_1 - 3L_2)L_1^2 & 6L_1L_2 & -3(L_1 + L_2) & 2 \\ 2L_2^2L_1^2 & -(4L_1^2 + L_1L_2 + L_2^2)L_2 & 2(L_1^2 + L_1L_2 + L_2^2) & -L_1 - L_2 \\ -2L_2^2L_1^2 & (L_1^2 + L_1L_2 + 4L_2^2)L_2 & -2(L_1^2 + L_1L_2 + L_2^2) & L_1 + L_2 \end{bmatrix} \frac{1}{(L_1 - L_2)^3} \begin{bmatrix} \bar{S}_0 \\ \bar{S}_1 \\ \bar{S}_2 \\ \bar{S}_3 \end{bmatrix}. \quad (3.83)$$

If $N=3$ the PSD is described by three delta functions, and

$$\mathbf{A} = \begin{bmatrix} 1 & 1 & 1 & 0 & 0 & 0 \\ 0 & 0 & 0 & 1 & 1 & 1 \\ -L_1^2 & -L_2^2 & -L_3^2 & 2L_1 & 2L_2 & 2L_3 \\ -2L_1^3 & -2L_2^3 & -2L_3^3 & 3L_1^2 & 3L_2^2 & 3L_3^2 \\ -3L_1^4 & -3L_2^4 & -3L_3^4 & 4L_1^3 & 4L_2^3 & 4L_3^3 \\ -4L_1^5 & -4L_2^5 & -4L_3^5 & 5L_1^4 & 5L_2^4 & 5L_3^4 \end{bmatrix}, \quad (3.84)$$

and thus inverting \mathbf{A}

$$\begin{bmatrix} a_1 \\ a_2 \\ a_3 \\ b_1 \\ b_2 \\ b_3 \end{bmatrix} = \mathbf{A}^{-1} \begin{bmatrix} \bar{S}_0 \\ \bar{S}_1 \\ \bar{S}_2 \\ \bar{S}_3 \\ \bar{S}_4 \\ \bar{S}_5 \end{bmatrix}. \quad (3.85)$$

3.2.2 Bivariate Population Balance

The PSD defined in terms of two internal coordinates - particle size L and particle temperature T can be written as:

$$n(L, T; \mathbf{x}, t) = \sum_{\alpha=1}^N \omega_{\alpha}(\mathbf{x}, t) \delta[L - L_{\alpha}(\mathbf{x}, t)] \delta[T - T_{\alpha}(\mathbf{x}, t)]. \quad (3.86)$$

In this case, the governing equation for the bivariate population balance is:

$$\frac{\partial n(L, T; \mathbf{x}, t)}{\partial t} + \nabla \cdot [(\mathbf{u}_s | L) n(L, T; \mathbf{x}, t)] = S(L, T; \mathbf{x}, t), \quad (3.87)$$

where $S(L, T; \mathbf{x}, t)$ is the source term due to aggregation, breakage and growth. If Eq. 3.86 is substituted into Eq. 3.87 the population balance becomes:

$$\begin{aligned} \sum_{\alpha=1}^N \delta(L - L_{\alpha}) \delta(T - T_{\alpha}) a_{\alpha} - \sum_{\alpha=1}^N \delta'(L - L_{\alpha}) \delta(T - T_{\alpha}) [b_{\alpha} - L_{\alpha} a_{\alpha}] \\ - \sum_{\alpha=1}^N \delta(L - L_{\alpha}) \delta'(T - T_{\alpha}) [c_{\alpha} - T_{\alpha} a_{\alpha}] = S(L, T), \end{aligned} \quad (3.88)$$

where

$$\frac{\partial \omega_{\alpha}}{\partial t} + \nabla \cdot (\omega_{\alpha} \mathbf{u}_{s\alpha}) = a_{\alpha}, \quad (3.89)$$

$$\frac{\partial (\omega_{\alpha} L_{\alpha})}{\partial t} + \nabla \cdot (\omega_{\alpha} L_{\alpha} \mathbf{u}_{s\alpha}) = b_{\alpha}, \quad (3.90)$$

$$\frac{\partial (\omega_{\alpha} T_{\alpha})}{\partial t} + \nabla \cdot (\omega_{\alpha} T_{\alpha} \mathbf{u}_{s\alpha}) = c_{\alpha}. \quad (3.91)$$

In order to obtain the source terms of the transport equations for ω_{α} , $\omega_{\alpha} L_{\alpha}$, $\omega_{\alpha} T_{\alpha}$, it is necessary to apply the moment transformation. We now define the moment of mixed order k, l

as follows:

$$m_{k,l}(\mathbf{x}, t) = \int_0^\infty \int_0^\infty n(L, T; \mathbf{x}, t) L^k T^l dL dT \approx \sum_{\alpha=1}^N \omega_\alpha L_\alpha^k T_\alpha^l. \quad (3.92)$$

If the moment transformation is applied to Eq. 3.88, the following system of linear equations is obtained:

$$\sum_{\alpha=1}^N a_\alpha L_\alpha^k T_\alpha^l [1 - k - l] + k b_\alpha L_\alpha^{k-1} T_\alpha^l + l c_\alpha L_\alpha^k T_\alpha^{l-1} = \bar{S}_{k,l}, \quad (3.93)$$

where the mixed moments $\bar{S}_{k,l}$ of the source term are:

$$\bar{S}_{k,l}(\mathbf{x}, t) = \int_0^\infty \int_0^\infty S(L, T) L^k T^l dL dT. \quad (3.94)$$

This linear system of $3N$ equations can be written in matrix form

$$\mathbf{A}\mathbf{x} = \mathbf{d}, \quad (3.95)$$

where the \mathbf{A} is a square matrix of rank $3N$ and where

$$\mathbf{x} = \begin{bmatrix} a_1 & \cdots & a_N & b_1 & \cdots & b_N & c_1 & \cdots & c_N \end{bmatrix}^T = \begin{bmatrix} \mathbf{a} \\ \mathbf{b} \\ \mathbf{c} \end{bmatrix}. \quad (3.96)$$

In what follows \mathbf{A} and \mathbf{d} will be derived for $N = 1, 2, 3$.

If $N = 1$ the PSD is represented by only one delta function and \mathbf{A} is the identity matrix.

The source terms are:

$$\begin{bmatrix} a_1 \\ b_1 \\ c_1 \end{bmatrix} = \begin{bmatrix} \bar{S}_{0,0} \\ \bar{S}_{1,0} \\ \bar{S}_{0,1} \end{bmatrix}. \quad (3.97)$$

If $N = 2$ the PSD is described by two delta functions; since each delta function is determined by three parameters ω_α , L_α , T_α , six mixed moments have to be calculated to close the moments. There is not an unique way to close the problem, as follows, in order to relate the moments to the ones used in monovariate case, the orders $\{k, l\} = \{0, 0; 1, 0; 2, 0; 3, 0\}$ and $\{k, l\} = \{0, 1; 3, 1\}$ are chosen. Note that the last moment $\{3, 1\}$ corresponds to particle thermal energy.

Then the linear system has the following form:

$$\mathbf{A} = \begin{bmatrix} 1 & 1 & 0 & 0 & 0 & 0 \\ 0 & 0 & 1 & 1 & 0 & 0 \\ -L_1^2 & -L_2^2 & 2L_1 & 2L_2 & 0 & 0 \\ -2L_1^3 & -2L_2^3 & 3L_1^2 & 3L_2^2 & 0 & 0 \\ 0 & 0 & 0 & 0 & 1 & 1 \\ -3L_1^3T_1 & -3L_2^3T_2 & 3L_1^2T_1 & 3L_2^2T_2 & L_1^3 & L_2^3 \end{bmatrix}, \quad (3.98)$$

$$\mathbf{x} = \begin{bmatrix} a_1 & a_2 & b_1 & b_2 & c_1 & c_2 \end{bmatrix}^T = \begin{bmatrix} \mathbf{a} \\ \mathbf{b} \\ \mathbf{c} \end{bmatrix}, \quad (3.99)$$

and

$$\mathbf{d} = \begin{bmatrix} \bar{S}_{0,0} & \bar{S}_{1,0} & \bar{S}_{2,0} & \bar{S}_{3,0} & \bar{S}_{0,1} & \bar{S}_{3,1} \end{bmatrix}^T. \quad (3.100)$$

We can rewrite the matrix as:

$$\begin{bmatrix} \mathcal{A}_1 & 0 \\ \mathcal{A}_2 & \mathcal{A}_3 \end{bmatrix} \begin{bmatrix} \mathcal{X}_1 \\ \mathcal{X}_2 \end{bmatrix} = \begin{bmatrix} \mathcal{D}_1 \\ \mathcal{D}_2 \end{bmatrix}, \quad (3.101)$$

where

$$\mathcal{A}_1 = \begin{bmatrix} 1 & 1 & 0 & 0 \\ 0 & 0 & 1 & 1 \\ -L_1^2 & -L_2^2 & 2L_1 & 2L_2 \\ -2L_1^3 & -2L_2^3 & 3L_1^2 & 3L_2^2 \end{bmatrix}, \quad (3.102)$$

$$\mathcal{X}_1 = \begin{bmatrix} a_1 & a_2 & b_1 & b_2 \end{bmatrix}^T, \quad (3.103)$$

and

$$\mathcal{D}_1 = \begin{bmatrix} \bar{S}_{0,0} & \bar{S}_{1,0} & \bar{S}_{2,0} & \bar{S}_{3,0} \end{bmatrix}^T. \quad (3.104)$$

\mathcal{A}_1 , \mathcal{X}_1 and \mathcal{D}_1 are the same matrices we used in monovariate case for $N = 2$, thus the source terms a_1, a_2, b_1, b_2 have the same value as the monovariate case. The source term $\mathcal{X}_2 = [c_1, c_2]^T$ can be obtained by solving following equation:

$$\mathcal{A}_2\mathcal{X}_1 + \mathcal{A}_3\mathcal{X}_2 = \mathcal{D}_2, \quad (3.105)$$

and

$$\mathcal{X}_2 = \mathcal{A}_3^{-1}(\mathcal{D}_2 - \mathcal{A}_2 \mathcal{X}_1) = \mathcal{A}_3^{-1}(\mathcal{D}_2 - \mathcal{A}_2 \mathcal{A}_1^{-1} \mathcal{D}_1), \quad (3.106)$$

where

$$\mathcal{A}_2 = \begin{bmatrix} 0 & 0 & 0 & 0 \\ -3L_1^3 T_1 & -3L_2^3 T_2 & 3L_1^2 T_1 & 3L_2^2 T_2 \end{bmatrix}, \quad (3.107)$$

$$\mathcal{A}_3 = \begin{bmatrix} 1 & 1 \\ L_1^3 & L_2^3 \end{bmatrix}, \quad (3.108)$$

and

$$\mathcal{D}_2 = \begin{bmatrix} \bar{S}_{0,1} & \bar{S}_{3,1} \end{bmatrix}^T. \quad (3.109)$$

If $N = 3$, the PSD is described through three delta functions. Since each delta function is determined by three parameters $\omega_\alpha, L_\alpha, T_\alpha$, nine mixed moments have to be used to close the problem. In this case, the following moments will be used to close the problem $\{k, l\} = \{0, 0; 1, 0; 2, 0; 3, 0; 4, 0; 5, 0\}$ and $\{k, l\} = \{0, 1; 1, 1; 3, 1\}$. Consequently the linear system has the following form:

$$\mathbf{A} = \begin{bmatrix} 1 & 1 & 1 & 0 & 0 & 0 & 0 & 0 & 0 \\ 0 & 0 & 0 & 1 & 1 & 1 & 0 & 0 & 0 \\ -L_1^2 & -L_2^2 & -L_3^2 & 2L_1 & 2L_2 & 2L_3 & 0 & 0 & 0 \\ -2L_1^3 & -2L_2^3 & -2L_3^3 & 3L_1^2 & 3L_2^2 & 3L_3^2 & 0 & 0 & 0 \\ -3L_1^4 & -3L_2^4 & -3L_3^4 & 4L_1^3 & 4L_2^3 & 4L_3^3 & 0 & 0 & 0 \\ -4L_1^5 & -4L_2^5 & -4L_3^5 & 5L_1^4 & 5L_2^4 & 5L_3^4 & 0 & 0 & 0 \\ 0 & 0 & 0 & 0 & 0 & 0 & 1 & 1 & 1 \\ -L_1 T_1 & -L_2 T_2 & -L_3 T_3 & T_1 & T_2 & T_3 & L_1 & L_2 & L_3 \\ -3L_1^3 T_1 & -3L_2^3 T_2 & -3L_3^3 T_3 & 3L_1^2 T_1 & 3L_2^2 T_2 & 3L_3^2 T_3 & L_1^3 & L_2^3 & L_3^3 \end{bmatrix}, \quad (3.110)$$

$$\mathbf{x} = \begin{bmatrix} a_1 & a_2 & a_3 & b_1 & b_2 & b_3 & c_1 & c_2 & c_3 \end{bmatrix}^T = \begin{bmatrix} \mathbf{a} & \mathbf{b} & \mathbf{c} \end{bmatrix}^T, \quad (3.111)$$

and

$$\mathbf{d} = \begin{bmatrix} \bar{S}_{0,0} & \bar{S}_{1,0} & \bar{S}_{2,0} & \bar{S}_{3,0} & \bar{S}_{4,0} & \bar{S}_{5,0} & \bar{S}_{0,1} & \bar{S}_{1,1} & \bar{S}_{3,1} \end{bmatrix}^T. \quad (3.112)$$

using the same method as for $N = 2$ to divide the matrix to four small matrices, the source terms $\mathcal{X}_2 = [c_1, c_2, c_3]^T$ can be get from the equation,

$$\mathcal{X}_2 = \mathcal{A}_3^{-1}(\mathcal{D}_2 - \mathcal{A}_2\mathcal{A}_1^{-1}\mathcal{D}_1). \quad (3.113)$$

3.2.3 Aggregation and Breakage Equation

For monovariate case, the moment transform of the source term only with aggregation and breakage (the molecular growth rate is zero) is:

$$\bar{S}_k(\mathbf{x}, t) = \bar{B}_k^a(\mathbf{x}, t) - \bar{D}_k^a(\mathbf{x}, t) + \bar{B}_k^b(\mathbf{x}, t) - \bar{D}_k^b(\mathbf{x}, t), \quad (3.114)$$

where

$$\bar{B}_k^a = \frac{1}{2} \int_0^\infty n(\lambda; \mathbf{x}, t) \int_0^\infty \beta(u, \lambda)(u^3 + \lambda^3)^{k/3} n(u; \mathbf{x}, t) du d\lambda, \quad (3.115)$$

$$\bar{D}_k^a = \int_0^\infty L^k n(L; \mathbf{x}, t) \int_0^\infty \beta(L, \lambda) n(\lambda; \mathbf{x}, t) d\lambda dL, \quad (3.116)$$

$$\bar{B}_k^b = \int_0^\infty L^k \int_0^\infty a(\lambda) b(L|\lambda) n(\lambda; \mathbf{x}, t) d\lambda dL, \quad (3.117)$$

$$\bar{D}_k^b = \int_0^\infty L^k a(L) n(L; \mathbf{x}, t) dL, \quad (3.118)$$

are respectively the moments of the birth and death rates for aggregation and breakage. The detail derivation about the aggregation and breakage moments can be found in the work of Marchisio, Vigil, and Fox (2003b). In the equation $\beta(L, \lambda)$ is the aggregation kernel that is the frequency of collision of two particles with length L and λ , $a(L)$ is the breakage kernel that is the frequency of disruption of a particle of length L , and $b(L|\lambda)$ is the fragment distribution function that contains information on the fragments produced by a breakage event.

Applying the quadrature approximation reported in Eq. 3.72, the source term becomes :

$$\bar{S}_k = \frac{1}{2} \sum_{i=1}^N \omega_i \sum_{j=1}^N \omega_j (L_i^3 + L_j^3)^{k/3} \beta_{ij} - \sum_{i=1}^N L_i^k \omega_i \sum_{j=1}^N \beta_{ij} \omega_j + \sum_{i=1}^N a_i \bar{b}_i^{(k)} \omega_i - \sum_{i=1}^N L_i^k a_i \omega_i, \quad (3.119)$$

where $\beta_{ij} = \beta(L_i, L_j)$, $a_i = a(L_i)$, and

$$\bar{b}_i^{(k)} = \int_0^{+\infty} L^k b(L|L_i) dL. \quad (3.120)$$

For the bivariate case, the source term for the pure aggregation and breakage case (without particle growth) can be expressed as:

$$\bar{S}_{k,l}(\mathbf{x}, t) = \bar{B}_{k,l}^a(\mathbf{x}, t) - \bar{D}_{k,l}^a(\mathbf{x}, t) + \bar{B}_{k,l}^b(\mathbf{x}, t) - \bar{D}_{k,l}^b(\mathbf{x}, t), \quad (3.121)$$

and the first term represents birth due to aggregation, the second term is death due to aggregation, the third one is birth due to breakage and the last term is death due to breakage. In what follows, the detailed derivation to obtain these four terms is presented.

The general aggregation-breakage equation for a homogeneous system with two variables (volume $v = L^3$, $\epsilon = \lambda^3$ and energy $e = TL^3$, $e' = T'\lambda^3$) can be expressed as:

$$\begin{aligned} \frac{\partial n'(v, e)}{\partial t} &= \frac{1}{2} \int_0^\infty \int_0^\infty \beta'(v - \epsilon, \epsilon, e - e', e') n'(v - \epsilon, e - e') n'(\epsilon, e') d\epsilon de' \\ &\quad - n'(v, e) \int_0^\infty \int_0^\infty \beta'(v, \epsilon, e, e') n'(\epsilon, e') d\epsilon de' \\ &\quad + \int_0^\infty \int_0^\infty a'(\epsilon, e') b'(v, e | \epsilon, e') n'(\epsilon, e') d\epsilon de' \\ &\quad - a'(v, e) n'(v, e). \end{aligned} \quad (3.122)$$

Using the Jacobian matrix:

$$\frac{\partial(v, e)}{\partial(L, T)} = \begin{vmatrix} 3L^2 & 0 \\ 3L^2 T & L^3 \end{vmatrix} = 3L^5 \quad \text{and} \quad \frac{\partial(\epsilon, e')}{\partial(\lambda, T')} = \begin{vmatrix} 3\lambda^2 & 0 \\ 3\lambda^2 T' & \lambda^3 \end{vmatrix} = 3\lambda^5, \quad (3.123)$$

it is possible to change the number density function to length and temperature based one. The two density functions are related by:

$$\begin{aligned} n'(v, e) dvde &= n'(L^3, L^3 T) 3L^5 dLdT = n(L, T) dLdT, \\ n'(\epsilon, e') d\epsilon de' &= n'(\lambda^3, \lambda^3 T') 3\lambda^5 d\lambda dT' = n(\lambda, T') d\lambda dT'. \end{aligned} \quad (3.124)$$

Multiplying $3L^5$ on both sides of Eq. 3.122, we get:

$$\frac{\partial n(L, T)}{\partial t} = B^a(L, T) - D^a(L, T) + B^b(L, T) - D^b(L, T). \quad (3.125)$$

The first term will be:

$$\begin{aligned}
B^a(L, T) &= \frac{3L^5}{2} \int_0^\infty \int_0^\infty \beta'(v - \epsilon, \epsilon, e - e', e') n'(v - \epsilon, e - e') n'(\epsilon, e') d\epsilon de' \\
&= \frac{3L^5}{2} \int_0^\infty \int_0^\infty \beta'(L^3 - \lambda^3, \lambda, e - e', T') n'(L^3 - \lambda^3, e - e') n(\lambda, T') d\lambda dT' \\
&= \frac{3L^5}{2} \int_0^\infty \int_0^\infty \beta((L^3 - \lambda^3)^{1/3}, \lambda, T'', T') \frac{n((L^3 - \lambda^3)^{1/3}, T'')}{3(L^3 - \lambda^3)^{5/3}} n(\lambda, T') d\lambda dT' \\
&= \frac{L^5}{2} \int_0^\infty \int_0^\infty \beta((L^3 - \lambda^3)^{1/3}, \lambda, T'', T') \frac{n((L^3 - \lambda^3)^{1/3}, T'')}{(L^3 - \lambda^3)^{5/3}} n(\lambda, T') d\lambda dT', \quad (3.126)
\end{aligned}$$

and from the conservation of the energy, we get:

$$T'' = \frac{L^3 T - \lambda^3 T'}{L^3 - \lambda^3}. \quad (3.127)$$

The second term is:

$$\begin{aligned}
D^a(L, T) &= 3L^5 n'(v, e) \int_0^\infty \int_0^\infty \beta'(v, \epsilon, e, e') n'(\epsilon, e') d\epsilon de' \\
&= 3L^5 n'(L^3, L^3 T) \int_0^\infty \int_0^\infty \beta'(L^3, \lambda, e, T') n(\lambda, T') d\lambda dT' \\
&= n(L, T) \int_0^\infty \int_0^\infty \beta(L, \lambda, T, T') n(\lambda, T') d\lambda dT'. \quad (3.128)
\end{aligned}$$

Applying the same methods, the third term and the last term are:

$$B^b(L, T) = \int_0^\infty \int_0^\infty a(\lambda, T') b(L, T | \lambda, T') n(\lambda, T') d\lambda dT', \quad (3.129)$$

$$D^b(L, T) = a(L, T) n(L, T). \quad (3.130)$$

If moment transformation is applied on all these four terms and we use:

$$\begin{aligned}
u^3 &= L^3 - \lambda^3, \\
dL &= \frac{u^2}{L^2} du, \\
dT &= \frac{u^3}{L^3} dT'', \quad (3.131)
\end{aligned}$$

we get:

$$\begin{aligned}
\overline{B}_{k,l}^a &= \frac{1}{2} \int_0^\infty \int_0^\infty \int_0^\infty \int_0^\infty \beta L^5 L^k T^l \frac{n((L^3 - \lambda^3)^{1/3}, T'')}{(L^3 - \lambda^3)^{5/3}} n(\lambda, T') d\lambda dT' dT dL \\
&= \frac{1}{2} \int_0^\infty \int_0^\infty \int_0^\infty \int_0^\infty \beta L^5 (u^3 + \lambda^3)^{k/3} \left(\frac{\lambda^3 T' + u^3 T''}{\lambda^3 + u^3} \right)^l \\
&\quad \frac{1}{u^5} n(u, T'') n(\lambda, T') \frac{u^5}{L^5} du d\lambda dT' dT'' \\
&= \frac{1}{2} \int_0^\infty \int_0^\infty \int_0^\infty \int_0^\infty \beta (u^3 + \lambda^3)^{k/3} \left(\frac{\lambda^3 T' + u^3 T''}{\lambda^3 + u^3} \right)^l n(u, T'') n(\lambda, T') du d\lambda dT' dT'', \\
\overline{D}_{k,l}^a &= \int_0^\infty \int_0^\infty \int_0^\infty \int_0^\infty \beta L^k T^l n(L, T) n(\lambda, T') d\lambda dL dT' dT, \tag{3.132}
\end{aligned}$$

$$\overline{B}_{k,l}^b = \int_0^\infty \int_0^\infty \int_0^\infty \int_0^\infty a(\lambda, T') b(L, T | \lambda, T') L^k T^l n(\lambda, T') d\lambda dL dT' dT, \tag{3.133}$$

$$\overline{D}_{k,l}^b = \int_0^\infty \int_0^\infty L^k T^l a(L, T) n(L, T) dL dT. \tag{3.134}$$

Employing the DQMOM method, use Eq. 3.92, the source term can be calculated as:

$$\begin{aligned}
\overline{S}_{k,l} &= \frac{1}{2} \sum_{i=1}^N \omega_i \sum_{j=1}^N \omega_j (L_i^3 + L_j^3)^{k/3} \beta_{ij} \left(\frac{L_i^3 T_i + L_j^3 T_j}{L_i^3 + L_j^3} \right)^l \\
&\quad - \sum_{i=1}^N L_i^k T_i^l \omega_i \sum_{j=1}^N \beta_{ij} \omega_j + \sum_{i=1}^N T_i^l a_i \overline{b}_i^{(k)} \omega_i - \sum_{i=1}^N L_i^k T_i^l a_i \omega_i, \tag{3.135}
\end{aligned}$$

where

$$\overline{b}_i^{(k)} = \int_0^\infty \int_0^\infty L^k T^l b(L, T | \lambda, T') dL dT. \tag{3.136}$$

3.2.4 DQMOM-Multi-Fluid Model

In order to be consistent with the variables used in the multi-fluid model, we need to associate the weights ω_α and abscissas L_α with the solid volume fraction $\varepsilon_{s\alpha}$ and the effective length $\varepsilon_{s\alpha} L_\alpha$ for each solid phase. The volume fraction of each solid phase is related to the abscissas L_α and weights ω_α by

$$\varepsilon_{s\alpha} = k_v L_\alpha^3 \omega_\alpha = k_v \frac{\mathcal{L}_\alpha^3}{\omega_\alpha^2}, \tag{3.137}$$

and the effective length of the solid phase is

$$\varepsilon_{s\alpha} L_\alpha = k_v L_\alpha^4 \omega_\alpha = k_v \frac{\mathcal{L}_\alpha^4}{\omega_\alpha^3}, \tag{3.138}$$

where k_v is a volumetric shape factor (e.g., for spherical particles $k_v = \pi/6$) and $\mathcal{L}_\alpha = \omega_\alpha L_\alpha$. If Eqs. 3.137 is substituted into the transport equation for $\varepsilon_{s\alpha}$, the following equation can be obtained:

$$\begin{aligned}
& \frac{\partial(\varepsilon_{s\alpha}\rho_{s\alpha})}{\partial t} + \nabla \cdot (\varepsilon_{s\alpha}\rho_{s\alpha}\mathbf{u}_{s\alpha}) \\
&= k_v\rho_{s\alpha} \left[\frac{\partial(\mathcal{L}_\alpha^3/\omega_\alpha^2)}{\partial t} + \nabla \cdot \left(\frac{\mathcal{L}_\alpha^3}{\omega_\alpha^2} \mathbf{u}_{s\alpha} \right) \right] \\
&= k_v\rho_{s\alpha} \left[3\frac{\mathcal{L}_\alpha^2}{\omega_\alpha^2} \frac{\partial\mathcal{L}_\alpha}{\partial t} - 2\frac{\mathcal{L}_\alpha^3}{\omega_\alpha^3} \frac{\partial\omega_\alpha}{\partial t} + \frac{\mathcal{L}_\alpha^3}{\omega_\alpha^2} (\nabla \cdot \mathbf{u}_{s\alpha}) + \mathbf{u}_{s\alpha} \cdot \nabla \left(\frac{\mathcal{L}_\alpha^3}{\omega_\alpha^2} \right) \right] \\
&= k_v\rho_{s\alpha} \left[3\frac{\mathcal{L}_\alpha^2}{\omega_\alpha^2} \frac{\partial\mathcal{L}_\alpha}{\partial t} - 2\frac{\mathcal{L}_\alpha^3}{\omega_\alpha^3} \frac{\partial\omega_\alpha}{\partial t} + \frac{\mathcal{L}_\alpha^3}{\omega_\alpha^2} (\nabla \cdot \mathbf{u}_{s\alpha}) + 3\frac{\mathcal{L}_\alpha^2}{\omega_\alpha^2} \mathbf{u}_{s\alpha} \cdot \nabla\mathcal{L}_\alpha - 2\frac{\mathcal{L}_\alpha^3}{\omega_\alpha^3} \mathbf{u}_{s\alpha} \cdot \nabla\omega_\alpha \right] \\
&= 3k_v\rho_{s\alpha} \frac{\mathcal{L}_\alpha^2}{\omega_\alpha^2} \left(\frac{\partial\mathcal{L}_\alpha}{\partial t} + \mathbf{u}_{s\alpha} \cdot \nabla\mathcal{L}_\alpha + \mathcal{L}_\alpha \nabla \cdot \mathbf{u}_{s\alpha} \right) - 2k_v\rho_{s\alpha} \frac{\mathcal{L}_\alpha^3}{\omega_\alpha^3} \left(\frac{\partial\omega_\alpha}{\partial t} + \mathbf{u}_{s\alpha} \cdot \nabla\omega_\alpha + \omega_\alpha \nabla \cdot \mathbf{u}_{s\alpha} \right) \\
&= 3k_v\rho_{s\alpha} \frac{\mathcal{L}_\alpha^2}{\omega_\alpha^2} \left[\frac{\partial\mathcal{L}_\alpha}{\partial t} + \nabla \cdot (\mathcal{L}_\alpha \mathbf{u}_{s\alpha}) \right] - 2k_v\rho_{s\alpha} \frac{\mathcal{L}_\alpha^3}{\omega_\alpha^3} \left[\frac{\partial\omega_\alpha}{\partial t} + \nabla \cdot (\omega_\alpha \mathbf{u}_{s\alpha}) \right] \\
&= 3k_v\rho_{s\alpha} L_\alpha^2 b_\alpha - 2k_v\rho_{s\alpha} L_\alpha^3 a_\alpha. \tag{3.139}
\end{aligned}$$

If we substitute Eqs. 3.138 into the transport equation for $\varepsilon_{s\alpha}L_\alpha$, we can also get:

$$\begin{aligned}
& \frac{\partial(\varepsilon_{s\alpha}L_\alpha\rho_{s\alpha})}{\partial t} + \nabla \cdot (\varepsilon_{s\alpha}L_\alpha\rho_{s\alpha}\mathbf{u}_{s\alpha}) \\
&= k_v\rho_{s\alpha} \left[\frac{\partial(\mathcal{L}_\alpha^4/\omega_\alpha^3)}{\partial t} + \nabla \cdot \left(\frac{\mathcal{L}_\alpha^4}{\omega_\alpha^3} \mathbf{u}_{s\alpha} \right) \right] \\
&= k_v\rho_{s\alpha} \left[4\frac{\mathcal{L}_\alpha^3}{\omega_\alpha^3} \frac{\partial\mathcal{L}_\alpha}{\partial t} - 3\frac{\mathcal{L}_\alpha^4}{\omega_\alpha^4} \frac{\partial\omega_\alpha}{\partial t} + \frac{\mathcal{L}_\alpha^4}{\omega_\alpha^3} (\nabla \cdot \mathbf{u}_{s\alpha}) + \mathbf{u}_{s\alpha} \cdot \nabla \left(\frac{\mathcal{L}_\alpha^4}{\omega_\alpha^3} \right) \right] \\
&= k_v\rho_{s\alpha} \left[4\frac{\mathcal{L}_\alpha^3}{\omega_\alpha^3} \frac{\partial\mathcal{L}_\alpha}{\partial t} - 3\frac{\mathcal{L}_\alpha^4}{\omega_\alpha^4} \frac{\partial\omega_\alpha}{\partial t} + \frac{\mathcal{L}_\alpha^4}{\omega_\alpha^3} (\nabla \cdot \mathbf{u}_{s\alpha}) + 4\frac{\mathcal{L}_\alpha^3}{\omega_\alpha^3} \mathbf{u}_{s\alpha} \cdot \nabla\mathcal{L}_\alpha - 3\frac{\mathcal{L}_\alpha^4}{\omega_\alpha^4} \mathbf{u}_{s\alpha} \cdot \nabla\omega_\alpha \right] \\
&= 4k_v\rho_{s\alpha} \frac{\mathcal{L}_\alpha^3}{\omega_\alpha^3} \left(\frac{\partial\mathcal{L}_\alpha}{\partial t} + \mathbf{u}_{s\alpha} \cdot \nabla\mathcal{L}_\alpha + \mathcal{L}_\alpha \nabla \cdot \mathbf{u}_{s\alpha} \right) - 3k_v\rho_{s\alpha} \frac{\mathcal{L}_\alpha^4}{\omega_\alpha^4} \left(\frac{\partial\omega_\alpha}{\partial t} + \mathbf{u}_{s\alpha} \cdot \nabla\omega_\alpha + \omega_\alpha \nabla \cdot \mathbf{u}_{s\alpha} \right) \\
&= 4k_v\rho_{s\alpha} \frac{\mathcal{L}_\alpha^3}{\omega_\alpha^3} \left[\frac{\partial\mathcal{L}_\alpha}{\partial t} + \nabla \cdot (\mathcal{L}_\alpha \mathbf{u}_{s\alpha}) \right] - 3k_v\rho_{s\alpha} \frac{\mathcal{L}_\alpha^4}{\omega_\alpha^4} \left[\frac{\partial\omega_\alpha}{\partial t} + \nabla \cdot (\omega_\alpha \mathbf{u}_{s\alpha}) \right] \\
&= 4k_v\rho_{s\alpha} L_\alpha^3 b_\alpha - 3k_v\rho_{s\alpha} L_\alpha^4 a_\alpha. \tag{3.140}
\end{aligned}$$

The first transport equation (Eq. 3.139) represents the continuity equation for the α^{th} solid phase in the presence of aggregation and breakage (cf. Eq. 3.3) but without mass transfer between gas and solids. It is straightforward to verify that the summation of the transport equations over the N solid phases leads to a null source term. This implies that aggregation and breakage do not change the total solid volume fraction (i.e., the solid volume fraction is

preserved). Thus, the source term for the gas volume fraction ε_g in the presence of aggregation and breakage is null, and the relative volume fractions of the different solid phases change due to aggregation and breakage. The Eq. 3.140 is just a new scalar equation for particle length L_α for each solid phase.

For the bivariate case with two variables L_α and T_α , a new term accounting for the aggregation and breakage will appear on the right hand side of the solid energy equation. From Eq. 3.91, we can get:

$$\begin{aligned}
& \frac{\partial(\omega_\alpha T_\alpha)}{\partial t} + \nabla \cdot (\omega_\alpha T_\alpha \mathbf{u}_{s\alpha}) \\
&= \omega_\alpha \frac{\partial T_\alpha}{\partial t} + T_\alpha \frac{\partial \omega_\alpha}{\partial t} + T_\alpha \mathbf{u}_{s\alpha} \cdot \nabla \omega_\alpha + \omega_\alpha \mathbf{u}_{s\alpha} \cdot \nabla T_\alpha + \omega_\alpha T_\alpha \nabla \cdot \mathbf{u}_{s\alpha} \\
&= \omega_\alpha \left[\frac{\partial T_\alpha}{\partial t} + \mathbf{u}_{s\alpha} \cdot \nabla T_\alpha \right] + T_\alpha \left[\frac{\partial \omega_\alpha}{\partial t} + \mathbf{u}_{s\alpha} \cdot \nabla \omega_\alpha + \omega_\alpha \nabla \cdot \mathbf{u}_{s\alpha} \right] \\
&= \omega_\alpha \left[\frac{\partial T_\alpha}{\partial t} + \mathbf{u}_{s\alpha} \cdot \nabla T_\alpha \right] + T_\alpha \left[\frac{\partial \omega_\alpha}{\partial t} + \nabla \cdot (\omega_\alpha \mathbf{u}_{s\alpha}) \right] \\
&= \omega_\alpha \left[\frac{\partial T_\alpha}{\partial t} + \mathbf{u}_{s\alpha} \cdot \nabla T_\alpha \right] + T_\alpha a_\alpha \\
&= c_\alpha
\end{aligned} \tag{3.141}$$

After some manipulation, the following equation can be obtained:

$$\frac{\partial T_\alpha}{\partial t} + \mathbf{u}_{s\alpha} \cdot \nabla T_\alpha = \frac{c_\alpha - T_\alpha a_\alpha}{\omega_\alpha}. \tag{3.142}$$

Multiplying $\varepsilon_{s\alpha} \rho_{s\alpha} C_{ps\alpha}$ on both side of Eq. 3.142, the equation becomes:

$$\varepsilon_{s\alpha} \rho_{s\alpha} C_{ps\alpha} \left(\frac{\partial T_\alpha}{\partial t} + \mathbf{u}_{s\alpha} \cdot \nabla T_\alpha \right) = k_v L_\alpha^3 \rho_{s\alpha} C_{ps\alpha} (c_\alpha - T_\alpha a_\alpha). \tag{3.143}$$

In summary, the three transport equations for solid void fraction, particle length and particle temperature with pure aggregation and breakage are:

$$\frac{\partial(\varepsilon_{s\alpha} \rho_{s\alpha})}{\partial t} + \nabla \cdot (\mathbf{u}_{s\alpha} \varepsilon_{s\alpha} \rho_{s\alpha}) = 3k_v \rho_{s\alpha} L_\alpha^2 b_\alpha - 2k_v \rho_{s\alpha} L_\alpha^3 a_\alpha, \tag{3.144}$$

$$\frac{\partial(\varepsilon_{s\alpha} L_\alpha \rho_{s\alpha})}{\partial t} + \nabla \cdot (\mathbf{u}_{s\alpha} \varepsilon_{s\alpha} L_\alpha \rho_{s\alpha}) = 4k_v \rho_{s\alpha} L_\alpha^3 b_\alpha - 3k_v \rho_{s\alpha} L_\alpha^4 a_\alpha, \tag{3.145}$$

$$\varepsilon_{s\alpha} \rho_{s\alpha} C_{ps\alpha} \left(\frac{\partial T_\alpha}{\partial t} + \mathbf{u}_{s\alpha} \cdot \nabla T_\alpha \right) = k_v L_\alpha^3 \rho_{s\alpha} C_{ps\alpha} c_\alpha - k_v L_\alpha^3 \rho_{s\alpha} C_{ps\alpha} T_\alpha a_\alpha. \tag{3.146}$$

3.3 Numerical Methods

3.3.1 Discretization

A staggered grid is used for discretizing PDEs specified in the previous sections. Scalars, such as pressure, void fraction, temperature and mass fraction are stored at the cell centers and the components of the velocity vector are stored at the cell faces. The grid arrangement for a computation cell is shown in Fig. 3.3. All the scalars equation are solved on the main grid, and the equations for the velocity vector components are solved on the staggered grids. Thus there are four grids used for the solution. Patankar (1980) pointed out that when pressure and velocity components are stored at the same grid locations, a checkerboard pressure can develop as an acceptable solution, so a staggered grid is used to prevent such unphysical pressure fields.

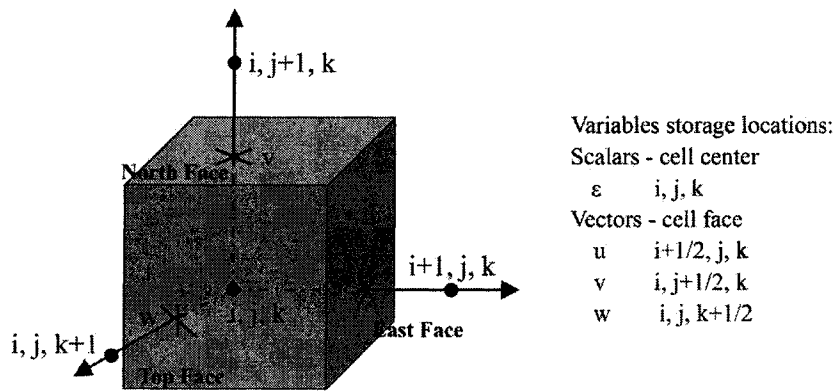


Figure 3.3 A staggered grid for a computation cell

In multiphase flow calculation, a finite volume or control volume (CV) method is usually preferred. This method has an advantage to ensure the global conservation of mass, momentum and even energy on coarse grid (Patankar, 1980). Since a fine grid is computation expensive, CV method is more attractive in practical application. For the discretization, second-order difference is used for diffusive flux terms. The discretization of the convection terms is a more difficult task to do and at the early stage of the work, first-order upwind (FOU) scheme is used. In order to improve the accuracy and avoid numerical diffusion, high-order schemes, such as Superbee is preferred. The detailed information about Superbee and other second-

order schemes can be found in the numerical technique report by Syamlal (1998).

3.3.2 Solution Algorithm

A modified semi-implicit method for pressure-linked equations (SIMPLE) is used for solving the discretized equation for the multiphase flow. A solid volume fraction correction equation, instead of fluid-pressure correction equation are used, which appear to help convergence in the loosely packed region. Solids pressure correction equation requires that $\partial P_s / \partial \varepsilon_s$ does not vanish when $\varepsilon_s \rightarrow 0$. Solids volume fraction correction equation does not have such a restriction, but must account for the effect of solids pressure so that the computation in the densely packed regions are stabilized. To speed up the code, automatic time-step adjustment is applied. This change ensures that the run progresses always at its highest execution speed. It can be demonstrated that this adjustment is 3-30 times faster than the constant time-step. The multiphase momentum equations are strongly coupled through the momentum exchange term, totally decoupling of the equations by calculating the inter-phase transfer term from the previous iteration values will make the iteration unstable or force the time step to be very small, so the partial elimination algorithm (PEA) of Spalding (1980) is introduced to decouple the equations.

An outline of the solution algorithm - modified SIMPLE - is described as the follow steps:

1. At the beginning of the time step, calculate physical properties, exchange coefficients and reaction rates.
2. Calculate velocity fields \mathbf{u}_m^* based on a guessed pressure field. ($m = 0$ to M , 0 denotes gas phase, 1 to M denote solid phases.)
3. Calculate fluid pressure correction P'_g
4. Update fluid pressure field applying an under relaxation: $P_g = P_g^* + \omega_{pg} P'_g$, then calculate velocity corrections \mathbf{u}'_m from P'_g and update velocity fields: $\mathbf{u}_m = \mathbf{u}_m^* + \mathbf{u}'_m$. (For solids phases, \mathbf{u}_m calculated in this step is denoted as \mathbf{u}_m^* in Step 6.)

5. Calculate the gradients $\partial P_m / \partial \varepsilon_m$ for each solid phase, which will be used in the solid volume correction equation, then calculate solids volume fraction correction ε'_m .
6. Update solids volume fraction $\varepsilon_m = \varepsilon_m^* + \omega_{ps} \varepsilon'_m$. Under relax only in the region, where solids are densely packed and the solid volume fraction is increasing. Calculate solid velocity correction and update solid velocity fields again $\mathbf{u}_m = \mathbf{u}_m^* + \mathbf{u}'_m$.
7. Calculate the void fraction by:

$$\varepsilon_0 = 1 - \sum_{m \neq 0} \varepsilon_m$$

8. Calculate the solid pressure from the state equation $P_m = P_m(\varepsilon_m)$.
9. Calculate temperatures, species mass fractions and other scalar equations.
10. Use the normalized residuals calculated in Steps 2, 3, 5 and 9 to check for convergence. If the convergence criterion is not satisfied, the iteration is continued (step 2), otherwise go to next time-step (step 1).

3.3.3 Time-Splitting Method

Time-splitting method, or fractional step is used to decouple the source term for the aggregation, breakage and growth from the transport equations (Eqs. 3.139, 3.140 and 3.143). The transport equation can be generalized as:

$$\frac{d\Phi}{dt} = S(\Phi) + T(\Phi) \quad (3.147)$$

where Φ represents either solid volume fraction, particle length or particle temperature, $S(\Phi)$ is the change due to aggregation, breakage and growth, and $T(\Phi)$ is the change due to transport which includes convection and diffusion. Therefore, over a small time step Δt , the time-splitting method can be applied so that the different processes can be treated in separate fractional steps.

1. In the first fractional time step, the change due to the convection and diffusion is solved for every node using equations:

$$\frac{d\Phi}{dt} = T(\Phi) \quad \text{with} \quad \Phi(0) = \Phi(t). \quad (3.148)$$

The solution to Eq. 3.148 is denoted as $\Phi'(t + \Delta t)$.

2. In the next fractional time step, the change due to the aggregation, breakage and growth term is found separately for every node using $\Phi'(t + \Delta t)$ as the initial condition:

$$\frac{d\Phi}{dt} = S(\Phi) \quad \text{with} \quad \Phi(0) = \Phi'(t + \Delta t). \quad (3.149)$$

This equation yields $\Phi(t + \Delta t)$ as the approximation of the solution of Eq. 3.147.

The overall time-splitting method can be represented as:

$$\Phi \xrightarrow{\text{transport}} \Phi'(t + \Delta t) \xrightarrow[\text{growth}]{\text{aggregation, breakage}} \Phi(t + \Delta t), \quad (3.150)$$

thus the aggregation, breakage and growth term is decoupled from the transport equation and can be treated with the most efficient numerical methods. For example, a stiff ODE solver or ISAT can be used to solve Eq. 3.149.

3.3.4 Grid Resolution Study

Grid resolution results are performed in a dilute riser simulation where period boundary conditions are used on both vertical and horizontal directions. Period boundary conditions are used to ignore the effect of the wall and the effect of inflow and outflow. To account for gas movement, a periodic boundary with pressure drop 200 Pa in the vertical direction are used. Simulations are conducted in a 2D channel, where the width is 10 cm and the height is 40 cm (Fig. 3.4). The initial static bed height is 2 cm and the average solid volume fraction for the entire domain has a constant value of 0.03. The particle diameter used in the simulations is 75 μm . Values of the other parameters are listed in Table 3.1.

Three kinds of resolution are used in the simulation. The coarse-grid is 16×64 cells, and the cell size is 6.25 mm× 6.25 mm. The medium grid is 32×128, and the cell size is 3.125 mm×3.125 mm. The fine resolution is 2 mm×2 mm, and the number of grids is 50×200. The instantaneous contour plots of gas volume fraction, vector plots of gas velocity and contour plots of granular temperature at 5 s with different resolutions are shown in Figs. 3.5, 3.6

Table 3.1 Particle properties and parameters used in the simulation.

Width, D	cm	10
Height, L	cm	40
Initial static bed height, H	cm	2
Particle diameter, d_p	μm	75
Particle density, ρ_s	kg/m^3	1500
Gas density, ρ_g	kg/m^3	1.3
Gas viscosity, μ_g	$kg/(m \cdot s)$	1.8×10^{-5}
Coefficient of restitution, e		0.9
Initial gas pressure, $P_{g,in}$	kPa	101.0
Vertical gas velocity, $V_{g,in}$	cm/s	100
Initial gas temperature, $T_{g,in}$	K	298
Pressure drop along the height, ΔP	Pa	200

and 3.7. The graphs show that, if a coarse grid is used, the flow is almost uniform and not many details of the flow are resolved. The gas velocity is also nearly uniform and there are not many fluctuations on the magnitude of the velocity and not any recirculation on the gas flow. The granular temperature is also very uniform except a few large value at some region where the solid volume fraction is high. When the grid becomes finer, more fine bands and structures appear, and the length of the structures becomes finer. For the gas velocity, the gas recirculates in some region and more fluctuations appear. For the granular temperature, more small structures are also observed. It is safe to say that, when the meshes becomes finer and finer, the flow will continue to change and even smaller structure will be appear.

In multiphase flow, the grid size dependence result is a qualitative measurement of the average bed behavior rather than a point to point convergence. Therefore, the average slip velocity in vertical direction over 13 s is compared in the Table 3.2 for three different resolutions. The comparison shows that, the finer grid, the longer CPU time. When the grid becomes finer, the average slip velocity become closer. The CPU time for the fine grid is 23 times the CPU time of the coarse grid. So very fine grid simulation is computationally expensive. The mean slip velocity on a coarse grid is much lower than the values on medium and fine grids. Due to

Table 3.2 Results comparison for three different resolutions.

	1	2	3
Number of grids	16×64	32×128	50×200
CPU time used(s)	7547	48769	170915
Average V_g over the whole domain (cm/s)	157.08	105.82	87.27
Average V_s over the whole domain (cm/s)	127.35	69.52	49.31
Average slip velocity at y direction (cm/s)	29.73	36.30	37.96

the costly CPU time for the fine grid, the result from medium grid can be used as a “grid size independent” result. The acceptable grid is around 3 mm.

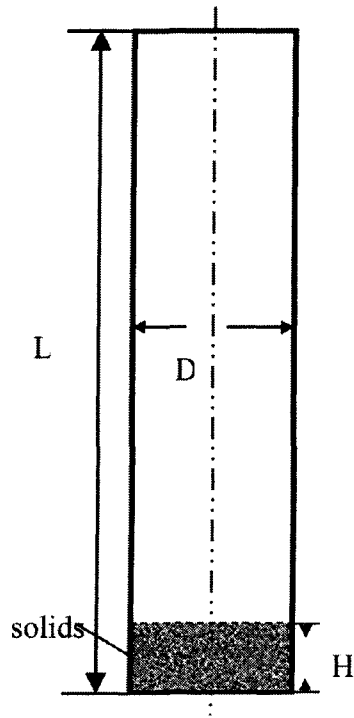


Figure 3.4 The fluidized bed geometry for the simulation

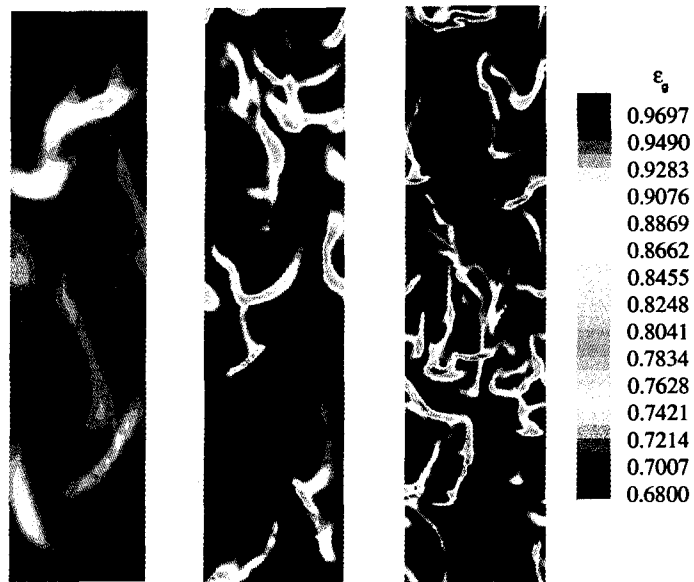


Figure 3.5 Instantaneous contour plots of gas volume fraction at 5s with different resolutions. Left: coarse grid. Middle: medium grid. Right: fine grid.

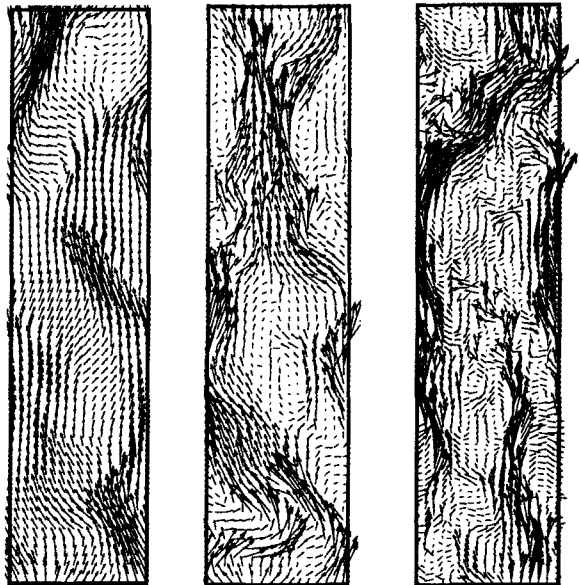


Figure 3.6 Instantaneous vector plots of gas velocity at 5s with different resolutions. Left: coarse grid. Middle: medium grid. Right: fine grid.

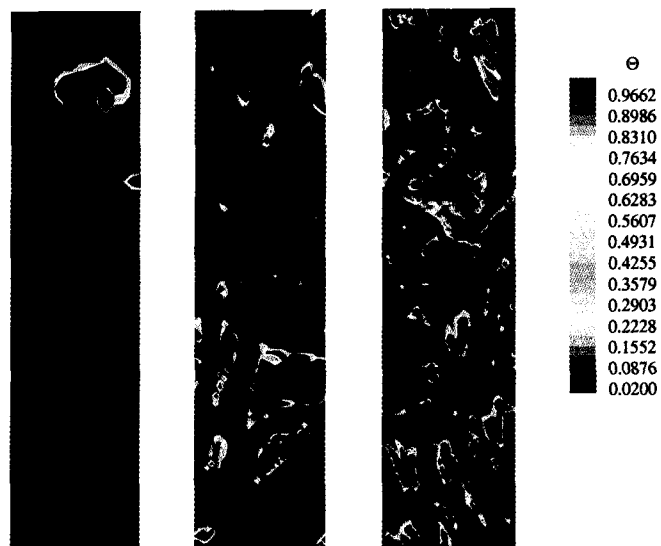


Figure 3.7 Instantaneous contour plots of granular temperature at 5s with different resolutions. Left: coarse grid. Middle: medium grid. Right: fine grid.

CHAPTER 4. APPLICATION OF DQMOM TO POLYDISPERSE GAS-SOLID FLUIDIZED BEDS

4.1 Introduction

FB polymerization reactors have been long recognized as one of the main technologies for producing polyolefins (PP and PE). Compared to other reactors, fluidized beds have several advantages such as the capability of continuous operation and transport of solids in and out of the bed; high heat- and mass-transfer rates from gas to particles leading to fast reaction and uniform temperature in the bed, and a high solids mixing rate (Fan and Zhu, 1998). Much research has been done on FB polymerization reactors, and most current research focuses on the kinetic aspects. However, from the industrial viewpoint, the behavior of these reactors must be studied in consideration of particle and fluid dynamics in the reactor. With the development of high-speed computers, CFD has become available to provide valuable information concerning time-dependent phenomena in the fluidized bed, such as particle overheating, excessive agglomeration and bed defluidization. These pieces of information can help for reactor design, scale up, and optimization.

FB reactors are widely used in many unit operations in the chemical, petroleum, pharmaceutical, agricultural, food and biochemical industries. They are well known as excellent reactors for their superior rates of heat and mass transfer between the gas and the solid particles, and for the efficient mixing of reacting species. With the development of high-speed computers, CFD has played an important role in understanding the flow behavior of these two-phase flow systems. As is well known, most of today's CFD calculations for gas-solid flows are based on the assumption of a monodispersed solid phase (e.g., all particles have the same characteristic size) or on the assumption of a constant PSD (e.g, particles may be represented

by a few different size classes but no changes in the PSD are accounted for (Mathiesen et al., 2000)). However, in many practical cases solid particles belong to a PSD, which changes continuously according to the operating conditions. For example, in FB polyolefin reactors, small catalyst particles (e.g., 20-80 μm) are introduced at a point above the gas distributor, and when exposed to the gas flow containing the monomer, polymerization occurs. At the early stage of polymerization, the catalyst particles fragment into a large number of small particles, which are quickly encapsulated by the newly-formed polymer and grow continuously, reaching a typical size of 200-3000 μm . Due to the differences in the polymer particle sizes, segregation occurs and fully-grown polymer particles migrate to the bottom where they are removed from the reactor. The smaller pre-polymerized particles and fresh catalyst particles tend to migrate to the upper portions of the reactor and continue to react with monomers (Kim and Choi, 2001). In addition, under certain undesirable operating conditions (e.g., when the reactor operates close to the polymer softening temperature), polymer particles can become “sticky” and during collisions can form large agglomerates that can possibly undergo sintering and cause defluidization. In the opposite situation, if the bed is too cold, the particles can become brittle and may fracture forming small fragments that elutriate with the gas (Hatzantonis, Goulas, and Kiparissides, 1998; Yiannoulakis, Yiagopoulos, and Kiparissides, 2001). Successful CFD models for FB poly-olefin reactors must be capable of describing such events in order to guide reactor design, scale up and optimization.

Recent research efforts have been directed towards the investigation of the effect of the PSD on the fluid dynamics of FB reactors. However, most work has focused on the segregation of binary mixtures. van Wachem and coworkers (2001), using kinetic theory applied to a bimodal particle mixture, predicted the expansion of the bed with respect to a monodisperse PSD. Howley and Glasser (2002) examined a general continuum model for a multi-particle fluidized bed and provided a description of the observed phenomenon of “layer inversion” for a binary mixture. In the work of Hoomans et al. (1996), discrete particle simulations were used to investigate segregation phenomena in binary and ternary mixtures, good agreement is obtained in comparison to experiments.

In order to rigorously account for particle-related phenomena (e.g, agglomeration and breakage), the population balance equation (PBE) must be solved along with the continuity and momentum balance equations. However, attempts to incorporate the PBE into multi-fluid codes and to describe the evolution of the PSD in a FB reactor are very few. Recently, researchers have tried to couple the PBE with an Euler-Euler two-fluid model to simulate bubble-column reactors (Olmos et al., 2001; Lo, 1996). In their work, the dispersed phase was represented by ten different size groups but only the momentum balance for the mixture was solved due to the significant reduction in the computing time. Thus the ten different classes were convected in the computational domain with the same mean algebraic velocity. Results showed good agreement with experiments for some hydrodynamic variables, but underestimated the global hold up. Other researchers have also tried to solve the PBE with the multi-fluid code simultaneously, but most work was done in gas-liquid systems, not in gas-solid systems (Lehr and Mewes, 2001; Venneker et al., 2002; Buwa and Ranade, 2002).

For spatially homogeneous systems, many different methods exist for solving the PBE and a lucid description of the mathematical and numerical issues involved can be found in Ramakrishna's book (2000). The most direct method is the DPB approach or CM, in which the internal coordinate (e.g, particle length or volume) is discretized into a finite series of bins. In order to get reasonable results, a large number of classes must be used (e.g., 20-30), so that the DPB method is not a feasible approach for CFD calculations. An alternative approach uses Monte-Carlo simulations. This approach is based on the solution of the PBE in terms of its stochastic equivalent. A population of particles undergoes the "real" physical processes, and events occur according to the appropriate probabilities. For more details on this approach see the papers of Smith and Matsoukas (1998) and Lee and Matsoukas (2000). Although this approach is theoretically applicable, especially for Lagrangian-Eulerian simulations, in order to reduce the statistical error a very large number of particles must be used. Due to limitations on the computational resources, the full incorporation of Monte-Carlo methods with CFD codes is at the moment intractable (Madec, Falk, and Plasari, 2001, 2003).

An attractive alternative is represented by the method of moments where the PSD is

tracked through its moments by integrating out the internal coordinate. The main advantage of MOM is that the number of scalars required is very small (i.e., usually 4-6), which makes the implementation in CFD codes feasible. However, due to the difficulties related with expressing transport equations in terms of the moments themselves, the method has been scarcely applied. This is the so-called closure problem, pointed out first by Hulburt and Katz (1964), and recently reviewed by Diemer and Olson (2002). As an alternative, McGraw (1997) developed the so-called QMOM, which is based on the approximation of the unclosed terms by using an ad-hoc quadrature formula. The quadrature approximation (i.e., its abscissas and weights) can be determined from the lower-order moments (Dette and Studden, 1997) by resorting to the product-difference (PD) algorithm (Gordon, 1968). QMOM has been extensively validated for several problems with different internal coordinates (Barret and Webb, 1998; Marchisio, Vigil, and Fox, 2003b; Marchisio, Pikturna, Fox, Vigil, and Barresi, 2003a). One of the main limitations of QMOM is that since the solid phase is represented through the moments of the distribution, the phase-average velocity of the different solid phases must be used to solve the transport equations for the moments. Thus, in order to use this method in the context of the multiphase flows, it is necessary to extend QMOM to handle cases where each particle size is convected by its own velocity.

In order to address these issues, the DQMOM has been formulated and validated by Marchisio and Fox (2005). DQMOM is based on the direct solution of the transport equations for weights and abscissas of the quadrature approximation. The calculation of the quadrature approximation through this direct formulation presents the advantage of being directly applicable to multi-variate PBE (i.e., PBE with more than one internal coordinate). Moreover, as it will become clear below, each node of the quadrature approximation can be treated as a distinct solid phase. DQMOM thus offers a powerful approach for describing polydisperse solids undergoing segregation, growth, aggregation and breakage processes in the context of CFD simulations.

In this work, DQMOM is implemented in a multi-fluid model for simulating polydisperse gas-solid FB reactors. First, the general governing equations for the multi-fluid model are

presented in Sec. 4.2. Next, in Sec. 4.3, the implementation of aggregation and breakage in the DQMOM multi-fluid model is described. Finally, CFD predictions for the evolution of the PSD in a FB reactor with aggregation and breakage are presented in Sec. 4.4. Conclusions are drawn in Sec 4.5.

4.2 The DQMOM-Multi-Fluid Model

The detailed mathematical modeling of FB reactors is very complex since it involves interactions between closely coupled phenomena, such as multiphase flow dynamics, mass transfer, heat transfer, chemical reactions, and particulate processes such as aggregation and breakage. The simultaneous numerical solution of the equations for continuity, momentum, energy, chemical species is required. In addition, for polydisperse solids a PBE is needed. For simplicity, in this work the FB is assumed to be isothermal with no chemical reactions, and the PSD changes only due to aggregation and breakage. Thus, our goal is to build the link between the PBE and the continuity and momentum balance equations, and to obtain an economical but accurate method for describing the time evolution of the PSD and the gas and solids flow fields. In what follows, the multi-fluid model for gas-solid FB reactors is first described briefly. The implementation of DQMOM in the multi-fluid model is then described in some detail.

4.2.1 Multi-Fluid Model for Gas-Solid Flow

The multi-fluid model has been described in detail in Sec. 3.1 and here we limit the discuss to the equations used in this work and all the variables are same as described before. The continuity equation for the gas phase is

$$\frac{\partial \varepsilon_g \rho_g}{\partial t} + \nabla \cdot (\varepsilon_g \rho_g \mathbf{u}_g) = 0, \quad (4.1)$$

In the absence of aggregation and breakage, the continuity equation of the α^{th} solid phase is

$$\frac{\partial \varepsilon_{s\alpha} \rho_{s\alpha}}{\partial t} + \nabla \cdot (\varepsilon_{s\alpha} \rho_{s\alpha} \mathbf{u}_{s\alpha}) = 0, \quad (4.2)$$

As will be shown below, aggregation and breakage processes will result in additional terms on the right-hand side of Eq. 4.2. The momentum balance for the gas and solid phase are

$$\frac{\partial}{\partial t} (\varepsilon_g \rho_g \mathbf{u}_g) + \nabla \cdot (\varepsilon_g \rho_g \mathbf{u}_g \mathbf{u}_g) = \nabla \cdot \boldsymbol{\sigma}_g + \sum_{\alpha=1}^N \mathbf{f}_{g\alpha} + \varepsilon_g \rho_g \mathbf{g}. \quad (4.3)$$

$$\frac{\partial}{\partial t} (\varepsilon_{s\alpha} \rho_{s\alpha} \mathbf{u}_{s\alpha}) + \nabla \cdot (\varepsilon_{s\alpha} \rho_{s\alpha} \mathbf{u}_{s\alpha} \mathbf{u}_{s\alpha}) = \nabla \cdot \boldsymbol{\sigma}_{s\alpha} - \mathbf{f}_{g\alpha} + \sum_{\beta=1}^N \mathbf{f}_{\beta\alpha} + \varepsilon_{s\alpha} \rho_{s\alpha} \mathbf{g}, \quad (4.4)$$

A simple Newtonian closure is used for the gas-phase stress tensor. Two entirely different methods are used to calculate the solid stress tensor in different regimes. For the plastic or slowly shearing regime, the theories from the study of soil mechanics are used. For the viscous or rapidly shearing regime, kinetic theory is used (Syamlal et al., 1993; Gidaspow, 1994; Lun et al., 1984). The constitutive relations for the gas and solids stress tensors are summarized in Table 4.1. Studies on the dynamics of a single particle in a fluid have shown that many forces contribute to the gas-solid interactions (Fan and Zhu, 1998), but in this work only the drag force and the buoyancy force are accounted for. The drag correlation used was derived by Gidaspow (1994). The interaction forces between the different solid phases are expressed in terms of the drag force and the enduring contact force in the plastic regime, as described by Syamlal et al. (1993). The gas-solid and solid-solid interaction forces are listed in Table 4.2. A detailed discussion of the parameters in the multi-fluid model can be found in Sec. 3.1. The reader should keep in mind that the solid stress tensor and drag formulation appearing in Tables 4.1 and 4.2 are slight modifications of the corresponding monodisperse solids models. Thus the simulation results found using other polydisperse models (Mathiesen, Solberg, and Hjertager, 2000; Arnarson and Willits, 1998) may differ quantitatively from those reported here.

Table 4.1 Constitutive relations for gas and solids stress tensors and the solids collision parameters.

Gas stress tensor:

$$\begin{aligned}\sigma_g &= -P_g \mathbf{I} + \tau_g \\ \tau_g &= 2\varepsilon_g \mu_g \mathbf{D}_g - \frac{2}{3} \varepsilon_g \mu_g \text{Tr}(\mathbf{D}_g) \mathbf{I} \\ \mathbf{D}_g &= \frac{1}{2} [\nabla \mathbf{u}_g + (\nabla \mathbf{u}_g)^T]\end{aligned}$$

Solids stress tensor (viscous regime):

$$\begin{aligned}\sigma_{s\alpha}^v &= -P_{s\alpha}^v \mathbf{I} + \tau_{s\alpha}^v \\ P_{s\alpha}^v &= K_{1\alpha} \varepsilon_{s\alpha}^2 \theta_\alpha \\ \tau_{s\alpha}^v &= 2\mu_{s\alpha}^v \mathbf{D}_{s\alpha} + \lambda_{s\alpha}^v \text{Tr}(\mathbf{D}_{s\alpha}) \mathbf{I} \\ \theta_\alpha &= \left(\frac{-K_{1\alpha} \varepsilon_{s\alpha} \text{Tr}(\mathbf{D}_{s\alpha}) + \sqrt{K_{1\alpha}^2 \text{Tr}^2(\mathbf{D}_{s\alpha}) \varepsilon_{s\alpha}^2 + 4K_{4\alpha} \varepsilon_{s\alpha} [K_{2\alpha} \text{Tr}^2(\mathbf{D}_{s\alpha}) + 2K_{3\alpha} \text{Tr}(\mathbf{D}_{s\alpha}^2)]}}{2\varepsilon_{s\alpha} K_{4\alpha}} \right)^2 \\ \lambda_{s\alpha}^v &= K_{2\alpha} \varepsilon_{s\alpha} \sqrt{\theta_\alpha} \\ \mu_{s\alpha}^v &= K_{3\alpha} \varepsilon_{s\alpha} \sqrt{\theta_\alpha} \\ K_{1\alpha} &= 2(1+e) \rho_{s\alpha} g_{0\alpha\alpha} \\ K_{2\alpha} &= 4d_{p\alpha} \rho_{s\alpha} (1+e) \frac{\varepsilon_{s\alpha} g_{0\alpha\alpha}}{3\sqrt{\pi}} - \frac{2}{3} K_{3\alpha} \\ K_{3\alpha} &= \frac{d_{p\alpha} \rho_{s\alpha}}{2} \left[\frac{\sqrt{\pi}}{3(3-e)} [1 + 0.4(1+e)(3e-1) \varepsilon_{s\alpha} g_{0\alpha\alpha}] + \frac{8\varepsilon_{s\alpha} g_{0\alpha\alpha} (1+e)}{5\sqrt{\pi}} \right] \\ K_{4\alpha} &= \frac{12(1-e^2) \rho_{s\alpha} g_{0\alpha\alpha}}{d_{p\alpha} \sqrt{\pi}} \\ g_{0\alpha\alpha} &= \frac{1}{\varepsilon_g} + \frac{3d_{p\alpha}}{2\varepsilon_g^2} \sum_{\lambda=1}^N \frac{\varepsilon_{s\lambda}}{d_{p\lambda}} \\ \mathbf{D}_{s\alpha} &= \frac{1}{2} [\nabla \mathbf{u}_{s\alpha} + (\nabla \mathbf{u}_{s\alpha})^T]\end{aligned}$$

Solids collision parameters:

$$\begin{aligned}g_{0\beta\alpha} &= \frac{1}{\varepsilon_g} + \frac{3d_{p\alpha} d_{p\beta}}{\varepsilon_g^2 (d_{p\alpha} + d_{p\beta})} \sum_{\lambda=1}^N \frac{\varepsilon_{s\lambda}}{d_{p\lambda}} \\ \sigma_{\beta\alpha} &= (d_\alpha + d_\beta)/2 \\ \theta_s &= \frac{\varepsilon_{s\alpha} \rho_{s\alpha} \theta_\alpha + \varepsilon_{s\beta} \rho_{s\beta} \theta_\beta}{\varepsilon_{s\alpha} \rho_{s\alpha} + \varepsilon_{s\beta} \rho_{s\beta}} (m_\alpha + m_\beta) \\ m_\alpha &= \frac{\pi}{6} d_{p\alpha}^3 \rho_{s\alpha}\end{aligned}$$

*to be consistent with the notation used in MFIX, the abscissa L_α and $d_{p\alpha}$ are equivalent, and represent the particle size for the α^{th} solid phase.

Table 4.2 Gas-solid and solid-solid interaction forces

Gas-solid interaction force:

$$\mathbf{f}_{g\alpha} = -\varepsilon_{s\alpha} \nabla P_g - F_{g\alpha}(\mathbf{u}_{s\alpha} - \mathbf{u}_g)$$

$$F_{g\alpha} = \begin{cases} 150 \frac{\varepsilon_{s\alpha}^2 \mu_g}{\varepsilon_g d_{p\alpha}^2} + 1.75 \frac{\varepsilon_{s\alpha} \rho_g |\mathbf{u}_g - \mathbf{u}_{s\alpha}|}{d_{p\alpha}} & \text{if } \varepsilon_g \leq 0.8 \\ \frac{3}{4} C_D \frac{\varepsilon_{s\alpha} \rho_g \varepsilon_g |\mathbf{u}_g - \mathbf{u}_{s\alpha}|}{d_{p\alpha}} \varepsilon_g^{-2.65} & \text{if } \varepsilon_g > 0.8 \end{cases}$$

$$C_D = \begin{cases} \frac{24}{Re_{p\alpha}} (1 + 0.15 Re_{p\alpha}^{0.687}) & \text{if } Re_{p\alpha} \leq 1000 \\ 0.44 & \text{if } Re_{p\alpha} > 1000 \end{cases}$$

$$Re_{p\alpha} = \frac{\varepsilon_g \rho_g |\mathbf{u}_g - \mathbf{u}_{s\alpha}| d_{p\alpha}}{\mu_g}$$

Solid-solid interaction force:

$$\mathbf{f}_{\beta\alpha} = -(F_{\beta\alpha} + F')(\mathbf{u}_{s\alpha} - \mathbf{u}_{s\beta})$$

$$F_{\beta\alpha} = \frac{3(1+e) \left(\frac{\pi}{2} + \frac{C_f \beta \alpha \pi^2}{8} \right) \varepsilon_{s\beta} \rho_{s\beta} \varepsilon_{s\alpha} \rho_{s\alpha} (d_{p\beta} + d_{p\alpha})^2 g_{0\beta\alpha} |\mathbf{u}_{s\beta} - \mathbf{u}_{s\alpha}|}{2\pi (\rho_{s\beta} d_{p\beta}^3 + \rho_{s\alpha} d_{p\alpha}^3)}$$

$$F' = \begin{cases} 2.0 \times 10^8 (\varepsilon_g - \varepsilon_g^*)^3 & \text{if } \varepsilon_g \leq \varepsilon_g^* \\ 0 & \text{if } \varepsilon_g > \varepsilon_g^* \end{cases}$$

4.2.2 Direct Quadrature Method of Moments

A polydisperse solid phase can be modeled by a multi-variate distribution function $n(L, \mathbf{u}_s)$ for the characteristic particle size L and the particle velocity vector \mathbf{u}_s whose transport equation is (Marchisio and Fox, 2005):

$$\frac{\partial n(L, \mathbf{u}_s; \mathbf{x}, t)}{\partial t} + \nabla \cdot [\mathbf{u}_s n(L, \mathbf{u}_s; \mathbf{x}, t)] + \nabla_{\mathbf{u}_s} \cdot [\mathbf{F} n(L, \mathbf{u}_s; \mathbf{x}, t)] = S(L, \mathbf{u}_s; \mathbf{x}, t), \quad (4.5)$$

where \mathbf{x} is the spatial coordinate, and t is time. In this expression, $S(L, \mathbf{u}_s; \mathbf{x}, t)$ is a “source” term that represents discontinuous jumps in property space (i.e., due to aggregation and breakage events), whereas \mathbf{F} is the force acting to accelerate the particles. Note that when Eq. 4.5 is used to evaluate the size-conditioned average velocity of a particle $\mathbf{u}_{s\alpha} = \langle \mathbf{u}_s | L = L_\alpha \rangle$, the size-conditioned average force $\langle \mathbf{F} | L = L_\alpha \rangle$ must be consistent with the terms on the right-hand

side of Eq. 4.4. In this work, we will circumvent the difficulty of finding a consistent definition for \mathbf{F} by simply using Eq. 4.4 to define $\mathbf{u}_{s\alpha}$.

Using DQMOM, the distribution function $n(L, \mathbf{u}_s)$ is approximated by a summation of N Dirac delta functions:

$$n(L, \mathbf{u}_s; \mathbf{x}, t) = \sum_{\alpha=1}^N \omega_{\alpha}(\mathbf{x}, t) \delta[L - L_{\alpha}(\mathbf{x}, t)] \delta[\mathbf{u}_s - \mathbf{u}_{s\alpha}(\mathbf{x}, t)], \quad (4.6)$$

where ω_{α} is the weight of the delta function centered at the characteristic particle size L_{α} and the characteristic velocity $\mathbf{u}_{s\alpha}$. If Eq. 4.6 is inserted into Eq. 4.5, and a moment transformation is applied, it is possible to derive the transport equations for the N weights ω_{α} (zero-order moment) and the N abscissas L_{α} (first-order moment with respect to length). As noted above, the conditional first-order moment of \mathbf{u}_s can be used to derive the momentum balances for the N velocities $\mathbf{u}_{s\alpha}$. However, since we will assume that Eq. 4.4 holds, the transport equations for the N weights ω_{α} and N abscissas L_{α} can be found from the DQMOM representation of the PSD:

$$n(L; \mathbf{x}, t) = \int_{-\infty}^{+\infty} n(L, \mathbf{u}_s; \mathbf{x}, t) d\mathbf{u}_s = \sum_{\alpha=1}^N \omega_{\alpha}(\mathbf{x}, t) \delta[L - L_{\alpha}(\mathbf{x}, t)]. \quad (4.7)$$

Integrating out the velocity in Eq. 4.5, we obtain the solid-phase PBE:

$$\frac{\partial n(L; \mathbf{x}, t)}{\partial t} + \nabla \cdot [\langle \mathbf{u}_s | L \rangle n(L; \mathbf{x}, t)] = S(L; \mathbf{x}, t), \quad (4.8)$$

where $\langle \mathbf{u}_s | L \rangle$ is the mean velocity conditioned on L :

$$\langle \mathbf{u}_s | L \rangle n(L; \mathbf{x}, t) = \int_{-\infty}^{+\infty} \mathbf{u}_s n(L, \mathbf{u}_s; \mathbf{x}, t) d\mathbf{u}_s, \quad (4.9)$$

and $S(L; \mathbf{x}, t)$ is the size-dependent source term for aggregation and breakage. Notice that, by definition, $\langle \mathbf{u}_s | L = L_{\alpha} \rangle = \mathbf{u}_{s\alpha}$.

Before explaining how to obtain transport equations for the weights ω_{α} and abscissas L_{α} , it is important to highlight that previous validation studies of DQMOM and comparison of its performance with QMOM have demonstrated that by using as few as $N = 2$ or 3 nodes, the lower-order moments of the PSD:

$$m_k(\mathbf{x}, t) = \int_0^{\infty} n(L; \mathbf{x}, t) L^k dL \approx \sum_{\alpha=1}^N \omega_{\alpha}(\mathbf{x}, t) L_{\alpha}^k(\mathbf{x}, t), \quad (4.10)$$

are tracked with surprisingly small errors (Marchisio, Vigil, and Fox, 2003b; Marchisio, Pikturina, Fox, Vigil, and Barresi, 2003a; Marchisio and Fox, 2005). The DQMOM approach has been tested for predicting the time evolution of the PSD under aggregation, breakage and molecular growth (Marchisio and Fox, 2005). The ability of the model to track the moments of the PSD does not give any physical meaning to the nodes of the quadrature approximation and, as explained in the original formulation of the model (McGraw, 1997), the weights ω_α and abscissas L_α are simply the quadrature approximation for the moments. However, it has been shown that the nodes can be thought of as different solid phases with characteristic particle size L_α and velocity $\mathbf{u}_{s\alpha}$, and that the quadrature approximation actually resembles the shape of the underlying PSD (Marchisio and Fox, 2005). It is thus clear that each node of the quadrature approximation is calculated in order to guarantee that the moments of the PSD are tracked with high accuracy but, at the same time, each node is treated as a distinct solid phase giving the DQMOM-multi-fluid model the ability to treat polydisperse solids.

The rigorous derivation of the transport equations for the weights ω_α and weighted abscissas \mathcal{L}_α ($\mathcal{L}_\alpha = L_\alpha \omega_\alpha$) is in Sec. 3.2. Here we limit our discussion to a brief review of the mathematical approach. The transport equations for the weights and weighted abscissas can be written as:

$$\begin{aligned} \frac{\partial \omega_\alpha}{\partial t} + \nabla \cdot (\mathbf{u}_{s\alpha} \omega_\alpha) &= a_\alpha, \\ \frac{\partial \mathcal{L}_\alpha}{\partial t} + \nabla \cdot (\mathbf{u}_{s\alpha} \mathcal{L}_\alpha) &= b_\alpha, \end{aligned} \tag{4.11}$$

where a_α and b_α are defined through a linear system found from the first $2N$ moments (e.g., $k = 0, \dots, 2N - 1$) of the PSD. This linear system can be written in matrix form as:

$$\mathbf{A}\boldsymbol{\alpha} = \mathbf{d}, \tag{4.12}$$

where the $2N \times 2N$ coefficient matrix $\mathbf{A} = \begin{bmatrix} \mathbf{A}_1 & \mathbf{A}_2 \end{bmatrix}$ is defined by

$$\mathbf{A}_1 = \begin{bmatrix} 1 & \dots & 1 \\ 0 & \dots & 0 \\ -L_1^2 & \dots & -L_N^2 \\ \vdots & \ddots & \vdots \\ 2(1-N)L_1^{2N-1} & \dots & 2(1-N)L_N^{2N-1} \end{bmatrix} \quad (4.13)$$

and

$$\mathbf{A}_2 = \begin{bmatrix} 0 & \dots & 0 \\ 1 & \dots & 1 \\ 2L_1 & \dots & 2L_N \\ \vdots & \ddots & \vdots \\ (2N-1)L_1^{2N-2} & \dots & (2N-1)L_N^{2N-2} \end{bmatrix}. \quad (4.14)$$

The $2N$ vector of unknowns $\boldsymbol{\alpha}$ is defined by

$$\boldsymbol{\alpha} = \begin{bmatrix} a_1 & \dots & a_N & b_1 & \dots & b_N \end{bmatrix}^T = \begin{bmatrix} \mathbf{a} \\ \mathbf{b} \end{bmatrix}, \quad (4.15)$$

and the known right-hand side is

$$\mathbf{d} = \begin{bmatrix} \bar{S}_0^{(N)} & \dots & \bar{S}_{2N-1}^{(N)} \end{bmatrix}^T. \quad (4.16)$$

The source term for the k^{th} moment $\bar{S}_k^{(N)}$ is defined by

$$\bar{S}_k^{(N)}(\mathbf{x}, t) = \int_0^\infty L^k S(L; \mathbf{x}, t) dL. \quad (4.17)$$

As shown below, with the DQMOM approximation the right-hand side of Eq. 4.17 is closed in terms of the N weights and abscissas. The superscript (N) on $\bar{S}_k^{(N)}$ is a reminder that N nodes are used to approximate the integral. As N increases, the quadrature approximation will approach the exact value, albeit at a higher computational cost.

If the abscissas L_α are unique, then \mathbf{A} will be full rank. For this case, the source terms for the transport equations of the weights ω_α and weighted lengths \mathcal{L}_α can be found simply by inverting \mathbf{A} in Eq. 4.12:

$$\boldsymbol{\alpha} = \mathbf{A}^{-1} \mathbf{d}. \quad (4.18)$$

If at any point in the computational domain two abscissas are equal, then the matrix \mathbf{A} is not full rank (or the matrix is singular), and therefore it is impossible to invert it. In order to overcome this problem, a small perturbation can be added to the abscissas to make \mathbf{A} full rank. However, this method does not work very well as the number of nodes increases, and alternative approaches can be used.

First of all, it is important to develop a reliable technique to detect any singularity of the matrix \mathbf{A} . The matrix can be singular (or nearly singular) when two abscissas become too close to each other with an increase in the number of nodes. In such situations, the inverse of the matrix can still be calculated, but it has a large error. Thus a safe way to detect a singularity is to calculate the condition number of the matrix \mathbf{A} when $N > 3$. Here, the condition number is defined as the ratio between the largest and smallest singular values. The reciprocal of the condition number can be used as a control variable to monitor singularity of the matrix \mathbf{A} . If it is smaller than a small number (e.g., 1.0×10^{-12}), the matrix is considered singular.

When a singularity is detected, two possible approaches can be used to overcome the problem. In the first one, for the computational cells where singularity happens the matrix \mathbf{A} is not inverted and the source vector $\boldsymbol{\alpha}$ is simply set to zero. In this case, convection in physical space will “solve” the singularity. If the second approach is used, the source vector $\boldsymbol{\alpha}$ is estimated from the average of the source vectors from neighboring cells. However it is important to highlight that the frequency of this event is very low in the simulations. This result is also confirmed by the fact that the abscissas L_α are equal to each other only if the final PSD is a monodispersed distribution centered at a unique value, which is not the case in most practical applications. It is also clear that this singularity problem of the matrix \mathbf{A} is more related to boundary or initial conditions where monodispersed distributions might be used.

In order to be consistent with the variables used in the multi-fluid model, we need to relate the weights and abscissas to the solid volume fraction $\varepsilon_{s\alpha}$ and the effective length $\varepsilon_{s\alpha}L_\alpha$ for each solid phase. The volume fraction of each solid phase is related to the abscissas L_α and

weights ω_α by

$$\varepsilon_{s\alpha} = k_v L_\alpha^3 \omega_\alpha = k_v \frac{\mathcal{L}_\alpha^3}{\omega_\alpha^2}, \quad (4.19)$$

and the effective length of the solid phase is

$$\varepsilon_{s\alpha} L_\alpha = k_v L_\alpha^4 \omega_\alpha = k_v \frac{\mathcal{L}_\alpha^4}{\omega_\alpha^3}, \quad (4.20)$$

where k_v is a volumetric shape factor (e.g., for spherical particles $k_v = \pi/6$). Using Eqs. 4.19 and 4.20, the transport equations for $\varepsilon_{s\alpha}$ and L_α can be written as

$$\begin{aligned} \frac{\partial \varepsilon_{s\alpha} \rho_{s\alpha}}{\partial t} + \nabla \cdot (\mathbf{u}_{s\alpha} \varepsilon_{s\alpha} \rho_{s\alpha}) &= 3k_v \rho_{s\alpha} L_\alpha^2 b_\alpha - 2k_v \rho_{s\alpha} L_\alpha^3 a_\alpha, \\ \frac{\partial \varepsilon_{s\alpha} L_\alpha \rho_{s\alpha}}{\partial t} + \nabla \cdot (\mathbf{u}_{s\alpha} \varepsilon_{s\alpha} L_\alpha \rho_{s\alpha}) &= 4k_v \rho_{s\alpha} L_\alpha^3 b_\alpha - 3k_v \rho_{s\alpha} L_\alpha^4 a_\alpha. \end{aligned} \quad (4.21)$$

The first equation represents the continuity equation for the α^{th} solid phase in the presence of aggregation and breakage (cf. Eq. 4.2). It is clear that because of aggregation and breakage the volume fraction of each solid phase will change according to its characteristic length L_α is order to mimic the evolution of the PSD. It is straightforward to verify that the summation of the transport equations over the N solid phases leads to a null source term. This implies that aggregation and breakage do not change the total solid volume fraction (i.e., the solid volume fraction is preserved). Thus, the source term for the gas volume fraction ε_g is null, and the relative volume fractions of the different solid phases change due to aggregation and breakage. The second equation in Eq. 4.21 is solved in the multi-fluid model as a set of user-defined scalars. Finally, note that using Eq. 4.19 the weights ω_α can be computed from $\varepsilon_{s\alpha}$ and L_α whenever they are needed (e.g., to compute \mathbf{d}) during the course of a simulation. Equations 4.4 and 4.21 constitute the DQMOM-multi-fluid model for a polydisperse solid phase. The only remaining task is to relate \mathbf{d} in Eq. 4.12 to the well-known expressions for aggregation and breakage from the theory of population balances (Ramakrishna, 2000).

4.3 Implementation of Aggregation and Breakage

In this work, we will consider changes in the PSD due only to aggregation and breakage. For this case, the moment transform of the aggregation and breakage source term is (Marchisio,

Vigil, and Fox, 2003b)

$$\overline{S}_k^{(N)}(\mathbf{x}, t) = \overline{B}_k^a(\mathbf{x}, t) - \overline{D}_k^a(\mathbf{x}, t) + \overline{B}_k^b(\mathbf{x}, t) - \overline{D}_k^b(\mathbf{x}, t), \quad (4.22)$$

where the moments of the birth and death rates are defined by

$$\overline{B}_k^a(\mathbf{x}, t) = \frac{1}{2} \int_0^\infty \int_0^\infty \beta(L, \lambda) (L^3 + \lambda^3)^{k/3} n(\lambda; \mathbf{x}, t) n(L; \mathbf{x}, t) d\lambda dL, \quad (4.23)$$

$$\overline{D}_k^a(\mathbf{x}, t) = \int_0^\infty \int_0^\infty L^k \beta(L, \lambda) n(\lambda; \mathbf{x}, t) n(L; \mathbf{x}, t) d\lambda dL, \quad (4.24)$$

$$\overline{B}_k^b(\mathbf{x}, t) = \int_0^\infty \int_0^\infty L^k a(\lambda) b(L|\lambda) n(\lambda; \mathbf{x}, t) d\lambda dL, \quad (4.25)$$

$$\overline{D}_k^b(\mathbf{x}, t) = \int_0^\infty L^k a(L) n(L; \mathbf{x}, t) dL. \quad (4.26)$$

In these expressions, $\beta(L, \lambda)$ is the aggregation kernel, which is proportional to the frequency of collision of two particles with lengths L and λ , $a(L)$ is the breakage kernel, which is the frequency of disruption of a particle of length L , and $b(L|\lambda)$ is the fragment distribution function, which contains information on the fragments produced by a breakage event.

DQMOM is based on the quadrature approximation reported in Eq. 4.7. Thus, using this approximation the source term in Eq. 4.22 is closed:

$$\begin{aligned} \overline{S}_k^{(N)}(\mathbf{x}, t) = & \frac{1}{2} \sum_{\alpha=1}^N \sum_{\gamma=1}^N w_\alpha w_\gamma (L_\alpha^3 + L_\gamma^3)^{k/3} \beta_{\alpha\gamma} - \sum_{\alpha=1}^N \sum_{\gamma=1}^N w_\alpha w_\gamma L_\alpha^k \beta_{\alpha\gamma} \\ & + \sum_{\alpha=1}^N w_\alpha a_\alpha^* \bar{b}_\alpha^{(k)} - \sum_{\alpha=1}^N w_\alpha L_\alpha^k a_\alpha^*, \end{aligned} \quad (4.27)$$

where $\beta_{\alpha\gamma} = \beta(L_\alpha, L_\gamma)$, $a_\alpha^* = a(L_\alpha)$, and

$$\bar{b}_\alpha^{(k)} = \int_0^{+\infty} L^k b(L|L_\alpha) dL. \quad (4.28)$$

As concerns the daughter distribution function, the following expression has been used (Marchisio, Vigil, and Fox, 2003b)

$$\bar{b}_\alpha^{(k)} = L_\alpha^k \frac{m^{k/3} + n^{k/3}}{(m+n)^{k/3}}. \quad (4.29)$$

where m and n represent the mass ratios between the two fragments. For example, if $m = 1$ and $n = 1$ the two fragments have the same volume and thus symmetric fragmentation is considered. If $m \neq n$ then fragmentation is not symmetric and a particular case is when

$m \gg n$ (or $n \gg m$) which is known as erosion. In this work, two different values of m and n have been considered. Most of the simulations were run with $m = n = 1$, but in Sec. 4.4.4 erosion is also investigated and compared with symmetric fragmentation.

The kinetic theory of granular flow can be applied to derive expressions for aggregation and breakage kernels in fluidized beds. According to this theory, the number of collisions per unit volume and time between particles with indices α and γ is given by Goldschmidt (2001)

$$N_{\alpha\gamma} = \pi\omega_\alpha\omega_\gamma\sigma_{\alpha\gamma}^3 g_{\alpha\gamma} \left[\frac{4}{\sigma_{\alpha\gamma}} \left(\frac{\theta_s m_\alpha + m_\gamma}{\pi 2m_\alpha m_\gamma} \right)^{1/2} - \frac{2}{3}(\nabla \cdot \mathbf{u}_s) \right], \quad (4.30)$$

where m_α and m_γ are the masses of the particles of size L_α and L_γ , respectively, $\sigma_{\alpha\gamma}$ and θ_s are the average particle size and average granular temperature of the solid mixture, respectively, and $g_{\alpha\gamma}$ is the radial distribution for the mixture. (See Table 4.1 for the definitions of these parameters.) Thus, the aggregation kernel can be expressed as

$$\beta_{\alpha\gamma} = \Psi_a \pi \sigma_{\alpha\gamma}^3 g_{\alpha\gamma} \left[\frac{4}{\sigma_{\alpha\gamma}} \left(\frac{\theta_s m_\alpha + m_\gamma}{\pi 2m_\alpha m_\gamma} \right)^{1/2} - \frac{2}{3}(\nabla \cdot \mathbf{u}_s) \right], \quad (4.31)$$

where Ψ_a is the success-factor for aggregation, which is usually a function of particle temperature, particle velocity and particle position. Likewise, the breakage kernel can be expressed as

$$a_\alpha^* = \Psi_b \sum_{\lambda=1}^N \frac{N_{\alpha\lambda}}{\omega_\alpha} \quad (4.32)$$

where Ψ_b is the success-factor for breakage. In this work, we will simply assume that Ψ_a and Ψ_b are constant.

If we neglect the divergence of the particle velocity field and assume that particles have equal density, Eq. 4.31 can be rewritten as

$$\beta_{\alpha\gamma} = \Psi_a g_{\alpha\gamma} \left(\frac{3\theta_s}{\rho_s} \right)^{1/2} (L_\alpha + L_\gamma)^2 \left(\frac{1}{L_\alpha^3} + \frac{1}{L_\gamma^3} \right)^{1/2}. \quad (4.33)$$

Likewise, Eq. 4.32 can be rewritten as

$$a_\alpha^* = \Psi_b \sum_{\lambda=1}^N \omega_\lambda g_{\alpha\lambda} \left(\frac{3\theta_s}{\rho_s} \right)^{1/2} (L_\alpha + L_\lambda)^2 \left(\frac{1}{L_\alpha^3} + \frac{1}{L_\lambda^3} \right)^{1/2}. \quad (4.34)$$

These are the kinetic-theory kernels used in the simulations reported in Sec. 4.4.

4.4 Results and Discussion

The mathematical model described above is incorporated in the multi-fluid CFD code MFIX, which is a general-purpose hydrodynamic model for describing dense or dilute gas-solids flows. The SIMPLE scheme and automatic time-step adjustment are used to speed up the calculation. A second-order spatial discretization method is adopted to increase the accuracy of the code. Due to the strong coupling between the phases through the drag forces, the partial elimination algorithm of Spalding (PEAS) is used to handle the interphase coupling (Syamlal, 1998). All of the simulations reported here were run on an Alpha Cluster made up of Compaq XP1000 workstations. The average time step Δt for the simulation was approximately 3×10^{-4} s.

Two-dimensional simulations were carried out for a FB reactor. The computational domain and solid physical properties are reported in Table 4.3. The initial static bed height was 15.9 cm. The gas velocity was 20 cm/s, and the density and viscosity of air at room temperature were used in the simulation. First, the code was tested with constant aggregation and breakage kernels and then by using the expressions derived from kinetic theory (Eqs. 4.33 and 4.34). The effect of the number of nodes N has been tested and predictions with $N = 2, 3$ and 4 have been compared. The comparison was made with the same initial PSD, and thus the initial conditions have been calculated by using the same set of moments m_k (see Table 4.4) for all values of N . In order to initialize the fields, starting from the first $2N$ moments m_k ($k = 0, \dots, 2N - 1$) the N weights w_α and the N abscissas L_α were calculated by using the PD algorithm (Gordon, 1968; Marchisio and Fox, 2005) and assumed to be homogeneously distributed in the initial static bed.

Table 4.3 The computational domain and solids physical properties in the simulation.

<i>Computational domain</i>	
Width (cm)	10.1
Height (cm)	50.0
Number of grid cells	15×50
Cell width, Δx (cm)	0.67
Cell height, Δy (cm)	1.0
<i>Particle physical properties</i>	
Particle density, ρ_s (kg/m ³)	2530
Coefficient of restitution, e	0.8
Packed bed void fraction, ε_g^*	0.38

Table 4.4 Initial values of particle diameters ($d_{p\alpha}$) and solid-phase volume fractions ($\varepsilon_{s\alpha}$) for $N = 2, 3$ and 4 for the same initial PSD. ($m_0 = 32050.825 \text{ cm}^{-3}$, $m_1 = 670.285 \text{ cm}^{-2}$, $m_2 = 15.245 \text{ cm}^{-1}$, $m_3 = 0.385$, $m_4 = 1.09 \times 10^{-2} \text{ cm}$, $m_5 = 3.43 \times 10^{-4} \text{ cm}^2$, $m_6 = 1.18 \times 10^{-5} \text{ cm}^3$, $m_7 = 4.28 \times 10^{-7} \text{ cm}^4$)

	N	$\alpha = 1$	$\alpha = 2$	$\alpha = 3$	$\alpha = 4$
Particle diameter, $d_{p\alpha}$ (μm)	2	183	356		
	3	174	263	409	
	4	171	225	316	420
Phase volume fraction, $\varepsilon_{s\alpha}$	2	0.274	0.356		
	3	0.196	0.229	0.205	
	4	0.157	0.157	0.157	0.157

4.4.1 Constant Kernels

In the first set of simulations, constant aggregation and breakage kernels were used. Thus, the aggregation kernel $\beta_{\alpha\gamma}$ and the breakage kernel a_α were assumed to be independent of the particle diameter, velocity and other properties. The values of model parameters used in the simulations are listed in the Table 4.4. Three cases have been investigated and compared. In Case 1, the aggregation and breakage kernels are both set equal to zero. In Case 2, the aggregation kernel was set equal to $1 \times 10^{-5} \text{ m}^3/\text{s}$, and the breakage kernel to 0.1 s^{-1} . In Case 3, the aggregation kernel was set equal to $1 \times 10^{-5} \text{ m}^3/\text{s}$, and the breakage kernel to 1 s^{-1} . For future reference, note that Case 2 will be dominated by aggregation, while Case 3 will be dominated by breakage.

If no aggregation and breakage are present (Case 1), the PSD does not change with time and the volume-average mean particle size is constant. However, due to the differences in size between the N solid phases and therefore the difference in the drag force, particle segregation by size will occur. Indeed, smaller particles will tend to reside in the upper part of the bed, whereas bigger particles will tend to stay near the bottom. For Case 2, aggregation is dominant and the particles become larger and larger, so the volume-average mean particle size will increase with the time. For Case 3, breakage is dominant and the particles become smaller and smaller, and the volume-average mean particle size decreases with the time. The volume-average mean particle size in the fluidized bed for these three cases are shown in Fig. 4.1 for $N = 2, 3$ and 4. Note that the volume-average mean particle size reported here is d_{32} , namely the ratio between the third moment m_3 and the second moment m_2 of the PSD. Note that the results are nearly independent of N for constant aggregation and breakage. There are significant fluctuations for Case 3, caused by the dilute system resulting from high breakage.

As already mentioned the DQMOM is based on a presumed functional form of the PSD that allows us to solve the closure problem and track with excellent accuracy the moments of the distribution. Moreover, the different delta functions are treated as distinct solid phases. Although the underlying PSD could be retrieved by a sufficiently large number of moments (Diemer and Olson, 2002) in what follows we use a volume-fraction versus particle-size diagram to report

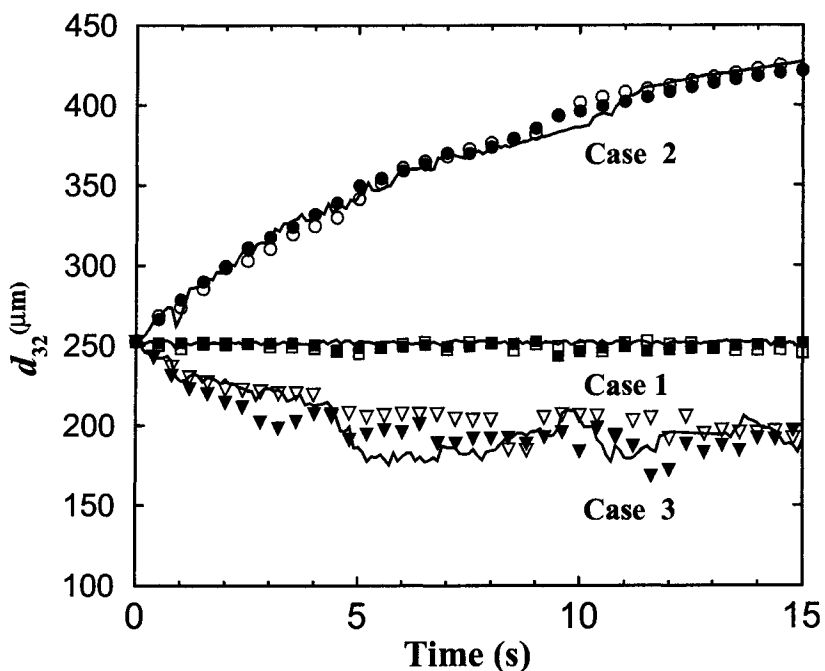


Figure 4.1 Volume-average mean particle size (d_{32}) for $N = 2$ (filled symbols), $N = 3$ (empty symbols) and $N = 4$ (lines).

on the position of the N delta functions. As explained in our previous work (Marchisio, Vigil, and Fox, 2003b) this can give some insight into the shape of the underlying PSD, although the real and presumed PSDs share only a fixed set of moments.

The PSD at the middle of the FB bed for Cases 2 and 3 at selected times are shown in Figs. 4.2 and 4.3, respectively. At time zero, there are four particles with different particle sizes and the same solid void fraction for both cases. For the aggregation dominated case (Fig. 4.2), smaller particles aggregate and produce large particles, and the volume fraction for smaller particles decreases with time. At 15 s, a broad distribution of particle sizes exists in the bed. For the breakage dominated case (Fig. 4.3), particles become smaller due to breakage. Indeed, more and more smaller particles are produced due to the excessive breakage. The bed becomes more dilute with the newly formed smaller particles, and the PSD changes very quickly. Thus the PSD at different times are quite different.

As discussed in Sec. 4.1, DQMOM was developed from QMOM. By using DQMOM, we do not need to solve the transport equations for the moments. Nevertheless, information about the

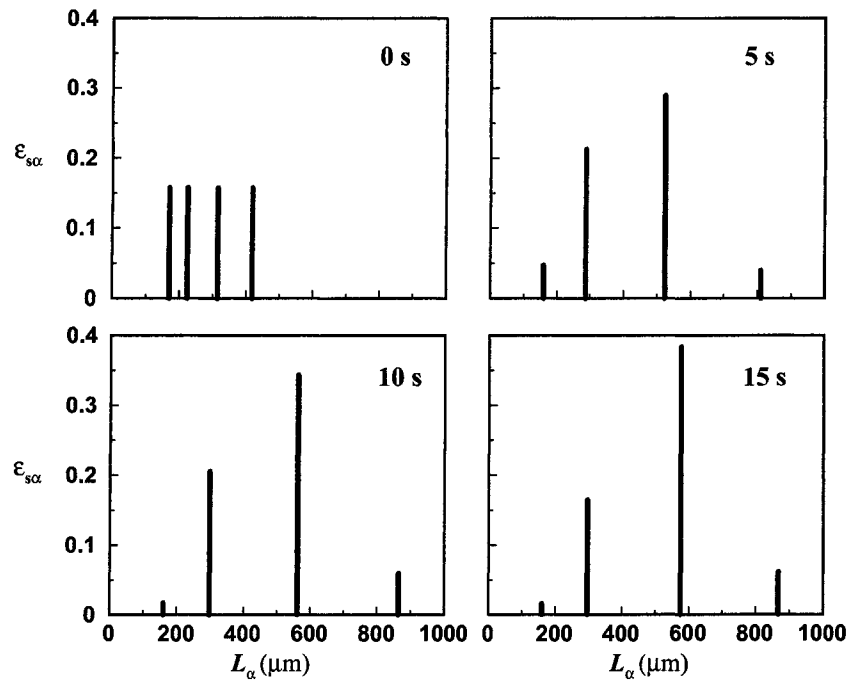


Figure 4.2 PSD at the middle of the FB at 0, 5, 10 and 15 s for Case 2.

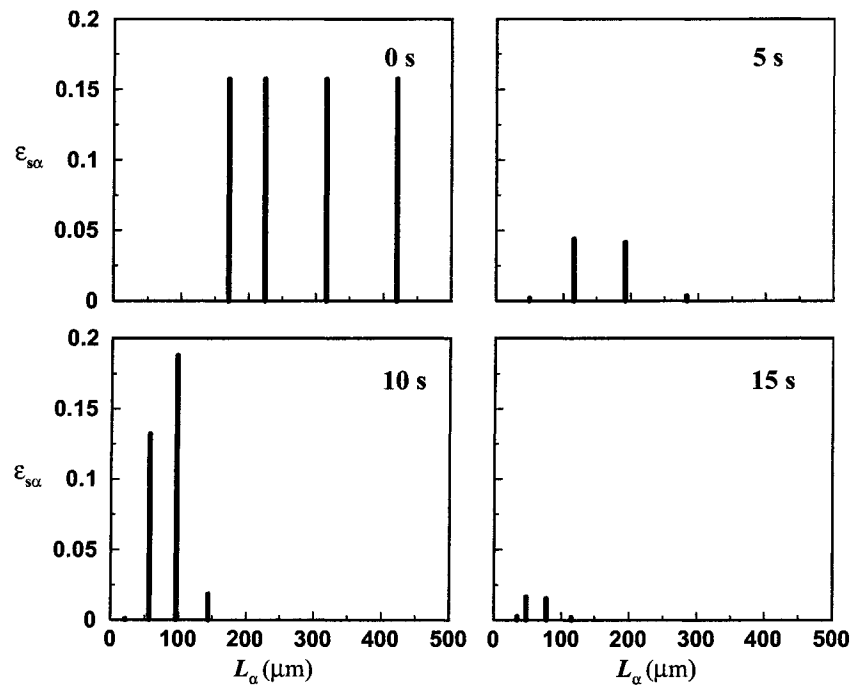


Figure 4.3 PSD at the middle of the FB at 0, 5, 10 and 15 s for Case 3.

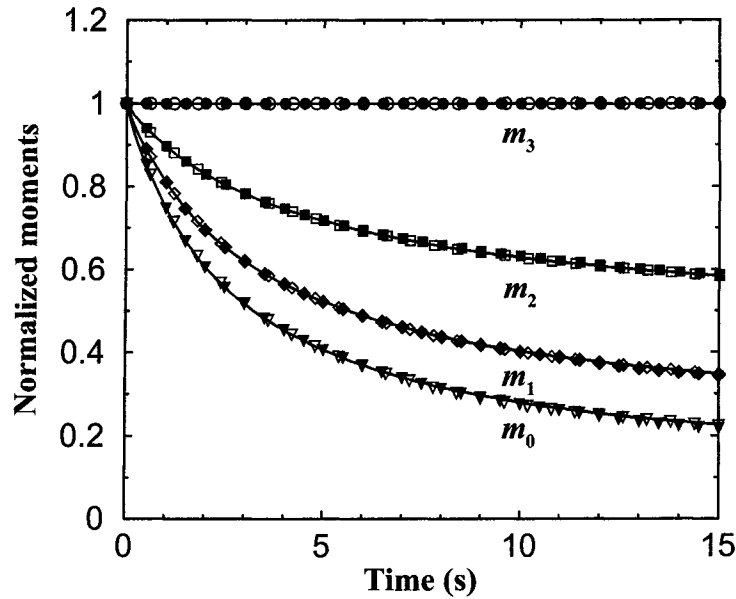


Figure 4.4 Volume-average normalized moments for Case 2 using $N = 2$ (filled symbols), $N = 3$ (empty symbols) and $N = 4$ (lines).

moments is still valuable. Comparisons of the volume-average normalized moments for Cases 2 and 3 are given in Figs. 4.4 and 4.5, respectively. The normalized moments are calculated by dividing the volume-average moments by their values at time $t = 0$:

$$\mu_k(t) = \frac{\bar{m}_k(t)}{\bar{m}_k(0)}. \quad (4.35)$$

Some moments have particular physical meaning. For example, m_0 represents the total particle number density, whereas m_2 is related to the total particle area, and m_3 is related to the total particle volume. For Case 2, it is possible to see that $N = 2, 3$ and 4 gives very similar predictions. In Fig. 4.4, the expected effects of aggregation are observed: the total particle number density (m_0) decreases, as do m_1 and m_2 , whereas the total particle volume m_3 remains constant.

For Case 2, strong segregation occurs in the bed while particles are aggregating. Large particles migrate to the bottom of the fluidized bed and small particles move to the top. Aggregation continues after segregation and the big particles in the bottom keep aggregating and getting larger until large regions of the bed become defluidized. This transition is shown in Figs. 4.6–4.8, where contour plots of the mean particle size d_{32} at $t = 5, 10$ and 15 s, using

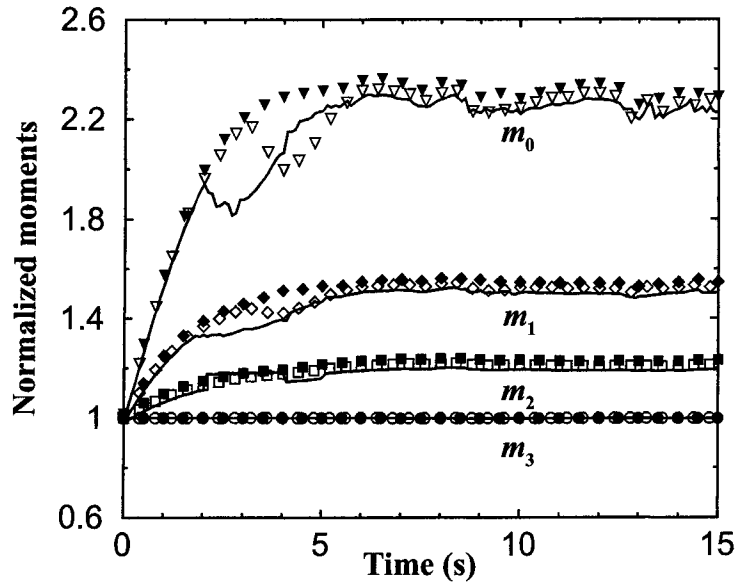


Figure 4.5 Volume-average, normalized moments for Case 3 using $N = 2$ (filled symbols), $N = 3$ (empty symbols) and $N = 4$ (lines).

$N = 2, 3$ and 4 are reported. From the plots, we can see that although the mean particle size d_{32} over the whole domain is nearly the same for all N , the contour plots of d_{32} at different time are slightly different. The contour plots for $N = 3$ and 4 are more similar. Notice that because the kernels are constant for this case, even after defluidization particles continue to grow. This artifact can be eliminated by using the kinetic-theory kernels as described below.

For Case 3 it is possible to see from Fig. 4.5 that the evolution of the moments is opposite of Case 2 (i.e. m_0, m_1 and m_2 increase). However, as before m_3 remains constant, since breakage is also a volume-preserving process. In this case some differences between $N = 2, 3$ and 4 are detected. The different behavior can be attributed to elutriation of the smallest particles. Because of the higher breakage rates, some very small particles are produced and depending on the gas velocity these particles can leave the bed from the top. This strongly affects the total number of particles m_0 , but the effect of this loss of particles is less important for m_1, m_2 and almost negligible for m_3 . In fact, because the particles leaving the domain are very small, they represent a very small fraction of the volume of the bed and thus m_3 does not change appreciably. For Case 3, no defluidization is observed. In fact, due to the higher breakage

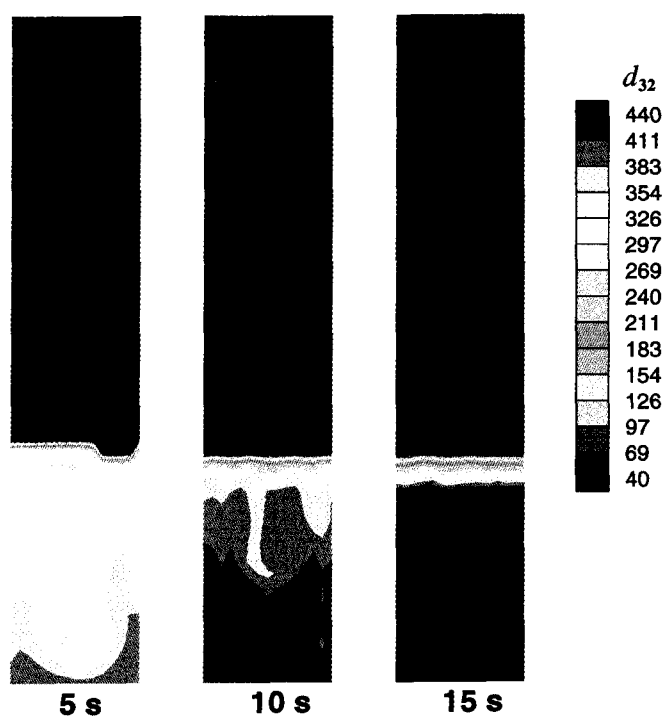


Figure 4.6 Time evolution of the spatial distribution of the mean particle size (d_{32}) for Case 2 using $N = 2$.

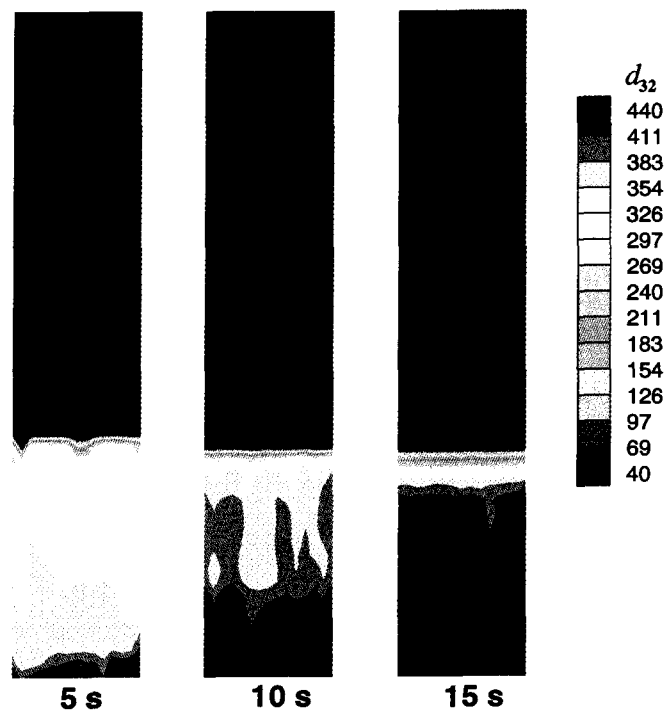


Figure 4.7 Time evolution of the spatial distribution of the mean particle size (d_{32}) for Case 2 using $N = 3$.

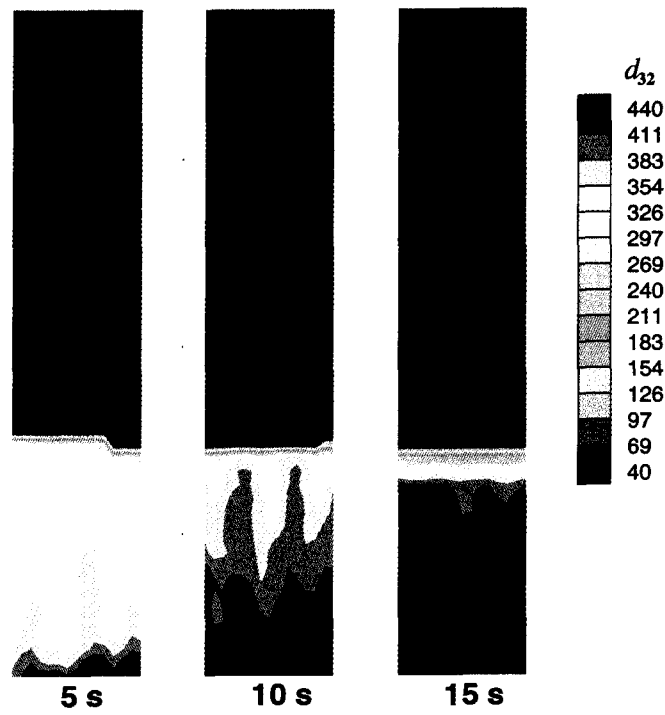


Figure 4.8 Time evolution of the spatial distribution of the mean particle size (d_{32}) for Case 2 using $N = 4$.

rates, the volume-average mean particle size d_{32} decreases, and particles are kept well mixed by the gas flow. Because of the reduction in the mean particle size, the bed expands and the total particle number density locally decreases, reducing the breakage rate.

Overall, from the constant-kernel cases we can conclude that our numerical implementation of the DQMOM-multi-fluid model in MFIX works as expected. From a computational point of view, the additional CPU time needed to include DQMOM is small relative to the total CPU time needed to solve the multi-fluid model with the same value of N but without aggregation and breakage. For example, using four nodes, the additional time for calculating the source term for DQMOM is only 18%. Regarding the dependence of the results on the number of nodes used in the quadrature, we find that for the constant-kernel cases reasonably accurate results can be obtained with only $N = 2$. This is consistent with our earlier QMOM work (Marchisio, Vigil, and Fox, 2003b) where it was shown that even for complicated aggregation and breakage kernels, the errors in the lower-order moments with $N \leq 4$ are uniformly small.

4.4.2 Kinetic-Theory Kernels

As noted above, constant aggregation and breakage kernels can not represent the FB reactor realistically. This problem can be addressed by using the aggregation and breakage kernels from kinetic theory reported in Eqs. 4.31 and 4.32. Simulations have been carried out for $N = 2, 3$ and 4. The simulation conditions in Table 4.3 were again used for the kinetic-theory kernels. Two different cases were investigated and compared. In Case 4, the aggregation success factor Ψ_a was 0.001 and the breakage success factor Ψ_b was 0.0001. In Case 5, the success factors for aggregation and breakage had the same value: 0.001.

In Fig. 4.9 the volume-average mean particle size d_{32} is reported for Case 4. As it is possible to see, d_{32} increases with time. Several phenomena occur simultaneously. First, particles begin to aggregate and, due to their increased size, move to the bottom of the reactor. Particles near the bottom of the reactor continue to aggregate until defluidization occurs. At this point, the granular temperature θ_s is null and thus the aggregation and breakage kernels are null. No further particle aggregation (nor breakage) can occur. Although the volume-average mean

particle size predicted by using two, three and four nodes are very similar, some difference in the defluidization dynamics can be observed. Generally speaking, a higher number of nodes represents the system more accurately, but increases the computational time. For example, the CPU time required for running a simulation with $N = 4$ is 1.8 times higher than with $N = 3$, and 3.4 times higher than with $N = 2$.

Results for Case 5 are reported in Fig. 4.10. As it is possible to see, also for this case the volume-average mean particle size predicted by the DQMOM using two, three and four nodes is very similar. From Cases 4 and 5, we note that the mean particle size distributions are nearly the same when breakage dominates or when mixing is significant. However, when segregation is significant, using different values of N produces different results. Nevertheless, as N increases, the results show closer agreement. In consideration of the computation cost, simulations with three nodes appears to be sufficient to represent the PSD.

The instantaneous contour plots for the gas void fraction at 6 s using $N = 3$ for Cases 4 and 5 are compared with Case 1 (no aggregation and breakage) in Fig. 4.11. It can be clearly seen that with aggregation the fluidized bed becomes defluidized and the bed height decreases compared to no aggregation and breakage (Case 1). Due to the high degree of aggregation, the particles become larger and the fluidized bed becomes a packed bed. (The void fraction is near to the maximum packed void fraction.) Only a few bubbles are observed near the top of the bed. For the case dominated by breakage, the particles become smaller and remain well mixed. The bed height expands compared to Case 1, and larger bubbles are observed in the fluidized bed.

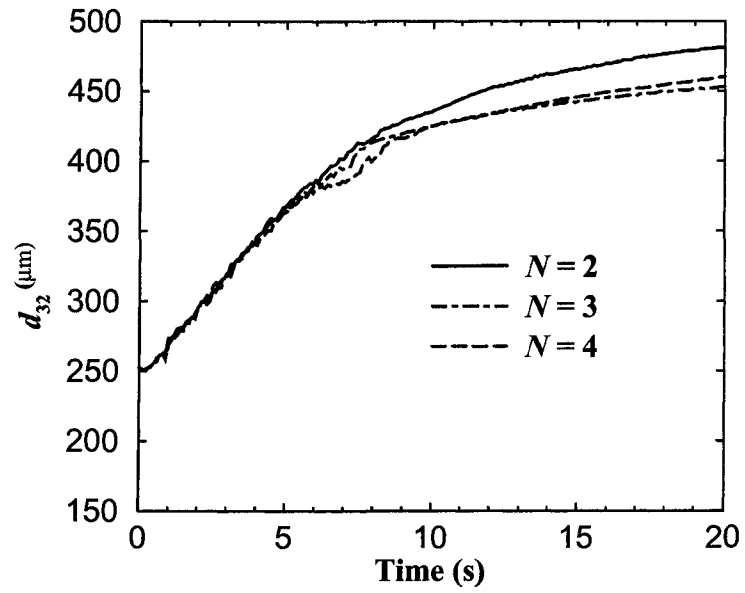


Figure 4.9 Volume-average mean particle size for Case 4.

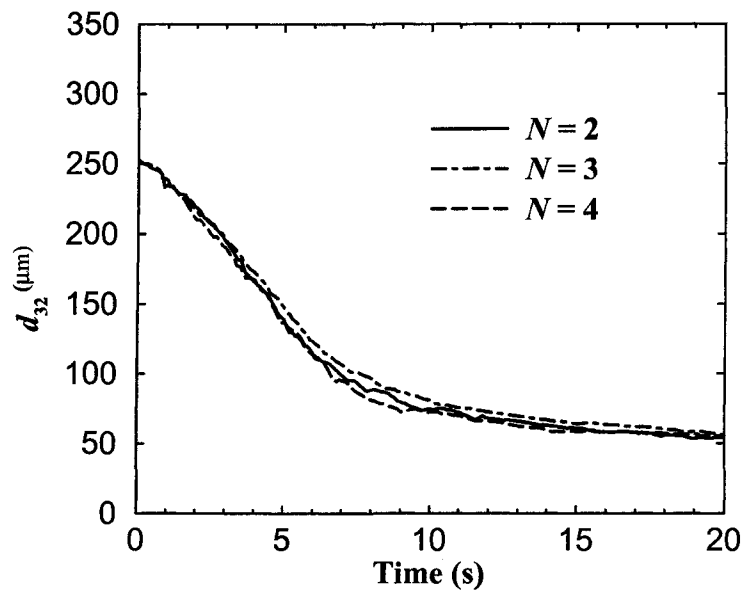


Figure 4.10 Volume-average mean particle size for Case 5.

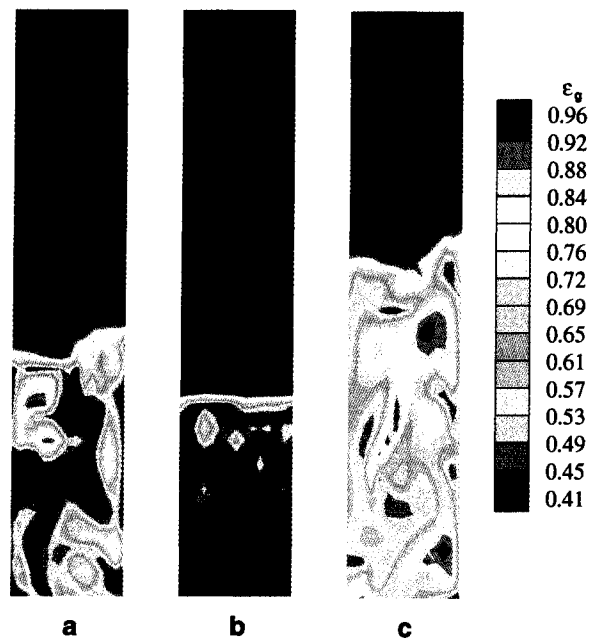


Figure 4.11 Contour plots of the gas volume fraction at 6 s. a: Case 1. b: Case 4. c: Case 5.

4.4.3 Effect of the Aggregation Success Factor

The success factor for aggregation Ψ_a is a very important parameter that affects the PSD evolution and defluidization dynamics. The role of this parameter has been investigated for $N = 3$, and three different values of the success factor $\Psi_a = 0.001$, 0.0005 and 0.0001 were tested. In these simulations, the success factor for breakage Ψ_b was set to zero. Results are first compared in terms of the pressure-drop fluctuations in the gas-solid fluidized bed for different values of Ψ_a in Fig. 4.12. Notice that the pressure-drop fluctuations go to zero when the bed becomes totally defluidized. The time for defluidization using the success factors reported above is 6, 11.5 and 50 s, respectively. Results show that an increase in the success factor causes earlier defluidization of the bed. Moreover, an increase in Ψ_a causes an increase in the final mean particle size, as shown in Fig. 4.13.

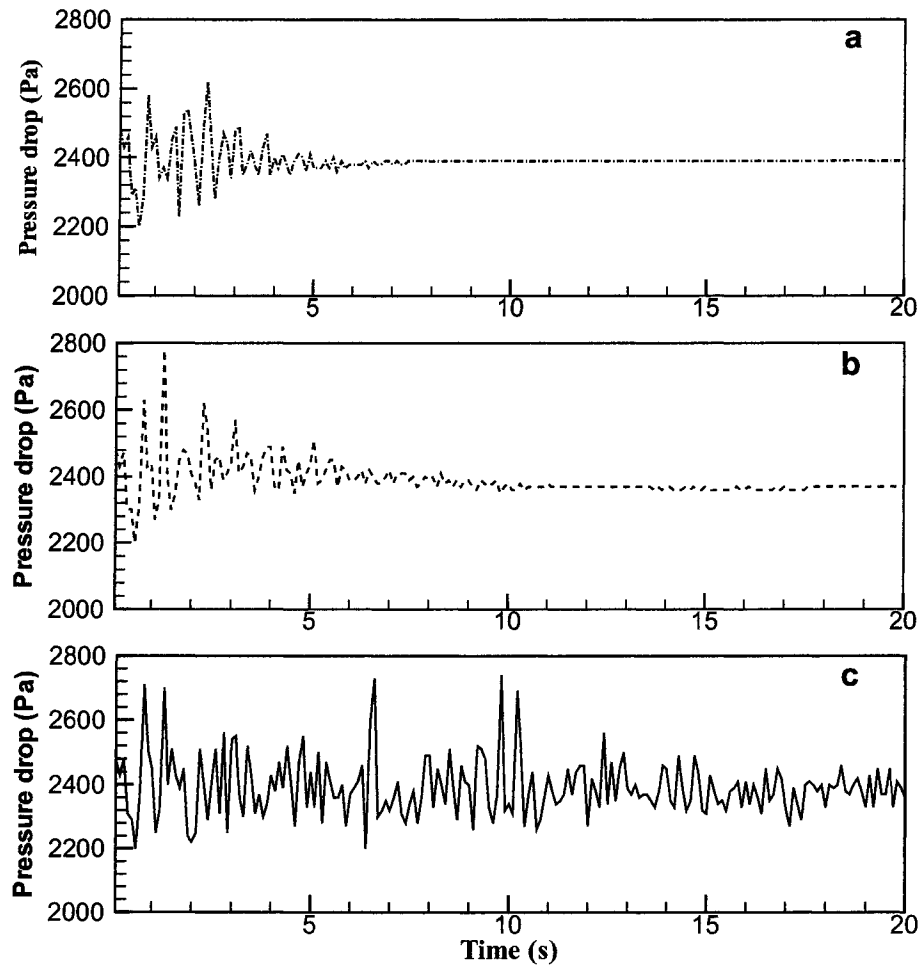


Figure 4.12 Pressure drop fluctuations in gas-solid fluidized bed for three different values of the aggregation success factor. a: $\Psi_a = 0.001$. b: $\Psi_a = 0.0005$. c: $\Psi_a = 0.0001$. Note that the pressure fluctuations cease when the bed defluidizes.

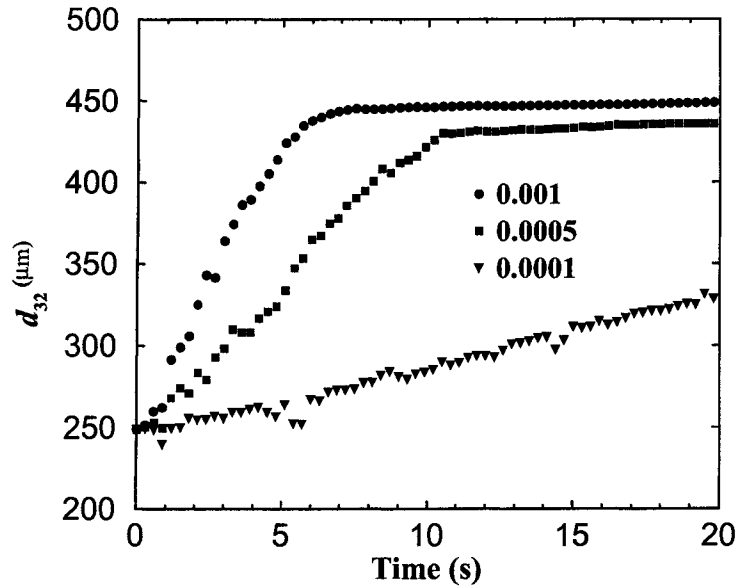


Figure 4.13 Effect of the value of the aggregation success factor (Ψ_a) on the volume-average mean particle size.

4.4.4 Effect of the Fragment Distribution Function

All the simulations above have been carried out using symmetric fragmentation, but erosion can also be very important in fluidized beds. Erosion is a fragmentation process which results in the formation of a small and a big fragment, and thus it is the separation of a small “chip” from a larger particle. Indeed, different mass ratios can be considered which still belong to the erosion-type fragmentation mechanism. In what follows the results from Case 5 (where in Eq. 4.29, $m = n = 1$) are compared with results obtained under the same operating conditions but with $m = 9$ and $n = 1$ (which implies the formation of a fragment whose volume is nine times smaller than the volume of the other fragment) using $N = 3$. Figure 4.14 shows a comparison between symmetric fragmentation and erosion for the volume-average mean particle size. Results show that erosion causes a delay in the dynamic response of the mean particle size. This is due to the fact that erosion is a less effective breakage mechanism in the presence of aggregation. With symmetric fragmentation particles reduce their volume by a factor of two, whereas with erosion a large particle generates a small fragment and a second fragment which has nearly the original volume.

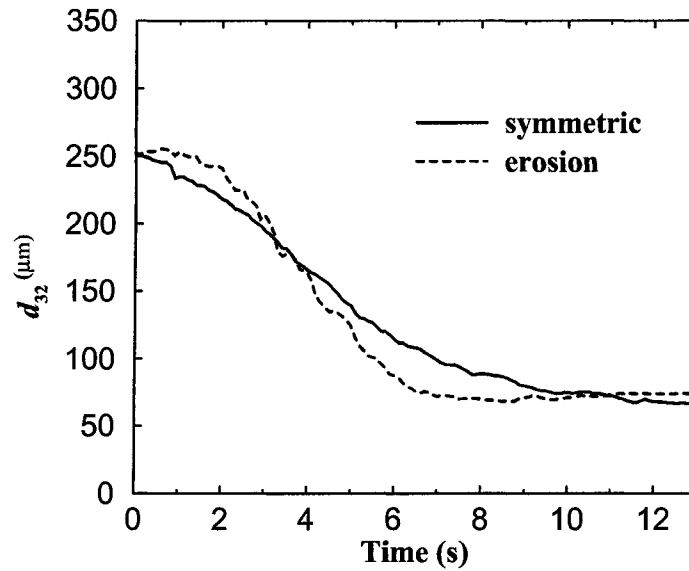


Figure 4.14 Effect of symmetric fragmentation versus erosion on the volume-average mean particle size.

It is interesting to note that with erosion another phenomenon can occur. The small fragments generated in the erosion process become smaller at a faster rate than with symmetric fragmentation and in a finite time an infinite number of particles with null size can be generated. This phenomenon goes under the name of shattering and can be detected by a net loss of mass. In Fig. 4.15, the three volume-average abscissas L_α , volume fractions $\varepsilon_{s\alpha}$ and weights ω_α are reported for symmetric fragmentation and erosion. As it is possible to see, with erosion the smallest class L_1 become null in a finite time (about 12 seconds) and the corresponding volume fraction ε_{s1} becomes zero. The corresponding weight ω_1 should become infinite but since the equation are not directly solved for ω_α , it tends to zero instead.

4.5 Conclusions

Simulation results show that the DQMOM-multi-fluid model is an effective approach to represent the evolution of the PSD due to aggregation and breakage in FB reactors. Two different sets of aggregation and breakage kernels were tested. For FB reactors, the kernel developed from kinetic theory should be more accurate than the constant kernel. With the kinetic-theory

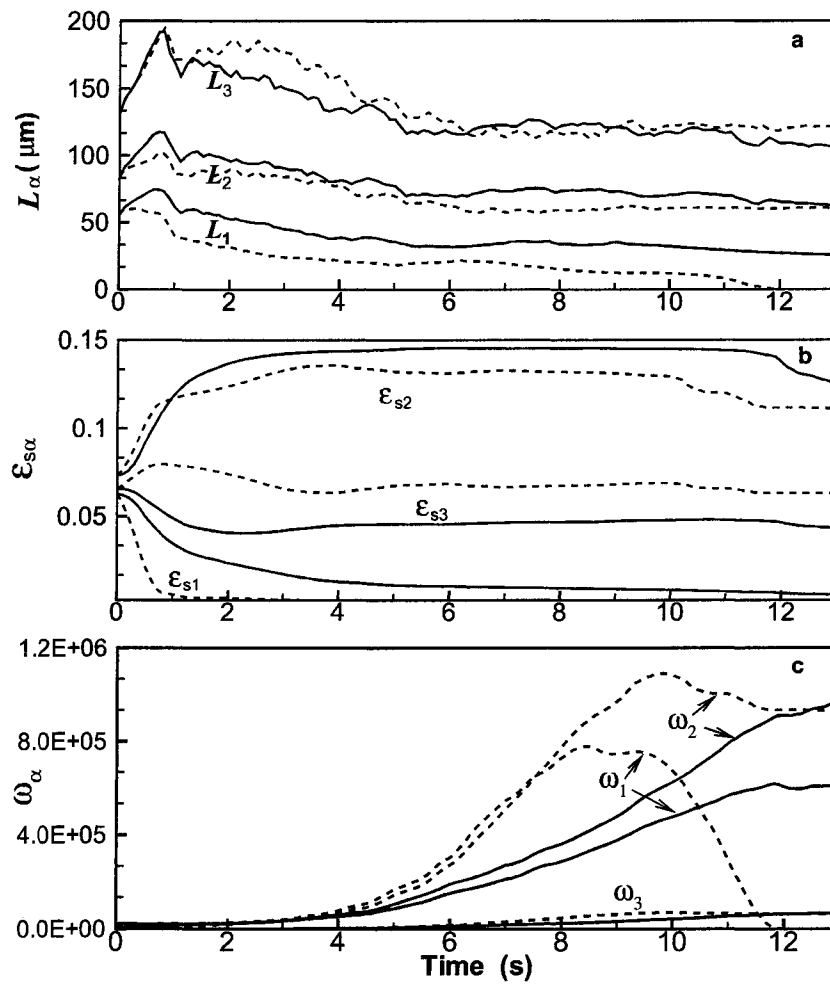


Figure 4.15 Comparison between symmetric fragmentation (solid lines) and erosion (dashed lines). a: abscissas. b: solid volume fractions. c: weights.

kernel, the mean particle size stops increasing when the fluidized bed becomes totally defluidization. Nevertheless, both kernels can describe the phenomena of particle growth, segregation, and elutriation due to aggregation and breakage. The performance of the DQMOM-multi-fluid model using two, three and four nodes has been tested. Results show that model predictions are very similar for $N = 2-4$. However, for some cases, using three or four nodes produces similar results, which are different than those found with two nodes. Considering the increase in computational time with an increasing number of nodes, three nodes appears to be a good choice for representing FB reactors. The effect of the success factor for aggregation Ψ_a was investigated for the kinetic-theory kernel. As expected, a high success factor Ψ_a leads to a shorter time for reaching complete defluidization.

For modeling real systems, several additional features (e.g., heat and mass transfer, chemical reactions, etc.) must be added to the CFD model proposed in this work. However, the conceptual framework of the DQMOM-multi-fluid model need not be changed to accommodate these additional features. In other work, we apply the CFD modeling approach developed in this work to FB poly-olefin reactors used to produce high-density polyethylene as well as other polymers. For these reactors, the formation of hot spots can lead to aggregation of the polymer particles and eventually to reactor shutdown. For this reason, the ability to describe polydisperse, aggregating particles is a central requirement of any CFD model for FB poly-olefin reactors. The DQMOM-multi-fluid model developed here provides a computationally efficient and robust method for attaining this objective.

CHAPTER 5. SEGREGATION IN POLYDISPERSE FLUIDIZED BEDS: VALIDATION OF A MULTI-FLUID MODEL

5.1 Introduction

Fluidized bed reactors have been widely used in the food, chemical, pharmaceutical and metallurgical industries. The process of particle mixing and segregation change the distribution of mixture components in the bed, and thus play a very important role. For example, in a catalytic gas-phase olefin polymerization reactor, small catalyst particles are continuously fed into the bed, and react with the incoming monomer gas to produce a broad size distribution of polymer particles. Due to the differences in the polymer particle sizes, segregation occurs and fully-grown polymer particles migrate to the bottom where they are removed from the reactor. Meanwhile, the smaller pre-polymerized particles and fresh catalyst particles tend to migrate to the upper portions of the reactor and continue to react with monomer. Bubbles are known to play an intricate and ambiguous role in the reactor. On the one hand, bubbles cause segregation of larger particles. On the other hand, the rising bubbles also provide a mixing action to equalize the particle size and density distribution (Wu and Baeyens, 1998). Both the chemical reaction and mass/heat transfer depend on the local particle size distribution in the bed. Therefore, a better understanding of the distribution of different solid components for a given mixture system is required to improve the design, operation and scale-up of gas-fluidized bed processes.

An extensive literature has been published on the segregation and mixing behavior of particles of different sizes and densities in fluidized-bed reactors. Attention has been focused mostly on segregation in gas-solid fluidized beds with binary mixtures (i.e., two particles differing in size and/or density) (Nienow et al., 1987; Formisani et al., 2001; Hoffmann et al.,

1993; Goldschmidt et al., 2003). Marzocella et al. (2000) experimentally studied segregation behavior and transient fluidization of binary mixtures of particles in a bubbling fluidized bed. A defluidized bottom layer was observed in a segmented fluidization column. The fluidization behavior of rice husk-sand mixture in a biomass fluidized bed was studied by Sun et al. (2005). The distribution of mass fraction of rice husk particles along the bed height were measured, the profiles of the mean particle diameter of the mixture were determined. With the increasing computer power, simulation studies of segregation in gas-solid fluidized beds with binary mixture have been conducted (van Wachem et al., 2001; Cooper and Coronella, 2005; Feng et al., 2004). Lu et al. (2003) used an Eulerian-Eulerian approach to simulate the segregation patterns of a binary mixture differing in particle size with the same density. In their model, both the gas phase and solids phase are interpenetrating continua. Separate transport equations are used for each particle class, allowing for interactions between size classes. For smaller fluidized bed systems, a more detailed discrete particle simulation (DPS) has been used to describe the dynamic behavior of a polydisperse mixture of particles (Hoomans et al., 2000; Bokkers et al., 2004). In this Eulerian-Lagrangian model, each particle is tracked individually by Newton's second law of motion, the gas phase is computed by solving the volume-average Navier-Stokes equations. The particle collisions are described by a hard-sphere or a soft-sphere model and no additional closure equations are needed for the interaction forces between particles.

Although many experiments and simulations were conducted for binary systems, many industrial fluidized beds contain particles with continuous size distributions, and the experimental and simulation works on this subject are few. Hoffman and Romp (1991) performed experiments in a gas-solid fluidized bed with a continuous size distribution ranging from 150 to 1000 μm . They noticed that the intermediate size particles behaved as jetsam (larger particles) at lower velocities and flotsam (smaller particles) at high velocities. Similarly, Wormsbecker et al. (2005) studied a bimodal distribution of pharmaceutical granulate mixtures in a conical fluidized bed. Both axial and radial segregation are observed in the bed. Large granule tended to accumulate at the center of the bed and became better mixed as the gas velocity increased. Only a few researchers reported simulation work on the segregation in gas-solid fluidized beds

with a continuous size distribution. Mathiesen et al. (2000) studied the flow behavior in a circulating fluidized bed by approximating a realistic particle size distribution as three discrete particle sizes. An Eulerian-Eulerian model was used in the simulation and axial segregation was observed for a wide-ranging particle size distribution, and no segregation for a narrow size distribution.

More recently, Dahl and Hrenya (2005) used a discrete-particle model to study the segregation phenomena in gas-solid fluidized beds with a continuous size distribution. Both Gaussian and lognormal distributions were investigated over a range of distribution widths and gas velocities. The simulations show that the local distribution remains of the same type as the overall particle size distribution with a few notable exceptions. However, due to the computational cost of the method, the results are limited to low-velocity, small fluidized beds. Thus, developing an Eulerian-Eulerian model, which can describe the segregation and mixing for a continuous PSD is very crucial for larger industrial-scale fluidized beds. In this work, the recently developed DQMOM is incorporated in the Eulerian-Eulerian model frame to represent the PSD by a finite number of nodes (Fan et al., 2004). The PSD is tracked through the moments, not the actual nodes, so only a few nodes are enough to represent it. In order to validate the model we employed in this work, the results of the model are first compared with experiments performed by Goldschmidt et al. (2003) for a binary mixture. Then, the results for the continuous PSD are compared with the DPS simulation results of Dahl and Hrenya (2005).

5.2 Multi-Fluid Model Description

In this work, the multi-fluid model (MFM) based on the Eulerian-Eulerian approach is employed to describe particle segregation in a fluidized bed. In the model, both the gas phase and solid phases are described as interpenetrating continua. The gas phase is considered as the primary phase, whereas the solid phases are considered as secondary or dispersed phases. Each solid phase is characterized by a specific diameter, density and other properties.

The continuity and momentum equations for the gas and solid phases are

$$\frac{\partial(\varepsilon_g \rho_g)}{\partial t} + \nabla \cdot (\varepsilon_g \rho_g \mathbf{u}_g) = 0, \quad (5.1)$$

$$\frac{\partial(\varepsilon_{s\alpha} \rho_{s\alpha})}{\partial t} + \nabla \cdot (\varepsilon_{s\alpha} \rho_{s\alpha} \mathbf{u}_{s\alpha}) = 0, \quad (5.2)$$

$$\frac{\partial}{\partial t} (\varepsilon_g \rho_g \mathbf{u}_g) + \nabla \cdot (\varepsilon_g \rho_g \mathbf{u}_g \mathbf{u}_g) = \nabla \cdot \boldsymbol{\sigma}_g + \sum_{\alpha=1}^N \mathbf{f}_{g\alpha} + \varepsilon_g \rho_g \mathbf{g}, \quad (5.3)$$

$$\frac{\partial}{\partial t} (\varepsilon_{s\alpha} \rho_{s\alpha} \mathbf{u}_{s\alpha}) + \nabla \cdot (\varepsilon_{s\alpha} \rho_{s\alpha} \mathbf{u}_{s\alpha} \mathbf{u}_{s\alpha}) = \nabla \cdot \boldsymbol{\sigma}_{s\alpha} - \mathbf{f}_{g\alpha} + \sum_{\beta=1, \beta \neq \alpha}^N \mathbf{f}_{\beta\alpha} + \varepsilon_{s\alpha} \rho_{s\alpha} \mathbf{g}. \quad (5.4)$$

All the variables are same as described in Sec. 3.1 and a simple Newtonian closure is used for the gas-phase tensor. The kinetic theory of granular flow and the theory from the study of soil mechanics are combined to calculate the solid stress tensor in the viscous and plastic regimes. The constitutive relations for the gas and solids stress tensor are summarized in Table 5.1. A more detailed discussion about the parameters can be found in Sec. 3.1.

The interaction forces between phases (both solid and gas phase and solid-solid phase) are very crucial to model the segregation and mixing phenomena in the reactor. The interaction force between the gas phase and the α^{th} solid phase, $\mathbf{f}_{g\alpha}$, can be written as

$$\mathbf{f}_{g\alpha} = -\varepsilon_{s\alpha} \nabla P_g - F_{g\alpha} (\mathbf{u}_{s\alpha} - \mathbf{u}_g). \quad (5.5)$$

The first term on the right hand side of Eq. 5.5 describes the buoyancy force, and the second term is the drag force. The drag model derived by Gidaspow (1994) is used here, and

$$F_{g\alpha} = \begin{cases} 150 \frac{\varepsilon_{s\alpha} (1 - \varepsilon_g) \mu_g}{\varepsilon_g d_{p\alpha}^2} + 1.75 \frac{\varepsilon_{s\alpha} \rho_g |\mathbf{u}_g - \mathbf{u}_{s\alpha}|}{d_{p\alpha}} & \text{if } \varepsilon_g \leq 0.8 \\ \frac{3}{4} C_D \frac{\varepsilon_{s\alpha} \rho_g \varepsilon_g |\mathbf{u}_g - \mathbf{u}_{s\alpha}|}{d_{p\alpha}} \varepsilon_g^{-2.65} & \text{if } \varepsilon_g > 0.8 \end{cases} \quad (5.6)$$

and

$$C_D = \begin{cases} \frac{24}{Re_{p\alpha}} (1 + 0.15 Re_{p\alpha}^{0.687}) & \text{if } Re_{p\alpha} \leq 1000 \\ 0.44 & \text{if } Re_{p\alpha} > 1000 \end{cases} \quad (5.7)$$

Table 5.1 Constitutive relations for gas and solids stress tensors.

Gas stress tensor:

$$\boldsymbol{\sigma}_g = -P_g \mathbf{I} + \varepsilon_g \mu_g [\nabla \mathbf{u}_g + (\nabla \mathbf{u}_g)^T] - \frac{2}{3} \varepsilon_g \mu_g \nabla \cdot \mathbf{u}_g \mathbf{I}$$

Solids stress tensor:

$$\boldsymbol{\sigma}_{s\alpha} = \begin{cases} -P_{s\alpha}^p \mathbf{I} + \boldsymbol{\tau}_{s\alpha}^p & \text{if } \varepsilon_g \leq \varepsilon_g^* \quad \text{plastic regime} \\ -P_{s\alpha}^v \mathbf{I} + \boldsymbol{\tau}_{s\alpha}^v & \text{if } \varepsilon_g > \varepsilon_g^* \quad \text{viscous regime} \end{cases}$$

plastic regime

$$P_{s\alpha}^p = \varepsilon_{s\alpha} P^*$$

$$\boldsymbol{\tau}_{s\alpha}^p = 2\mu_{s\alpha}^p \mathbf{D}_{s\alpha}$$

$$\mathbf{D}_{s\alpha} = \frac{1}{2} [\nabla \mathbf{u}_{s\alpha} + (\nabla \mathbf{u}_{s\alpha})^T]$$

$$\mu_{s\alpha}^p = \frac{P^* \sin \phi}{2\sqrt{I_{2D}}}$$

$$P^* = 10^{25} (\varepsilon_g^* - \varepsilon_g)^{10}$$

viscous regime

$$P_{s\alpha}^v = K_{1\alpha} \varepsilon_{s\alpha}^2 \theta_\alpha$$

$$\boldsymbol{\tau}_{s\alpha}^v = \mu_{s\alpha}^v [\nabla \mathbf{u}_{s\alpha} + (\nabla \mathbf{u}_{s\alpha})^T] + \lambda_{s\alpha}^v \nabla \cdot \mathbf{u}_{s\alpha} \mathbf{I}$$

$$\theta_\alpha = \left(\frac{-K_{1\alpha} \varepsilon_{s\alpha} \text{Tr}(\mathbf{D}_{s\alpha}) + \sqrt{K_{1\alpha}^2 \text{Tr}^2(\mathbf{D}_{s\alpha}) \varepsilon_{s\alpha}^2 + 4K_{4\alpha} \varepsilon_{s\alpha} [K_{2\alpha} \text{Tr}^2(\mathbf{D}_{s\alpha}) + 2K_{3\alpha} \text{Tr}(\mathbf{D}_{s\alpha}^2)]}}{2\varepsilon_{s\alpha} K_{4\alpha}} \right)^2$$

$$\lambda_{s\alpha}^v = K_{2\alpha} \varepsilon_{s\alpha} \sqrt{\theta_\alpha}$$

$$\mu_{s\alpha}^v = K_{3\alpha} \varepsilon_{s\alpha} \sqrt{\theta_\alpha}$$

$$K_{1\alpha} = 2(1+e) \rho_{s\alpha} g_{0\alpha\alpha}$$

$$K_{2\alpha} = 4d_{p\alpha} \rho_{s\alpha} (1+e) \frac{\varepsilon_{s\alpha} g_{0\alpha\alpha}}{3\sqrt{\pi}} - \frac{2}{3} K_{3\alpha}$$

$$K_{3\alpha} = \frac{d_{p\alpha} \rho_{s\alpha}}{2} \left[\frac{\sqrt{\pi}}{3(3-e)} [1 + 0.4(1+e)(3e-1) \varepsilon_{s\alpha} g_{0\alpha\alpha}] + \frac{8\varepsilon_{s\alpha} g_{0\alpha\alpha} (1+e)}{5\sqrt{\pi}} \right]$$

$$K_{4\alpha} = \frac{12(1-e^2) \rho_{s\alpha} g_{0\alpha\alpha}}{d_{p\alpha} \sqrt{\pi}}$$

$$g_{0\alpha\alpha} = \frac{1}{\varepsilon_g} + \frac{3d_{p\alpha}}{2\varepsilon_g^2} \sum_{\lambda=1}^N \frac{\varepsilon_{s\lambda}}{d_{p\lambda}}$$

where

$$Re_{p\alpha} = \varepsilon_g \rho_g |\mathbf{u}_g - \mathbf{u}_{s\alpha}| d_{p\alpha} / \mu_g. \quad (5.8)$$

The interaction force between the β^{th} solid phase and α^{th} solid phase, $\mathbf{f}_{\beta\alpha}$, is written as

$$\mathbf{f}_{\beta\alpha} = -F_{\beta\alpha}(\mathbf{u}_{s\alpha} - \mathbf{u}_{s\beta}) \quad (5.9)$$

with

$$F_{\beta\alpha} = \frac{3(1+e)(\pi/2 + C_{f\beta\alpha}\pi^2/8) \varepsilon_{s\beta} \rho_{s\beta} \varepsilon_{s\alpha} \rho_{s\alpha} (d_{p\beta} + d_{p\alpha})^2 g_{0\beta\alpha} |\mathbf{u}_{s\beta} - \mathbf{u}_{s\alpha}|}{2\pi (\rho_{s\beta} d_{p\beta}^3 + \rho_{s\alpha} d_{p\alpha}^3)} + C_1 P^* \quad (5.10)$$

where $g_{0\alpha\beta}$ is the radial distribution function at contact, and

$$g_{0\beta\alpha} = \frac{1}{\varepsilon_g} + \frac{3d_{p\alpha}d_{p\beta}}{\varepsilon_g^2(d_{p\alpha} + d_{p\beta})} \sum_{\lambda=1}^M \frac{\varepsilon_{s\lambda}}{d_{p\lambda}}. \quad (5.11)$$

The first term on the right-hand side of Eq. 5.10 was derived by Syamlal (1987) from kinetic theory accounting for the momentum transfer between the solid phases due to the collisions and sliding. e and $C_{f\beta\alpha}$ are the coefficient of restitution and coefficient of friction between particles. During the recent study done by Gera, Syamlal, and O'Brien (2004), it was found that a new term (the second term in the interaction force) is required to account for the "hindrance effect", otherwise the two solid phases will segregate even when they are packed or at low velocities. It is because when we consider the solid phases as two distinct phases, the small particles can go through the interstices of the packed bed, but in reality they do not experience any buoyant force from solids pressure gradient and actually behave like a single solid phase, so no segregation happens. Thus, an arbitrary function $C_1 P^*$ that makes the particle-particle drag sufficiently large is added, and this force accounts for the "hindrance effect" so that the two solid phases will move together and, in effect, behave as one phase when they are packed. The "hindrance pressure" is defined as

$$P^* = \begin{cases} 10^{25}(\varepsilon_g^* - \varepsilon_g)^{10} & \text{if } \varepsilon_g \leq \varepsilon_g^* \\ 0 & \text{if } \varepsilon_g > \varepsilon_g^* \end{cases} \quad (5.12)$$

and C_1 is adjusted to different mixtures to match the actual segregation rate. In the systems we studied, a value of 0.3 was found to resemble the experiment data for all cases investigated.

5.3 Results and Discussion

5.3.1 Binary PSD

The Eulerian-Eulerian model described above is incorporated in an open source CFD code MFIX. The MFIX code employs a staggered finite-volume mesh system. To speed up the code, the SIMPLE scheme and automatic time-step adjustment are used (Syamlal, 1998). For all the simulations, a second-order spatial discretization method is used to improve the accuracy of the calculation. The model is first validated with the experiments conducted by Goldschmidt et al. (2003) for a binary mixture. The experiments were carried out in a 15 cm wide, 70 cm high, 1.5 cm deep pseudo two-dimensional gas fluidized bed, and the initial bed height was 15 cm. The particles used in the experiment are relatively large spherical glass beads, which qualify as Geldart D type particles. Three different cases are selected for the simulations. The bed compositions (ratio of mass fraction of small particles x_{small} to large particles x_{large}), superficial gas velocities and solid void fractions for small and large particles are summarized in Table 5.2. Two-dimensional simulations assuming no gradient exist in the third direction were carried out for a free-bubbling fluidized bed. The width of the simulated bed is 15 cm and the height is 50 cm. The computational grid consisted of 30×80 rectangular cells. The properties of solid phases are listed in Table 5.3.

In order to compare the simulation results with experimental data obtained from Goldschmidt et al. (2003), the average height of solid phases, $\langle h_\alpha \rangle$ (α =small or large), is defined as

$$\langle h_\alpha \rangle = \frac{\sum_{cell} \varepsilon_{\alpha, cell} h_{cell}}{\sum_{cell} \varepsilon_{\alpha, cell}}. \quad (5.13)$$

The relative segregation rate is calculated from the average bed height for small and large particles and has the form of

$$s = \frac{S - 1}{S_{max} - 1} \quad (5.14)$$

where $S = \langle h_{small} \rangle / \langle h_{large} \rangle$ and $S_{max} = (2 - x_{small}) / (1 - x_{small})$. The relative segregation rate $s = 0$ when the particles are perfectly mixed, and $s = 1$ when the particles are completely segregated.

Table 5.2 Different cases simulated with Eulerian-Eulerian model

	x_{small}/x_{large}	\mathbf{u}_g	ε_{small}	ε_{large}
Base case	0.25/0.75	1.20 m/s	0.145	0.435
Case 1	0.50/0.50	1.10 m/s	0.29	0.29
Case 2	0.50/0.50	1.25 m/s	0.29	0.29

Table 5.3 Properties of solid phases used in the Eulerian-Eulerian simulation.

	small particle	larger particles
Particle density, ρ_s	2526 kg/m ³	2526 kg/m ³
Particle diameter, d_p	1500 μm	2500 μm
Coefficient of restitution, e	0.97	0.97
Coefficient of friction, C_f	0.15	0.15
Minimum fluidization velocity	0.78 m/s	1.25 m/s

The base case has 25% small particles and 75% large particles, and the superficial velocity is 1.20 m/s, which is between the minimum fluidization velocity for the small and large particles. The relative segregation rate calculated from average bed height from the Eulerian-Eulerian simulation is compared with experiments in Fig. 5.1. The simulation follows the trend well and the particles are well-mixed at the beginning, the relative segregation rate is small, close to zero. When segregation happens, the small particles moves to the top and the large particles move to the bottom of the bed, the relative segregation rate increases slowly. At 30 s, the value is around 0.4.

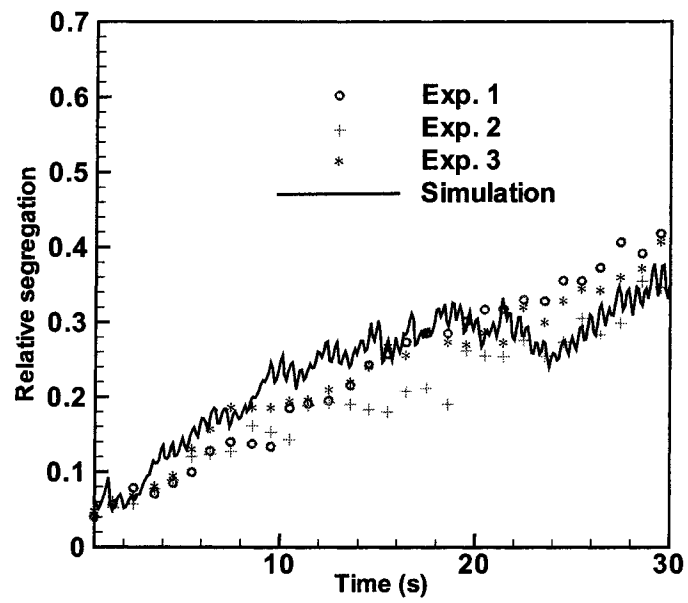


Figure 5.1 Evolution of relative segregation with time for base case.

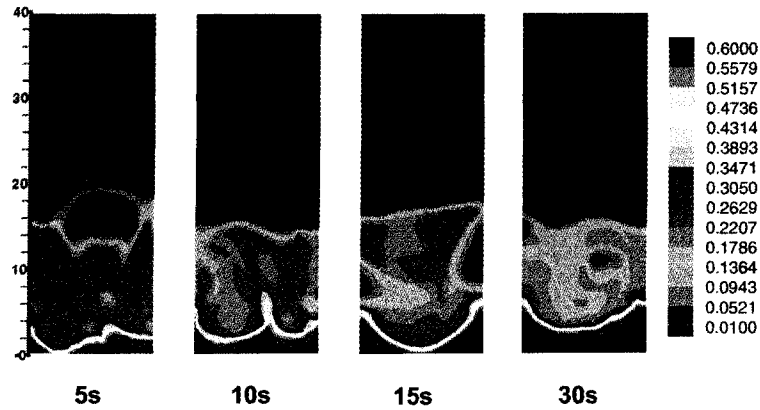


Figure 5.2 Snapshots of the void fraction of large particles from simulation for case 1.

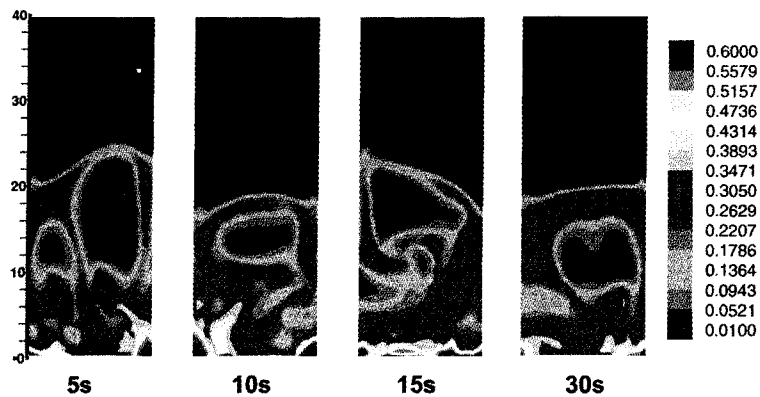


Figure 5.3 Snapshots of the void fraction of large particles from simulation for case 2.

Two other cases were chosen to study the effect of superficial gas velocity and the mixture composition. Case 1 has a different bed composition than the base case. It consists of 50% small particles and 50% larger particles, and the superficial gas velocity is 1.10 m/s. Case 2 has the same bed composition as case 1 but with a higher superficial gas velocity, 1.25 m/s. The snapshot of void fraction of large particles for cases 1 and 2 at 5, 10, 15 and 30 sec are shown in Figs 5.2 and 5.3. For case 1, a layer of jetsam (larger particles) is formed at the

bottom of the bed due to segregation. Bubbles are only observed near the top which is rich in small particles. Due to the accumulation of the large particles near the bottom, the bottom of the bed defluidized with time. For case 2, it is clearly seen that no layer of jetsam is formed at the bottom, only a few big particles accumulate around the corners. The higher superficial gas velocity produces more larger bubbles, and the bed is well-mixed with a higher bed height than case 1.

The evolution of the relative segregation rate in time for cases 1 and 2 are compared with experiments in Fig. 5.4. The simulation slightly overpredicts case 1 for the first 10 sec, but overall the prediction is reasonably good. Compared to case 1, the simulation for case 2 resembles the experiment results much better. From these two cases, we can conclude that the simulations can capture the transient fluidization, segregation and mixing of binary mixture of particles. In an intermediate gas-velocity range, transient fluidization takes place where the bed is initially fluidized and then segregation gradually occurs. In the end, the larger particles go to the bottom and the small particles move to the top so that there is a defluidized bottom rich in jetsam and a top layer rich in flotsam (small particles). The relative segregation rate is higher (usually around 0.3-0.4). At high gas velocity (equal or higher than the minimum fluidization velocity of larger particles), the fluidized bed is fully fluidized, so that effective bed mixing overtakes defluidization at the bottom and the segregation rate is rather low (smaller than 0.1).

The granular temperature is a key parameter in the Eulerian-Eulerian model, and it measures the small-scale fluctuating random motion of the particles in the fluid. The volume-fraction-weighted, bed-averaged granular temperatures as a function of time for cases 1 and 2 are shown in Fig. 5.5. The simulation results show that, for both cases, the granular temperature of the small particles remains nearly the same, with small fluctuations. For case 1, due to the segregation, the larger particles move to the bottom of the bed and since the superficial gas velocity is lower than the minimum fluidization velocity of the large particles, the bottom part of the bed defluidized. The granular temperature of the larger particles decreases with time. For case 2, the superficial gas velocity is equal to the minimum fluidization velocity of

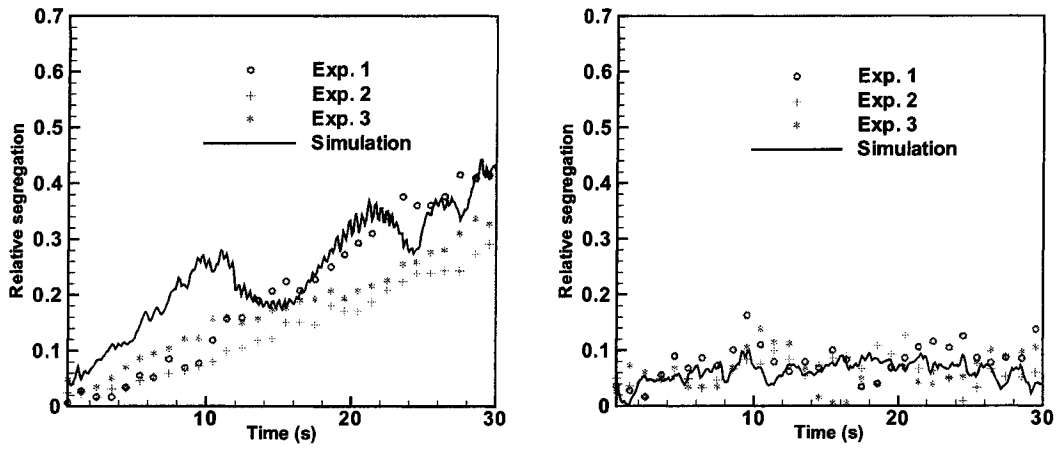


Figure 5.4 Evolution of relative segregation rate with time. Left: case 1. Right: case 2.

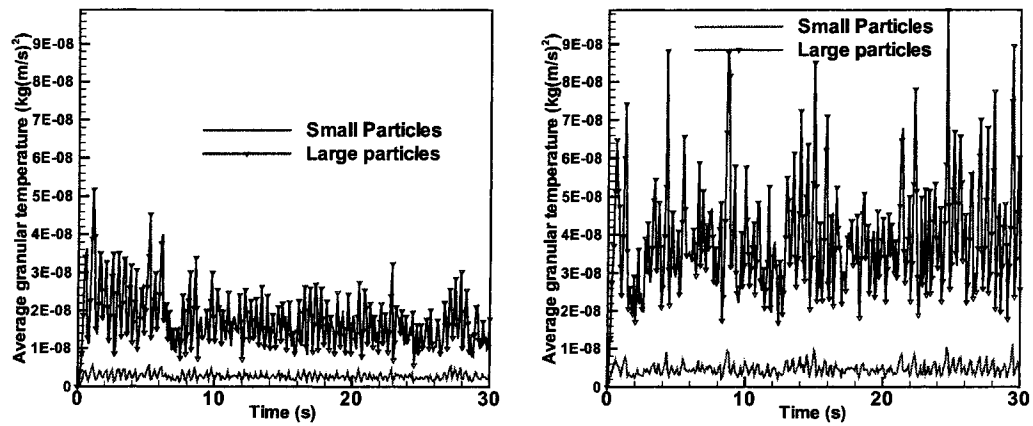


Figure 5.5 The volume-fraction-weighted, bed-averaged granular temperature as a function of time from simulation. Left: case 1. Right: case 2.

the large particles, and the bed is well-mixed. No defluidization is observed in case 2. The statistics of granular temperature for the larger particles also remain constant.

5.3.2 Continuous PSD

After attaining good agreement with experiments for binary systems, segregation phenomena in gas-solid fluidized beds with a continuous PSD were investigated. The simulation results are compared with the DPS results of Dahl and Hrenya (2005). As in their work, the simulation is conducted in a small two-dimensional rectangular fluidized bed, the width of the bed is 0.1 m and the height is 0.5 m. The density of the particles is 2525 kg/m^3 . For all the DPS simulations, at time zero the particles are released and allowed to fall under the influence of gravity and gas-solid drag. At a specific start time, $t_{start} = 0.1 \text{ s}$, the gas uniformly flows through the bed from the bottom. The gas velocity is linearly increased until the point ($t_{set} = 0.15 \text{ s}$) where a desired gas fluidization velocity is achieved. Then the simulation proceeds through time until the target simulation time ($t_{final} = 30 \text{ s}$) is obtained. In the Eulerian-Eulerian model, the simulations start with a well-mixed bed, at time zero the gas is uniformly distributed at the bottom of the bed with the desired velocity, and the simulations run to 30 s, and the last 10 seconds were used to get the average particle diameter and standard deviation for comparison with the DPS simulations. For the gas phase, air is used. The density of gas is 1.28 kg/m^3 and the viscosity is $1.7 \times 10^{-5} \text{ kg/m}\cdot\text{s}$.

Four systems were chosen for the comparisons. The overall size distribution, ratio of the standard deviation (σ) of the PSD to the mean particle diameter (d_{ave}), coefficient of restitution (e), coefficient of friction (C_f), the superficial gas velocity (\mathbf{u}_g) and the root mean square diameter (d_{rms}) are listed in Table 5.4. One thing noticed in the table is that different superficial velocities were used from Dahl and Hrenya's work (2005). This was because the DPS simulation used in their work were a strictly two dimensional (2D) simulation. However Eulerian-Eulerian model is a three dimensional (3D) simulation, and the particles were assumed to be packed in a 3D unit cube, compared to DPS simulation, where the particles were packed in a 2D hexagonal lattice. In the DPS simulations, this effect was taken into account by

Table 5.4 Simulation system properties.

System	PSD	σ/d_{ave}	e	C_f	$\mathbf{u}_g(\text{m/s})$	$d_{rms} (\mu\text{m})$
1	Gaussian	0.3	0.95	0.15	0.80 (1.00)*	1000
2	Gaussian	0.3	0.95	0.15	1.00 (1.25)*	1000
3	Gaussian	0.1	0.95	0.15	0.80 (1.00)*	1000
4	Lognormal	0.5	0.99	0.01	1.0 (1.25)*	1000

*superficial gas velocity used in DPS simulation

transformation between 2D gas-phase void fraction and 3D gas-phase void fraction (Hoomans et al., 1996):

$$\varepsilon_{3D} = 1 - \frac{2}{\sqrt{\pi\sqrt{3}}}(1 - \varepsilon_{2D})^{1.5} \quad (5.15)$$

However, it is an equation derived for monodisperse particles. During the work, it was found that the superficial gas velocity had to be reduced to 80% of the velocity used in the DPS simulation to match the minimum fluidization velocity for a mixture with continuous PSD in Eulerian-Eulerian simulations.

In the Eulerian-Eulerian model, the recently developed DQMOM is used to represent the continuous PSD by a summation of Dirac delta function (Fan et al., 2004). The distribution is approximated by a number of specific particle size classes, and tracked by the development of the moments. According to the previous work (Fan et al., 2004), only a few (3 or 4) size classes are needed to represent the PSD, so this method has a significant advantage over conventional methods, such as the sectional method, on the computational cost.

For a Gaussian distribution with a wide distribution $\sigma/d_{ave} = 0.3$ (System 1), the j^{th} moment, m_j , can be calculated as (Randolph and Larson, 1971)

$$m_j = \sum_r \sigma^{j-r} (d_{ave})^r \frac{j! \cdot 1 \cdot 3 \cdots (j-r-1)}{(j-r)! r!} \quad (5.16)$$

$r = 0, 2, 4, \dots, j$ for j even

$r = 1, 3, 5, \dots, j$ for j odd.

Table 5.5 Particle diameters and weights for System 1 with $N = 2 - 4$

	N	$\alpha = 1$	$\alpha = 2$	$\alpha = 3$	$\alpha = 4$
Particle diameter $d_{p\alpha}$, μm	2	670	1245		
	3	460	958	1456	
	4	287	745	1171	1629
Weights ω_α	2	0.5	0.5		
	3	0.1667	0.6666	0.1667	
	4	0.0459	0.4541	0.4541	0.0459

According to DQMOM method, the moments can be approximated by quadrature:

$$m_j(\mathbf{x}, t) = \int_0^\infty n(L; \mathbf{x}, t) L^j dL \approx \sum_{\alpha=1}^N \omega_\alpha L_\alpha^j, \quad (5.17)$$

By using the product difference(PD) algorithm (Gordon, 1968), the particle diameter (L_α or $d_{p\alpha}$, $\alpha = 1, \dots, N$) and weights (ω_α) can be obtained from the first $2N$ moments. For System 1, with $N = 2 - 4$, the corresponding particle diameters and weights are listed in Table 5.5.

From the DPS simulation, the fluidization behavior of the mixture can be best described as low-energy bubbling, the bed height only increases from 5 to 6.5 cm. The segregation phenomena can be clearly seen for System 1. The normalized mean diameter of the local size distribution (scaled by the mean diameter of the overall size distribution, $d_{\text{ave overall}}$) along the bed height were calculated and compared with DPS in Fig. 5.6 using 2-4 nodes. The DPS results shows that, near the left wall ($x=0.5$ cm), the segregation is not very noticeable, the normalized mean diameter is around 1.0. The segregation in the interior of the bed ($x=2.5$ cm and 4.5 cm) was much stronger, the normalized mean diameter decreases with increasing height. However, the Eulerian-Eulerian model gives slightly different results. The segregation is very strong at all points in the bed, either near the wall or inside of the bed. Due to segregation, at the bottom of the bed, the normalized mean diameter is large with a value of 1.4. Near the top of the bed, the normalized mean diameter is small with a value of 0.6. For the effect of nodes number, If two nodes are used, the bed height is slightly higher than using three nodes

and four nodes. Thus the mean diameter at the top of the bed is slightly larger than the DPS simulation.

The standard deviation (σ) of the local size distribution (scaled by the standard deviation of the overall size distribution, σ_{overall}) along the bed height for System 1 was also computed and compared with DPS simulations in Fig. 5.7. Also some differences can be observed in the comparison. The DPS simulation shows that the standard deviation for each curve is different, only near the left wall, the normalized standard deviation decreases with the height, and then stays around 1.0. For other two curves ($x=2.5$ cm and 4.5 cm), the normalized standard deviations are lower than 1.0. However using the Eulerian-Eulerian model, it can not simulate the lateral segregation across the bed, the curves are the same for all three locations (near the wall and inside of the bed). Notice in the graphs, if two nodes are used, the normalized standard deviation is 1.0, which means the local distribution are identical to the overall distribution. It shows representing the continuous PSD by two nodes are not adequate, as it can not catch the difference between local distribution and overall distribution. With the increase of the number of nodes, for all three locations, the normalized standard deviation decreases from 1.4 to around 1.0. The local distribution are different at different locations. A wider distribution near the bottom, and a narrow distribution near the top of the bed.

If we plot the normalized mean diameter and standard deviation of the local size distribution across the bed (Figs. 5.8 and 5.9), the difference between Eulerian-Eulerian model and DPS simulation are more easily observed. As we can see, DPS simulation shows there is lateral segregation at the bottom ($y=0.5$ cm) and at the top of the bed ($y=6.5$ cm). Larger particles tend to accumulate in the middle of the bed, and less large particles are found near the wall. The average particle diameter doesn't change with the height, and not much axial segregation is observed near the wall. However inside of the bed ($y=2.5$ cm and 4.5 cm), no lateral segregation is observed, and the normalized mean diameter across the bed remains constant, same as the overall mean diameter in the bed. For the Eulerian-Eulerian simulation, even if we increase the number of nodes, the lateral segregation at the bottom and top of the bed can not be observed. The normalized mean diameter remains constant across the bed at all

locations ($y=0.5, 2.5, 4.5$ and 6.5 cm). So axial segregation is found everywhere, even near the wall. The same phenomena can also be found in Fig. 5.9 and there is no difference in standard deviation across the bed.

The reason that current model can not catch the lateral segregation is probably because that the current kinetic theory model assumes the collisions are binary and quasi-instantaneous and neglect the long-term and multi-particle contacts. However, in regions with high particle volume fraction, such as near the wall or the corner, frictional stresses are more important. There are more particle-particle and particle-wall contact and the flow behavior is effected by the frictional model at high solid volume fractions. Due to neglect of the frictional stresses, the Eulerian-Eulerian is not able to catch the less segregated region near the wall and shows no difference at near the wall and inside of the bed. We believe DPS with a periodic boundary condition (ignoring the wall effect) would give more similar results for DPS and the Eulerian-Eulerian model.

Even though the above system is a low-energy fluidized bed, a significant segregation along the height is observed from both simulations. According to the simulations and experiments for the binary system, increasing the gas flow rate will lead to better mixing and produce more bubbles. Segregation will be overtaken by the mixing, and segregation phenomena will no longer exist. Thus, the effect of the superficial gas velocity is studied in System 2, which has the same properties as System 1, but with a higher superficial gas velocity $\mathbf{u}_g = 1.0$ m/s (1.25 times of the gas velocity of System 1). The normalized mean diameter of the local size distribution along the bed height for System 2 using 2-4 nodes are compared with DPS simulation results in Fig. 5.10. Compared with Fig. 5.6 (System 1), both DPS simulation and our simulation shows that the segregation along the height is greatly reduced, segregation only happens at the very bottom of the bed, and the normalized mean diameter at the bottom is only around 1.1, smaller than the one observed in System 1. Also notice that, increasing the number of nodes doesn't change the results very much. With better mixing, two nodes are enough to represent the whole system.

The third system (System 3) has the same properties as System 1, but with a narrow

Gaussian distribution, the ratio of the standard deviation of the particle size to the mean particle size σ/d_{ave} reduces to 0.1. Since the particle size distribution changed, the moments are different, and the corresponding particle nodes for System 3 are different. With a narrow distribution, the variance between particle diameters for each node is smaller, less segregation is expected. The mean diameter of the local size distribution along the bed height doesn't change, same as the overall diameter. The local distribution is same as the overall distribution, no axial and lateral segregation are observed along the bed height and across the bed. Similar to System 2, when the distribution is narrow, better-mixed is achieved, and less nodes need to be used in DQMOM.

After the analysis of segregation and mixing phenomena in a Gaussian mixture, a study for the effect of the distribution was also conducted. Since log-normal distributions are common in industrial fluidized beds, a log-normal distribution with $\sigma/d_{ave} = 0.5$ (System 4) was studied. Similar to System 3, the particles are slightly elastic ($e = 0.99$) and less frictional ($C_f = 0.01$). Due to the long tail of the lognormal distribution, the maximum particle size is almost 3 or 4 times of the average particle size, so the minimum fluidization velocity for System 4 is higher than System 1. Thus the superficial gas velocity increases from 0.8 m/s to 1.0 m/s.

The j^{th} moment of the log-normal distribution can be gotten from equation (Randolph and Larson, 1971):

$$m_j = (d_{ave})^j \exp\left(\frac{j^2}{2}\sigma^2\right) \quad (5.18)$$

By using PD algorithm, the corresponding weights and particle diameters that represent System 4 with nodes from 2 to 4 are listed in Table 5.6.

The normalized mean diameter and standard deviation of the local size distribution along the bed height for System 4 are calculated and compared in Figs. 5.11 and 5.12. According to the simulation, due to the bigger particles in the tail for the log-normal distribution, the segregation is much stronger. The bigger particles quickly move to the bottom of the bed, and then the bed defluidized at the bottom, and a stagnant layer forms with the average mean

Table 5.6 Particle diameters and weights for System 4 using $N = 2 - 4$.

	N	$\alpha = 1$	$\alpha = 2$	$\alpha = 3$	$\alpha = 4$
Particle diameter $d_{p\alpha}$, μm	2	682	1834		
	3	584	1398	3347	
	4	527	1193	2558	5794
Weights ω_α	2	0.8148	0.1852		
	3	0.6375	0.3544	8.1×10^{-3}	
	4	0.5134	0.4549	0.0315	2.0×10^{-4}

particle size rather large, around 2.0 times of average particle size for the whole bed. The Eulerian-Eulerian simulation shows that two nodes are not enough to represent the continuous particle size. If two nodes are used, the node, which has the large particle diameter, accumulates at the bottom and another node, the smaller particles, moves to the top. The two nodes become completely segregated and form two layers in the simulation. The normalized average particle size suddenly drops from 2.0 to 0.5, not a smooth curve as showed in DPS. Thus more nodes are needed to represent the lognormal distribution. With the increase of the nodes to $N = 3$ or $N = 4$, the Eulerian-Eulerian model agrees with DPS better. The mean particle size gradually decreases with increasing height. Also notice in Fig. 5.11, the DPS simulation shows there is lateral segregation near the bottom. Same as in the previous simulations, the Eulerian-Eulerian model can not catch the lateral segregation for System 4. The variation of the mean diameter and standard deviation of the local size distribution across the bed for System 4 are also shown in Figs. 5.13 and 5.14. The difference between DPS and Eulerian-Eulerian model is more easily observed in these two figures. For Eulerian-Eulerian model, all the curves are almost horizontal lines, with a little fluctuation at the top of the bed. In contrast, DPS simulation showed lateral segregation at the bottom of the bed (the curve for $y=0.5$ cm), the larger particles tend to accumulate in the middle of the bed. Note that using either $N=3$ or 4 yields acceptable agreement with DPS results.

5.4 Conclusions

An Eulerian-Eulerian model for polydisperse fluidized beds was studied for a binary system and a few systems with continuous PSD. The simulations for the binary system were compared with the experiments conducted by Goldschmidt et al., and the model reproduced the segregation and mixing phenomena in the binary mixture experiments. When the superficial gas velocity was low, smaller than the minimum fluidization velocity for the large particles, segregation occurred, the larger particles moved to the bottom and the small particles moved to the top, formed a layer of rich in jetsam at the bottom, the fluidized bed defluidized at the bottom. When the superficial gas velocity was equal to or larger than the minimum fluidization velocity, more bubbles were observed in the bed, and better mixing was achieved. The segregation in the bed was greatly reduced, and the segregation rate was very low, around 0.1.

Many industrial fluidized beds contain particles with continuous PSD, thus segregation and mixing phenomena for a continuous size distribution were also studied. The first three systems had a Gaussian distribution. System 1 had a wide distribution with $\sigma/d_{ave} = 0.3$ and System 2 has the same distribution as System 1 but with a higher superficial gas velocity. System 3 had a narrow distribution with $\sigma/d_{ave} = 0.1$. The last system (System 4) had a log-normal distribution with $\sigma/d_{ave} = 0.5$. As expected, the wide Gaussian distribution showed more segregation than the narrow one, and the lognormal distribution showed the greatest segregation. Increasing superficial gas velocity generated more bubbles, better mixing, and reduced the segregation. The simulation results were compared with DPS simulations conducted by Dahl and Hrenya, and showed that the Eulerian-Eulerian model can reproduce the segregation along the bed height, but can not reproduce the lateral segregation across the bed observed in DPS simulations. In the simulations, DQMOM is used to represent the underlining distribution, the effect of the node numbers was also studied. The results showed that, when the distribution was narrow or the superficial gas velocity was high, the mixing dominated the segregation, and less nodes were needed. For a wide distribution with strong segregation, at least three nodes were needed to represent the distribution.

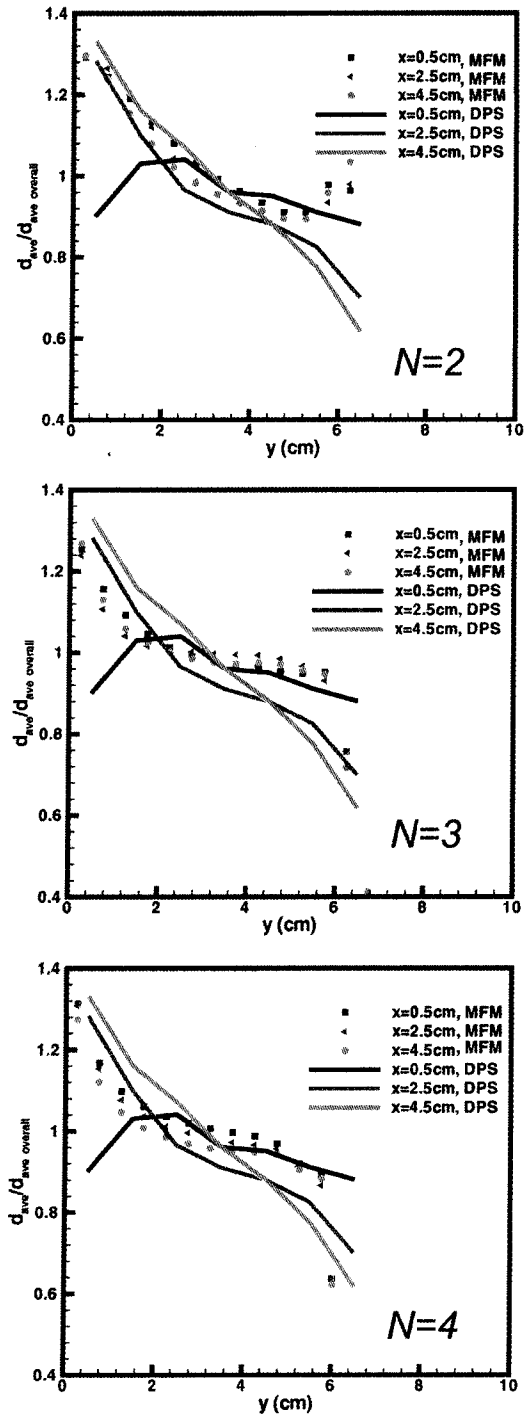


Figure 5.6 The normalized mean diameter of the local size distribution along the bed height for System 1.

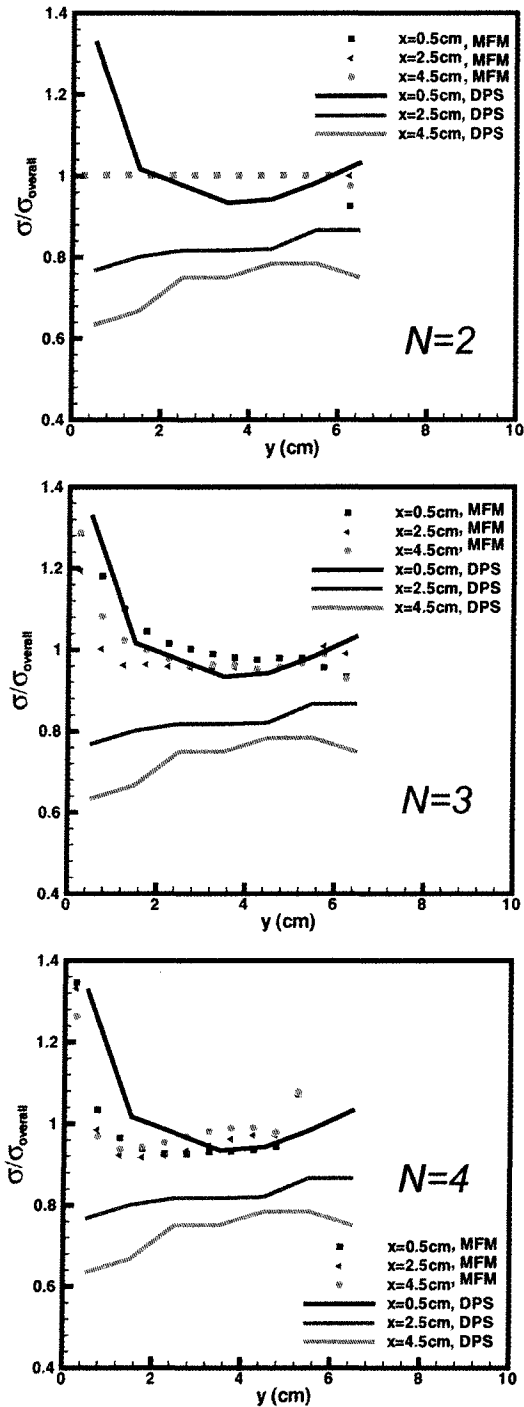


Figure 5.7 The normalized standard deviation of the local size distribution along the bed height for System 1.

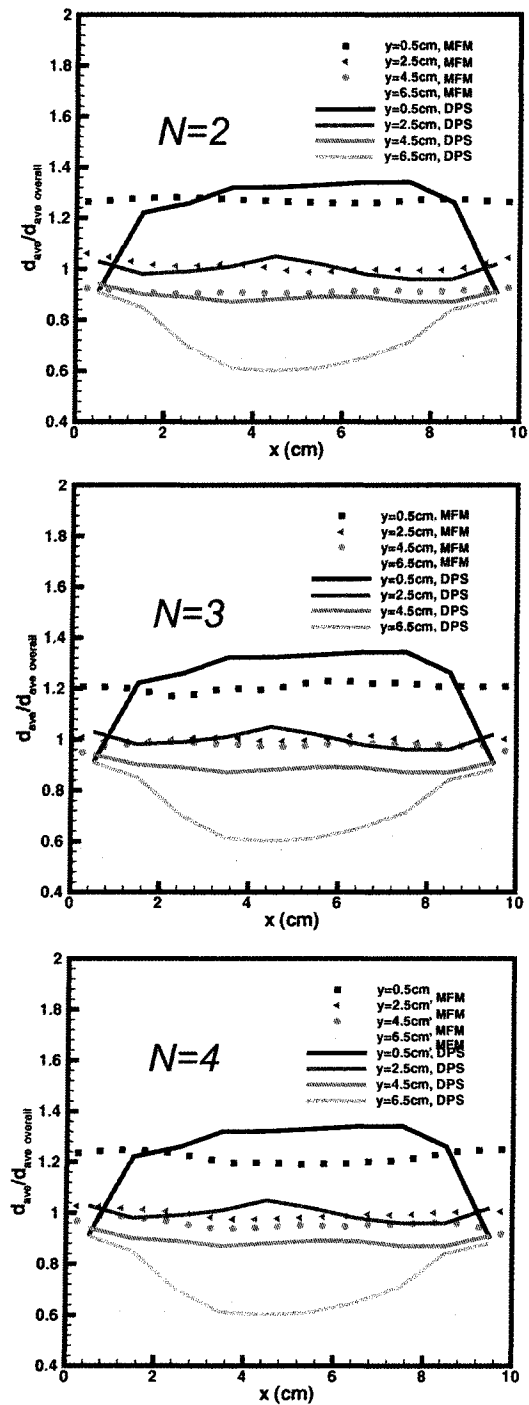


Figure 5.8 The normalized mean diameter of the local size distribution across the bed for System 1.

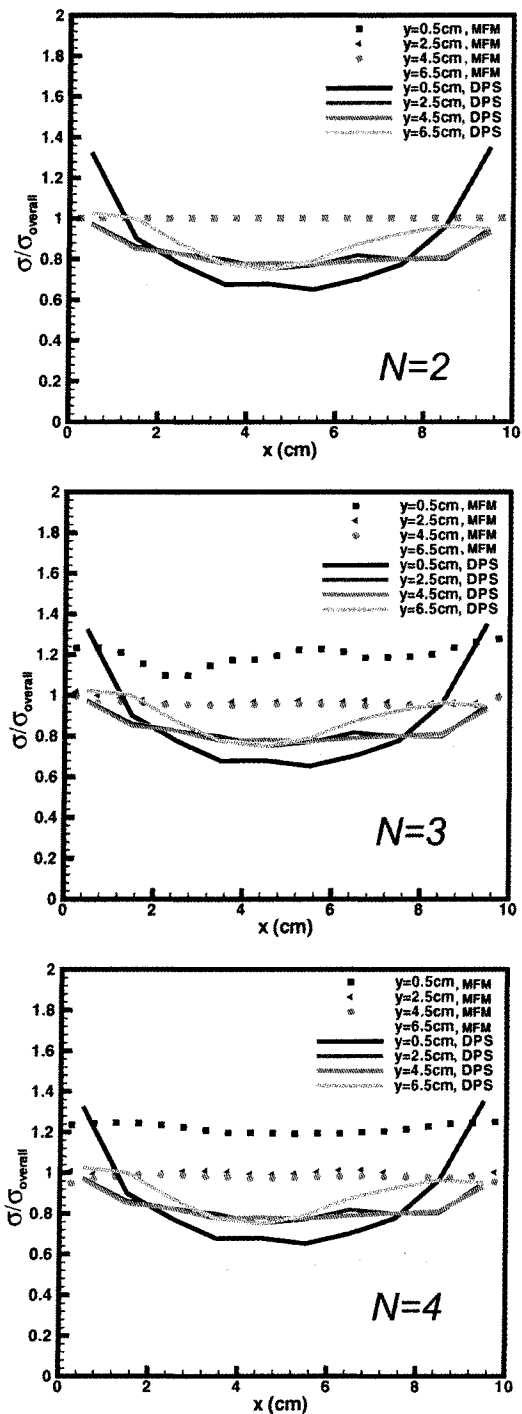


Figure 5.9 The normalized standard deviation of the local size distribution across the bed for System 1.

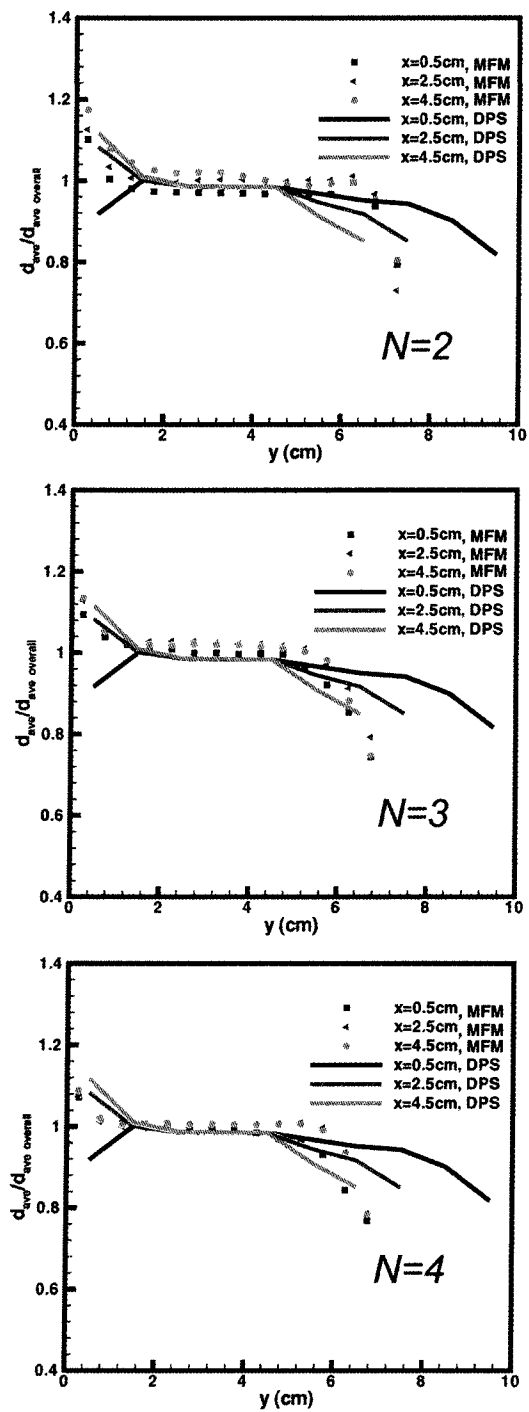


Figure 5.10 The normalized mean diameter of the local size distribution along the bed height for System 2.

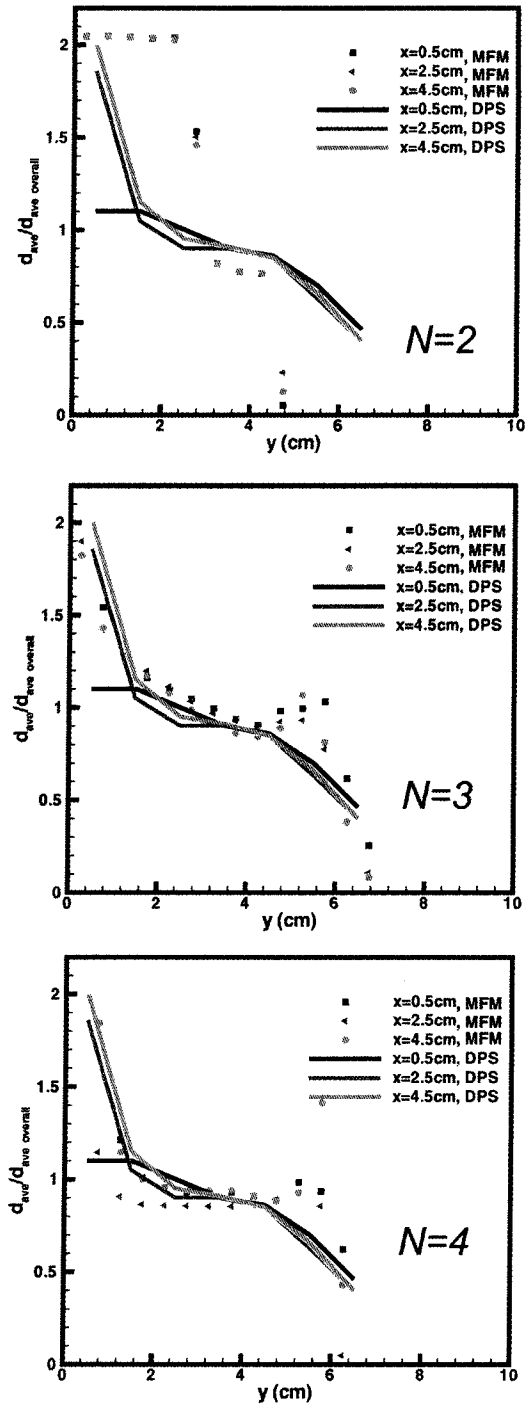


Figure 5.11 The normalized mean diameter of the local size distribution along the bed height for System 4.

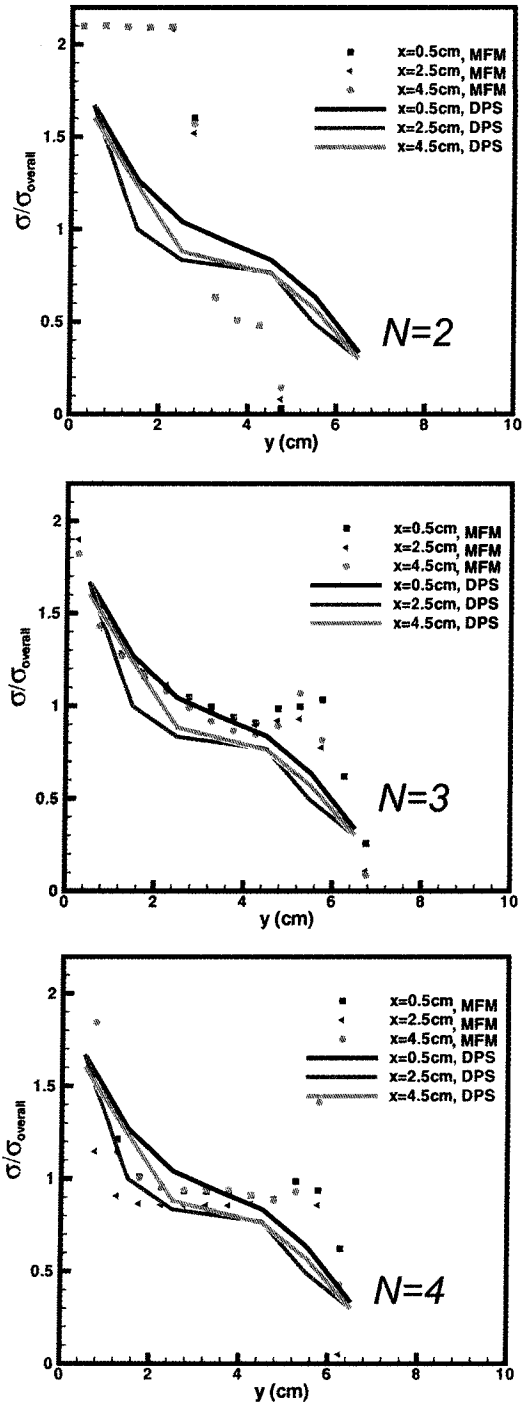


Figure 5.12 The normalized standard deviation of the local size distribution along the bed height for System 4.

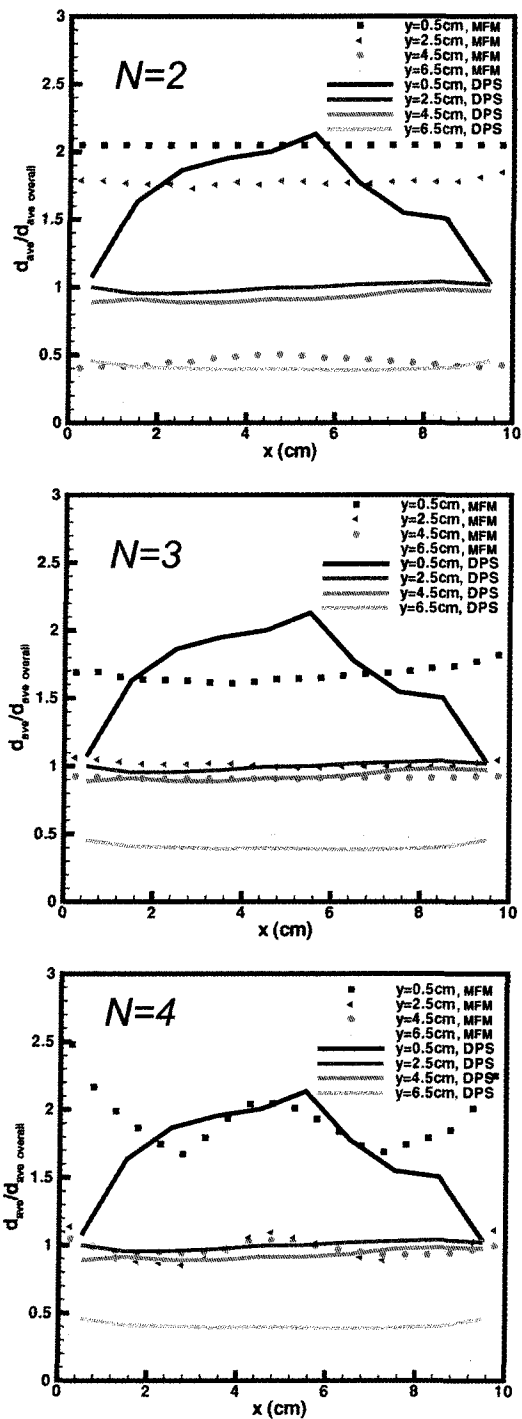


Figure 5.13 The normalized mean diameter of the local size distribution across the bed for System 4.

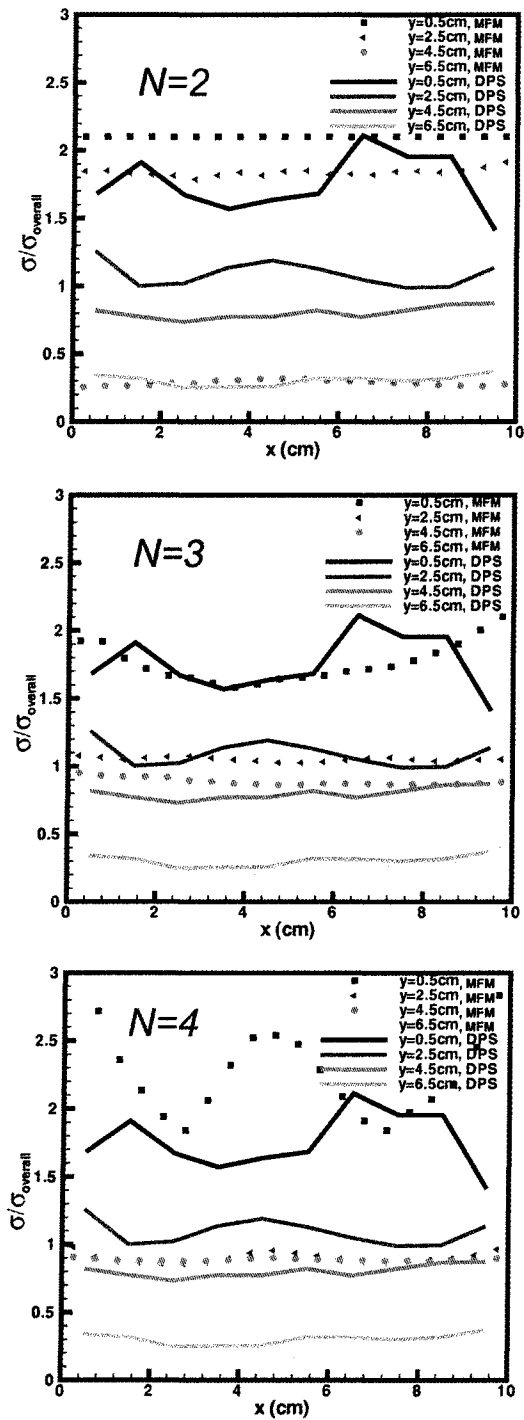


Figure 5.14 The normalized standard deviation of the local size distribution across the bed for System 4.

CHAPTER 6. COMPUTATIONAL FLUID DYNAMICS MODELING OF UNIPOL GAS-PHASE REACTORS

6.1 Introduction

Polyolefins, especially PP and PE, have become the most popular resins due to the merit of low price, flexibility of molding and ease of disposal or recycling (Kaneko, Shiojima, and Horio, 1999). Based on production data for 1999 and 2000, 85-95 million tons of polyolefins are produced around the world. This already impressive market is still in full growth, Foxely (1998) predicted that the growth rates is about 30% for PP and about 18% for PE products for the period from 2000 to 2005. Nowadays, most polyolefin polymerization processes are executed in a liquid- or gas-phase reactor or a combination of both. Because there is no need for drying and separation of olefins from solvents, a gas-phase process is more advantageous than conventional liquid slurry processes. For the gas-phase process, four reactor types commercialized so far are the fluidized bed type (UNIPOL process), the vertical stirred-bed type (NOVOLEN process), the horizontal stirred-bed type (AMOCO process) and multizone circulating reactor type (Basel process). The use of a gas-fluidized bed with its inherent excellent mixing and heat-transfer characteristics is a major strength of gas phase processes such as the UNIPOL process. the UNIPOL process. The UNIPOL process has been licensed extensively with over 100 reactor lines in 24 different countries comprising approximately 17,000,000 metric tons of PE capacity. As such it represents 25% of global PE capacity. The UNIPOL PP process have been implemented in 15 countries, on six continents. There are over 30 reactor lines using UNIPOL PP in operation worldwide with a production capacity of over 5 million tons per year (Burdett et al., 2001).

Although the gas phase process has been commonly employed in the production of PE

since 1980s, some inherent features of the process remain as a challenge for an engineering breakthrough. One of the main problems in gas-solid fluidized beds, not only for PE but other processes as well, is particle agglomeration (Mckenna and Soares, 2001). Two main factors contribute to the agglomeration in the bed, one is the “hot spots” formed in the bed and another is the electrostatic charge. In nature, olefin polymerization is a highly exothermic reaction. The temperature of the polymer particles tend to rise and sometimes it will exceed the melting point of the polymer (usually 430K). If the heat removal is poor, local “hot spots” are formed and the hot spot becomes a nucleus for polymerization at a much more rapid rate. Then the particles can melt and stick together to form bigger particles or fuse into a sheet or large chunk. On the other hand, when polymer particles are fluidized within the reactor, electrostatic charges are generated from surface charge polarization and separation due to friction among gas, particles and reactor walls (Park et al., 2002). When two particles (or particle and reactor wall) with dissimilar electrical charge meet, they are attractive to each other and form loose agglomerates. The electrostatic force induced by these charges can change the hydrodynamics of gas-solid fluidized bed and more importantly unintentional accumulation of electrostatic charges can lead to fused particle agglomerates. This is a major problem for commercial-scale processes since it interferes with the performance of the reactors. In extreme cases this can lead to FB reactor defluidization, and then the whole process needs to be shut down.

Many people have investigated the particle overheating and electrostatic charge in the fluidized beds. Several models of a single polymer particle for olefin polymerization on supported catalysts were developed in recent years to study the particle overheating, such as a simple steady-state model of the non-growing particle by Hutchinson and Ray (1987); polymeric-flow model used by Schmeal and Street (1971), Hoel et al. (1994) and Veera et al. (2002); more sophisticated multi-grain models developed by Floyd et al. (1986), Hutchinson et al. (1992) and Debling and Ray (1995); and a novel, simple lumped-thermal model used by Song (2004). Electrostatic charge are measured and modelled in gas-solid fluidized beds by Professor Bi's group (Park et al., 2002; Mehrani et al., 2005). The study shows that the increased electrostatic

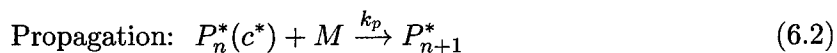
charge levels occur in fluidized beds with increased fluidization gas velocity, increased particle size, increased bubble size and increased bed circulation rate. The particle size determines the polarity, large particles and small particles having opposite polarity, so in order to know the electrostatic field in the bed, it is very essential to study the particle size distribution and fluidized bed hydrodynamics (Hendrickson, 2006).

With the development of high-performance computers and multiphase models, CFD has become a powerful tool for the understanding of the effect of fluid dynamics on chemical-reactor performance. In the previous work, Mckenna et al. (1999) studied the overheating problem for a single particle or a system of two or three touching particles or a single particle attached to the wall using CFD. The study shows that the contact between small hot particles and larger cool ones helps to avoid overheating and the early models of heat transfer in olefin polymerization overpredict the temperature rise during early stages of polymerization. Meanwhile, Kaneko et al. (1999) also studied the motion of the particles and nonuniform distribution of temperature in a small fluidized bed using Discrete Element Model (DEM). However the work on CFD simulation of pilot-scale fluidized beds is very few. Due to the large dimension of the industrial-scale fluidized bed, the simulation work can only be done in Eulerian-Eulerian frame. Gobin et al. (2003) presented some preliminary fluid dynamic simulation results of larger scale ethylene polymerization dense fluidized bed using Eulerian model. The results are in good qualitative agreement with the observed bed height, pressure drop and mean flow organization. In their work, the solid phase consists of spherical particles with a constant particle size, but in reality, the solid phase consists of different particle sizes with different age time. Thus in our work, a multi-fluid model and chemical reaction engineering model are combined to investigate the fluid dynamics, mass/heat transfer and particle size distribution in a pilot-scale fluidized bed. These information not only can provide the visualization of the flow pattern of the fluidized bed, but it also can provide important mechanistic understanding regarding particle overheating and potential agglomeration problems.

6.2 Polymerization Kinetics and Multi-fluid Model

6.2.1 Polymerization Kinetics for Metallocene Catalyst

A simplified mechanistic scheme for the metallocene catalyst kinetics is used here. Compared to more widely used kinetics in the literature, chain transfer is ignored, only three fundamental reactions: initiation, propagation and decay are considered. The approach is one of engineering the catalyst design rather than a detailed mechanistic understanding of the various copolymerization and chain transfer reactions. This is necessary since activation energies for these reactions are seldom measured. The rate constants for initiation (k_i), propagation (k_p) and decay (k_d) are defined below:



where c is a potential catalyst active site and c^* is an active catalyst site. P_n^* is a living polymer with chain length n . M is monomer, P_n is a dead polymer segment of length n that can not undergo any further reaction, and c^0 is the deactivated catalyst site or dead site. For each rate constant, an Arrhenius equation is considered,

$$k = k_0 \exp(-E_a/RT_s) \quad (6.4)$$

where k_0 is the pre-exponential factor and E_a is the activation energy.

All the reactions are first order reactions, and k_i and k_d has the unit of hr^{-1} , k_p has the unit of g/gcat hr . The rate and activation energy can be parameterized based on results from laboratory-scale experiments using a stirred gas-phase bed reactor. During the study, it was found that most rate profiles have a “peak” profile at the start of the polymerization and a two site model fit the data better. The first site has a fast decay and initiation rate, accounting for the initial peak in the reaction rate. The second site has a slow decay and initiation rate, accounting for the slow decay at the end in the rate profile.

6.2.2 Multi-Fluid Model

The multi-fluid model used in this work was extended from the two-fluid continuum model by Syamlal et al. (1993). In this model, gas and N solid phases are treated as interpenetrating continua using an Eulerian model. Each solid phase is characterized by a “particle” diameter, density and other properties, and each phase has its own set of governing hydrodynamic equations. The averaging approach is applied to derive the equations for both gas and solid phases. The phasic volume fractions are introduced to track the fraction of the averaging volume occupied by various phases. By definition, the volume fraction of all the phases must sum to one:

$$\varepsilon_g + \sum_{\alpha=1}^N \varepsilon_{s\alpha} = 1, \quad (6.5)$$

where ε_g and $\varepsilon_{s\alpha}$ are the volume fractions of the gas and solid phases, respectively.

The mass balances for the gas and solid phases are

$$\frac{\partial}{\partial t}(\varepsilon_g \rho_g) + \nabla \cdot (\varepsilon_g \rho_g \mathbf{u}_g) = - \sum_{\alpha=1}^N M_{g\alpha} \quad (6.6)$$

and

$$\frac{\partial}{\partial t}(\varepsilon_{s\alpha} \rho_s) + \nabla \cdot (\varepsilon_{s\alpha} \rho_s \mathbf{u}_{s\alpha}) = M_{g\alpha} + 3k_v \rho_s L_\alpha^2 b_\alpha - 2k_v \rho_s L_\alpha^3 a_\alpha, \quad (6.7)$$

where ρ_g and ρ_s are the gas- and solid-phase densities, \mathbf{u}_g and $\mathbf{u}_{s\alpha}$ are the gas- and solid-phase velocities, and $M_{g\alpha}$ is the mass-transfer rate from the gas to the α^{th} solid phase due to polymerization reaction. The last two terms in the solid continuity equation account for the effect of aggregation and breakage. Since aggregation and breakage will not change the total solid volume fraction, there are no extra terms in the gas continuity equation. Only monomer (ethylene) is assumed to transfer from gas phase to solid phase since it is the primary heat source for the polymerization rate ($\sim 90\%$), and the mass-transfer model is

$$M_{g\alpha} = \varepsilon_{s\alpha} k_{c\alpha} a_v (c_g - c_{M\alpha}) M_W. \quad (6.8)$$

$k_{c\alpha}$ is mass-transfer coefficient and it is related to Sherwood number Sh_α by

$$k_{c\alpha} = 2D_b \frac{Sh_\alpha}{L_\alpha}, \quad (6.9)$$

where D_b is the diffusivity of monomer in the bulk phase of the reactor. a_v is the ratio of particle external surface area to volume, and for a spherical particle, $a_v = 6/L_\alpha$. c_g and $c_{M\alpha}$ are the monomer concentration in the gas phase and solid phase, respectively. $c_{M\alpha}$ is related to the mass fraction of monomer in the solid phase $X_{sM\alpha}$ by $c_{M\alpha} = \rho_s X_{sM\alpha}/M_W$.

The momentum balances for the gas and solid phases are

$$\frac{\partial}{\partial t}(\varepsilon_g \rho_g \mathbf{u}_g) + \nabla \cdot (\varepsilon_g \rho_g \mathbf{u}_g \mathbf{u}_g) = \nabla \cdot \boldsymbol{\sigma}_g + \sum_{\alpha=1}^N \mathbf{f}_{g\alpha} + \varepsilon_g \rho_g \mathbf{g} \quad (6.10)$$

and

$$\frac{\partial}{\partial t}(\varepsilon_{s\alpha} \rho_s \mathbf{u}_{s\alpha}) + \nabla \cdot (\varepsilon_{s\alpha} \rho_s \mathbf{u}_{s\alpha} \mathbf{u}_{s\alpha}) = \nabla \cdot \boldsymbol{\sigma}_{s\alpha} - \mathbf{f}_{g\alpha} + \sum_{\beta=1, \beta \neq \alpha}^N \mathbf{f}_{\beta\alpha} + \varepsilon_{s\alpha} \rho_s \mathbf{g}, \quad (6.11)$$

where $\boldsymbol{\sigma}_g$ and $\boldsymbol{\sigma}_{s\alpha}$ are the gas- and solid-phase stress tensors, $\mathbf{f}_{g\alpha}$ is the interaction force between the gas and the α^{th} solid phase, $\mathbf{f}_{\beta\alpha}$ is the interaction force between the β^{th} and α^{th} solid phases, and \mathbf{g} is the gravity vector. A simple Newtonian closure is used for the gas-phase stress tensor, and kinetic theory is used to calculate the solid-phase stress tensor in the viscous regime (Syamlal, Rogers, and O'Brien, 1993).

For the energy balance equations, the heat produced from polymerization reaction is assigned to solid phase. The energy balance for gas and solid phase are

$$\varepsilon_g \rho_g C_{pg} \left(\frac{\partial T_g}{\partial t} + \mathbf{u}_g \cdot \nabla T_g \right) = -\nabla \cdot \mathbf{q}_g - \sum_{\alpha=1}^M H_{g\alpha} + H_{wall}(T_{wall} - T_g), \quad (6.12)$$

$$\varepsilon_{s\alpha} \rho_s C_{ps} \left(\frac{\partial T_{s\alpha}}{\partial t} + \mathbf{u}_{s\alpha} \cdot \nabla T_{s\alpha} \right) = -\nabla \cdot \mathbf{q}_{s\alpha} + H_{g\alpha} - \Delta H_{rs\alpha}, \quad (6.13)$$

where T_g and $T_{s\alpha}$ are the gas and solid-phase temperature. \mathbf{q}_g and $\mathbf{q}_{s\alpha}$ are the conductive heat flux for gas and solid phase. $H_{g\alpha}$ is the heat transfer between gas and solid phase and it can be modelled as

$$H_{g\alpha} = -\varepsilon_{s\alpha} h_{f\alpha} a_v (T_{s\alpha} - T_g), \quad (6.14)$$

where $h_{f\alpha}$ is the heat-transfer coefficient and it is related to Nusselt number by

$$h_{f\alpha} = 2\lambda_g Nu_\alpha / L_\alpha. \quad (6.15)$$

λ_g is the thermal conductivity of the gas phase.

The heat produced from polymerization reaction is $\Delta H_{rs\alpha} = -\varepsilon\eta_\alpha k'_p [c^*] c_{M\alpha} \Delta H_r$, where $k'_p = k_p/[c_0]$ has units of $\text{cm}^3/\text{mol-sites s}$. $[c_0]$ is the initial potential active catalyst site concentration. The lumped-thermal model is used here and it assumes that the temperature of the particle is uniform, but different from that of the surrounding, and the active sites are uniformly distributed within the particle during the growth. The intraparticle heat transfer is ignored and the intraparticle species diffusion resistance is accounted for by an isothermal effectiveness-factor η_α , which has a form of

$$\eta_\alpha = \frac{3[\phi_\alpha \coth h(\phi_\alpha) - 1]}{\phi_\alpha^2} \quad (6.16)$$

where ϕ_α is the non-isothermal Thiele modulus and

$$\phi_\alpha = \frac{L_\alpha}{2} \sqrt{\frac{k'_p [c^*]_\alpha}{D_{eA}}} \quad (6.17)$$

D_{eA} is the effective diffusivity and for heterogeneous catalyst, $D_{eA} = D_b \varepsilon / \tau$, where ε and τ are the porosity and tortuosity of the macroparticle, respectively.

Typically, in a UNIPOL polyethylene process, there are four species in the gas phase: C_2H_4 (monomer), an α -olefin (copolymer), N_2 and H_2 . For each species, the mass fraction is X_1 , X_2 , X_3 and X_4 respectively. Only monomer (C_2H_4) is transferred from gas phase to solid phase, thus the equation for each species can be written as

$$\frac{\partial}{\partial t}(\varepsilon_g \rho_g X_1) + \nabla \cdot (\varepsilon_g \rho_g X_1 \mathbf{u}_g) = - \sum_{\alpha=1}^N M_{g\alpha}, \quad (6.18)$$

$$\frac{\partial}{\partial t}(\varepsilon_g \rho_g X_2) + \nabla \cdot (\varepsilon_g \rho_g X_2 \mathbf{u}_g) = 0, \quad (6.19)$$

$$\frac{\partial}{\partial t}(\varepsilon_g \rho_g X_3) + \nabla \cdot (\varepsilon_g \rho_g X_3 \mathbf{u}_g) = 0, \quad (6.20)$$

$$\frac{\partial}{\partial t}(\varepsilon_g \rho_g X_4) + \nabla \cdot (\varepsilon_g \rho_g X_4 \mathbf{u}_g) = 0. \quad (6.21)$$

In each solid phase, the mass fraction of monomer in the solid phase needs to be solved, and

$$\frac{\partial}{\partial t}(\varepsilon_{s\alpha} \rho_s X_{sM\alpha}) + \nabla \cdot (\varepsilon_{s\alpha} \rho_s X_{sM\alpha} \mathbf{u}_{s\alpha}) = M_{g\alpha} - \eta_\alpha \varepsilon_{s\alpha} \rho_s k'_p X_{sM\alpha} [c^*]_\alpha. \quad (6.22)$$

Noticed in this equation, mass transfer and chemical reaction are coupled. For polymerization reaction, mass transfer is very fast and the reaction is controlled by the polymerization reaction

rate. The mass fraction of monomer in the solid phase is a constant. If there is no aggregation and breakage, combining Eq. 6.7 with Eq. 6.2.2, we can get:

$$M_{g\alpha}(1 - X_{sM\alpha}) = \eta_{\alpha}\varepsilon_{s\alpha}\rho_s k'_p X_{sM\alpha} [c^*]_{\alpha}. \quad (6.23)$$

Thus when all the active sites become dead sites, $[c^*] = 0$, both mass transfer and reaction terms are zero, and particles will stop growing.

The species equations for potential active sites $[c]$, active site $[c^*]$ and dead sites $[c^0]$ are

$$\frac{\partial}{\partial t}(\varepsilon_{s\alpha}\rho_s[c]) + \nabla \cdot (\varepsilon_{s\alpha}\rho_s[c]\mathbf{u}_{s\alpha}) = -\varepsilon_{s\alpha}\rho_s k_i[c], \quad (6.24)$$

$$\frac{\partial}{\partial t}(\varepsilon_{s\alpha}\rho_s[c^*]) + \nabla \cdot (\varepsilon_{s\alpha}\rho_s[c^*]\mathbf{u}_{s\alpha}) = \varepsilon_{s\alpha}\rho_s k_i[c] - \varepsilon_{s\alpha}\rho_s k_d[c^*], \quad (6.25)$$

$$\frac{\partial}{\partial t}(\varepsilon_{s\alpha}\rho_s[c^0]) + \nabla \cdot (\varepsilon_{s\alpha}\rho_s[c^0]\mathbf{u}_{s\alpha}) = \varepsilon_{s\alpha}\rho_s k_d[c^*]. \quad (6.26)$$

where k_i , k_p and k_d are the rate constant for initiation, propagation and decay, respectively. Note that fresh catalyst has only potential active sites, and no active sites and dead sites, so $[c^*] = [c^0] = 0$.

Particle size changes due to polymerization reaction, aggregation and breakage. If no aggregation and breakage are considered, the particle length is related to solid void fraction by a constant. In this way, transport equations for particle length or particle volume are not needed. But if aggregation and breakage are considered, such equations are needed to be solved with other equations simultaneously.

6.3 Results and Discussion

In a UNIPOL PE process (Fig. 6.1), the fluidized bed reactor consists of a reaction zone and disengagement zone. The main reaction zone has a height to diameter ratio of about 4-6. The disengagement zone above the main reaction zone has a larger diameter in order to reduce the gas velocity, so that the particles entrained by the gas can fall back into the main section of the bed. It is essential that the bed always contain polymer particles to entrap and distribute the powdery catalyst. On start up, the reaction zone of the fluidized bed is charged with polymer before gas flow is initiated. Gas mixture (monomer (C_2H_4), comonomer, inert(N_2))

and H_2) is introduced to the settled bed from the bottom with a velocity sufficiently high to fluidize the polymer particles in the reactor. After the bed reaches steady state, fresh catalyst particles (with diameter of 20-100 μm) are injected from a position above the distributor and reacts with the incoming monomer. The catalyst particles are quickly encapsulated by the newly formed polymer and grow to form bigger particles. The fully-grown polymer particles accumulate in the fluidized bed and cause the bed level to rise. When the bed level reaches a certain height, the product is removed intermittently from the bottom portion of the fluidized bed. The particle entrainment together with the unreacted, gas pass through the enlarged disengagement zone and leave the reactor from the top. The entrainment can be further reduced by a cyclone and a filter to avoid deposition of polymer on heat-transfer surfaces and compressor blades. The effluent stream has a higher monomer concentration since the single-pass monomer conversion in the FB polymerization reactors is low, only 2% to 5%. The effluent gas is compressed, cooled and recycled back to the reactor where it continues to react with the catalyst. The resin leaving the reactor contains absorbed hydrocarbons. After degassing, the reactor produces a granular resin with a consistent particle size distribution which is readily pelletized.

6.3.1 Validation of Fluid Dynamics for a PE Pilot-Scale Fluidized Bed

In order to validate the fluid dynamics using CFD, start-up cases were evaluated for which catalyst is not injected into the bed, and no product is removed from the bed. First, two-dimensional (2D) simulations were carried out for a pilot FB polyethylene reactor using MFIX. The height of the main reaction zone is on the order of 100~1000 cm, and will be referred as L . The total height of the reactor with expansion and dome area is about $2 \sim 3 L$. The diameter of the main reaction zone is in the range of 10~100 cm, and will be referred as D . The diameter of the dome area is about $2.0D$. The sketch of the PE pilot-scale fluidized bed reactor is shown in Fig. 6.2. Non-uniform cartesian grids are used in 2D simulation and the number of grid cells are 127×251 . In MFIX, it is hard to build a mesh for a complex reactor like this. In the simulation, a mesh for a larger rectangle is used, and then the red regions inside

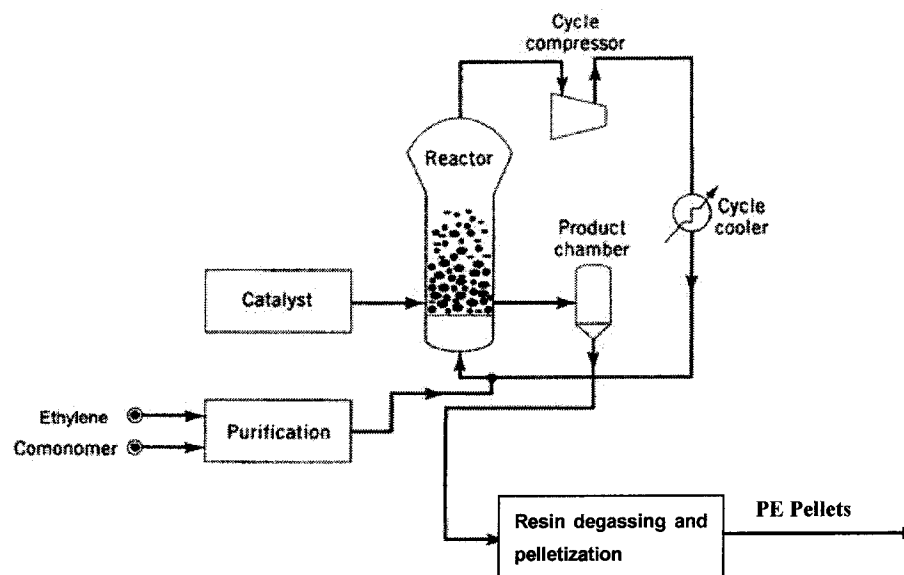


Figure 6.1 Gas-phase fluidized bed olefin polymerization process (UNIPOL process)

of the rectangle are set as no-slip wall (NSW) to cut out the shape of the reactor (blue region in Fig. 6.2). Thus only about 60% cells are fluid cells among all the cells. For the boundary condition, at the bottom of the bed, gas is uniformly distributed, and a mass inflow (MI) for gas phase is specified. At the top, a pressure outflow (PO) is specified. If catalyst is injected into the fluidized bed, a mass inflow for solid phase is set at the inlet. If product is removed from the bed, a mass outflow (MO) is set at the outlet. The typical operating conditions for gas-phase polymerization reactors are listed in Table 6.1. The mathematical model used in the simulation is described in Sec. 6.2.2, and the detail information about the gas and solid stress tensor and interaction force between phases are same as described in Chapter 3. For the drag model between gas and solid phase, the Gidaspow model is used in the simulation.

Fig. 6.3 shows the instantaneous gas void fraction at the beginning of the fluidization. The simulation results show slug-flow behavior, thereby confirming visual observations of the reactor through a high-pressure viewing port on the pilot plant reactor. However the predicted bed height from 2D simulation is 32% higher than the experimentally measured value. The simulation value for the average pressure drop between two pressure taps is only 21 mmHg,

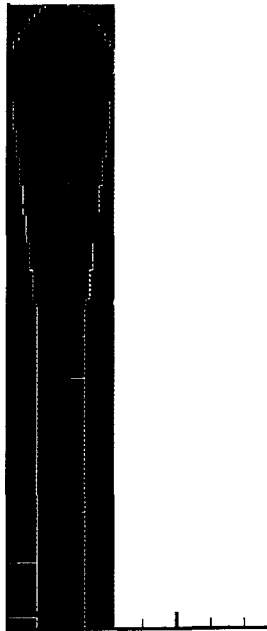


Figure 6.2 Sketch of PE pilot-scale fluidized bed reactor

Table 6.1 Typical operating conditions for gas-phase polymerization reactors.

<i>Gas properties</i>	Units	Value
Density, ρ_g	g/cm ³	0.0221
Viscosity, μ_g	Pa·s	1.427×10^{-5}
Heat capacity, C_{pg}	cal/(g·K)	0.3~0.4
Pressure, P_g	bar	10~30
Inlet temperature, T_g	K	343~363
Superficial gas velocity, \mathbf{u}_g	cm/s	40~100
<i>Particles properties</i>		
Density, ρ_s	g/cm ³	0.843
Heat capacity, C_{ps}	cal/(g·K)	0.168
Average catalyst size	μm	10~100
Average polymer particle size	μm	1000
Thermal conductivity, λ_f	cal/(cm·s·K)	$3 \sim 7 \times 10^{-5}$
Monomer bulk diffusivity, D_b	cm ² /s	$2 \sim 6 \times 10^{-3}$
Effective diffusivity, D_{eA}	cm ² /s	$1 \sim 5 \times 10^{-4}$
Coefficient of restitution, e	-	0.8
Heat release of polymerization reaction, $-\Delta H_r$	cal/mol	2.5×10^4

and is lower than the experimental value of 29.30 mmHg. The average hold up for the 2D simulation is higher than the one from experiments. Since it is very important to match this value for validation of the fluid dynamics of the pilot-scale fluidized bed, the drag model was modified to match the bed height from experiments. Results showed that by modifying the drag model, the bed height from 2D simulation is lower, and the pressure drop is closer to the experimental value. However the slug-flow behavior is no longer observed.

According to a study by Peirano et al. (2001) on 2D and 3D simulation of a turbulent gas-solid fluidized bed, 2D simulation should be used with caution, and will be more likely to be successful in cases where the flow is by nature two dimensional. However, for industrial fluidized beds, the radial direction is very large and cannot be ignored. For this reason, a 3D simulation of the pilot-scale fluidized bed was carried out for comparison. Cylindrical grids are used in the 3D simulation and the number of grid cells are $28 \times 189 \times 12$. Coarse grids are used in 3D simulation due to long running time. As in the 2D simulation, the geometry of the PE pilot-scale reactor is cut out from a larger cylindrical column, and only about 50% cells are

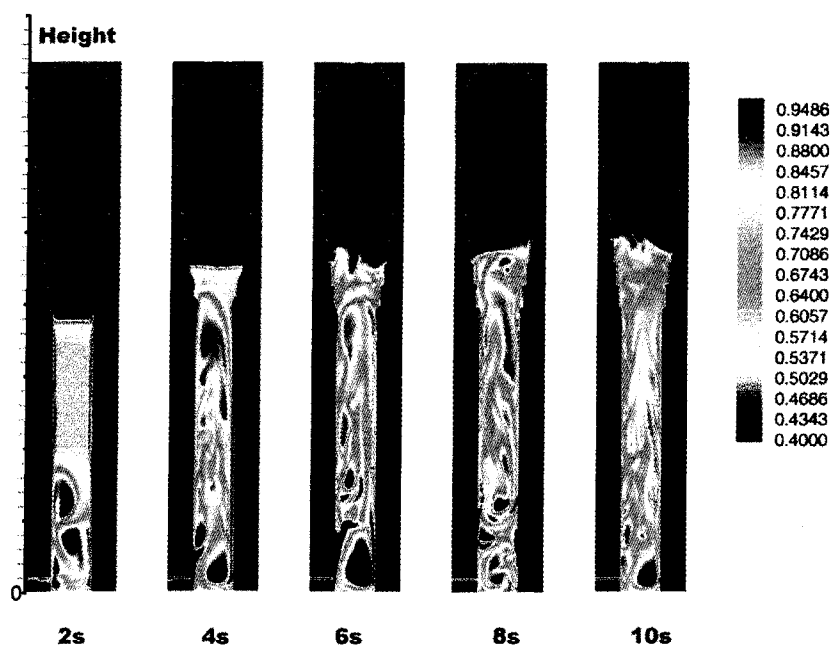


Figure 6.3 Instantaneous gas void fraction at 2 s, 4 s, 6 s, 8 s and 10 s from 2D simulation.

fluid cells and other cells are set as non-fluid cells. The instantaneous gas void fraction at the beginning of the fluidization for a 3D simulation is shown in Fig. 6.4. Similar to the 2D results, slug flow is observed at around 4 seconds. However, the differences between the results of 2D and 3D are striking: by simply adding a third dimension to the simulation, while keeping all other numerical parameter unchanged (same drag model), the expansion of the bed changed significantly. The bed height drops from 132% to 105% of the experimental value. Average hold up for the FB decreases and small bubbles appeared in the 3D simulation. The pressure drop along the two taps increased from 21 mmHg to 26.25 mmHg (Fig. 6.5). The pressure decreases almost linearly in the 2D and 3D simulations, however the slope of the pressure drop for the 3D simulation is lower than for the 2D simulation.

Time-averaged gas-velocity fields for 2D and 3D simulations are compared in Fig. 6.6. The time-averaged solid-velocity fields for 2D and 3D simulation are similar to this profile. It is also clearly seen that the flow patterns for these two simulations are different. In the 2D case, the average gas velocities are lower and more symmetrical. In both 2D and 3D simulations, a

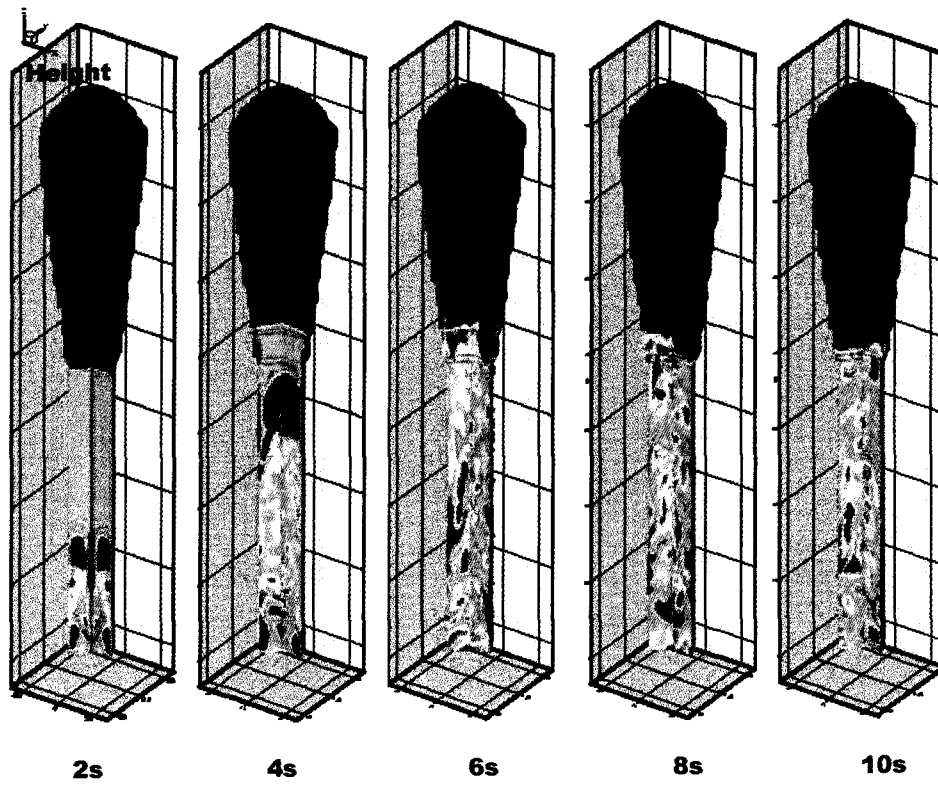


Figure 6.4 Instantaneous gas void fraction at 2 s, 4 s, 6 s, 8 s and 10 s from 3D simulation.

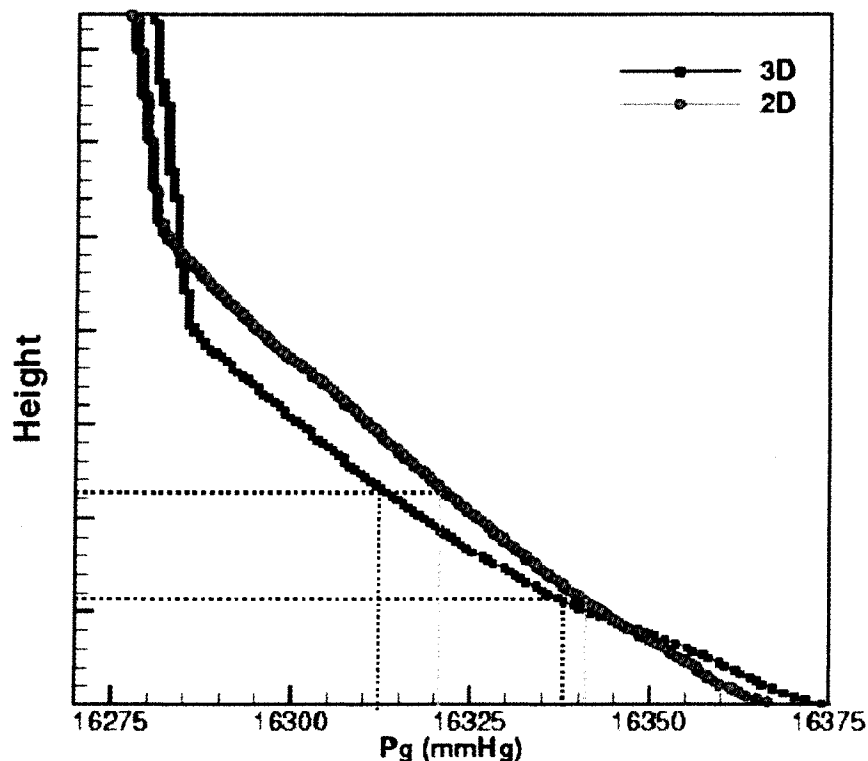


Figure 6.5 Comparison of pressure drop along the two taps for 2D and 3D simulations.

core/wall layer structure is observed, and gas (or solid) flow is predicted to occur in a downward direction along the wall. The average gas velocity at different heights, $0.24L$, $0.27L$ and L , is also compared in Fig. 6.6. For 2D simulation, the average solid velocity does not vary much at different heights. However, for the 3D simulation, the solid velocity in the middle decreases with bed height. The maximum gas velocity in the middle exceeds 300 cm/s at a height of $0.24L$.

The normalized pressure drop signal from experiment is compared with 2D and 3D simulation in Fig. 6.7. The graph shows that the fluctuation of experiment data is very strong and with a higher amplitude. The signal for 2D simulation is relatively smooth compared to 3D simulation, but both have a smaller amplitude. The bed pressure drop signal from experiment and simulations can be used to determine the power spectrum. These results were used to fine tune the model to match the observed fluidized-bed dynamics. The power spectra

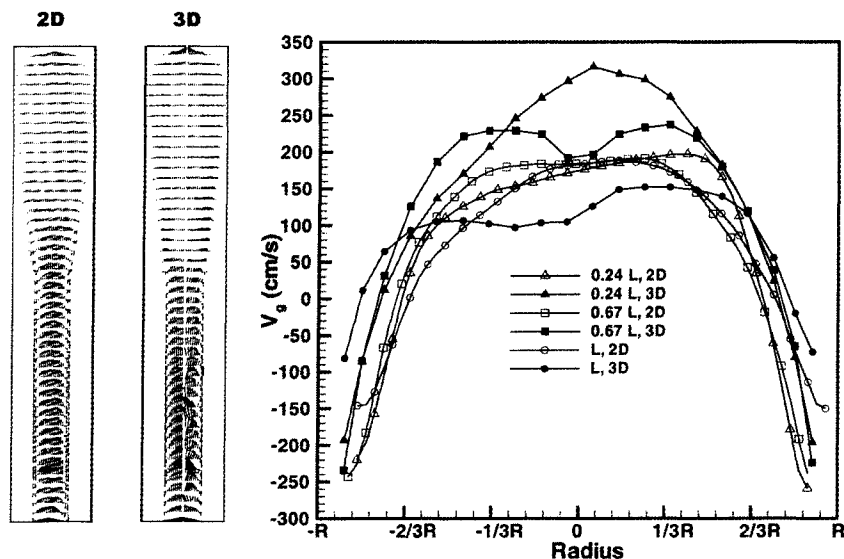


Figure 6.6 Comparison of time-averaged gas velocity for 2D (blue) and 3D (red) simulations.

of the pressure fluctuations from experiments and 2D, 3D simulations (100 Hz sample data) are compared in Fig. 6.8. In order to convert to the frequency domain, the discrete Fourier transform of the noisy signals of experiment and simulations are found by taking the 512-point fast Fourier transform (FFT). In Fig. 6.8, the blue line and green line are the 2D and 3D simulation results and the red line is the experimental result. From the results, we can also come to the conclusion that 3D simulation results match the experimental data better. The results at low frequency (the magnitude change to linear) are compared for experiment, 2D and 3D simulations in Fig. 6.9. The graph shows that 3D simulation can reproduce the first and second peak in the experimental data, but with a higher magnitude. However 2D simulation can only get one peak and the frequency is in the middle of the two peaks. As expected, both 2D and 3D simulations cannot reproduce the high frequency in the experiment data due to the limit of the model derivation (In the kinetic theory of the solid phases, higher frequency of collisions of particles is ignored during model derivation). Usually the first peak indicates the frequency of slug flow, so the energy for 3D simulation is a little bit higher than the experimental data.

Three-dimensional PE pilot fluidized-bed simulations are computationally expensive, even

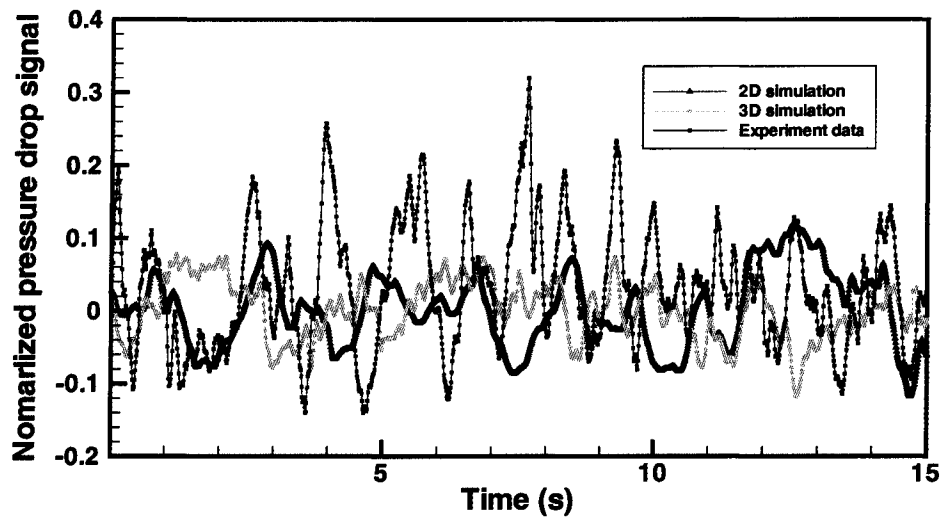


Figure 6.7 The normalized pressure drop signal for experiment, 2D and 3D simulations.

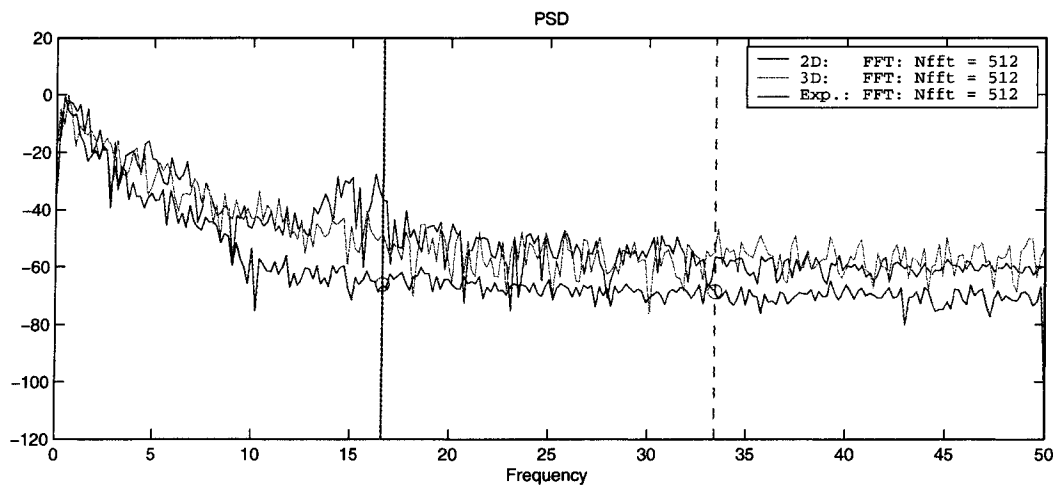


Figure 6.8 The power spectra of the pressure fluctuation from experiments, 2D and 3D simulations

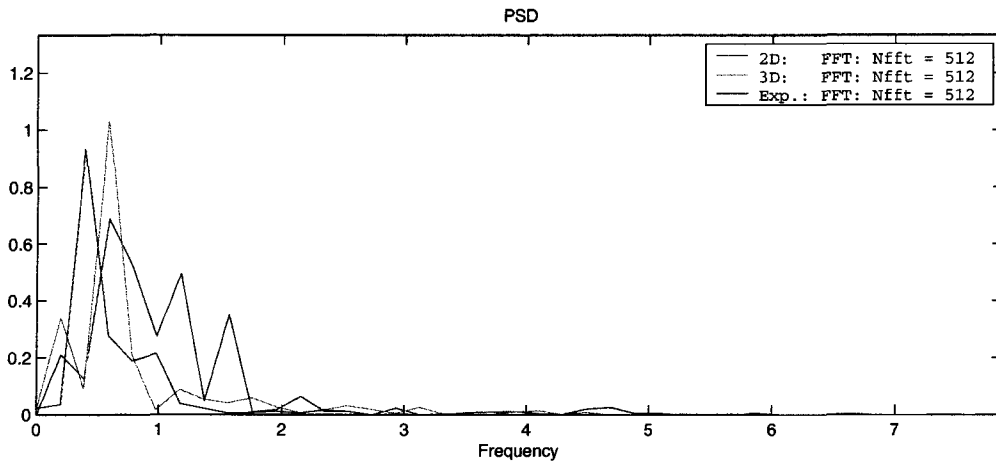


Figure 6.9 Power spectra results at low frequency from experiments, 2D and 3D simulations.

when a parallel code (Distributed Memory Parallelization) for multiprocessors is used to reduce the computation time. Multiprocessor performance for the 3D simulation is compared for 2, 4, 8, 16 and 32 processors in Table 6.2. The grids number on radical direction (I direction) is 28, on vertical direction (J direction) is 189 and on azimuthal direction (K direction) is 12. The influence of the parallelization direction was also investigated and the results for speed up (S_n) and efficiency (E_n) for 3D simulation are presented in Fig 6.10 and Fig. 6.11. Parallelization in the vertical direction (J direction) has the maximum speed-up value and best efficiency. By using 4 processors in the J direction, the speed up can reach to 3.28 and the efficiency is 81.97%. If the processors increase to 8 and 16, the speed up increases to 5.50 and 8.47 with an efficiency of 68.74% and 52.91%. The speed up increase with the increase of the number of processors, but the efficiency decreases at the same time. With the trade off between the computation time and computer resources, 8 processors were chosen for this 3D simulation.

Table 6.2 Multiprocessor performance for 3D simulations using 2, 4, 8, 16 and 32 processors.

Number of process		CPU Time(s)	Wall Time (s)	Sn	En (%)
1	I=1 J=1 K=1	55855	55970	1.00	100.0
2	I=1 J=2 K=1	35399	35497	1.58	78.84
2	I=2 J=1 K=1	37470	37572	1.49	74.48
2	I=1 J=1 K=2	50385	50497	1.11	55.42
4	I=1 J=4 K=1	16963	17070	3.28	81.97
4	I=2 J=2 K=1	19104	19211	2.91	72.84
4	I=4 J=1 K=1	24321	24435	2.29	57.26
4	I=1 J=2 K=2	32727	32844	1.70	42.60
8	I=1 J=8 K=1	10070	10178	5.50	68.74
8	I=2 J=4 K=1	10486	10599	5.28	66.01
8	I=4 J=2 K=1	12758	12875	4.35	54.34
8	I=1 J=4 K=2	16567	16686	3.35	41.93
16	I=1 J=16 K=1	6496	6611	8.47	52.91
16	I=4 J=4 K=1	6995	7115	7.87	49.17
16	I=2 J=8 K=1	7334	7452	7.51	46.94
32	I=2 J=16 K=1	4586	4714	11.87	37.10
32	I=1 J=32 K=1	4690	4823	11.60	36.27
32	I=4 J=8 K=1	4981	5111	10.95	34.22

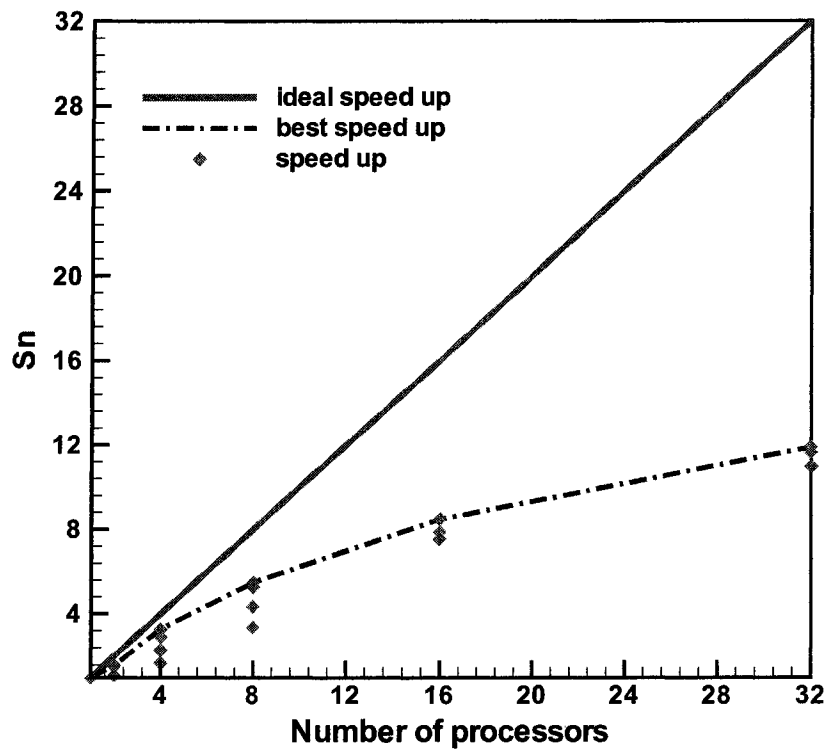


Figure 6.10 Speed up for 3D simulations of pilot-scale fluidized bed using 2, 4, 8, 16 and 32 processors on hpc3.

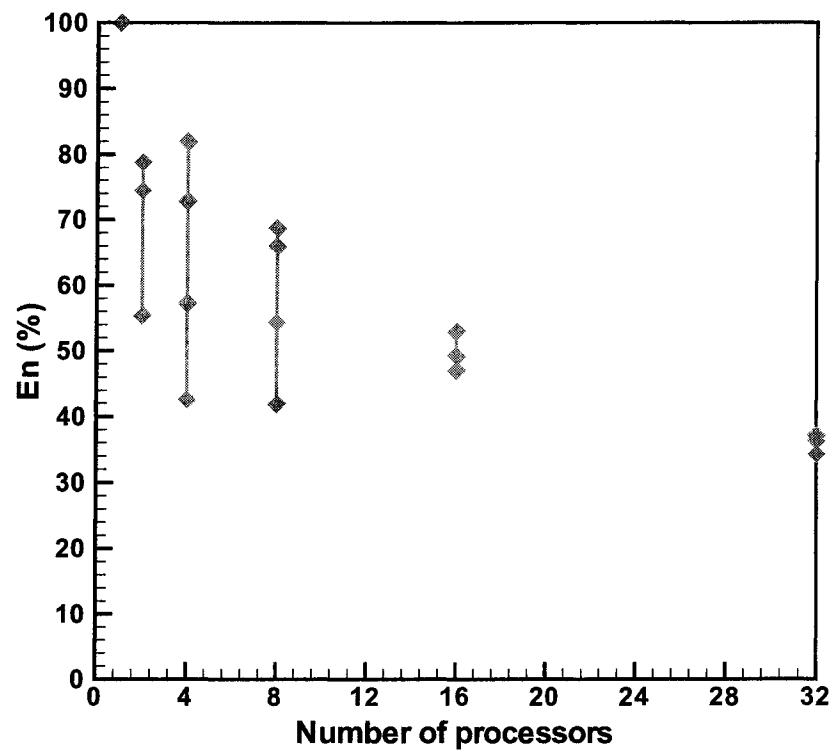


Figure 6.11 Efficiency for 3D simulations of pilot-scale fluidized bed using 2, 4, 8, 16 and 32 processors on hpc3.

6.3.2 Chemical Reaction Engineering Model and Kinetic Parameters Study

After validation of the fluid dynamics for start-up cases, the work on incorporating the energy, species, and population balance equations was undertaken. However, the solid phase residence time for a PE polymerization reactor is on the order of hours, and the fluid dynamics of a fluidized bed is on the order of seconds. It is intractable to run a 3D simulation for hours using the current CFD code. Hence, the time scale for fluid dynamics and polymerization reaction is separated in the following work, and the polymerization reaction equations are solved outside of CFD simulation. The CFD simulations is initialized to a steady state with a distribution of particle size, age time and temperature. In order to accomplish this, a reaction-engineering model based on the age of particles was used. The simulations started with this steady state and were run for a few seconds. During this short period, since the polymerization reaction is so slow, we can assume that the particle will not grow and the particle temperature will not change due to reaction.

In the reaction engineering model, it is assumed that the gas phase is at steady state, so equations for the gas phase from multi-fluid model do not need to be solved. The equations for the solid phases from the multi-fluid model are solved using an ODE solver in Matlab after dropping the inhomogeneous terms. Thus, the equations for the engineering model are as follows:

$$\rho_s \frac{d\varepsilon_s}{d\tau} = \varepsilon_s k_c a_v (c_g - c_M) M_W \quad (6.27)$$

$$\frac{d}{d\tau} (\varepsilon_s [c]) = -\varepsilon_s k_i [c] \quad (6.28)$$

$$\frac{d}{d\tau} (\varepsilon_s [c^*]) = \varepsilon_s k_i [c] - \varepsilon_s k_d [c^*] \quad (6.29)$$

$$\frac{d}{d\tau} (\varepsilon_s [c^0]) = \varepsilon_s k_d [c^*] \quad (6.30)$$

$$\varepsilon_s \rho_s C_{ps} \frac{dT_s}{d\tau} = \varepsilon_s h_f a_v (T_g - T_s) - \varepsilon_s \eta k_p' [c^*] c_M \Delta H_r \quad (6.31)$$

$$\rho_s \frac{d}{d\tau} (\varepsilon_s X_{sM}) = \varepsilon_s k_c a_v (c_g - c_M) M_W - \eta \varepsilon_s \rho_s k_p' X_{sM} [c^*] \quad (6.32)$$

where $c_M = \rho_s X_{sM} / M_w$. τ is residence time of the particles. If we assume the solid phase in the fluidized bed as a well-mixed CSTR, then the particle residence time distribution function

(RTD) is:

$$h(\tau) = \frac{1}{\tau_s} e^{-\tau/\tau_s}. \quad (6.33)$$

τ_s is the mean residence time, for a typical PE reactor, it is around 1~10 hours.

The mass/heat transfer and heat produced from polymerization reaction are same as described before in the multi-fluid model. If no aggregation and breakage are considered, the solid void fraction relates to the particle diameter by a constant, and $\epsilon_s = cL_s^3$. The constant c correspond to the number of particles per unit volume and can be estimated from average hold up in the fluidized bed from experiment. Since the average hold up is:

$$\langle \epsilon_s \rangle = \int_0^\infty \epsilon_s(\tau) h(\tau) d\tau = c \int_0^\infty L_s^3(\tau) h(\tau) d\tau. \quad (6.34)$$

The corresponding initial conditions for Eq. 6.27~Eq. 6.32 are:

$$\epsilon_s = cL_{s0}^3, T_s = T_g, X_{sM} = 0, \quad (6.35)$$

$$[c] = [c_0], [c^*] = 0, [c^0] = 0. \quad (6.36)$$

It is difficult to get the initial potential active catalyst site concentration from experiment, so in the simulation, $[c_0]$ is estimated from the production rate of the polymer by forcing the average particle size equal to the measured average polymer particle size. The average particle size can be calculated as:

$$\langle L_s \rangle = \int_0^\infty L_s(\tau) h(\tau) d\tau. \quad (6.37)$$

First, the chemical reaction engineering model is used to fit the experimental data and obtain the kinetic rate parameters. A set of experiments were conducted at Univation Technologies around a center point for different flow-feed ratios of comonomer/ monomer and hydrogen/monomer in the lab reactor (see Table 6.3). Three experiments were conducted at three temperatures (indicated by low, middle and high temperature). The reaction rates of monomer $R_{M,exp}$ are available for each case at different temperatures from lab reactor. In order to do the fitting, the reaction rates of monomer at different temperatures are calculated from the chemical reaction engineering model using a two site model (i indicates different site

Table 6.3 Different cases conducted in Univation Technology for a lab reactor.

Case	C_X/C_2	H_2/C_2
1	low	low
2	low	high
3	high	high
4	high	low
5	center	center

type, $i = 1, 2$), and

$$R_M = \sum_{i=1,2} \eta_i k_{p_i} [c^*]_i = \sum_{i=1,2} \eta_i k'_{p_i} [c^*]_i / [c_0]_i \quad (6.38)$$

The optimization tool box *lsqcurvefit* in Matlab is used to do the three curves fitting (Matlab codes are: *drive-fitting.m*, *objfunc.m*, *odefunc.m*), and the minimum value of $\sum (R_M - R_{M,exp})^2$ is determined with the best fitted rate constants and activation energies k_i , k_p , k_d , ΔE_i , ΔE_p and ΔE_d .

The comparisons of model fitting with lab data for Case 1 to 5 are shown in Fig. 6.12-6.16. The kinetic rate data for Case 1-5 from model fitting at middle temperature are listed in Table 6.4. Generally speaking, the two site model fit the curves quite nicely, and the initiation rate data can be determined with a high degree of accuracy. The initiation rates for both sites at middle temperature varied by a factor of 5. The propagation rate for both sites varied by a factor of 5. First site has fast decay, and the rate varied by a factor of 2 and the second site has slower decay and the decay rate is small and varied by a factor of 6. These rate data are very useful and they can be used to model single particle temperature rise for each case and later it will be used to investigate the hot spots in the fluidized beds in the multi-phase simulation. Since case 5 has the highest “peak” at the beginning when the operation temperature is high, this case is the worst case for particle overheating.

Table 6.4 Kinetic rate data ($\ln k = \ln k_0 - \Delta E/RT$) for Cases 1-5 obtained from two sites model fitting at middle temperature [normalized by the rate data of case 5 (site 2)].

Case	Initiation		Propagation		Decay		
	$\ln k_{0,i}$ (hr^{-1})	$-\Delta E_i/RT_s$	$\ln k_{0,p}$ (g/gcat-hr)	$-\Delta E_p/RT_s$	$\ln k_{0,d}$ (hr^{-1})	$-\Delta E_d/RT_s$	
1	Site 1	0.6018	7.34	1.671	-10.82	0.8190	5.24
	Site 2	0.4842	9.71	1.502	-8.66	3.8692	-35.97
2	Site 1	0.6761	6.68	1.3236	-4.88	1.0628	2.57
	Site 2	1.1735	-3.55	0.9486	0.33	1.8518	-10.35
3	Site 1	0.5818	9.14	1.0729	-1.29	0.8890	4.9
	Site 2	1.6884	-12.38	0.6912	5.03	0.0880	10.86
4	Site 1	0.6871	8.376	1.3746	-10.66	0.7972	6.1
	Site 2	0.4975	9.68	1.5085	-8.15	3.8757	-35.88
5	Site 1	0.8975	2.43	2.413	-21.17	1.3374	0.33
	Site 2	1.00	0.00	1.00	0.00	1.00	0.00

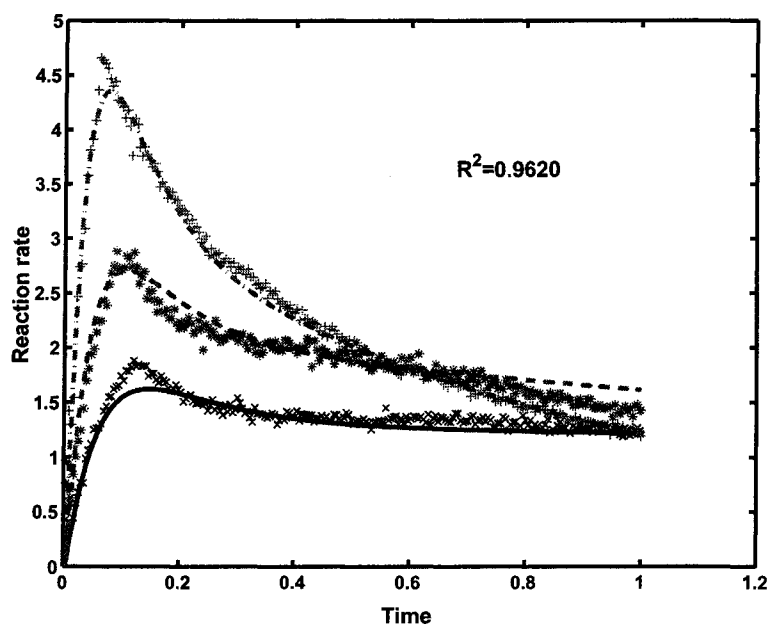


Figure 6.12 Two sites model fitted with experimental data for Case 1. Red: high temperature; Green: middle temperature; Blue: Low temperature) (the reaction rate and time are scaled by a constant).

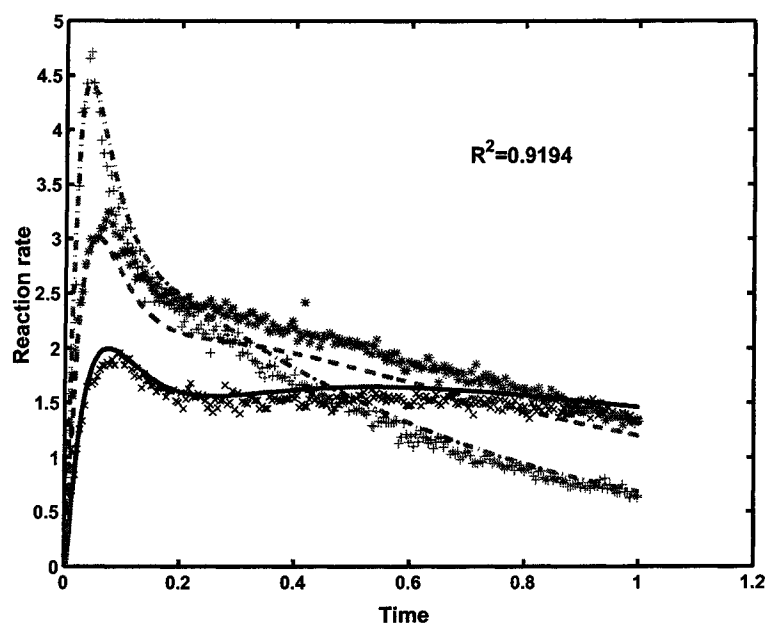


Figure 6.13 Two sites model fitted with experimental data for Case 2. Red: high temperature; Green: middle temperature; Blue: Low temperature) (the reaction rate and time are scaled by a constant).

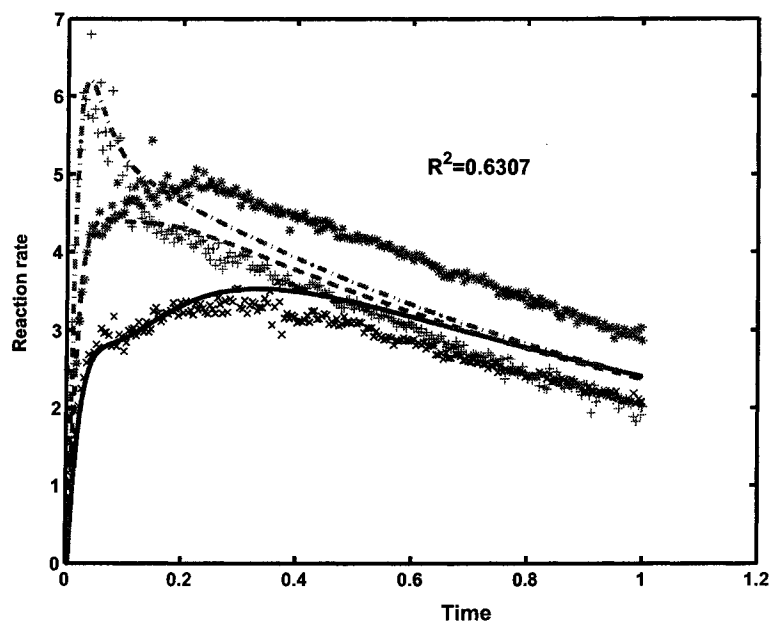


Figure 6.14 Two sites model fitted with experimental data for Case 3. Red: high temperature; Green: middle temperature; Blue: Low temperature) (the reaction rate and time are scaled by a constant).

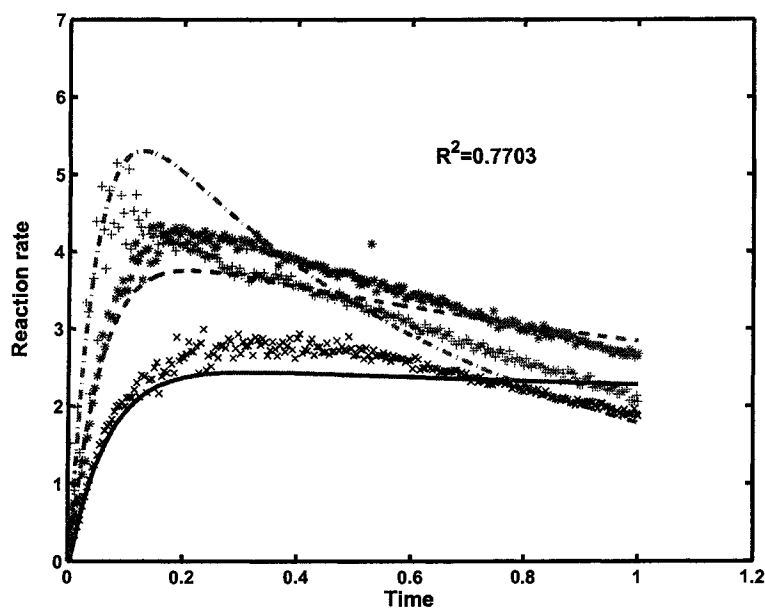


Figure 6.15 Two sites model fitted with experimental data for Case 4. Red: high temperature; Green: middle temperature; Blue: Low temperature) (the reaction rate and time are scaled by a constant).

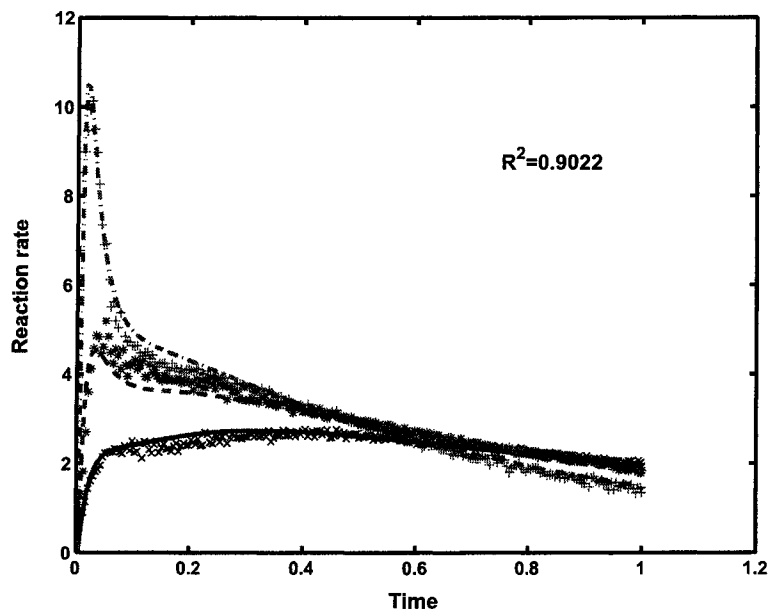


Figure 6.16 Two sites model fitted with experimental data for Case 5. Red: high temperature; Green: middle temperature; Blue: Low temperature) (the reaction rate and time are scaled by a constant).

6.3.3 Effect of Catalyst PSD on the Overheating and Final Polymer PSD

Commercial gas-phase reactors are critically dependent upon good mixing for heat removal and prevention of sintered polymer agglomerates. It has been found that to a large extent, good mixing is related to the polymer particle size and the distribution of these particle sizes in the bed. The polymer particle size distribution is governed by the feed catalyst particle size. These catalyst particles grow by a factor of 15-20 at a rate determined by the intrinsic kinetics of the polymerization. This time dependent process generates the resulting polymer particle size distribution in the fluid bed reactor. The polymer represents over 99.9% of the total bed mass. So far most models have taken the catalyst particle as a single particle size with an average value. However the large particles produced by the polymerization reaction can not be predicted using such an assumption and more importantly it underestimates the overheating in the fluidized bed.

In this work, QMOM is combined with chemical reaction engineering (CRE) model to study the effect of catalyst PSD on the overheating and final PSD of polymer. The flow chart of the process is shown in Fig. 6.17. First, moments of catalyst are calculated from its distribution function $f(L)$. In order to consider the effect of catalyst PSD, by using QMOM, two or three nodes can be used to represent the underlying distribution, each node has its own diameter and weight. The CRE model is applied to each node by assuming that the initial particle size L_{s0} has the diameter of the node. With CRE model, the evolution of particle diameter with age for each node can be obtained. According to the definition of moments, the moments of final product for each node can be obtained by integrating each curve with its age distribution. If there is no aggregation and breakage, the number of particles will not change and the weight for each node will not change, thus, the moments of final polymer can be calculated as a sum of weighted moments of each node. The detailed information of this method and results will be shown in this section. Once we know the moments of polymer, by using QMOM, two or three nodes can be used to represent the PSD of the polymer. Meanwhile, with the CRE model, the particle diameters are associated with particle temperature. A 3D CFD simulation is conducted to investigate the segregation and hot spots in the fluidized bed. The detailed

information about the 3D simulation is described in Sec. 6.3.5

The catalyst size distribution from experimental data is plotted in Fig 6.18. The distribution is a log-normal distribution but with a small "bump" at the low end of the PSD. The average particle size is in the range of 10-100 μm , it will be referred as d_{ave} and the standard deviation is around 25 μm . The normalized moments of the catalyst distribution can be calculated from the definition:

$$m_{k,catalyst} = \int_0^{+\infty} f(L)L^k dL \quad (6.39)$$

and the first six moments are: $m_0 = 1.0$, $m_1 = 6.618132 \times 10^{-3} \text{ cm}$, $m_2 = 4.825101 \times 10^{-5} \text{ cm}^2$, $m_3 = 3.835720 \times 10^{-7} \text{ cm}^3$, $m_4 = 3.298252 \times 10^{-9} \text{ cm}^4$, $m_5 = 3.035996 \times 10^{-11} \text{ cm}^5$. With QMOM, two or three nodes can be used to represent the catalyst distribution. If two nodes are used, one node is $0.91d_{ave}$ and the second node is $1.71d_{ave}$. The weight percentage of the first node is 63.87% and the second node is 36.13%. If three nodes are used to represent the PSD, the three nodes are $0.69d_{ave}$, $1.25d_{ave}$ and $2.03d_{ave}$. The percentage of the weight for each node is: 24.57%, 63.81% and 11.62%, respectively.

As we know, case 5 is the worst case for particle overheating, so the kinetic rate data for case 5 are used in the following discussions. If two nodes are used for representing the catalyst PSD, the chemical reaction engineering mode is employed for each node. The evolutions of particle size and temperature rise with age using two nodes are plotted in Fig. 6.19 and 6.20. For each node, the moments of the PSD of polymer can be obtained by integrating the length over the particle age distribution in the bed. The k^{th} moment of PSD for each node can be written as:

$$m_{k\alpha,polymer} = \int_0^{\infty} L_{s\alpha}^k(\tau)h(\tau)d\tau \quad (6.40)$$

If two nodes are used, the moments of the final polymer are found from weighted averages:

$$m_{k,polymer} = \omega_1 m_{k1} + \omega_2 m_{k2} \quad (6.41)$$

where $\omega_1 = 63.87\%$ and $\omega_2 = 36.14\%$ as discussed earlier. By integrating the two curves in Fig. 6.19 from zero to $t_f = 80 \text{ hr}$ (a time between 10-20 times of mean average resident time), the moments of the predicted size distribution can be determined, and $m_0 = 1.0$, $m_1 =$

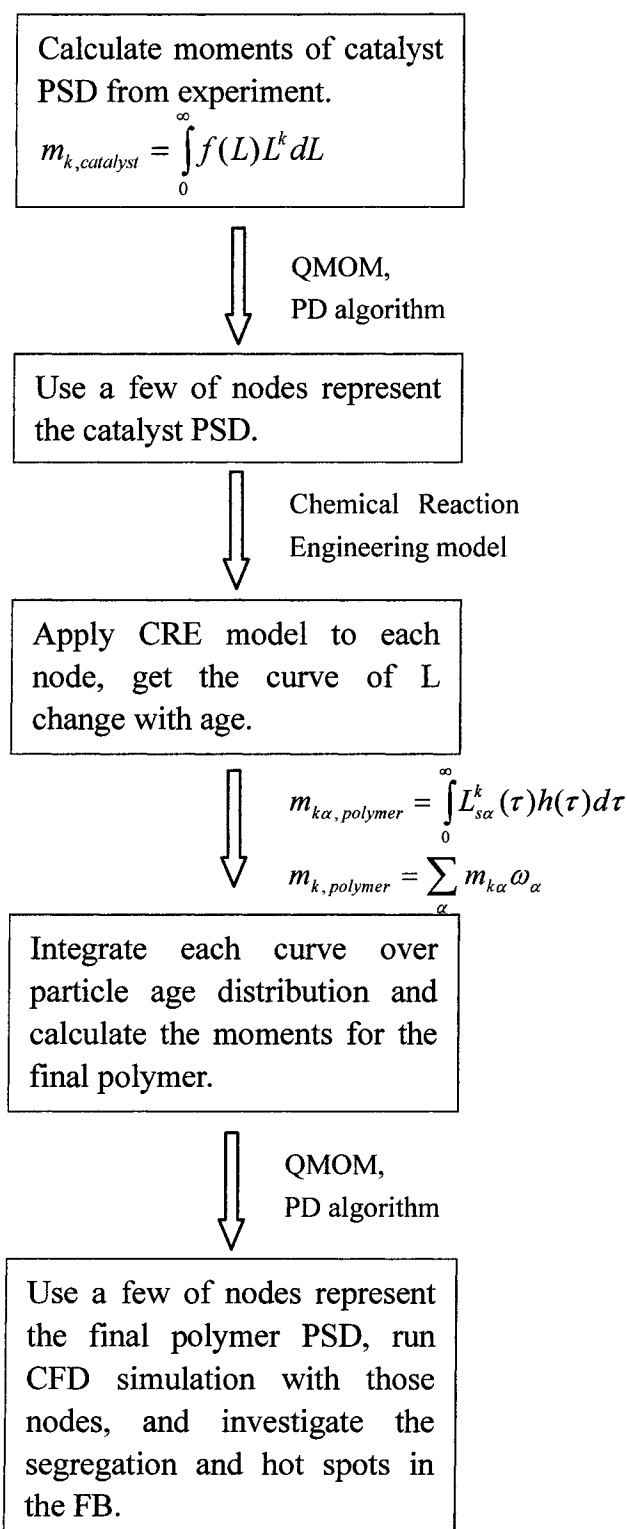


Figure 6.17 Flow chart of combining QMOM with CRE model to investigate the effect of catalyst PSD on the overheating and final polymer PSD (drive-moments.m, odefunc.m, quad.m).

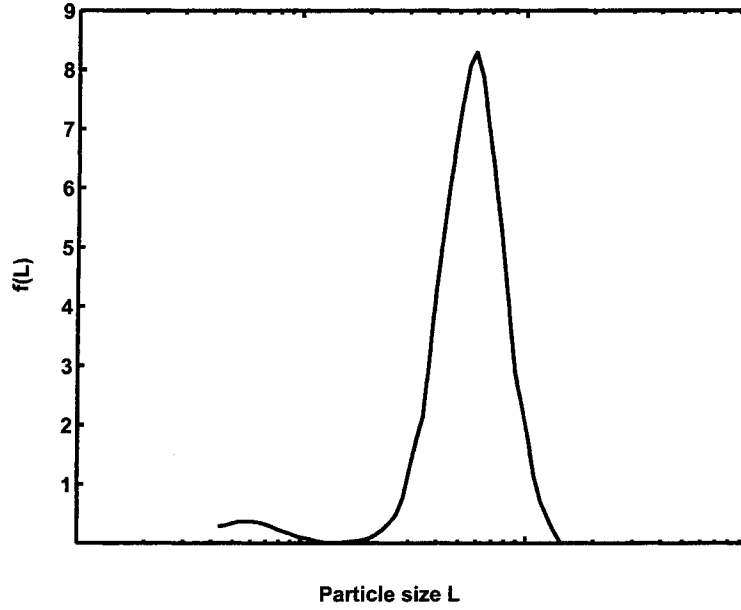


Figure 6.18 Catalyst particle size distribution.

$1.305570 \times 10^{-1} \text{ cm}$, $m_2 = 1.903549 \times 10^{-2} \text{ cm}^2$, $m_3 = 3.010876 \times 10^{-3} \text{ cm}^3$, $m_4 = 5.079755 \times 10^{-4} \text{ cm}^4$, $m_5 = 9.024098 \times 10^{-5} \text{ cm}^5$. The standard deviation (σ) of the polymer PSD and the “width” of the distribution can be calculated from those moments:

$$\sigma = \sqrt{(m_2 - m_1^2)},$$

$$c.v = \sigma/\bar{L} = \sqrt{(m_2 - m_1^2)}/m_1 = 0.34171.$$

If three nodes are used for representing the catalyst PSD, for the first node, the three nodes are $0.69d_{ave}$, $1.25d_{ave}$ and $2.03d_{ave}$. The evolutions of the particle size and temperature increase with age using three nodes are shown in Fig. 6.21 and Fig. 6.22 respectively. Similar to two nodes, the moments of this distribution can be calculated by:

$$m_{k,polymer} = \omega_1 m_{k1} + \omega_2 m_{k2} + \omega_3 m_{k3} \quad (6.42)$$

where $\omega_1 = 24.57\%$, $\omega_2 = 63.81\%$ and $\omega_3 = 11.62\%$. By integrating over the three curves in Fig. 6.21, the moments of the predicted size distribution are: $m_0 = 1.0$, $m_1 = 1.304596 \times 10^{-1} \text{ cm}$, $m_2 = 1.904223 \times 10^{-2} \text{ cm}^2$, $m_3 = 3.011871 \times 10^{-3} \text{ cm}^3$, $m_4 = 5.075125 \times 10^{-4} \text{ cm}^4$, $m_5 = 9.013480 \times 10^{-5} \text{ cm}^5$. The “width” of the distribution can be calculated from those moments,

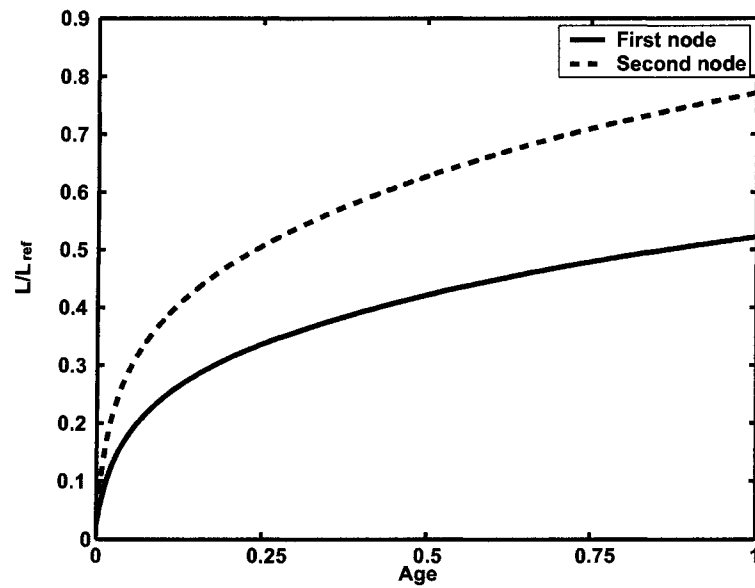


Figure 6.19 Evolution of particle diameters with age using two nodes for case 5.

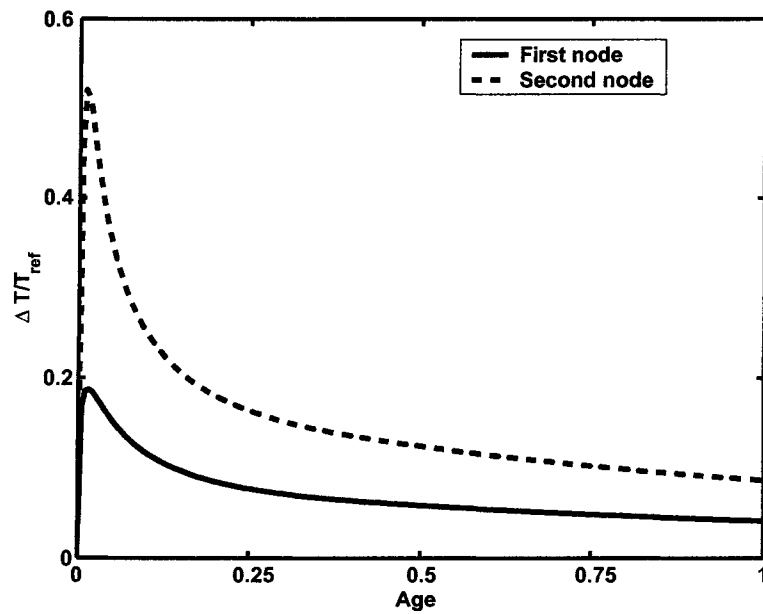


Figure 6.20 Evolution of particle temperature rise with age using two nodes for case 5.

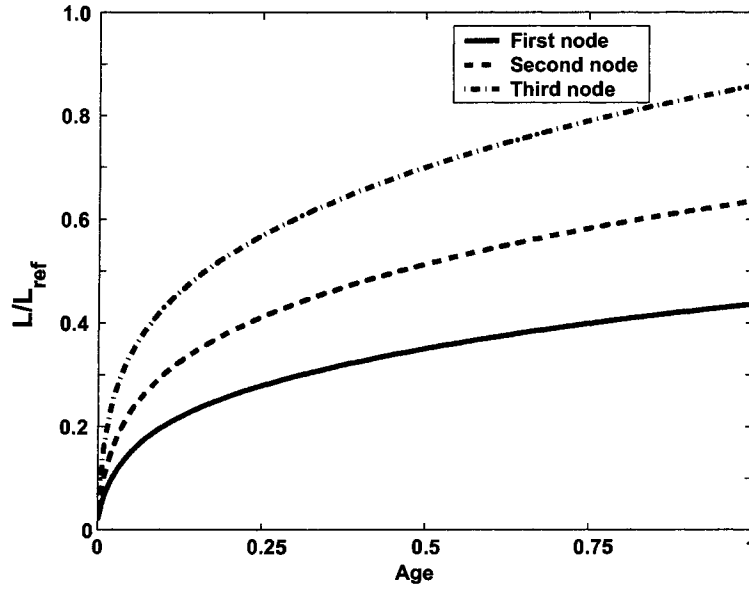


Figure 6.21 Evolution of particle diameters with age using three nodes for case 5.

and

$$c.v = \sigma/\bar{L} = \sqrt{(m_2 - m_1^2)/m_1} = 0.34472.$$

Note that these moments are slightly different than those found earlier with two nodes. Presumably, using three nodes should yield higher accuracy because it should yield a better representation of the log-normal distribution of catalyst PSD. And also notice that, the highest relative temperature increase by using three nodes is around 0.9, it is much higher than the highest relative temperature increase using two nodes, around 0.56. So using one or two nodes to represent the underlying distribution underestimates the overheating problem in the bed. Thus in future discussions, the catalyst PSD is represented by three nodes.

Some moments have special meaning, such as m_0 represent the total particle number density, in here m_0 is normalized to a unity. m_1 indicates the average particle size, m_2 is related to the particle area and m_3 is related to the total particle volume. In the simulations, in order to compare the results with experimental polymer PSD data, m_1 the average particle size is matched to the experimental value by changing the initial catalyst site concentration. According to the size distribution data obtained from Malvern's particle size analyzer, the moments

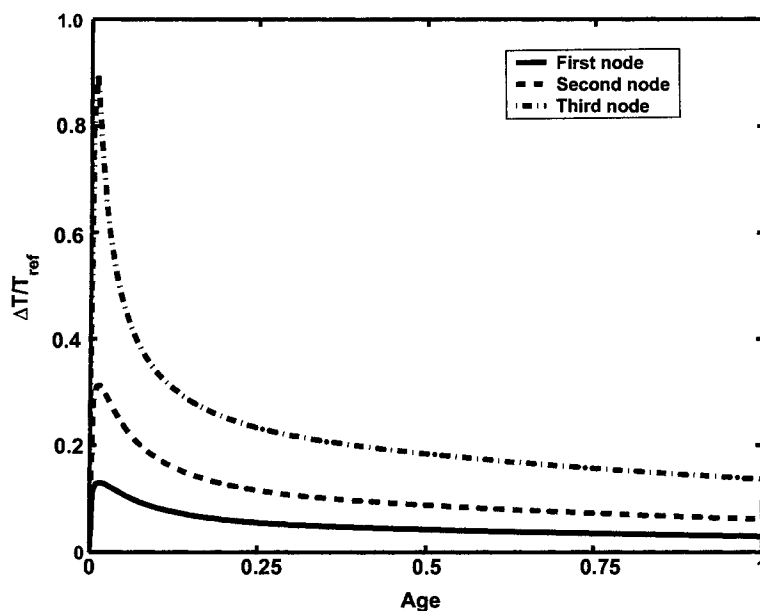


Figure 6.22 Evolution of particle temperature rise with age using three nodes for case 5.

for the final polymer are: $m_0 = 1.0$, $m_1 = 1.297835 \times 10^{-1} \text{cm}$, $m_2 = 1.852021 \times 10^{-2} \text{cm}^2$, $m_3 = 2.854163 \times 10^{-3} \text{cm}^3$, $m_4 = 4.678335 \times 10^{-4} \text{cm}^4$, $m_5 = 8.054136 \times 10^{-5} \text{cm}^5$. The “width” in this case is:

$$c.v = \sigma/\bar{L} = \sqrt{(m_2 - m_1^2)/m_1} = 0.31548.$$

Comparing the PSD from the reaction engineering model with the experimental data, the prediction overall is good, but the simulation has a higher standard deviation and larger width. This difference may be due to the assumption that the particles are well mixed (i.e., no segregation due to size), or due to how the experimental PSD is measured (i.e., at the outlet or taken from samples higher up in the bed).

The particle size distribution probability plot for the initial catalyst PSD and the final polymer PSD are shown in Fig. 6.23 as a solid line. The cumulative percent estimated from QMOM (three nodes for final polymer distribution) using two or three nodes to represent underlying catalyst distribution are also shown in Fig. 6.23 as symbols. We can see that the model predicts slightly larger particles as compared to the experimental data. Nevertheless, the overall predictions appear to be very good, indicating that combining the reaction engineering

model with QMOM is a promising method for predicting the polymer PSD in a PE reactor. The moments calculated from catalyst PSD (either using 2 or 3 nodes) are very similar. However, with three nodes to represent the catalyst PSD, we find a higher temperature increase for the final node. (Compare Figs. 6.20 and 6.22). The temperature profile in the bed is affected by the catalyst PSD. The larger the mean catalyst size, the larger the final polymer particle and the higher peak temperature increase in the solid phase. Also the breadth of catalyst PSD are important, since when the “width” increase, the nodes are more widely distributed and the biggest node have high chance to be overheated. Thus, in order to investigate the hot spots in the bed it is very crucial to represent the upper tail of the catalyst size distribution using QMOM. As we can see in Fig. 6.23, the tail is most accurately represented in QMOM by using $N=3$ (or more) nodes, so three nodes are choose in the following work. With Fig. 6.21 and 6.22, the information on the percentage of polymer particle above a certain temperature can be determined and it is plotted in Fig. 6.24. The graph shows for case 5, only less than 0.1% polymer’s relative temperature increase is over 0.6 and most polymer particle’s relative temperature increase (about 97%) is low, only 0-0.2. Such graphs are very useful in designing catalyst in industrial in future and the catalyst is designed to control the percentage of overheating particles in the range of 1-5%.

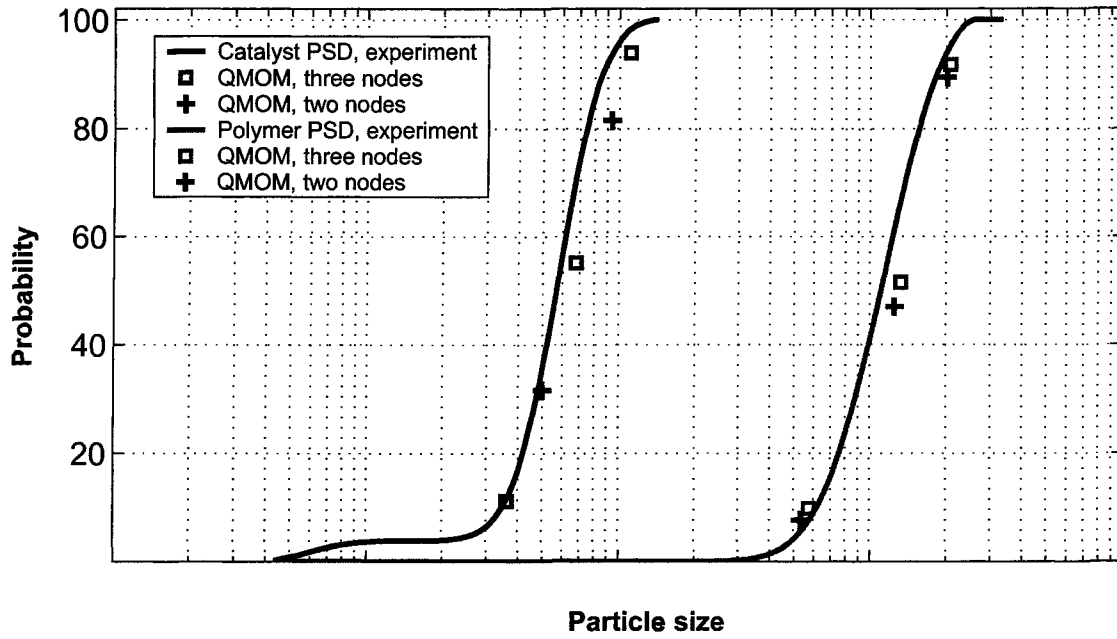


Figure 6.23 Comparison of PSD of catalyst and polymer with predicted PSD from QMOM using two nodes or three nodes for case 5.

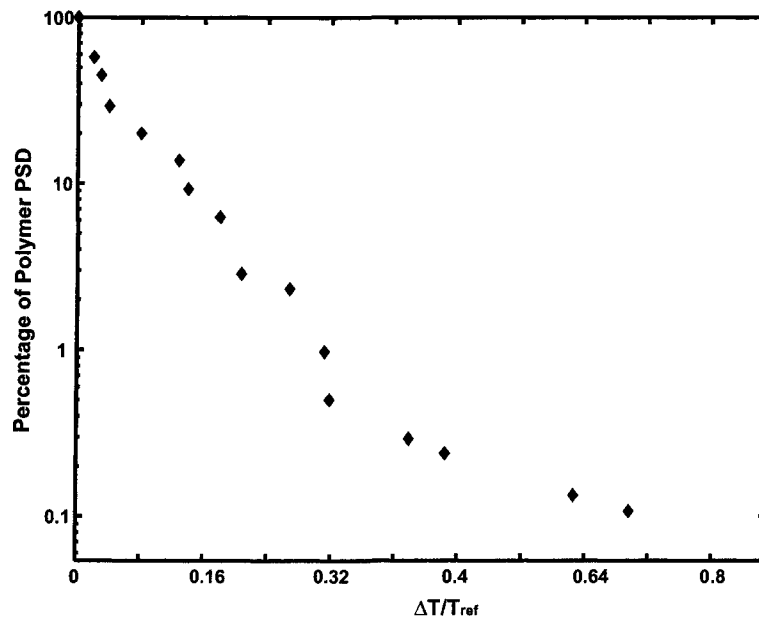


Figure 6.24 Percentage of polymer particle above a certain temperature for case 5.

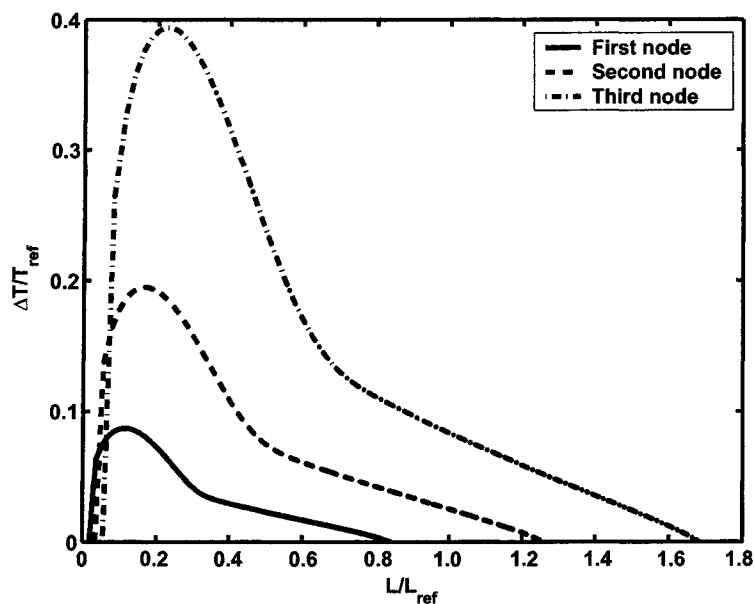


Figure 6.25 Evolution of particle temperature rise with particle size using three nodes for case 1.

6.3.4 Effect of Intrinsic Kinetics on the Overheating and Final Polymer PSD

Combining the CRE model and QMOM, it is possible to study the effect of intrinsic kinetics on the temperature rise of a growing polymer particle. The evolution of particle temperature rise with particle size using three nodes for cases 1-5 are plotted in Figs 6.25-6.29. As we can see, the temperature rise profile are different for each case, case 5 is the worst case for particle overheating, the relative temperature rise is about 0.9 for the biggest node. Case 4 has the lowest temperature rise compared to other cases. Also notice in the graphs, the intrinsic kinetics affects the final polymer PSD. Case 1 and 4 tend to produce larger particles than other cases, and the largest relative sized particle is around 1.8. The final polymer PSD predicted from CRE model for all the cases are compared with experimental data (case 5) in Fig 6.30. Similar to case 5, the model predicts slightly larger particles as compared to the experimental data, but overall, the prediction is good.

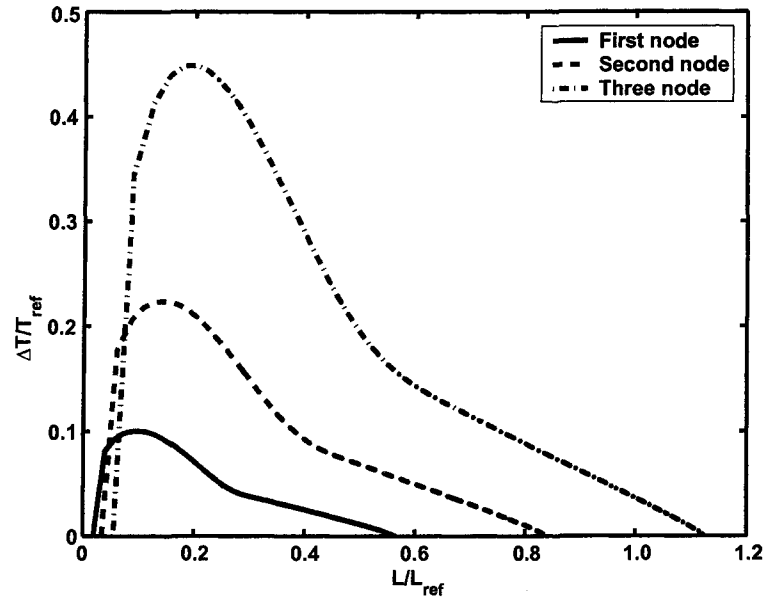


Figure 6.26 Evolution of particle temperature rise with particle size using three nodes for case 2.

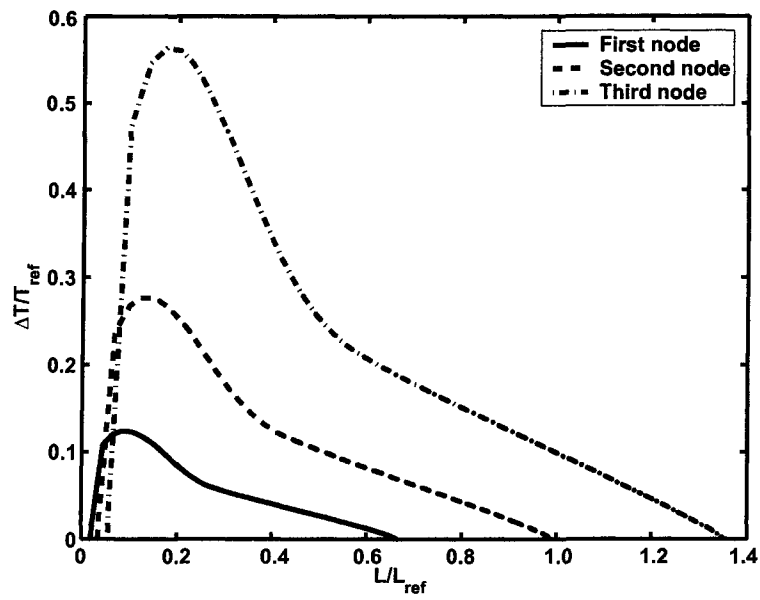


Figure 6.27 Evolution of particle temperature rise with particle size using three nodes for case 3.

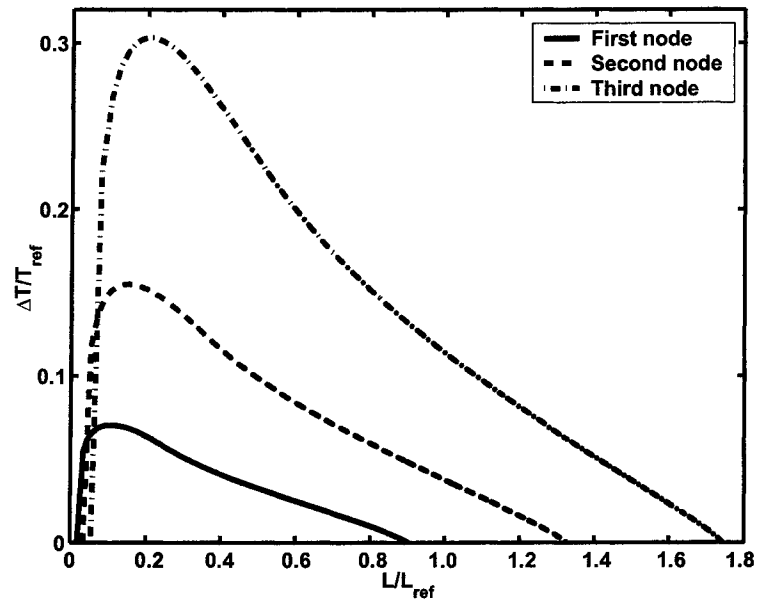


Figure 6.28 Evolution of particle temperature rise with particle size using three nodes for case 4.

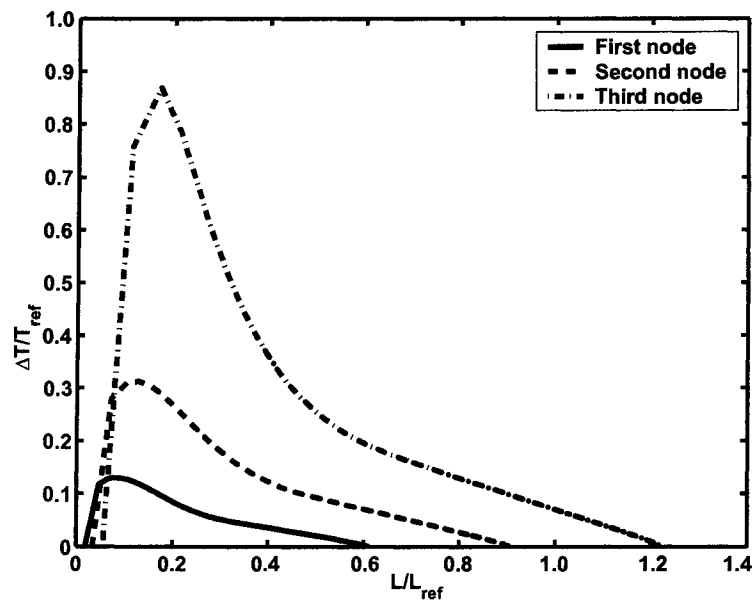


Figure 6.29 Evolution of particle temperature rise with particle size using three nodes for case 5.

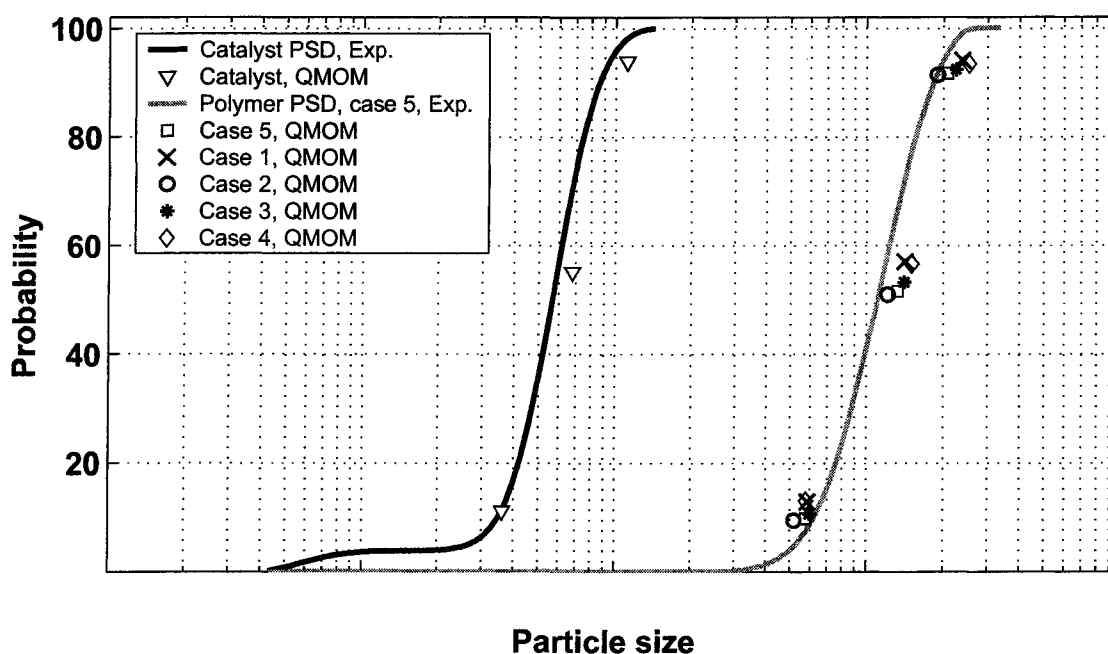


Figure 6.30 Comparison of PSD of catalyst and polymer with predicted PSD from QMOM using three nodes for case 1 to case 5.

6.3.5 Investigation of Particle Segregation and Hot Spots in a Fluidized Bed Using CFD

After successfully predicting the final polymer PSD, the moments are known, using QMOM, the PSD can be represented by two or three nodes in the CFD code to investigate the segregation and “hot spots”. Since case 5 is the worst case for the overheating, the following discussion uses the kinetic rate data from this case. For case 5, the predicted moments for the final polymer PSD are: $m_0 = 1.0$, $m_1 = 1.304596 \times 10^{-1} \text{ cm}$, $m_2 = 1.904223 \times 10^{-2} \text{ cm}^2$, $m_3 = 3.011871 \times 10^{-3} \text{ cm}^3$, $m_4 = 5.075125 \times 10^{-4} \text{ cm}^4$, $m_5 = 9.013480 \times 10^{-5} \text{ cm}^5$. Using the PD algorithm, three nodes can be used to represent this PSD, they are 0.288, 0.664 and 1.038 (dimensionless by L_{ref}). For each node, according Fig. 6.29, the temperature and age associated with this node are listed in Table. 6.5. Since in CFD simulation, we are not able to track the age time of a particle, for each particle size the highest possible relative temperature rise is 0.616, 0.172 and 0.06, the lowest possible temperature rise is 0.052, 0.056 and 0.06, and the average temperature rise is 0.285, 0.114 and 0.06.

Table 6.5 Relative temperature rise and age associated with each node

Node	Relative particle diameter	Relative temperature increase	Relative age
$\alpha = 1$	0.288	0.616	0.0275
		0.188	0.0875
		0.052	0.28
$\alpha = 2$	0.664	0.172	0.39
		0.056	1.145
$\alpha = 3$	1.038	0.06	1.995

A 3D simulation was run in the pilot scale fluidized bed with these three nodes, and the average particle size (normalized by the average particle size in the bed) along the bed height is plotted in Fig. 6.31, not much segregation was observed at the bottom of the bed, and the average particle size at the bottom is only about 1.1 times of the average size for the whole bed. However, most segregation is observed in the expansion and dome area. The average particle size at the top is only 50%-60% of the average particle size in the bed. Since we know that most sheeting problem happen in the expansion area, the number of particles for each node at this region are plotted in Fig. 6.32. From the graph, it is clearly to see that small particles are dominated in the expansion area. Although the number of small particles are very small (less than 50), small particles have high temperatures, hot spots are more likely to be observed. The average particle temperature rise profile for this simulation at 15 s is shown in Fig. 6.33 and the average solid temperature T_s is:

$$T_s = \frac{T_{s1}\omega_1 + T_{s2}\omega_2 + T_{s3}\omega_3}{\omega_1 + \omega_2 + \omega_3}. \quad (6.43)$$

From the graph, we can see that in the main reaction area, the temperature is almost uniform and without hot spots. However, in the expansion region, the average particle temperature are much higher. Those information will help us on locating the possible “hot spots” and agglomeration in the fluidized bed in the future.

6.4 Conclusion

2D and 3D simulations are conducted for a pilot-scale fluidized bed to validate the fluid dynamics. The simulations results for bed height, pressure drop along the two pressure taps

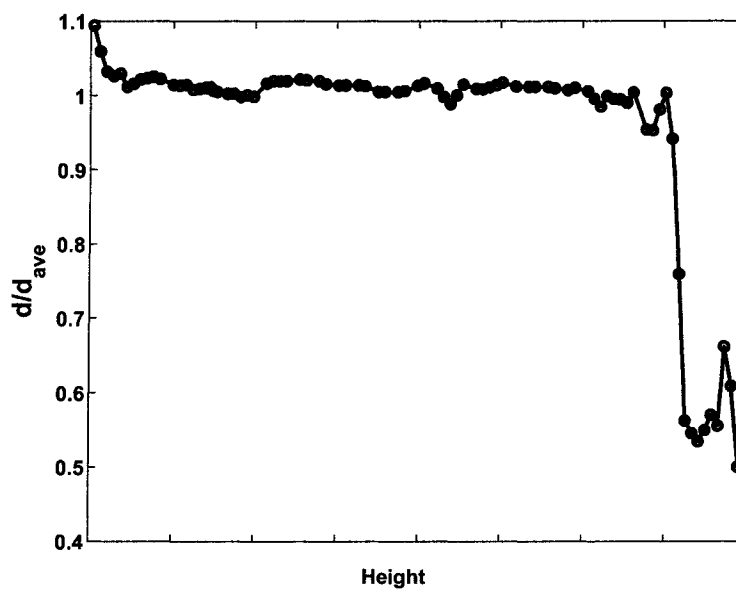


Figure 6.31 Average particle size along the bed height.

and pressure fluctuation signal are compared with available experimental data. Significant differences are observed between 2D and 3D simulations. The results shows that, for an industrial-scale fluidized bed, only 3D simulations are able to match statics (bed height and pressure drop) and the dynamics (pressure power spectra) properties of FB because of the natural three dimensionality of the flow. The 3D simulations have good agreement with experiment data on the bubble frequency and can describe the dynamic movement of the particles in the fluidized bed. Due to the different time scale for polymerization reaction and fluid dynamics, the polymerization reaction is solved outside of CFD simulation. The CRE model is solved in Matlab using the ODE solver, and the particle size, age and temperature distribution at steady state can be determined with this model. The catalyst PSD is represented by a few nodes using QMOM. Combining CRE and DQMOM, the final polymer PSD can be predicted with higher accuracy. Then a 3D simulation is conducted from this steady state and segregation and hot spots in the fluidized bed are investigated in the CFD simulation. For future work, the 3D simulation should incorporate the population balance to investigate aggregation and breakage of polymer particles. In a later stage, the electrical force component will also be incorporated into the multi-fluid model to determine the effect of particle charging

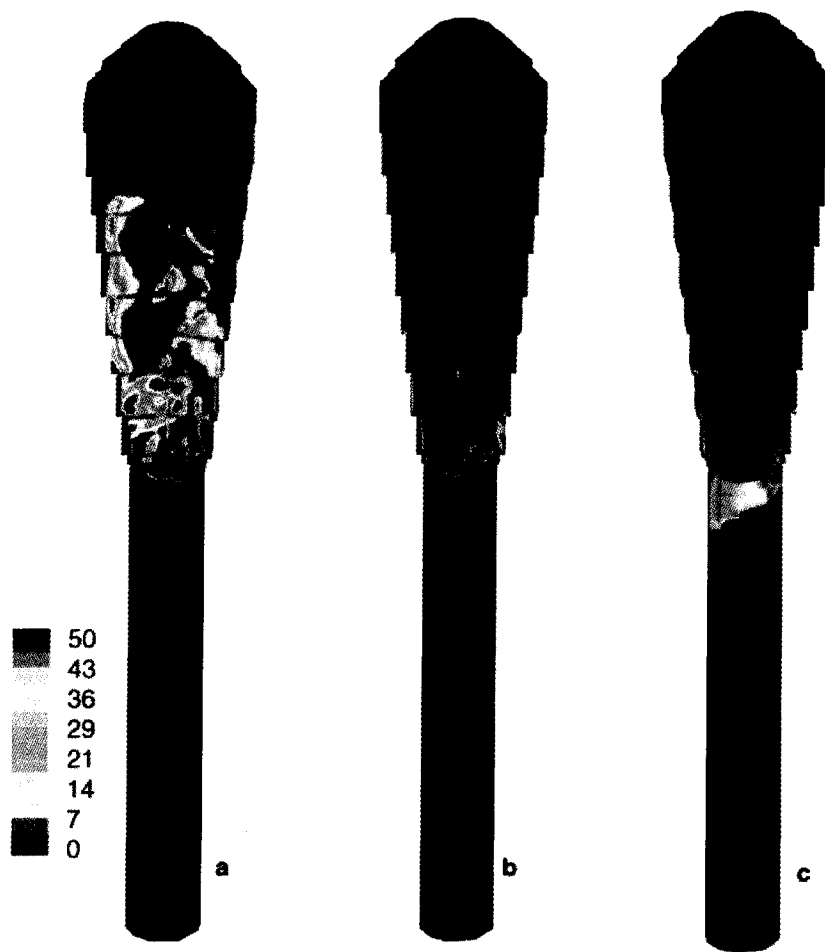


Figure 6.32 The number of particles for each node at 15 s, a: first node b: second node c: third node.

on the particle size distribution and overheating. After the work on validation of pilot-scale PE polymerization reactor, the validation on the commercial fluidized bed will be undertaken.

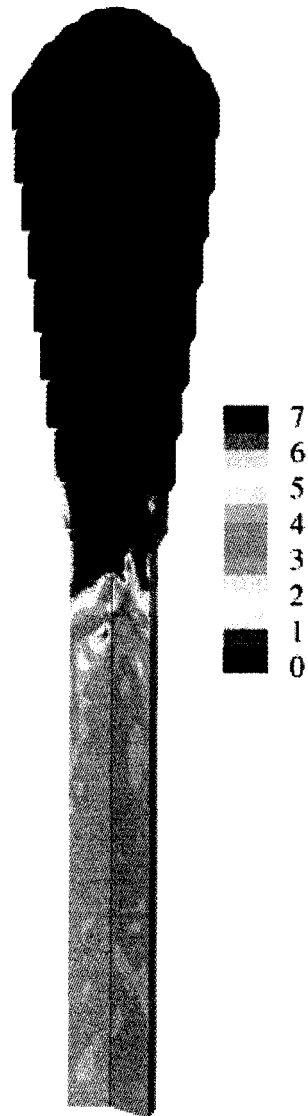


Figure 6.33 Average particle temperature rise profile at 15 s.

CHAPTER 7. Conclusion and Future Work

Gas-phase reactors are widely used in the polymerization industry due to their superior heat- and mass-transfer characteristics. However the detailed mathematical modeling of polymerization FB reactors is very complex and poses many challenges for us. In this work, a CFD algorithm for simulation of FB polymerization reactors is described. In order to rigorously account for the particle related phenomena, such as aggregation, breakage and growth, PBE must be solved along with other equations to describe the distribution of particle size in the bed. A novel approach - DQMOM is applied to polydisperse fluidized bed to solve PBE efficiently and effectively. DQMOM is an extension of QMOM, and also based on the solution of the PBE through its moments. However, compared to QMOM, each node has its own velocity, make it easily to implement into multi-phase CFD code. The DQMOM-Multi-Fluid model is developed by applying moment approach to the PBE for multi-fluid phase. For simplicity, the model is tested in a cold bed without chemical reaction, and the PSD change only due to aggregation and breakage. Simulation results show that the DQMOM-multi-fluid model is an effective approach to represent the evolution of the PSD due to aggregation and breakage in FB reactors. Constant aggregation and breakage kernel and the kernel developed from kinetic theory are implemented. Results show that the model predictions are very similar results for $N = 2-4$, however, for some cases, using three or four nodes produced similar results which are different than those found in two nodes. Considering the computational time increased with more nodes used, three nodes appears to be a good choice for representing FB reactors. The effect of the success factor for aggregation was also investigated for the kinetic theory kernel, a high success factor for aggregation leads to a shorter time for reaching defluidization. The effect of fragment distribution function is also studied. The results show that erosion causes a

delay in the dynamic response of the mean particle size compared to symmetric fragmentation. Erosion is a less effective breakage mechanism in the presence of aggregation.

After successfully developed the multi-fluid CFD model for polydisperse gas-solid flow, the next step is to valid the multi-fluid model with available experiments and simulation results to describe the mixing and segregation behavior in the gas-phase reactor. The multi-fluid model for polydisperse fluidized beds was studied for a binary system and a few systems with continuous PSD. The CFD simulations for the binary system are compared with the experiments conducted by Goldschmidt et al. (2003) for glass beads, the simulation results agree satisfactorily with the experimental data. At high gas velocity, the fluidized bed is fully fluidized so that excellent mixing is achieved and the segregation rate is low, around 0.1. In an intermediate gas-velocity range, transient fluidization takes place where in the bed is initially uniformly fluidized and then segregation gradually occurs. In the end, the large particles go to the bottom and the small particles move to the top so that there is a defluidized bottom rich in jetsam and a top layer rich in flotsam. The relative segregation rate is also much higher (usually around 0.3-0.4).

With the good agreement between simulation and experimental data for binary systems, segregation phenomena in gas-solid fluidized beds with a continuous PSD are investigated. For this study, the simulation results are compared with the discrete-particle simulations of Dahl and Hrenya (2005). Using the moments of the PSD from the discrete-particle simulations, the weights and abscissas (or nodes) used in DQMOM are initialized in the multi-fluid model. The segregation rate and the local moments of the PSD predicted by the multi-fluid model are compared to the discrete-particle simulations. Four systems are choose to do the comparison. The first three systems had a Gaussian distribution. System 1 had a wide distribution with $\sigma/d_{ave} = 0.3$ and System 2 has the same distribution as System 1 but with a higher superficial gas velocity. System 3 had a narrow distribution with $\sigma/d_{ave} = 0.1$. The last system (System 4) had a log-normal distribution with $\sigma/d_{ave} = 0.5$. As expected, the wide Gaussian distribution showed more segregation than the narrow one, and the lognormal distribution showed the greatest segregation. Increasing superficial gas velocity generated more bubbles, better mixing,

and reduced the segregation. The results showed that the multi-fluid model can reproduce the segregation along the bed height, but can not reproduce the lateral segregation across the bed observed in DPS simulations. The effect of the node numbers was also studied. The results showed that, when the distribution was narrow or the superficial gas velocity was high, the mixing dominated the segregation, and less nodes were needed. For a wide distribution with strong segregation, at least three nodes were needed to represent the underlying distribution.

After the model development and validation for the polydisperse gas-solid flow, CFD validation of a PE pilot-scale gas-phase reactor is undertaken. 2D and 3D simulations are conducted for a pilot-scale fluidized bed to validate the fluid dynamics. The simulation results for bed height, pressure drop along the two pressure taps and pressure fluctuation signal are compared with available experimental data. Significant differences are observed between 2D and 3D simulations. The results show that, for an industrial-scale fluidized bed, only 3D simulations are able to match the statics (bed height and pressure drop) and the dynamics (pressure power spectra) properties of the bed because of the natural three dimensionality of the flow. The 3D simulations agree fairly well with experiment data on the bubble frequency and can describe the dynamic movement of the particles in the fluidized bed. For the next step, the polymerization reaction, heat/mass transfer model are developed for PE pilot-scale fluidized bed. The residence time for a PE pilot reaction is on the order of hours, and the fluid dynamics is on the order of seconds. It is impossible to run a three-dimensional simulation for hours using current CFD codes. Due to the different time scale between reaction and fluid dynamics, a CRE model based on the age of particles is used to initialize the fluidized bed to a steady state, which has a presumed distribution of particle size, age and temperature. The catalyst PSD is represented by a few nodes using QMOM. Combining CRE and QMOM, the final polymer PSD can be predicted with higher accuracy. Then a 3D simulation is conducted to investigate segregation and hot spots in the bed. Results show there is not much segregation in the main reaction area, and the temperature profile in the fluidized bed is almost uniform. However, most segregation appears in the expansion area and dome area. Small particles are dominated in this area and since small particles have high temperature, hot spots are observed in this

area.

For the future work, the CFD model for polydisperse reacting gas-solid flow with aggregation and breakage has been successfully developed, but need to be validated with available experimental data. Currently, a constant aggregation and breakage kernel and the kernel from kinetic theory are tested, the kernel depend on particle temperature need to be developed and tested. For the work on CFD validation of a PE pilot-scale fluidized bed, the 3D simulation should also incorporate the population balance to investigate aggregation and breakage of polymer particles. In a later stage, the electrical force component will also be incorporated into the multi-fluid model to determine the effect of particle charging on the particle size distribution and overheating. After the work on validation of pilot-scale PE polymerization reactor, the work will be extended to commercial fluidized bed to study the scale-up.

Bibliography

- Anderson, T. B., Jackson, R., 1967. A fluid mechanical description of fluidized beds. *Industrial Engineering and Chemical Fundamental* 6, 527.
- Arnarson, B. O., Willits, J. T., 1998. Thermal diffusion in binary mixtures of smooth, nearly elastic spheres with and without gravity. *Physics Fluids* 10, 1324.
- Balzer, G., Boelle, A., Simonin, O., 1995. Eulerian gas-solid flow modeling of dense fluidized bed. In: *Fluidization VIII*. Engineering Foundation, New York, p. 409.
- Barret, J. C., Webb, N. A., 1998. A comparison of some approximate methods for solving the aerosol general dynamic equation. *Journal of Aerosol Science* 29, 31.
- Bokkers, G. A., van Sint Annaland, M., Kuipers, J. A. M., 2004. Mixing and segregation in a bidisperse gas-solid fluidised bed: a numerical and experimental study. *Powder Technology* 140, 176.
- Burdett, I. D., Eisinger, R. S., Cai, P., Lee, K. H., 2001. Gas-phase fluidization technology for production of polyolefins. Internal Univation Report.
- Buwa, V. V., Ranade, V. V., 2002. Dynamics of gas-liquid flow in a rectangular bubble column: experiments and single/multi-group CFD simulation. *Chemical Engineering Science* 57, 4715.
- Choi, K. Y., Ray, W. H., 1985. The dynamic behavior of fluidized bed reactors for solid catalyzed gas phase olefine polymerization. *Chemical Engineering Science* 40, 2261.
- Cooper, S., Coronella, C. J., 2005. CFD simulations of particle mixing in a binary fluidized bed. *Powder Technology* 151, 27.

- Dahl, S. R., Hrenya, C. M., 2005. Size segregation in gas - solid fluidized beds with continuous size distributions. *Chemical Engineering Science* 60, 6658.
- Dartevelle, S., 2003. Numerical and Granulometric Approaches to Geophysical Granular Flows. Ph.D. thesis, Michigan Technological University, Houghton, Michigan.
- Debling, J. A., Ray, W. H., 1995. Heat and mass transfer effects in multistage polymerization processes: Impact polypropylene. *Industrial and Engineering Chemical Research* 34, 3466.
- Detle, H., Studden, W. J., 1997. *The Theory of Canonical Moments with Applications in Statistics, Probability and Analysis*. John Wiley & Sons, New York.
- Diemer, R. B., Olson, J. H., 2002. A moment methodology for coagulation and breakage problems: Part 2 - moment models and distribution reconstruction. *Chemical Engineering Science* 57, 2211.
- Enwald, H., Peirano, E., Almstedt, A. E., 1996. Eulerian two-phase flow theory applied to fluidization. *International Journal of Multiphase Flow* 22, 21.
- F. Taghipour, N. E., Wong, C., 2005. Experimental and computational study of gas-solid fluidized bed hydrodynamics. *Chemical Engineering Science* 60, 6857.
- Fan, L. S., Zhu, C., 1998. *Principles of Gas-Solid Flows*. Cambridge University Press, New York.
- Fan, R., Marchisio, D. L., Fox, R. O., 2004. Application of the direct quadrature method of moments to polydisperse gas-solid fluidized beds. *Powder Technology* 139, 7.
- Feng, Y. Q., Xu, B. H., Zhang, S. J., Yu, A. B., 2004. Discrete particle simulation of gas fluidization of particle mixtures. *AIChE Journal* 50, 1713.
- Fernandes, F. A. N., Lona, L. M. F., 2002. Heterogeneous modeling of fluidized bed polymerization reactors. Influence of mass diffusion into the polymer particle. *Computers and Chemical Engineering* 26, 841.

- Floyd, S., Choi, K. Y., Taylor, T. W., Ray, W. H., 1986. Polymerization of olefins through heterogeneous catalysis. iii. polymer particle modelling with an analysis of intraparticle heat and mass transfer effects. *Journal of Applied Polymer Science* 32, 2935.
- Formisani, B., Cristofaro, G. D., Girimonte, R., 2001. A fundamental approach to the phenomenology of fluidization of size segregating binary mixtures of solids. *Chemical Engineering Science* 56, 109.
- Foxely, D., 1998. Innovation in the gas phase. *Chemistry and Industry*, 20 April, 305–308.
- Garside, J., Al-Dibouni, M. R., 1977. Velocity-voidage relationships for fluidization and sedimentation. *Industrial and Engineering Chemistry Process Design and Development* 16, 206.
- Gera, D., Syamlal, M., O'Brien, T. J., 2004. Hydrodynamics of particle segregation in fluidized beds. *International Journal of Multiphase Flow* 30, 419.
- Gidaspo, D., 1994. *Multiphase Flow and Fluidization*. Academic Press, San Diego.
- Gobin, A., Neau, H., Simonin, O., Llinas, J.-R., Reiling, V., Sélo, J.-L., 2003. Fluid dynamic numerical simulation of a gas phase polymerization reactor. *International Journal for Numerical Methods in Fluid* 43, 1199.
- Goldschmidt, M., 2001. *Hydrodynamic Modeling of Fluidized Bed Spray Granulation*. Ph.D. thesis, Twente University, The Netherlands.
- Goldschmidt, M. J. V., Link, J. M., Mellema, S., Kuipers, J. A. M., 2003. Digital image analysis measurements of bed expansion and segregation dynamics in dense gas-fluidized beds, powder technology. *AIChE Journal* 138, 135.
- Gordon, R. G., 1968. Error bounds in equilibrium statistical mechanics. *Journal of Mathematical Physics* 9, 655.
- Hatzantonis, H., Goulas, A., Kiparissides, C., 1998. A comprehensive model for the prediction of particle-size distribution in catalyzed olefine polymerization fluidized-bed reactors. *Chemical Engineering Science* 53, 3251.

- Hatzantonis, H., Yiannoulakis, H., Yiagopoulos, A., Kiparissides, C., 2000. Recent developments in modeling gas-phase catalyzed olefin polymerization fluidized-bed reactors: The effect of bubble size variation on the reactor's performance. *Chemical Engineering Science* 55, 3237.
- Hendrickson, G., 2006. Electrostatics and gas phase fluidized bed polymerization reactor wall sheeting. *Chemical Engineering Science* 61, 1041.
- Hoel, E. L., Cozewith, C., Byrne, G. D., 1994. Effect of diffusion on heterogeneous ethylene propylene copolymerization. *AIChE Journal* 40, 1669.
- Hoffman, A. C., Romp, E. J., 1991. Segregation in a fluidized powder of a continuous size distribution. *Powder Technology* 66, 119.
- Hoffmann, A. C., Janssen, L. P. B. M., Prins, J., 1993. Particle segregation in fluidized binary mixtures. *Chemical Engineering Science* 48, 1583.
- Hoomans, B. P. B., Kuipers, J. A. M., Briels, W. J., van Swaaij, W. P. M., 1996. Discrete particle simulation of bubble and slug formulation in a two-dimensional gas-fluidized bed: A hard-sphere approach. *Chemical Engineering Science* 51, 99.
- Hoomans, B. P. B., Kuipers, J. A. M., van Swaaij, W. P. M., 2000. Granular dynamics simulation of segregation phenomena in bubbling gas-fluidised beds. *Powder Technology* 109, 41.
- Howley, M. A., Glasser, B. J., 2002. Hydrodynamics of a uniform liquid-fluidized bed containing a binary mixture of particles. *Chemical Engineering Science* 57, 4209.
- Hulburt, H. M., Katz, S., 1964. Some problems in particle technology. *Chemical Engineering Science* 19, 555.
- Hutchinson, R. A., Chen, C. M., Ray, W. H., 1992. Polymerization of Olefins through heterogeneous catalysis X: Modeling of particle growth and morphology. *Journal of Applied Polymer Science* 44, 1389.

- Hutchinson, R. A., Ray, W. H., 1987. Polymerization of olefins through heterogeneous catalysis. vii. particle ignition and extinction phenomena. *Journal of Applied Polymer Science* 34, 657.
- Ishii, M., 1975. *Thermo-Fluid Dynamic Theory of Two Phase Flow*. Direction des Etudes et Recherches d'Electricite de France, Eyrolles, Paris.
- Kaneko, Y., Shiojima, Y. T., Horio, M., 1999. DEM simulation of fluidized beds for gas-phase olefin polymerization. *Chemical Engineering Science* 54, 5809.
- Kim, J. Y., Choi, K. Y., 2001. Modeling of particle segregation phenomena in a gas phase fluidized bed olefin polymerization reactor. *Chemical Engineering Science* 56, 4069.
- Kuipers, J. A. M., van Duin, K. J., van Beckum, F. B. H., 1992. A numerical model of gas-fluidized beds. *Chemical Engineering Science* 47, 1913.
- Kuwagi, K., Horio, M., 2002. A numerical study on agglomerate formation in a fluidized bed of fine cohesive particles. *Chemical Engineering Science* 57, 4737.
- Lebowitz, J. L., 1964. Exact solution of generalized Percus-Yevick equation for a mixture of hard spheres. *Physics Review A* 133, 895.
- Lee, K., Matsoukas, T., 2000. Simultaneous coagulation and break-up using constant-N Monte Carlo. *Powder Technology* 110, 82.
- Lehr, F., Mewes, D., 2001. A transport equation for the interfacial area density applied to bubble columns. *Chemical Engineering Science* 56, 1159.
- Lo, S., 1996. Application of population balance to CFD modeling of bubbly flow via the Musig model. AEA Technology, AEAT-1096.
- Lu, H., He, Y., Gidaspo, D., Yang, L., Qin, Y., 2003. Size segregation of binary mixture of solids in bubbling fluidized beds. *Powder Technology* 134, 86.
- Lun, C. K. K., Savage, S. B., Jeffrey, D. J., Chepur, N., 1984. Kinetic theories for granular flow: inelastic particles in Couette flow and slightly inelastic particles in a general flow field. *Journal of Fluid Mechanics* 223, 140.

- Madec, L., Falk, L., Plasari, E., 2001. Simulation of agglomeration reactors via a coupled CFD/direct Monte-Carlo method. *Chemical Engineering Science* 56, 1731.
- Madec, L., Falk, L., Plasari, E., 2003. Modeling of the agglomeration in suspension process with multidimensional kernels. *Powder Technology* 130, 147.
- Maggioris, D., Goulas, A., Alexopoulos, A. H., Chatzi, E. G., Kiparissides, C., 1998. Use of CFD in prediction of particle size distribution in suspension polymer reactors. *Computers and Chemical Engineering* 22, 315.
- Marchisio, D. L., Fox, R. O., 2005. Solution of population balance equations using the direct quadrature method of moments. *Journal of Aerosol Science* 36, 43.
- Marchisio, D. L., Pikturna, J. T., Fox, R. O., Vigil, R. D., Barresi, A. A., 2003a. Quadrature method of moments for population-balance equations. *AIChE Journal* 49, 1266.
- Marchisio, D. L., Vigil, R. D., Fox, R. O., 2003b. Quadrature method of moments for aggregation-breakage processes. *Journal of Colloid and Interface Science* 258, 322.
- Marzoccella, A., Salatino, P., Pastena, V. D., Lirer, L., 2000. Transient fluidization and segregation of binary mixtures of particles. *AIChE Journal* 46, 2175.
- Mathiesen, V., Solberg, T., Hjertager, B. H., 2000. Predictions of gas/particle flow with an eulerian model including a realistic particle size distribution. *Powder Technology* 112 (34).
- McAuley, K. B., Talbot, J. P., Harris, T. J., 1994. A comparison of two phase and well-mixed models for fluidized-bed polyethylene reactors. *Chemical Engineering Science* 49, 2035.
- McGraw, R., 1997. Description of aerosol dynamics by the quadrature method of moments. *Aerosol Science and Technology* 27, 255.
- Mckenna, T. F., Soares, J. B. P., 2001. Single particle modelling for olefin polymerization on supported catalysts: A review and proposals for future developments. *Chemical Engineering Science* 56, 3931.

- Mckenna, T. F., Spitz, R., Cokljat, D., 1999. Heat transfer from catalysts with computational fluid dynamics. *AIChE Journal* 45, 2392.
- Mehrani, P., Bi, H. T., Grace, J. R., 2005. Electrostatic charge generation in gas-solids fluidized beds. *Journal of Electrostatics* 63, 165.
- Nienow, A. W., Naimer, N. S., Chiba, T., 1987. Studies of segregation/mixing in fluidized beds of different size particles. *Chemical Engineering Science* 62, 52.
- Olmos, E., Gentric, C., Vial, C., Wild, G., Midoux, N., 2001. Numerical simulation of multiphase flow in bubble column reactors. influence of bubble coalescence and break-up. *Chemical Engineering Science* 56, 6359.
- Park, A. A., Bi, H. T., Grace, J. R., Chen, A., 2002. Modelling charge transfer and induction in gas-solid fluidized beds. *Journal of Electrostatics* 55 (135).
- Patankar, S. V., 1980. *Numerical Heat Transfer and Fluid Flow*. Hemisphere Publishing Corporation, New York.
- Peirano, E., Delloume, V., Leckner, B., 2001. Two- or three- dimensional simulations of turbulent gas-solid flow applied to fluidization. *Chemical Engineering Science* 56, 4787.
- Ramakrishna, D., 2000. *Population Balances*. Academic Press, London.
- Randolph, A. D., Larson, M. A., 1971. *Theory of Particulate Processes: Analysis and Techniques of Continuous Crystallization*. Academic Press.
- Schaeffer, D. G., 1987. Instability in the evolution equations describing incompressible granular flow. *Journal of Differential Equations* 66, 19.
- Schmeal, W. R., Street, J. R., 1971. Polymerization in expanding catalyst particles. *AIChE Journal* 17, 1189.
- Smith, M., Matsoukas, T., 1998. Constant-number Monte Carlo simulation of population balances. *Chemical Engineering Science* 53, 1777.

- Song, H., 2004. Bounds on Operating Conditions Leading to Melting during Olefin Polymerization. Ph.D. thesis, University of Houston, Houston, Texas.
- Spalding, D. B., 1980. Numerical computation of multiphase fluid flow and heat transfer. In: Recent Advances in Numerical Methods in Fluids. Pineridge Press.
- Sun, Q., Lu, H., Liu, W., He, Y., Yang, L., Gidaspow, D., 2005. Simulation and experiment of segregation/mixing of rice husk-sand mixture in a bubbling fluidized bed. *Fuel* 84, 1739.
- Syamlal, M., 1987. The particle-particle drag term in a multiparticle model of fluidization. DOE/MC/21353-2373, NTIS/DE87006500.
- Syamlal, M., 1998. MFIx Documentation: Numerical Technique. DOE/MC31346-5824, U. S. Department of Energy, Morgantown, WV.
- Syamlal, M., O'Brien, T. J., 1988. Simulation of granular layer inversion in liquid fluidized beds. *International Journal of Multiphase Flow* 14, 473.
- Syamlal, M., Rogers, W., O'Brien, T. J., 1993. MFIx Documentation: Theory Guide. U. S. Department of Energy, Morgantown, WV.
- Tsuji, Y., Kawaguchi, T., Tanaka, T., 1993. Discrete particle simulation of two-dimensional fluidized bed. *Powder Technology* 77, 79.
- van Wachem, B. G. M., Schouten, J. C., van den Bleek, C. M., Krishna, R., Sinclair, J. L., 2001. Comparative analysis of CFD models of dense gas-solid systems. *AICHE Journal* 47, 1035.
- Veera, U. P., Weickert, G., Agarwal, U. S., 2002. Modeling monomer transport by convection during olefin polymerization. *AICHE Journal* 48, 1062.
- Venneker, B. C. H., Derksen, J. J., van den Akker, H. E. A., 2002. Population balance modeling of aerated stirred vessels based on cfd. *AICHE Journal* 48, 673.
- Wen, C. Y., Yu, Y. H., 1966. Mechanics of fluidization. *Chemical Engineering Progress Symposium Series* 62, 100.

- Wormsbecker, M., Adams, A., Pugsley, T., Winters, C., 2005. Segregation by size difference in a conical fluidized bed of pharmaceutical granulate. *Powder Technology* 153, 72.
- Wu, S. Y., Baeyens, J., 1998. Segregation by size difference in gas fluidized beds. *Powder Technology* 98, 139.
- Xie, T., McAuley, K. B., Hsu, J. C. C., Bacon, D. W., 1994. Gas phase ethylene polymerization: Production processes, polymer properties, and reactor modeling. *Industrial Chemistry Research* 33, 449.
- Yao, K. Z., McAuley, K. B., Marchildon, E. K., 2003. Simulation of continuous solid-phase polymerization of nylon 6,6 (iii): simplified model, Preprint.
- Yiannoulakis, H., Yiagopoulos, A., Kiparissides, C., 2001. Recent developments in the particle size distribution modeling of fluidized-bed olefin polymerization reactors. *Chemical Engineering Science* 56, 917.

ACKNOWLEDGEMENTS

I would like to take this opportunity to express my thanks to those who helped me with various aspects of conducting research and the writing of this thesis. First and foremost, Dr. Rodney O. Fox for his guidance, patience and support throughout this research and the writing of this thesis. His insights and words of encouragement have often inspired me and renewed my hopes for completing my graduate education. I would also like to thank my committee members for their efforts and contributions to this work: Dr. David K. Hoffman, Dr. James C. Hill, Dr. Dennis R. Vigil and Dr. Francine Battaglia. I would like to thank Dr Daniele Marchisio's participation and discussions in the modeling development. It is a great pleasure to work with him and he is an inspiration of my professional life. I would like to thank Dr. Michael Muhle's insightful discussion and suggestions on the project with Univation Technologies. A warm thanks goes to the people who worked in Dr Fox's group: Sarah, Ying, Liguang, Sean, Mothi, Venkat, Alessandro, Vivek, Nitin, Anup and Chungying. You make the life at Ames much more enjoyable. Especially thank my officemate, Sarah's help on English editing and nice talks we had in the offices. Also I would like to thank Sean's help on using Matlab and Ying's discussion on research and life. At last, I would like to thank my friends at ISU and other universities and family for their support and encouragement during the good and difficult time of my graduate study. Without you, I would not be able to achieve any of my goals.

The financial supports from the National Energy Technology Laboratory of the U.S. Department of Energy and Univation Technologies are gratefully acknowledged. This work was performed at Ames Laboratory under Contract No. W-7405-Eng-82 with the U.S. Department of Energy. The United States government has assigned the DOE Report number IS-T2045 to this thesis.

APPENDIX Matlab codes used in Chapter 6

Calculate the lengths and weights of a PSD using PD algorithm. (quad.m)

```

%%%%%%%%%%%%%%%%%%%%%%%%%%%%%%%%%%%%%%%%%%%%%%%%%%%%%%%%%%%%%%%%%%%%%%%%
% Subroutine to calculate the lengths and weights of a PSD using PD algorithm.  %
% Input: First n moments: m                                                    %
%       Number of nodes: n/2                                                  %
% Output: Length of each node: a(n/2)                                         %
%       Weight of each node: w(n/2)                                           %
%%%%%%%%%%%%%%%%%%%%%%%%%%%%%%%%%%%%%%%%%%%%%%%%%%%%%%%%%%%%%%%%%%%%%%%%
function [a,w]=quad(m,n)
p(1,1)= 1.0;
for i=2:n+1
    p(i,1)=0.0;
end
for i=1:n
    p(i,2)=(-1)^(i-1)*m(i);
end
for j=3:n+1
    for i=1:n+2-j
        p(i,j)=p(1,j-1)*p(i+1,j-2)-p(1,j-2)*p(i+1,j-1);
    end
end
alfa(1)=0.0;
for i=2:n
    if p(1,i)*p(1,i-1)>0.0
        alfa(i)=p(1,i+1)/(p(1,i)*p(1,i-1));
    else
        alfa(i)=0.0;
    end
end
end

```

```

for i=1:n/2.
    z(i,i)=alfa(2*i)+alfa(2*i-1);
end
for i=1:n/2.-1.
    z(i,i+1) = -(abs(alfa(2*i+1)*alfa(2*i)))^0.5;
    z(i+1,i) = -(abs(alfa(2*i+1)*alfa(2*i)))^0.5;
end
[autovettori,autovalori]=eig(z);

for i=1:n/2.
    w(i)=autovettori(1,i)^2*m(1);
end
for i=1:n/2.
    a(i)=autovalori(i,i);
end

```

Two site model fitting. [drive_fitting.m, objfunc.m, odefunc.m]

```

%%%%%%%%%%%%%%%%%%%%%%%%%%%%%%%%%%%%%%%%%%%%%%%%%%%%%%%%%%%%%%%%%%%%%%%%
% Main program for two site model fitting, drive_fitting.m %
%%%%%%%%%%%%%%%%%%%%%%%%%%%%%%%%%%%%%%%%%%%%%%%%%%%%%%%%%%%%%%%%%%%%%%%%

clear all
close all
clc
format long

% Load experiment data experiment_hh, the first element is time t(min), and the
% second, third, fourth elements are the reaction rate at low, middle and high
% temperature, then put them into t_matrix and y_matrix.

load experiment_c.dat; t=experiment_c(:,1)/60.0;
y1=experiment_c(:,2); y2=experiment_c(:,3); y3=experiment_c(:,4);
w=[1,1,1]; t_matrix=[t,t,t]; y_matrix=[y1,y2,y3];

% Input: Initial guess for the rate constant and activation energy for site 1 and 2
% Site 1: ke0(1)=k_i, ke0(2)=k_d, ke0(3)=k_p,
%         ke0(4)=delta_E_i, ke0(5)=delta_E_d, ke0(6)=delta_E_p
% Site 2: ke0(7)=k_i, ke0(8)=k_d, ke0(9)=k_p,
%         ke0(10)=delta_E_i, ke0(11)=delta_E_d, ke0(12)=delta_E_p
ke0=[];

```

```

% Output: Return the final value for ke and resnorm (squared 2-norm of the residual)
% using toolbox-lsqcurvefit

[ke,resnorm,residual,exitflag]=lsqcurvefit(@objfunc,ke0,t_matrix,y_matrix);
ke
resnorm;

%%%%%%%%%%%%%%%%%%%%%%%%%%%%%%%%%%%%%%%%%%%%%%%%%%%%%%%%%%%%%%%%%%%%%%%%
% Plot three fitting curves and compared with experimental data %
%%%%%%%%%%%%%%%%%%%%%%%%%%%%%%%%%%%%%%%%%%%%%%%%%%%%%%%%%%%%%%%%%%%%%%%%

% Input data
% tspan: time,
% C and a: constants, explained in Chapter 6
% d0:initial catalyst diameter
% eps0 and c0:initial solid void fraction and initial concentration
% pgm: effect of pressure
% DeA: effective diffusivity
% T1 T2 T3: low, middle and high temperature

tspan=t_matrix(:,1); C=; a=; d0=; eps0=(d0)^3.0*pi/6.0*C;
c0=(d0)^3.0*pi/6.0; pgm=; DeA=; T1=; T2=; T3=;

% Initial value for y0_1[9], y0_2[9], y0_3[9] at low, middle and high temperature
% The nine elements are:
% initial value for solid void fraction, initial value for potential
% active site, active site, dead site for site 1(multiply by solid void
% fraction), initial value for potential active site, active site,
% dead site for site 2 (multiply by solid fraction), initial value for
% mass fraction of monomer in solid phase (multiply by solid fraction),
% initial value for solid temperature.

y0_1=[(d0)^3.0*pi/6.0*C,(d0)^3.0*pi/6.0,0.0,0.0,(d0)^3.0*pi/6.0,0.0,0.0,0.0,T1];
y0_2=[(d0)^3.0*pi/6.0*C,(d0)^3.0*pi/6.0,0.0,0.0,(d0)^3.0*pi/6.0,0.0,0.0,0.0,T2];
y0_3=[(d0)^3.0*pi/6.0*C,(d0)^3.0*pi/6.0,0.0,0.0,(d0)^3.0*pi/6.0,0.0,0.0,0.0,T3];

% Use ODE solver to solve reaction engineering model at different temperatures

options=odeset('RelTol',1.0e-6, 'AbsTol', 1.0e-8)

```

```

[x,y_T1_f]=ode15s(@odefunc,tspan,y0_1,options,ke, T1) ;
[x,y_T2_f]=ode15s(@odefunc,tspan,y0_2,options,ke, T2) ;
[x,y_T3_f]=ode15s(@odefunc,tspan,y0_3,options,ke, T3) ;

%%%%%%%%%%%%%%%%%%%%%%%%%%%%%%%%%%%%%%%%%%%%%%%%%%%%%%%%%%%%%%%%%%%%%%%%
% Calculate isothermal effectiveness-factor for site 1 and 2 and then %
% calculate the reaction rate from Reaction Engineering Model      %
%%%%%%%%%%%%%%%%%%%%%%%%%%%%%%%%%%%%%%%%%%%%%%%%%%%%%%%%%%%%%%%%%%%%%%%%

% Low temperature

small_number=1.0e-20;

dia_T1=((y_T1_f(:,1)/C)*6.0/pi).^(1.0/3.0);
phi1_T1=a*pgm*(dia_T1/2.0).*sqrt(exp(ke(3))*exp(ke(6)*1000./...
    (1.9872*y_T1_f(:,9))).*abs((C*y_T1_f(:,3)./y_T1_f(:,1)))/DeA+small_number);
eta1_T1=3.0*(phi1_T1.*coth(phi1_T1)-1)./(phi1_T1.*phi1_T1);
phi2_T1=a*pgm*(dia_T1/2.0).*sqrt(exp(ke(9))*exp(ke(12)*1000./...
    (1.9872*y_T1_f(:,9))).*abs((C*y_T1_f(:,6)./y_T1_f(:,1)))/DeA+small_number);
eta2_T1=3.0*(phi2_T1.*coth(phi2_T1)-1)./(phi2_T1.*phi2_T1);
RC2_T1_f=(pgm/c0)*(exp(ke(3))*exp(ke(6)*1000./(1.9872*y_T1_f(:,9))).*(y_T1_f(:,3))/60.0+...
    exp(ke(9))*exp(ke(12)*1000./(1.9872*y_T1_f(:,9))).*(y_T1_f(:,6))/60.0);

% Middle temperature

dia_T2=((y_T2_f(:,1)/C)*6.0/pi).^(1.0/3.0);
phi1_T2=a*pgm*(dia_T2/2.0).*sqrt(exp(ke(3))*exp(ke(6)*1000./...
    (1.9872*y_T2_f(:,9))).*abs((C*y_T2_f(:,3)./y_T2_f(:,1)))/DeA+small_number);
eta1_T2=3.0*(phi1_T2.*coth(phi1_T2)-1)./(phi1_T2.*phi1_T2);
phi2_T2=a*pgm*(dia_T2/2.0).*sqrt(exp(ke(9))*exp(ke(12)*1000./...
    (1.9872*y_T2_f(:,9))).*abs((C*y_T2_f(:,6)./y_T2_f(:,1)))/DeA+small_number);
eta2_T2=3.0*(phi2_T2.*coth(phi2_T2)-1)./(phi2_T2.*phi2_T2);
RC2_T2_f=(pgm/c0)*(exp(ke(3))*exp(ke(6)*1000./(1.9872*y_T2_f(:,9))).*(y_T2_f(:,3))/60.0+...
    exp(ke(9))*exp(ke(12)*1000./(1.9872*y_T2_f(:,9))).*(y_T2_f(:,6))/60.0);

% High temperature

dia_T3=((y_T3_f(:,1)/C)*6.0/pi).^(1.0/3.0);
phi1_T3=a*pgm*(dia_T3/2.0).*sqrt(exp(ke(3))*exp(ke(6)*1000./...
    (1.9872*y_T3_f(:,9))).*abs((C*y_T3_f(:,3)./y_T3_f(:,1)))/DeA+small_number);

```

```

eta1_T3=3.0*(phi1_T3.*coth(phi1_T3)-1)./(phi1_T3.*phi1_T3);
phi2_T3=a*pgm*(dia_T3/2.0).*sqrt(exp(ke(9))*exp(ke(12)*1000./...
    (1.9872*y_T3_f(:,9))).*abs((C*y_T3_f(:,6)./y_T3_f(:,1)))/DeA+small_number);
eta2_T3=3.0*(phi2_T3.*coth(phi2_T3)-1)./(phi2_T3.*phi2_T3);
RC2_T3_f=(pgm/c0)*(exp(ke(3))*exp(ke(6)*1000./(1.9872*y_T3_f(:,9))).*(y_T3_f(:,3))/60.0+...
    exp(ke(9))*exp(ke(12)*1000./(1.9872*y_T3_f(:,9))).*(y_T3_f(:,6))/60.0);

% plot the fitting curves from REM and compared with experimental data

figure
plot(t,y1(:),'x',t,y2(:),'*',t,y3(:),'+')
hold on
plot(x,RC2_T1_f,'-',x,RC2_T2_f,'--',x,RC2_T3_f,'-.','linewidth',2.5);
xlabel('Time'); ylabel('Reaction rate');

% Calculate R value

s(1)=sum((y1-RC2_T1_f).^2); s(2)=sum((y2-RC2_T2_f).^2);
s(3)=sum((y3-RC2_T3_f).^2);
q(1)=sum((RC2_T1_f-mean(RC2_T1_f)).^2);
q(2)=sum((RC2_T2_f-mean(RC2_T2_f)).^2);
q(3)=sum((RC2_T3_f-mean(RC2_T3_f)).^2); M=sum(w.*q); J=sum(w.*s);
R=(M-J)/M

%%%%%%%%%%%%%%%%%%%%%%%%%%%%%%%%%%%%%%%%%%%%%%%%%%%%%%%%%%%%%%%%%%%%%%%%
% Subroutine J=objfunc(ke, t_matrix, y_matrix) %
%%%%%%%%%%%%%%%%%%%%%%%%%%%%%%%%%%%%%%%%%%%%%%%%%%%%%%%%%%%%%%%%%%%%%%%%
function J=objfunc(ke,t_matrix,y_matrix)

% Input data
% tspan: time
% C and a: constants, explained in the thesis
% d0:initial catalyst diameter
% eps0 and c0:initial solid void fraction and initial concentration
% pgm: effect of pressure
% DeA: effective diffusivity
% T1 T2 T3: low middle and high temperature

tspan=t_matrix(:,1); C=a;d0=; eps0=(d0)^3.0*pi/6.0*C;
c0=(d0)^3.0*pi/6.0; pgm=; DeA=; T1=;T2=;T3=;

```

```

% Input data
% initial value for y0_1[9], y0_2[9], y0_3[9] at low, middle and high temperature
% The nine elements are:
% initial value for solid void fraction, initial value for potential active site,
% active site, dead site for site 1(multiply by solid void fraction),
% initial value for potential active site, active site, dead site for site 2
% (multiply by solid fraction), initial value for mass fraction of monomer in solid phase
% (multiply by solid fraction), initial value for solid temperature.

y0_1=[(d0)^3.0*pi/6.0*C,(d0)^3.0*pi/6.0,0.0,0.0,(d0)^3.0*pi/6.0,0.0,0.0,0.0,T1];
y0_2=[(d0)^3.0*pi/6.0*C,(d0)^3.0*pi/6.0,0.0,0.0,(d0)^3.0*pi/6.0,0.0,0.0,0.0,T2];
y0_3=[(d0)^3.0*pi/6.0*C,(d0)^3.0*pi/6.0,0.0,0.0,(d0)^3.0*pi/6.0,0.0,0.0,0.0,T3];

% Use ODE solver to solve reaction engineering model at different temperatures

options=odeset('RelTol',1.0e-6,'AbsTol',1.0e-8')
[x,y_T1]=ode15s(@odefunc,tspan,y0_1,options,ke,T1) ;
[x,y_T2]=ode15s(@odefunc,tspan,y0_2,options,ke,T2) ;
[x,y_T3]=ode15s(@odefunc,tspan,y0_3,options,ke,T3) ;

%calculate isothermal effectiveness-factor for site 1 and 2 and then calculate the
%reaction rate from Reaction Engineering Model

% Low temperature

small_number=1.0e-20;

dia_T1=((y_T1(:,1)/C)*6.0/pi)^(1.0/3.0);
phi1_T1=a*pgm*(dia_T1/2.0).*sqrt(exp(ke(3))*exp(ke(6)*1000./...
(1.9872*y_T1(:,9))).*abs((C*y_T1(:,3)./y_T1(:,1)))/DeA+small_number);
eta1_T1=3.0*(phi1_T1.*coth(phi1_T1)-1)/(phi1_T1.*phi1_T1);
phi2_T1=a*pgm*(dia_T1/2.0).*sqrt(exp(ke(9))*exp(ke(12)*1000./...
(1.9872*y_T1(:,9))).*abs((C*y_T1(:,6)./y_T1(:,1)))/DeA+small_number);
eta2_T1=3.0*(phi2_T1.*coth(phi2_T1)-1)/(phi2_T1.*phi2_T1);
RC2_T1=(pgm/c0)*(exp(ke(3))*exp(ke(6)*1000./(1.9872*y_T1(:,9))).*(y_T1(:,3))/60.0+...
exp(ke(9))*exp(ke(12)*1000./(1.9872*y_T1(:,9))).*(y_T1(:,6))/60.0);

% Middle temperature

dia_T2=((y_T2(:,1)/C)*6.0/pi)^(1.0/3.0);

```

```

phi1_T2=a*pgm*(dia_T2/2.0).*sqrt(exp(ke(3))*exp(ke(6)*1000./...
    (1.9872*y_T2(:,9))).*abs((C*y_T2(:,3)./y_T2(:,1))/DeA+small_number);
eta1_T2=3.0*(phi1_T2.*coth(phi1_T2)-1)./(phi1_T2.*phi1_T2);
phi2_T2=a*pgm*(dia_T2/2.0).*sqrt(exp(ke(9))*exp(ke(12)*1000./...
    (1.9872*y_T2(:,9))).*abs((C*y_T2(:,6)./y_T2(:,1))/DeA+small_number);
eta2_T2=3.0*(phi2_T2.*coth(phi2_T2)-1)./(phi2_T2.*phi2_T2);
RC2_T2=(pgm/c0)*(exp(ke(3))*exp(ke(6)*1000./(1.9872*y_T2(:,9))).*(y_T2(:,3))/60.0+...
    exp(ke(9))*exp(ke(12)*1000./(1.9872*y_T2(:,9))).*(y_T2(:,6))/60.0);

% High temperature

dia_T3=((y_T3(:,1)/C)*6.0/pi).^(1.0/3.0);
phi1_T3=a*pgm*(dia_T3/2.0).*sqrt(exp(ke(3))*exp(ke(6)*1000./...
    (1.9872*y_T3(:,9))).*abs((C*y_T3(:,3)./y_T3(:,1))/DeA+small_number);
eta1_T3=3.0*(phi1_T3.*coth(phi1_T3)-1)./(phi1_T3.*phi1_T3);
phi2_T3=a*pgm*(dia_T3/2.0).*sqrt(exp(ke(9))*exp(ke(12)*1000./...
    (1.9872*y_T3(:,9))).*abs((C*y_T3(:,6)./y_T3(:,1))/DeA+small_number);
eta2_T3=3.0*(phi2_T3.*coth(phi2_T3)-1)./(phi2_T3.*phi2_T3);
RC2_T3=(pgm/c0)*(exp(ke(3))*exp(ke(6)*1000./(1.9872*y_T3(:,9))).*(y_T3(:,3))/60.0+...
    exp(ke(9))*exp(ke(12)*1000./(1.9872*y_T3(:,9))).*(y_T3(:,6))/60.0);

% Return the reaction rates calculate from reaction engineering model
% at different temperatures using the current ke.

J=[RC2_T1,RC2_T2, RC2_T3];

%%%%%%%%%%%%%%%%%%%%%%%%%%%%%%%%%%%%%%%%%%%%%%%%%%%%%%%%%%%%%%%%%%%%%%%%%%
% Subroutine dydx=odefunc(t, y, ke, Tem) %
%%%%%%%%%%%%%%%%%%%%%%%%%%%%%%%%%%%%%%%%%%%%%%%%%%%%%%%%%%%%%%%%%%%%%%%%%%
function dydx=odefunc(t,y,ke,Tem)

% Assign the rate constant and active energy.
k11=ke(1); k21=ke(2); k31=ke(3); deltaE11=ke(4); deltaE21=ke(5);
deltaE31=ke(6); k12=ke(7); k22=ke(8); k32=ke(9); deltaE12=ke(10);
deltaE22=ke(11); deltaE32=ke(12);

% Input variables:
% C and a: Constants, explained in the thesis
% pgm: Effect of pressure
% Db: Monomer bulk diffusivity
% DeA: Effective diffusivity

```

```

% Cg: Monomer concentration in the gas phase
% rho_s: Polymer density
% Cp: Heat capacity of polymer
% Hr: Heat release of polymerization reaction
% lam_f: Thermal conductivity
% Sh: Sherwood number
% Nu: Nusselt number
% dia: Particle diameter calculated from solid void fraction

a=; C= ; pgm=; Db=; DeA=; Cg=; rhos=;
Cp=; Hr=; lam_f=; sh=; Nu=;
dia=((y(1)/C)*6.0/pi)^(1.0/3.0);

% Calculate isothermal effectiveness-factor for site 1 and site 2
small_number=1.0e-20;

phi1=a*(dia/2.0)*sqrt(exp(k31)*exp(deltaE31*1000/(1.9872*y(9)))*pgm*(abs(C*y(3)/y(1)))/DeA+small_number);
if (phi1>=1.0e-6)
    eta1=3.0*(phi1*coth(phi1)-1)/(phi1*phi1);
else
    eta1=1.0;
end

phi2=a*(dia/2.0)*sqrt(exp(k32)*exp(deltaE32*1000/(1.9872*y(9)))*pgm*(abs(C*y(6)/y(1)))/DeA+small_number);
if(phi2>=1.0e-6)
    eta2=3.0*(phi2*coth(phi2)-1)/(phi2*phi2);
else
    eta2=1.0;
end

% Solid void fraction
dydx1=(2.0*Db*sh/dia)*(6.0/dia)*(Cg*y(1)-y(8))*(28.0/rhos)*3600.0;

% First site: potential active site, active site, dead site
% (multiply by solid void fraction)

dydx2=-exp(k11)*exp(deltaE11*1000.0/(1.9872*y(9)))*y(2);
dydx3=exp(k11)*exp(deltaE11*1000.0/(1.9872*y(9)))*y(2)...
-exp(k21)*exp(deltaE21*1000.0/(1.9872*y(9)))*y(3);
dydx4=exp(k21)*exp(deltaE21*1000.0/(1.9872*y(9)))*y(3);

```

```

% Second site: potential active site, active site, dead site
% (multiply by solid void fraction)

dydx5=-exp(k12)*exp(deltaE12*1000.0/(1.9872*y(9)))*y(5);
dydx6=exp(k12)*exp(deltaE12*1000.0/(1.9872*y(9)))*y(5)...
-exp(k22)*exp(deltaE22*1000.0/(1.9872*y(9)))*y(6);
dydx7=exp(k22)*exp(deltaE22*1000.0/(1.9872*y(9)))*y(6);

% Mass transfer (multiply by solid fraction)

dydx8=(2.0*Db*sh/dia)*(6.0/dia)*(Cg*y(1)-y(8))*3600.0...
-a*eta1*exp(k31)*exp(deltaE31*1000/(1.9872*y(9)))*pgm*y(8)*(C*y(3)/y(1))...
-a*eta2*exp(k32)*exp(deltaE32*1000/(1.9872*y(9)))*pgm*y(8)*(C*y(6)/y(1));

% Energy balance, change to zero if you don't want to solve energy equation

dydx9=-(2.0*lam_f*Nu/dia)*(6.0/dia)*(y(9)-Tem)*3600.0/(Cp*rhos)...
-a*eta1*Hr*exp(k31)*exp(deltaE31*1000.0/(1.9872*y(9)))*(C*y(3)/y(1))*(y(8)/y(1))*pgm/(Cp*rhos)...
-a*eta2*Hr*exp(k32)*exp(deltaE32*1000.0/(1.9872*y(9)))*(C*y(6)/y(1))*(y(8)/y(1))*pgm/(Cp*rhos);

dydx=[dydx1;dydx2;dydx3;dydx4;dydx5;dydx6;dydx7;dydx8;dydx9];

```

Calculate moments of the PSD of initial catalyst and final polymer.[drive_moments.m, odefunc.m, quad.m]

```

%%%%%%%%%%%%%%%%%%%%%%%%%%%%%%%%%%%%%%%%%%%%%%%%%%%%%%%%%%%%%%%%%%%%%%%%
% Main program for calculate moments of the PSD of initial%
% catalyst and final polymer                                     %
%%%%%%%%%%%%%%%%%%%%%%%%%%%%%%%%%%%%%%%%%%%%%%%%%%%%%%%%%%%%%%%%%%%%%%%%

clear all
close all
clc
format long

% Load PSD of catalyst and polymer

load catalyst.txt; L=catalyst(:,1); f=catalyst(:,2);

```

```

load polymer.txt; L_p=polymer(:,1); f_p=polymer(:,2);

% Plot particle size distribution of catalyst

plot(L*10000,f); ylabel('f(L)'); xlabel('Particle size L')

% Calculate the first six moments of catalyst PSD

m_0_1=trapz(L, f);
m_0=m_0_1/m_0_1;
m_1=trapz(L,(f.*L))/m_0_1;
m_2=trapz(L,(f.*L.^2))/m_0_1;
m_3=trapz(L,(f.*L.^3))/m_0_1;
m_4=trapz(L,(f.*L.^4))/m_0_1;
m_5=trapz(L,(f.*L.^5))/m_0_1;
sigma=sqrt(m_2-m_1*m_1);
d43=m_4/m_3;
d32=m_3/m_2;
d30=(m_3/m_0)^(1/3);

% Calculate the probability of catalyst and final polymer

t=cumtrapz(f);
t_p=cumtrapz(f_p);

% Plot the normal probability plot of catalyst and final polymer

figure plot(L*10000,t,'r-', 'linewidth',2.0);
ylabel('Probability'); xlabel('Particle size L');
grid on
hold on
plot(L_p*10000,t_p,'g-', 'linewidth',2.0);

% Use PD algorithm to calculate the length and weights of each node to
% represent the catalyst PSD.
% the example use three nodes.

m(1)=m_0; m(2)=m_1; m(3)=m_2; m(4)=m_3; m(5)=m_4; m(6)=m_5;
n=6; [d,w]=quad(m,n);

```

```

% Plot the normal probability plot of catalyst calculated from QMOM

w1_new(1)=0; w1_new(2)=w(1); w1_new(3)=w(2); w1_new(4)=w(3);
d1_new(1)=0; d1_new(2)=d(1); d1_new(3)=d(2); d1_new(4)=d(3);
t1=cumtrapz(w1_new*100);
plot(d1_new*10000, t1, 'diamond')

% Input data,
% tau: Final integration time, usually it is 10 times of average residence time, tau_ave
% C:constant, explained in thesis
% ke: Rate constants and active energy from three curve fitting for each
% case
% T2: Operation temperature
% n: Number of nodes
% d0(n): Initial catalyst diameter for each node
% omega(n): Weights for each node for the initial catalyst PSD
% tau_ave: Average residence time

tau=; tspan=0:0.01:tau; C=; ke=[]; T2=;
omega_1=w(1);omega_2=w(2);omega_3=w(3);
omega=[omega_1;omega_2;omega_3];

% Apply chemical reaction engineering model on each node

% First node

d0(1)=d(1);
y0_1=[(d0(1))^3.0*pi/6.0*C, (d0(1))^3.0*pi/6.0,0.0,0.0, (d0(1))^3.0*pi/6.0,0.0,0.0,0.0,T2];
options=odeset('RelTol',1.0e-6, 'AbsTol', 1.0e-8)
[x,y1_T2_f]=ode15s(@odefunc,tspan,y0_1,options,ke, T2) ;

% second node

d0(2)=d(2);
y0_2=[(d0(2))^3.0*pi/6.0*C, (d0(2))^3.0*pi/6.0,0.0,0.0, (d0(2))^3.0*pi/6.0,0.0,0.0,0.0,T2];
options=odeset('RelTol',1.0e-6, 'AbsTol', 1.0e-8)
[x,y2_T2_f]=ode15s(@odefunc,tspan,y0_2,options,ke, T2) ;

% Third node

```

```

d0(3)=d(3);
y0_3=[(d0(3))^3.0*pi/6.0*C,(d0(3))^3.0*pi/6.0,0.0,0.0,(d0(3))^3.0*pi/6.0,0.0,0.0,0.0,T2];
options=odeset('RelTol',1.0e-6, 'AbsTol', 1.0e-8)
[x,y3_T2_f]=ode15s(@odefunc,tspan,y0_3,options,ke, T2) ;

% Integrate three curves (length change over the time) over the tspan, and
% then multiple by the weights for each node and get the final polymer's moments, m.

tau_ave=4.3;

m_0_1=trapz(x,(1/tau_ave).*exp(-x/tau_ave));
m_0_2=trapz(x,(1/tau_ave).*exp(-x/tau_ave));
m_0_3=trapz(x,(1/tau_ave).*exp(-x/tau_ave));

m_1_1=trapz(x,(6.*y1_T2_f(:,1)/(pi*C)).^(1/3)*(10000/tau_ave).*exp(-x/tau_ave));
m_1_2=trapz(x,(6.*y2_T2_f(:,1)/(pi*C)).^(1/3)*(10000/tau_ave).*exp(-x/tau_ave));
m_1_3=trapz(x,(6.*y3_T2_f(:,1)/(pi*C)).^(1/3)*(10000/tau_ave).*exp(-x/tau_ave));

m_2_1=trapz(x,((6.*y1_T2_f(:,1)/(pi*C)).^(1/3)*10000).^(2.0)*(1.0/tau_ave).*exp(-x/tau_ave));
m_2_2=trapz(x,((6.*y2_T2_f(:,1)/(pi*C)).^(1/3)*10000).^(2.0)*(1.0/tau_ave).*exp(-x/tau_ave));
m_2_3=trapz(x,((6.*y3_T2_f(:,1)/(pi*C)).^(1/3)*10000).^(2.0)*(1.0/tau_ave).*exp(-x/tau_ave));

m_3_1=trapz(x,((6.*y1_T2_f(:,1)/(pi*C)).^(1/3)*10000).^(3.0)*(1.0/tau_ave).*exp(-x/tau_ave));
m_3_2=trapz(x,((6.*y2_T2_f(:,1)/(pi*C)).^(1/3)*10000).^(3.0)*(1.0/tau_ave).*exp(-x/tau_ave));
m_3_3=trapz(x,((6.*y3_T2_f(:,1)/(pi*C)).^(1/3)*10000).^(3.0)*(1.0/tau_ave).*exp(-x/tau_ave));

m_4_1=trapz(x,((6.*y1_T2_f(:,1)/(pi*C)).^(1/3)*10000).^(4.0)*(1.0/tau_ave).*exp(-x/tau_ave));
m_4_2=trapz(x,((6.*y2_T2_f(:,1)/(pi*C)).^(1/3)*10000).^(4.0)*(1.0/tau_ave).*exp(-x/tau_ave));
m_4_3=trapz(x,((6.*y3_T2_f(:,1)/(pi*C)).^(1/3)*10000).^(4.0)*(1.0/tau_ave).*exp(-x/tau_ave));

m_5_1=trapz(x,((6.*y1_T2_f(:,1)/(pi*C)).^(1/3)*10000).^(5.0)*(1.0/tau_ave).*exp(-x/tau_ave));
m_5_2=trapz(x,((6.*y2_T2_f(:,1)/(pi*C)).^(1/3)*10000).^(5.0)*(1.0/tau_ave).*exp(-x/tau_ave));
m_5_3=trapz(x,((6.*y3_T2_f(:,1)/(pi*C)).^(1/3)*10000).^(5.0)*(1.0/tau_ave).*exp(-x/tau_ave));

% Calculate the first six moments of the final polymer

m_0=m_0_1*omega_1+m_0_2*omega_2+m_0_3*omega_3;
m_1=(m_1_1*omega_1+m_1_2*omega_2+m_1_3*omega_3)/m_0;

```

```

m_2=(m_2_1*omega_1+m_2_2*omega_2+m_2_3*omega_3)/m_0;
m_3=(m_3_1*omega_1+m_3_2*omega_2+m_3_3*omega_3)/m_0;
m_4=(m_4_1*omega_1+m_4_2*omega_2+m_4_3*omega_3)/m_0;
m_5=(m_5_1*omega_1+m_5_2*omega_2+m_5_3*omega_3)/m_0; m_0=m_0/m_0;

% Use PD algorithm to calculate the length and weights of each node to
% represent the final polymer PSD.
% Here we use three nodes.

m(1)=m_0; m(2)=m_1; m(3)=m_2; m(4)=m_3; m(5)=m_4; m(6)=m_5;
n=6; [d_p,w_p]=quad(m,n);

% Plot the normal probability plot of polymer calculated from QMOM

w2_new(1)=0; w2_new(2)=w_p(1); w2_new(3)=w_p(2); w2_new(4)=w_p(3);
d2_new(1)=0; d2_new(2)=d_p(1); d2_new(3)=d_p(2); d2_new(4)=d_p(3);
t2=cumtrapz(w2_new*100);
plot (d2_new, t2, 'square')
hold off

%%%%%%%%%%%%%%%%%%%%%%%%%%%%%%%%%%%%%%%%%%%%%%%%%%%%%%%%%%%%%%%%%%%%%%%%%%%%%%
% Plot the graphs for the particle diameter change with age, %
% Particle temperature increase with age %
% Particle temperature increase with particle diameter %
%%%%%%%%%%%%%%%%%%%%%%%%%%%%%%%%%%%%%%%%%%%%%%%%%%%%%%%%%%%%%%%%%%%%%%%%%%%%%%

figure
plot(x,(6.*y1_T2_f(:,1))/(pi*C)).^(1/3)*10000,'r-', 'linewidth',2);
hold on
plot(x,(6.*y2_T2_f(:,1))/(pi*C)).^(1/3)*10000,'b--', 'linewidth',2);
hold on
plot(x,(6.*y3_T2_f(:,1))/(pi*C)).^(1/3)*10000,'g-.', 'linewidth',2);
xlabel('Age'); ylabel('L'); axis([]);

figure
plot(x,y1_T2_f(:,9)-T2,'r-', 'linewidth',2);
hold on
plot(x,y2_T2_f(:,9)-T2,'b--', 'linewidth',2);
hold on
plot(x,y3_T2_f(:,9)-T2,'g-.', 'linewidth',2);

```

```
xlabel('Age');ylabel('T');axis([]);
```

```
figure
```

```
plot((6.*y1_T2_f(:,1)/(pi*C)).^(1/3)*10000,y1_T2_f(:,9)-T2,'r-', 'linewidth',2);
```

```
hold on
```

```
plot((6.*y2_T2_f(:,1)/(pi*C)).^(1/3)*10000,y2_T2_f(:,9)-T2,'b--', 'linewidth',2);
```

```
hold on
```

```
plot((6.*y3_T2_f(:,1)/(pi*C)).^(1/3)*10000,y3_T2_f(:,9)-T2,'g-.', 'linewidth',2);
```

```
xlabel('L'); ylabel('T');
```